A modern extraction of Compton Form Factors from Deeply Virtual Compton Scattering

Liliet Calero Diaz
Aurora, Illinois

Bachelor of Science in Nuclear Physics
Higher Institute of Applied Sciences and Technologies, Havana, Cuba, 2010

A Dissertation submitted to the Graduate Faculty
of the University of Virginia in Candidacy for the Degree of
Doctor of Philosophy

Department of Physics

University of Virginia
November 2023

Defense Committee Members
Prof. Dustin Keller, *Advisor*
Prof. Jeffrey Teo
Prof. Donal Day
Prof. Stephen Baek

A modern extraction of Compton Form Factors from Deeply Virtual Compton Scattering

Liliet Calero Diaz

(ABSTRACT)

Over the last 20 years, there has been intense experimental activity dedicated to the measurement of observables to help build a 3D description of the nucleon. Generalized Parton Distributions (GPDs) describe complementary aspects of the structure of hadrons, providing qualitative and quantitative information about the partonic structure and dynamics such as orbital angular momentum. The cleanest process to access GPDs is the Deeply Virtual Compton Scattering (DVCS), where the cross-section is parametrized in terms of Compton Form Factors (CFFs) which are convolutions of GPDs with coefficient functions computed from perturbative QCD. The CFFs are extracted from DVCS experimental data taken at Jefferson Lab, including the most recent Hall A data. This analysis consists of a novel local fitting technique using χ^2 maps to constrain the CFFs. The CFFs, $\Re e\mathcal{H}$, $\Re e\mathcal{E}$, and $\Re e\widetilde{\mathcal{H}}$ are determined independently in each kinematic bin for the unpolarized beam-target configuration at twist-2 approximation using the formalism developed by A.V. Belitsky, D. Müller, and A. Kirchner (BKM10). The resulting CFFs are used to train and regularize a Deep Neural Network (DNN) to obtain a global behavior of the CFFs with minimal model dependency. An advanced DNN-driven extraction with prediction capabilities that shows potential for improving the accuracy, precision, and reliability of future CFFs extractions is introduced. These procedures are tested and systematically studied using pseudo-data generated with kinematics mimicking the experimental data.

To my beloved parents.

Acknowledgments

I would like these acknowledgments to pay respect to those who have been instrumental in this endeavor. They are the unsung heroes whose unwavering support and contributions have been the driving force behind the fruition of this project. However, I must confess that my love and gratitude for the individuals mentioned here transcend the words I can capture in this manuscript. Their collective effort, dedication, and invaluable assistance have been the cornerstone of this undertaking. I am profoundly indebted to each and every one of them. Yet, I am acutely aware that the scope of my appreciation is beyond the reach of mere words. In their actions, their unwavering belief, and their steadfast encouragement, they have given life to this work, and for that, my heart is eternally grateful.

First I would like to extend my most heartfelt appreciation to my advisor Dustin Keller. His trust, support, and guidance have been unwavering throughout my academic journey. He was always available to offer advice or answer my questions whenever I needed his help. His support during my motherhood and encouragement during the difficult and stressful years of my PhD have been truly invaluable. He is always available to discuss scientific results and offers countless insights and valuable advice despite the increasing weight of administrative tasks he has had over the years. I will keep a moving memory of the warmth of the human relationship we built over my stay at UVA. The bonds we forged, the lessons I learned, and the support I received have left an indelible mark on my heart.

I want to express my deep appreciation to Donal Day, who, from the very first moment we met outside of his office, kindly welcomed me into the UVA Polarized Target group. His warm reception and willingness to extend a helping hand were the first steps in a journey that would lead me into the captivating world of spin physics at UVA. I feel fortunate to have crossed paths with Donal, and I am indebted to him for his unwavering belief in my potential and I am deeply appreciative of his mentorship as part of my research committee.

I would like to extend my gratitude to Zulkaida Akbar, with whom I closely worked on the extraction of CFFs and GPDs physics. His invaluable input, thoughtful discussions, and unwavering support during my time at UVA have been instru-

mental in my research journey. I am very thankful to him not just for the scientific collaborations we've shared but for the friendship and camaraderie that has developed along the way.

I want to thank all the UVA polarized target group at Fermilab. In particular, I want to express my deep appreciation to Ishara Fernando whom I closely work and whose support and friendship have been a source of strength and a reminder that we are not just colleagues but a close-knit family. Ishara's dedication, warmth, and the sense of unity he fosters within the group have made our journey a truly rewarding one.

I want to thank Simonetta Liuti, to whom I owe an immeasurable debt of gratitude. Her role as a scientist and mother is a true inspiration, and I will forever be thankful for her guidance and mentorship. Our discussions, ranging from the intricacies of lambda polarization to the complexities of CFFs, have been both intellectually stimulating and deeply enriching. I am honored to have had the privilege of learning from such an exceptional professor.

I want to extend my heartfelt thanks to my fellow classmates who have been on this academic journey with me. In particular, I'd like to express my deep gratitude to Sharon and Shammi, with whom I have forged a close friendship, and with whom I have shared numerous experiences and challenges. Your companionship has made this journey not just educational but truly memorable. I also want to thank Robin Thomas, whose resilience and commitment have been an inspiration to us all. A big thanks goes to Charlie, who has been an indispensable resource for all of us. I owe a debt of gratitude to Charlie for his invaluable office hours, his amazing tutoring skills, and his unwavering dedication to our success. He is not only an excellent tutor but also a genuinely caring human being who has made a significant difference in our academic lives. I am deeply thankful for his support, as are all my classmates.

I would like to extend my gratitude to every member of the physics department at UVA. The collective expertise and support from this community have played an integral role in my academic journey. In particular, I want to express my deep appreciation to Peter Cline, who has consistently been a guiding light for students. Whenever I've needed help or advice, Peter has been my go-to source of knowledge and support.

For the personal aspect of my journey, I want to extend my deepest gratitude to my parents, Dalia and Reinaldo, and my sister, Yuliet. My parents and sister have been my pillars of strength, always believing in my potential and pushing me to pursue my dreams. Their sacrifices have not gone unnoticed, and I am eternally

thankful for the family bond that has carried me through to this day.

I offer a profound and heartfelt thanks to my soulmate, Ernesto. He has been a constant presence through all the challenges and hardships of my graduate career, consistently believing in me and my potential. Without his unwavering love, boundless patience, and countless sacrifices, I would never have reached the point I am at today.

I extend immense thanks to the joy and the driving force of my life, my little son Marcelo. In his own way, helps create a quiet and focused space for 'mami' to work. He willingly closes doors and ensures a peaceful environment, understanding the importance of my pursuits. His unwavering support and his ability to adapt to the demands of my academic journey have been invaluable. Marcelo's presence constantly reminds me of the love and motivation that fuel my determination. Marcelo's sacrifices, big and small, are a testament to the resilience and understanding of a remarkable young individual. He is not only my source of joy but also an inspiration for me to keep striving for success. I am profoundly grateful for his presence in my life and for the sacrifices he makes to support my goals.

Finally, I want to express my heartfelt gratitude to my defense committee: Prof. Dustin Keller, Prof. Donal Day, Prof. Jeffrey Teo, and Prof. Stephen Baek. I am grateful for the time and effort they have dedicated to this process and for their commitment to academic excellence. It is a privilege to have had the opportunity to present my work to this exceptional committee, and their involvement has been a significant highlight of my academic journey.

Contents

List of Figures

List of Tables

List of Abbreviations

AM Angular Momentum
ANN Artificial Neural Network
BCA Beam Charge Asymmetry
BF Breit Frame
BH Bethe-Heitler
BKM Belitsky-Kirchner-Müller
BMJ Belitsky-Müller-Ji
BMMP Braun-Manashov-Müller-Pirnay
BNL Brookhaven National Lab
BSA Beam-Spin Asymmetries
CFF Compton form factor
DD Double Distribution
DDVCS Double Deeply Virtual Compton Scattering
DGLAP Dokshitzer-Gribov-Lipatov-Altarelli-Parisi
DIS Deep Inelastic Scattering
DNN Deep Neural Network
DSA Double-Spin Asymmetries
DVCS Deeply Virtual Compton Scattering
DVMP Deeply Virtual Meson Production
EIC Electron Ion Collider
EMT Energy Momentum Tensor
ERBL Efremov-Radyushkin-Brodsky-Lepage
FFs elastic Form Factors
GFF Gravitational Form Factor
GK Goloskokov-Kroll
GPD Generalised Parton Distribution
HERA Hadron-Electron Ring Accelerator
IMF Infinite Momentum Frame
IPD Impact Parameter Distribution
JLab Jefferson Lab

KM Kumerički-Müller
LMI Local Multivariate Inference
LO / NLO Leading Order / Next-to-Leading Order
OAM Orbital Angular Momentum
PDF Parton Distribution Function
QCD Quantum Chromodynamics
QED Quantum Electrodynamics
QPM Quark Parton Model
R-LMI Recursive Local Multivariate Inference
SLAC Stanford Linear Accelerator Center
SM Standard Model
TCS Time-like Compton Scattering
TMD Transverse Momentum Dependent PDF
TSA Target-Spin Asymmetries
VGG Vanderhaeghen-Guichon-Guidal
χ**MI** χ^2 Maps Inference

Introduction

Exploring the inner workings of strongly interacting systems through the analysis of quark and gluon structure is a cornerstone of particle physics. In the past few decades, comprehensive investigations of parton distribution functions (PDFs) have yielded detailed insights into the longitudinal momentum distribution of quarks and gluons, thereby offering a one-dimensional glimpse into the nature of hadrons. However, the comprehensive delineation of the multi-dimensional partonic structure of hadrons remains a paramount objective for ongoing experiments at esteemed facilities such as DESY, JLab, BNL, and CERN, as well as the prospective Electron-Ion Collider, where studying quantities revealing the transverse structure of hadrons is imperative. Among those quantities are a new class of light-cone matrix elements, called Generalized Parton Distributions (GPDs) introduced in the 1990s [1–5] and since then, they have been widely recognized as one of the key objects to explore the structure of hadrons.

The GPDs seemingly unify different physical quantities, such as the PDFs and nucleon form factors (FFs), into the same framework. This makes them complicated multi-variable functions with richer information than PDFs, encoding the largely unknown correlations between the transverse spatial structure of partons and their intrinsic longitudinal motion in the nucleon. This correlation provides a gateway to access the quark and gluon orbital angular momentum (OAM) and to elucidate the nucleon spin puzzle [6]. In particular, they provide 3D number densities of quarks and gluons within the nucleon [7–9], and a connection to the matrix elements of the energy-momentum tensor, making it possible to evaluate the total angular momentum and "mechanical" properties of hadrons, like pressure and shear stress at a given point of space [10, 11].

Experimental information on GPDs can be obtained from hard exclusive scattering processes such as deeply virtual Compton scattering (DVCS) [3], deeply virtual meson production (DVMP) [4], time-like Compton scattering (TCS) [12] and double deeply virtual Compton scattering (DDVCS) [13]. All of them allow us to study the transitions of hadrons from one state to another, with a unique insight into changes taking place at the partonic level. At leading twist, the scattering is produced off

a single parton of the nucleon with no other partons participating in the process and the nucleon structure is characterized by eight GPDs for each quark flavor: four GPDs conserving the helicity of the parton (chiral-even) and the other four flip the parton helicity (chiral-odd) [14, 15]. There also exist gluon GPDs. Each GPD depends on 3 variables x, ξ and t, where $x \pm \xi$ is the light-cone longitudinal momentum fraction of the struck quark before ("+" sign) and after ("−" sign) the scattering, resulting in a squared four-momentum transfer t to the nucleon (fig. 0.1). This gives rise to the division of the GPDs into two distinct regions, each carrying entirely different physical interpretations. An intuitive physical interpretation of the GPDs using light-cone coordinates for $x \in [\xi, 1]$ ($x \in [-1, -\xi]$) referred to as DGLAP [16–19] region, can be attributed to the amplitude of hitting a quark (antiquark) in the nucleon with momentum fraction $x + \xi$ ($\xi - x$) and putting it back with a different momentum fraction $x - \xi$ ($-\xi - x$) at a given transverse distance, relative to the transverse center of mass, in the nucleon. In the ERBL [20, 21] region, $x \in [-\xi, \xi]$ the GPD resemble distribution amplitudes governing the emission or absorption of a parton-antiparton pair with squared momentum t.

GPDs are most directly accessible in the DVCS process where an incoming photon with high virtuality Q^2, emitted by a high-energy lepton beam, hits a parton of the nucleon which radiates a final real photon ($\gamma^* p \rightarrow \gamma p$). The possibility of studying GPDs in suitable exclusive scattering processes rests on factorization theorems, as does the usual extraction of parton densities from inclusive and semi-inclusive measurements. The proven QCD factorization theorems [22, 23] demonstrate that the DVCS amplitude can be factorized into a hard photon-quark Compton scattering calculable in perturbative QCD and a soft part which encodes the complex unknown non-perturbative dynamics of the quarks in the nucleon described, in the QCD leading order framework, by the four chiral-even GPDs ($H, E, \widetilde{H}, \widetilde{E}$), in an expansion in inverse powers of Q^2 (twist-expansion) (fig. 0.1). This factorization has been shown to hold in the Bjorken limit for sufficiently large $Q^2 >> M^2$ as well as a small net momentum transfer to the proton $|t|/Q^2 << 1$ at fixed $x_B = Q^2/(2q \cdot P)$, where q and P are the virtual photon and initial proton four-momentum respectively. A consequence of the factorization is that GPDs are universal, as the differences between different processes are contained in the hard part. At the leading order, DVCS is not sensitive to the chiral-odd GPDs, but they can be measured in other exclusive processes such as pseudo-scalar meson production.

Although DVCS is one of the cleanest channels to access GPDs, it requires high enough luminosities to measure small cross sections, and a large combination of

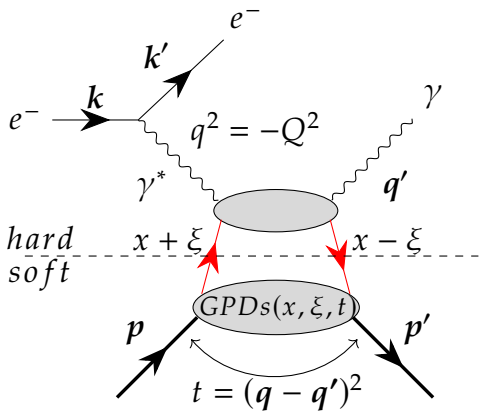

Figure 0.1: Factorisation of DVCS in the leading twist description at leading order.

experimental setups is needed in order to measure all the observables necessary to disentangle the contributions of the four GPDs. This includes different beam energies and beam charges, different kinematic coverages, DVCS on proton and neutron for quark GPDs flavor separation, and all possible unpolarized and polarized beam and target configurations. DVCS has been extensively studied in the last decade by DESY and JLab collaborations and recently by the completed COMPASS experiment at CERN, now turned into the AMBER experiment.

H1 [24, 25] and ZEUS [26] collider experiments at HERA measured the smallest $x_B \sim 10^{-4}$, and the largest $Q^2 \sim 100$ GeV^2 values where DVCS has been measured. Having access to both electron and positron beams, they published beam charge asymmetries as well as unpolarized cross sections at small x_B regions dominated by sea quarks and gluons. As of today, HERMES [27–33] experiment also at HERA, provided the most complete set of DVCS observables in x_B between 0.04 and 0.1 and Q^2 up to 7 GeV^2 using a fixed target which could be longitudinally or transversely polarized. At JLab [34–40], the CLAS (Hall-B) and Hall-A collaborations also made a series of high statistics DVCS dedicated experiments using a fixed target. They worked at a larger value of x_B of the order of 0.1 to 0.7 and Q^2 from 1 to 10 GeV^2, corresponding to the valence quarks region. In addition to unpolarized cross-sections, JLab has also provided asymmetry observables using a combination of longitudinally polarized beam and target. Among the available experimental data, only JLab has reported observables with high statistics and reasonably finely binned four-fold cross-sections and asymmetries. The Hall-A collaboration has also produced complementary neutron DVCS measurements that enable the separation of the u and d quark contributions to the leading GPDs [40]. DVCS cross-section measurements at $x_B = 0.056$ from the last runs taken by the COMPASS [41] exper-

iment at CERN with a fixed target, have been recently published.

Despite such a dedicated experimental program focused on DVCS significantly advanced worldwide, the intrinsic complexity of the GPDs needs more extensive and precise data to effectively constrain them in the multi-dimensional phase space of kinematic variables. Furthermore, one needs to cover this phase space with data collected for various processes and experimental setups, which is required to distinguish between many types of GPDs and contributions coming from various quark flavors and gluons. More data sensitive to GPDs will be delivered by the next generation of experiments. The upcoming DVCS experiment at COMPASS [42], which will employ a 160 GeV muon beam both positively and negatively charged, will collect data in a kinematic domain yet unexplored ($0.005 < x_B < 0.3$), between HERMES and the JLab experiments on the one hand, and the HERA collider experiments on the other hand, covering the region dominated by sea quarks. The upgraded CLAS12 spectrometer [43] in Hall B at JLab, will allow for precise tuning of GPD parametrizations and improve the statistics of the previous CLAS measurements. Approximately 85% of the new data covers a phase space in the valence quark region that has never been probed with DVCS before. With the first CLAS12 measurements on DVCS beam-spin asymmetries (BSA) published [44], measurements on unpolarized and polarised proton DVCS cross sections, as well as target-spin asymmetries (TSA) and double-spin asymmetries (DSA) with longitudinally and transversely polarized targets, are planned with a similar program for DVCS on the neutron. Additionally, new proposals are in preparation to utilize a future positron beam at JLab. Future electron-ion colliders like the EIC[45, 46], EicC [47], and LHeC [48], are at the center of a lot of attention thanks to their promise of a high luminosity coverage over an extended region at relatively small x_B and large Q^2 that will probe the gluon rich environment.

One major difficulty in the study of GPDs is that they appear in the DVCS amplitude as integrals over x from -1 to 1, as a consequence of the implied quark loop (fig. 0.1). Since x cannot be measured experimentally, the DVCS cross section is instead parametrized in terms of Compton Form Factors (CFFs) that are directly accessible. The factorization theorems allow us to express CFFs, as convolutions of GPDs with coefficient functions calculable at any order of perturbative QCD (pQCD).

At leading order and leading twist, the CFF $\mathcal{H}$ associated with the GPD H can

be expressed as:

$$\mathcal{H}(\xi,t) \equiv \sum_q \int_{-1}^{1} dx C_0^{q[-]}(x,\xi) H_q(x,\xi,t), \tag{1}$$

summing over all the quark flavors. At leading twist, the coefficient function has no scale dependence and reads [49]:

$$C_0^{q[\mp]}(x,\xi) = e_q^2\left(\frac{1}{\xi - x - i0} \mp \frac{1}{\xi + x - i0}\right), \tag{2}$$

where e_q^2 is the charge of the quarks in units of proton charge. Using the residue theorem, it is possible to decompose the integral (1) so that each CFF contains two real quantities, for the CFF $\mathcal{H}$ for example:

$$\mathcal{H}(\xi,t) = \Re e\mathcal{H}(\xi,t) + i\Im m\mathcal{H}(\xi,t) \tag{3}$$

where,

$$\Re e\mathcal{H}(\xi,t) = \sum_q \mathcal{P}\int_0^1 dx C_q^-[H_q(x,\xi,t) - H_q(-x,\xi,t)], \tag{4}$$

$$\Im m\mathcal{H}(\xi,t) = \pi \sum_q e_q^2\Big[H_q(\xi,\xi,t) - H_q(-\xi,\xi,t)\Big]. \tag{5}$$

$\mathcal{P}$ denotes the Cauchy principal value, the skewness ξ is related to x_B at leading twist as $\xi \approx x_B/(2-x_B)$ and,

$$C_q^{[\mp]}(x,\xi) = e_q^2\left(\frac{1}{\xi - x} \mp \frac{1}{\xi + x}\right). \tag{6}$$

Similar expressions hold for the CFFs $\mathcal{E}, \widetilde{\mathcal{H}}, \widetilde{\mathcal{E}}$ associated with the GPDs $E, \widetilde{H}, \widetilde{E}$ respectively, where the top sign in (6) applies for the unpolarized GPDs (H, E) and the bottom sign is for the polarized GPDs $(\widetilde{H}, \widetilde{E})$. Equations (4) and (5) show that observables sensitive to the imaginary part of the CFFs will only contain information along the line $x = \pm\xi$, whereas the real part probes GPD integrals over the momentum fraction x. Given the complicated kinematic dependence of the GPDs, retrieving them from CFFs is therefore a major challenge of the field, known as the deconvolution problem [50]. Thus, the maximum model-independent information which can be extracted from the DVCS reaction at leading twist are 8 CFFs, which depend on two variables, ξ and t, at QCD leading order. There is an additional Q^2 dependence in the CFFs (and in the GPDs) if QCD evolution is taken into account.

Since the CFFs are not practically invertible due to the large magnitude of uncertainty underlying the connection with GPDs [50, 51], inputs from theory play an important and complementary role in determining the GPDs. Current parametrizations of GPDs suffer from model dependency of phenomenological GPD models, like KM [52–54], GK [55] and VGG [56], which use a similar Ansätze with a rigid form and therefore cannot be considered as diverse sources for the estimation of model uncertainty. Recently, efforts were conducted to produce GPD models using artificial neural network (ANN) techniques and fulfilling theory-driven constraints, keeping model dependency to a minimum and providing flexible parametrizations that give a better account of the systematic effects associated with the ill-defined extraction of GPDs from exclusive processes [57]. In addition to the experimental inputs, a new source of information regarding GPDs has emerged through lattice QCD simulations where novel developments allow access to the nucleon structures from first principle calculation [58–60].

The subject of this thesis is focused on the extraction of the GPD-related quantities, the CFFs, in the least constrained and most challenging DVCS observable case where there is no polarization of the initial or final-state particles involved in the scattering process: the unpolarized cross section. The challenge in extracting the CFFs lies in the presence of 8 CFFs at twist-2 which results in an underconstrained problem, in disentangling the DVCS process from the Bethe-Heitler (BH) scattering competing processes and in obtaining precise experimental data over a wide range of kinematic variables. In this work, we developed extraction techniques that are capable of constraining the CFFs $\Re e\mathcal{H}$, $\Re e\mathcal{E}$ and $\Re e\widetilde{\mathcal{H}}$ from only one experimental observable. These techniques can also be applied to further polarized observables which can only improve the extraction accuracy and the number of CFFs that can be accessed as more constraints are included. The parametrization of the DVCS cross-section in terms of the CFFs at leading order and leading twist is convention-dependent and therefore not unique. Our extraction techniques are illustrated using the Belitsky, Müller and Kirchner DVCS formulation [61] but they can be applied to any formulation. An original recent computation of the DVCS cross-section conducted in reference [62] allows mapping into the various light-cone choices at leading twist which combined with our extraction frameworks can break new ground on what can be extracted from experimental observables.

The manuscript's structure is as follows: Chapter 1 provides a brief overview of our current understanding of the proton structure derived from elastic and inelastic scattering processes. Additionally, it highlights the open question regarding proton spin decomposition, where GPDs play a crucial role in unraveling the proton's

spin puzzle. This unresolved aspect is one of the primary motivations behind the research presented in this work. Chapter 2 presents the theoretical framework of the GPDs. It includes discussions on the definition, interpretations, and crucial properties of GPDs. Furthermore, it offers an overview of some existing modeling strategies of GPDs found in the existing literature. This chapter also emphasizes selected physical motivations for studying GPDs, highlighting their significance in accessing hadron tomography—the imaging of hadron structures—and their connection to the energy-momentum tensor (EMT), a fundamental quantity in physics that describes the distribution of energy and momentum within particles. Chapter 3 explores the practical application of GPDs in a phenomenological context, particularly focusing on their experimental exploration via the DVCS process, where GPDs manifest as CFFs. This chapter also covers an analysis of both the present and anticipated future status of experimental DVCS data. Additionally, it offers a comprehensive breakdown of the experimental datasets sourced from Jefferson Lab, which are utilized in this study. Chapter 4 delves into the specifics of this simulated data employed in this study. This pseudodata serves a dual purpose: firstly, to assess the accuracy and precision of our developed extraction techniques, and secondly, to conduct systematic studies aimed at understanding various factors influencing the analysis process. Chapter 5 provides an in-depth account of the extraction process for CFFs from the photon leptoproduction cross-section. This chapter introduces a pioneering extraction technique that relies on contour selection on 2-dimensional χ^2 maps, enhancing the precision and reliability of the extraction procedure. The validity and strength of this extraction method are established through the use of the generated pseudodata and systematic investigations, ensuring its robustness. The resulting CFFs extracted from the experimental data are presented in relation to key kinematic variables such as t, x_B, and Q^2, offering insights into their dependencies and behaviors within these parameters. Chapter 6 showcases contemporary extraction methodologies and the modeling of CFFs using Deep Neural Networks (DNNs). This section notably presents a novel extraction approach equipped with both interpolation and extrapolation capabilities. It introduces an iterative generating function improvement procedure that enhances the precision of CFFs extraction while providing a means to assess its accuracy in real experimental scenarios.

The proton structure 1

The proton was discovered in 1919 by Rutherford who noticed that a hydrogen nucleus is liberated from a nitrogen atom once disintegrated [63]. This hydrogen nucleus was thought of as an elementary particle, the proton, and its spin was confirmed to be 1/2 in 1927 [64]. The first hints of an internal structure of the proton came only in 1933 when experiments [65–68] shed light on its magnetic moment, much larger than what was expected for a point-like fermion obeying Dirac's equation. In other words, it was found to be:

$$\mu_p = (1 + \kappa)\frac{e}{2M} > \frac{e}{2M}, \tag{1.1}$$

where κ is the anomalous magnetic moment, e the positron charge and M the proton mass.

One key breakthrough in this endeavor was the measurement of nucleon Form Factors (FFs) through elastic scattering experiments. In the 1950s, experiments involving the elastic scattering of electrons off proton and deuteron targets [69, 70] hinted at the internal structure of nucleons and showed that indeed the proton was not a point-like particle and had a spatial extension. The FFs are related to the distribution of electric charge within the nucleon and provide insights into the transverse spatial distribution of partons, which are the constituents of nucleons.

Another significant advancement came through the measurement of Parton Distribution Functions (PDFs) using Deep Inelastic Scattering (DIS). The DIS experiments [71, 72] confirmed the existence of quarks and revealed information about the longitudinal momentum distribution of partons within nucleons. However, some aspects of nucleon structure remained elusive. For instance, FFs and PDFs couldn't capture the correlations between the spatial and momentum distributions of partons. Quantum Chromodynamics (QCD) effectively describes the dynamics of quarks and gluons at high energies, which make up hadrons like protons and neutrons. Nonetheless, at low energies, the theory loses its predictive power, and phenomena such as confinement (the inability to observe individual quarks and gluons) and hadronization (the formation of hadrons from quarks and

gluons) remain poorly understood. This knowledge gap necessitates experimental investigations to better understand QCD.

Generalized Parton Distributions (GPDs), introduced in the mid-90s, have the potential to bridge these knowledge gaps. GPDs generalize FFs and PDFs, encapsulating both while providing insights into the correlations between the spatial distributions of partons and their longitudinal momentum distributions within nucleons. This effectively allows for a 3-dimensional examination of nucleon structure. Additionally, GPDs offer insights into the contribution of quark orbital angular momentum to the nucleon's spin. Deeply Virtual Compton Scattering (DVCS) is one of the cleanest channels for experimentally accessing GPDs and provides valuable data for testing models and verifying GPD properties and sum rules.

The following Chapter gives a summary of today's understanding of the nucleons and the methods used to investigate their structure. These measurements provide experimental observables that allow us to study the nucleon properties and also give first hints about the nucleon being a composite particle of point-like constituents. These insights led to the development of the quark-parton model (QPM). The "spin crisis" and the proton spin decomposition are discussed in the last sections.

1.1 | Lepton-nucleon scattering

Lepton-nucleon scattering is a fundamental process in particle physics. This interaction involves a high-energy lepton, typically an electron or muon since they are structureless particles that only interact electromagnetically through the exchange of a virtual photon with a nucleon, which is a building block of atomic nuclei. This scattering process provides crucial insights into the internal structure of nucleons and is instrumental in probing the strong force, described by Quantum Chromodynamics (QCD), which binds quarks and gluons within the nucleon. By scattering high-energy leptons off nucleons, experiments can investigate the distribution of electric charge and magnetic properties within nucleons, revealing the spatial arrangement and behavior of their elementary constituents, quarks and gluons. Different modes of lepton-nucleon scattering, such as elastic scattering, inelastic scattering, and Deep Inelastic Scattering (DIS), have been employed in experiments to unveil the rich and intricate structure of nucleons, contributing significantly to our understanding of subatomic physics.

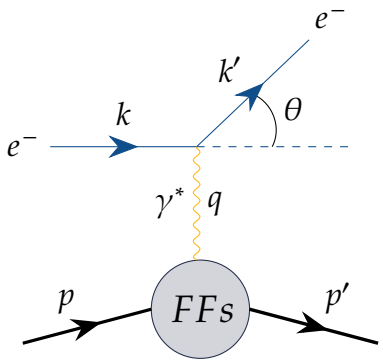

Figure 1.1: Illustration of the elastic lepton-nucleon scattering in the one-photon-exchange approximation.

1.1.1 | Elastic scattering

The term elastic refers to lepton-nucleon scattering processes with the same particles in their initial and final state. The topology of the reaction is summarized as:

$$e + p \rightarrow e' + p'$$

and it is illustrated in Figure 1.1 where k, k', p, p' are the four-momenta of the incident and scattered, electron and proton, respectively and q is the photon virtuality which is space-like ($q^2 < 0$), that is, there is a frame where the energy transfer is zero and only momentum is transferred:

$$q^2 = -Q^2 = (p' - p)^2 = (k - k')^2, \quad -Q^2 = \Delta^2 \equiv t = (p' - p)^2 < 0. \tag{1.2}$$

Since the late 1920s, it has been known that the proton is a charged, half-integer spin particle [64]. Due to the spin, the proton has a magnetic moment. The first experiments dedicated to studying the magnetic moment of the proton were performed by R. Frisch and O. Stern in 1933 [65]. These experiments and subsequent high-precision measurements in the late 1940s and early 1950s resulted in a larger value of the magnetic moment than what was expected for a point-like particle. This anomalous magnetic moment of the proton led to the conclusion that the proton must imply a complex structure. The electromagnetic structure of the proton was further studied in elastic lepton-nucleon scattering. First measurements using a 188 MeV electron beam and a hydrogen or helium target were performed at the Stanford Linear Accelerator Center (SLAC) in the mid-1950s by a team led by R. W. McAllister and R. Hofstadter [69]. In this study, the root mean square radii of charge were measured for both, the proton and the alpha particles with the hydrogen and helium targets respectively. Later, systematic measurements of

the cross sections for leptons scattering off light and heavy nuclei targets were also performed.

The study of the cross-sections allowed the determination of the elastic form factors (FFs). Its dependence on Q^2 can be described by a dipole form factor which is related to an exponentially decaying charge density through a Fourier transform that confirms the finite size of the proton.

1.1.1.1 | Elastic Form Factors

The lowest order approximation for electron nucleon scattering is the single virtual photon exchange process or Born term. The lab frame, i.e. the nucleon target rest frame differential cross section of elastic lepton-nucleon scattering in one-photon exchange approximation reads as [73]:

$$\begin{aligned}\frac{d\sigma}{d\Omega} = \left(\frac{d\sigma}{d\Omega}\right)_{Mott} \frac{E'}{E}\left(F_1^2\left(Q^2\right)\right. \\ \left. +\tau\left[F_2^2\left(Q^2\right) + 2\left[F_1\left(Q^2\right) + F_2\left(Q^2\right)\right]^2 \tan^2\frac{\theta}{2}\right]\right),\end{aligned} \tag{1.3}$$

with $\tau = Q^2/4M^2$. The Mott cross-section is:

$$\left(\frac{d\sigma}{d\Omega}\right)_{Mott} = \frac{\alpha^2\cos^2\frac{\theta}{2}}{4E^2\sin^4\frac{\theta}{2}}. \tag{1.4}$$

The incident electron (beam) and scattered electron energies are labeled E and E', respectively. The fraction E'/E in (1.3) is the recoil correction to the Mott cross section and $\alpha = \frac{e^2}{4\pi}$ is the QED coupling constant or fine structure constant. The independent variable θ is the angle between the incoming and outgoing electrons.

$F_1\left(Q^2\right)$ and $F_2\left(Q^2\right)$ are called Dirac and Pauli Form Factors (FFs) and they are normalized such that their value in the static limit, $Q^2 = 0$, gives respectively the charge of the nucleon (in units of the positron charge) and its anomalous magnetic moment κ. A point-like particle would have a vanishing Pauli Form Factor and a constant Dirac Form Factor. Another parametrization, from Sachs, is also possible in terms of electric and magnetic FFs G_E and G_M [74]:

$$G_E(Q^2) = F_1(Q^2) - \tau F_2(Q^2), \quad G_M(Q^2) = F_1(Q^2) + F_2(Q^2) \tag{1.5}$$

The scattering cross-section can then be written in a simpler form, without an interference term, leading to a separation method for G_E^2 and G_M^2 known as the Rosenbluth (or Longitudinal-Transverse) technique. Now the cross-section is:

$$\frac{d\sigma}{d\Omega} = \left(\frac{d\sigma}{d\Omega}\right)_{Mott} \frac{E'}{E}\frac{1}{1+\tau}\left(G_E^2 + \frac{\tau}{\epsilon}G_M^2\right), \tag{1.6}$$

where ϵ is the polarization of the virtual photon defined as:

$$\epsilon = \frac{1}{1 + 2(1+\tau)\tan^2\frac{\theta}{2}}. \tag{1.7}$$

The Rosenbluth separation technique takes advantage of the linear dependence in ϵ, in the reduced cross-section σ_{red} , based on (1.6), as follows:

$$\begin{aligned} \sigma_{\text{red}} &= \frac{\epsilon(1+\tau)}{\tau}\frac{E}{E'}\left(\frac{d\sigma}{d\Omega}\right) \Big/ \left(\frac{d\sigma}{d\Omega}\right)_{Mott} \\ &= G_M^2 + \frac{\epsilon}{\tau}G_E^2, \end{aligned} \tag{1.8}$$

showing that σ_{red} is expected to have a linear dependence on ϵ, with the slope proportional to G_E^2 and the intercept equal to G_M^2. By varying the angle θ, while keeping Q^2 fixed, for instance, it is possible to separate these Form Factors. See Figure 1.2 (right panel) for a recent compilation of measurements of the electric Form Factor where it is seen that the Q^2 dependence of these form factors can be approximately characterized up to a few GeV^2 by a dipole form factor:

$$G_D = \left(1 + \frac{Q^2}{0.71}\right)^{-2}. \tag{1.9}$$

The determination of G_E at Q^2 greater than 2 GeV^2 has suffered from large error bars. These Form Factors can be interpreted as the three-dimensional Fourier transform of the charge and magnetization densities, respectively, when one considers the Breit Frame (BF) [74, 75]. The left panel of Figure 1.2 shows the 3D charge distribution $J_B^0(\boldsymbol{r})$ in the BF given by the Fourier transform of the G_E Sachs FF, Eq. (1.10) , with and without the relativistic recoil correction factor $1/\sqrt{1+\tau}$.

$$J_B^0(\boldsymbol{r}) = \int \frac{d^3\Delta}{(2\pi)^3} e^{-i\Delta\cdot r}\frac{1}{\sqrt{1+\tau}}G_E(\Delta^2). \tag{1.10}$$

The root mean square (rms) charge radius can be inferred as:

$$< r^2 >= -6\left|\frac{dG_E}{dQ^2}\right|_{\text{at } Q^2=0}, \tag{1.11}$$

but an extrapolation is necessary, as experimentally we can access only finite values of Q^2. To this day, despite very precise measurements, the determination of the proton radius remains an open subject, due to significant discrepancies between the mean value obtained from all electron scattering experiments and the proton radius obtained in a completely complementary fashion from precise measurements of the

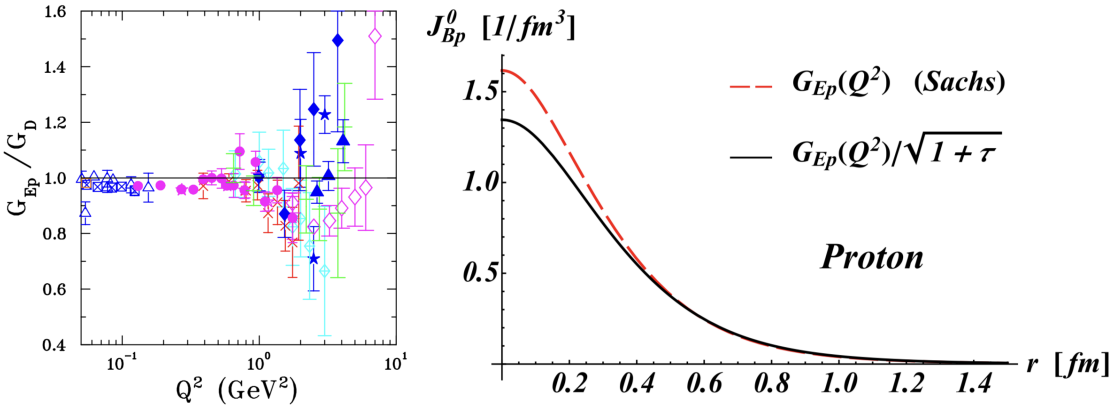

Figure 1.2: (left) Proton electric FF divided by the dipole FF (1.9). Data taken from worldwide experiments. See Ref. [79], where the figure was taken from, for details. (right) Proton radial charge distributions in the Breit frame, excluding (dashed red line) and including (solid black line) the kinematical factor. Taken from Ref. [80].

Lamb shift energies either in the hydrogen atom [76] or in muonic hydrogen [77]. This discrepancy by about 4% has become known as the proton radius puzzle, and its resolution has become a topic of great current interest, and the aim of several new and novel experimental efforts. We refer to Ref. [78], and references therein, for further details.

1.1.2 | Inelastic scattering

When studying the nucleon structure using higher beam energies and therefore at larger Q^2, additional reaction channels open up. In this kinematic regime, the scattering process is referred to as inelastic scattering. Unlike elastic scattering, where the colliding particles typically remain intact, in inelastic scattering, the final state particles are either excited states of the initial nucleon (nucleon resonances) or particles produced due to the fragmentation of the target nucleon. The scattering process is illustrated in Figure 1.3 and its topology is summarized as:

$$e + p \rightarrow e' + X.$$

Here, X summarizes all particles in the hadronic final state with invariant mass or missing mass is given by:

$$W^2 = (p + q)^2 = M^2 + 2M\nu + q^2 \tag{1.12}$$

where M is the proton mass and $\nu = pq/M$ is the electron energy loss given in the lab frame by $E - E'$.

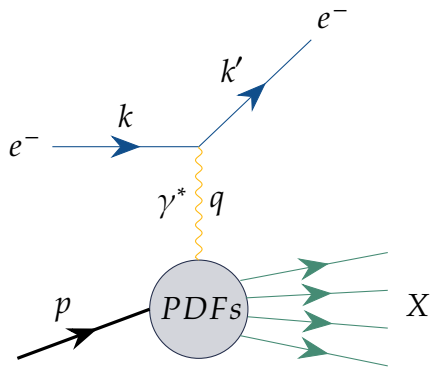

Figure 1.3: Illustration of the (deep) inelastic lepton-nucleon scattering in the one-photon-exchange approximation.

Inelastic scattering off a nucleon was first measured in an experimental program started at Stanford Linear Accelerator Center (SLAC) [71, 72] in collaboration with the Massachusetts Institute of Technology (MIT) at the end of the 1960s with the highest electron energies then available of up to 21 GeV. The measured cross-sections at a fixed electron energy and scattering angle are shown in Figure 1.4. In elastic scattering, the invariant mass corresponds to $W = M$ which is observed in the figure as the elastic peak followed by the region where nucleon resonances appear at $W \geq M + m_\pi$. m_π is the mass of the pion resulting from the first exited peak $ep \rightarrow e\Delta^+ \rightarrow ep\pi^0$. Above $W \sim 2$ GeV there is no visible resonance structure in the cross-section and the proton breaks up resulting in the 'continuum' or 'inelastic region'.

The deep inelastic regime is defined in the limit where both the virtuality $Q^2 = -q^2$ and ν are large but their ratio $x_B = Q^2/2M\nu$ called Bjorken's scaling stays finite. This is also called the Bjorken limit. Deep inelastic scattering (DIS) probes the composite nature of the nucleon: it gives us access to the parton distribution functions (PDFs) which measure the longitudinal momentum distributions of quarks and gluons inside the nucleon.

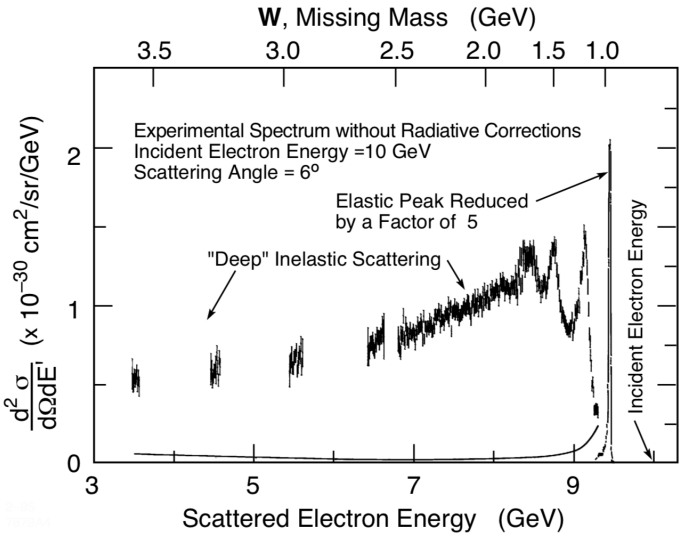

Figure 1.4: Early electron scattering cross-sections from the first inelastic scattering experiments performed at SLAC by the SLAC-MIT collaboration. Taken from [81].

1.1.2.1 | Structure functions

The inelastic double differential cross section for scattering off polarized leptons on polarized nucleons in LO QED is given by [82]:

$$\begin{aligned}\frac{d^2\sigma}{d\Omega dE'} &= \frac{\alpha^2}{2MQ^4}\frac{E'}{E}L_{\mu\nu}W^{\mu\nu} \\ &\propto \Big[L^{(S)}_{\mu\nu}(k;k')\,W^{\mu\nu(S)}(q;p) - L'^{(S)}_{\mu\nu}\left(k,s_l;k',s'_l\right)W^{\mu\nu(S)}(q;p) \\ &-L^{(A)}_{\mu\nu}(k,s_l;k')\,W^{\mu\nu(A)}(q;p,s_N) - L'^{(A)}_{\mu\nu}(k;k',s_l)\,W^{\mu\nu(A)}(q;p;s_N)\Big].\end{aligned} \tag{1.13}$$

The emission of a virtual photon and its absorption by the nucleon is described in terms of a leptonic and hadronic tensor ($L_{\mu v}$ and $W^{\mu v}$). The tensors are associated with the coupling of the lepton or nucleon to the exchange boson (virtual photon) and this coupling is expressed by leptonic and hadronic currents. For the full representation of the tensors see [82]. Those tensors can be divided into a symmetric (S), spin-independent part, and an asymmetric (A), spin-dependent part. Here, s_l and s'_l correspond to the spin of the initial and final state lepton and s_N to the spin of the initial state nucleon. While the emission of the virtual photon by the lepton is calculable in QED, its absorption by an extended nucleon with an unknown substructure is parameterized by *structure functions*.

The structure functions are underivable from the theory of strong interaction and must be obtained by dedicated experimental measurements.

Splitting the hadronic tensor into its symmetric and anti-symmetric parts:

$$W_{\mu v}\left(q;p,s_N\right) = W^{\mu v(S)}(q;p) + iW^{\mu v(A)}\left(q;p,s_N\right), \tag{1.14}$$

where:

$$\frac{1}{2M}W^{\mu v(S)}(q;p) = \left(-g_{\mu v} + \frac{q_\mu q_v}{q^2}\right)W_1 + \left[\left(p_\mu - \frac{p\cdot q}{q^2}q_\mu\right)\left(p_v - \frac{p\cdot q}{q^2}q_v\right)\right]\frac{W_2}{M^2}, \tag{1.15}$$

$$\frac{1}{2M}W^{\mu v(A)}\left(q;p,s_N\right) = \varepsilon_{\mu v\alpha\beta}q^\alpha\left\{Ms_N^\beta G_1 + \left[(p\cdot q)s_N^\beta - (s_N\cdot q)\,p^\beta\right]\frac{G_2}{M}\right\} \tag{1.16}$$

and taking into account the time and parity invariance of QED, in total, four structure functions are introduced. Two of those functions are averaged over the spin and therefore spin-independent (W_1 and W_2) [83], while the remaining two are spin-dependent functions (G_1 and G_2) [84]. The symbols $g_{\mu\nu}$ and $\varepsilon_{\mu v\alpha\beta}$ represent the metric and the antisymmetric Levi-Civita tensor. As the structure functions are not dimensionless, it is convenient to use the expressions[1]:

$$\begin{aligned} MW_1\left(\nu,Q^2\right) &= F_1\left(x_B,Q^2\right), \\ vW_2\left(\nu,Q^2\right) &= F_2\left(x_B,Q^2\right) \end{aligned} \tag{1.17}$$

and

$$\begin{aligned} M^2vG_1\left(\nu,Q^2\right) &= g_1\left(x_B,Q^2\right), \\ Mv^2G_2\left(\nu,Q^2\right) &= g_2\left(x_B,Q^2\right), \end{aligned} \tag{1.18}$$

Using these expressions, the differential cross section for deep inelastic scattering on unpolarized nucleons reads as [85]:

$$\frac{d^2\sigma}{dx_Bdy} = \frac{4\pi\alpha^2}{Q^2x_By}\left[\left(1-y-\frac{\gamma^2y^2}{4}\right)F_2 + x_By^2F_1\right] \text{ with } \gamma = \frac{2Mx_B}{Q}. \tag{1.19}$$

The spin-averaged structure functions can be extracted from dedicated cross-section measurements in a similar way as done for the elastic form factors by the Rosenbluth separation. As G_1 and G_2 and therefore also g_1 and g_2 only appear in the spin-dependent part of the hadronic tensor (see Eq. (1.18)), those functions are only accessible using polarized leptons and nucleons.

If, the target nucleon is longitudinally polarized ($\Leftarrow,\Rightarrow$) with respect to the lepton polarization ($\leftarrow$, $\rightarrow$), the differential cross-section difference is expressed as [85]:

$$\frac{d^3\sigma^{\leftarrow\Rightarrow}}{dx_Bdyd\phi} - \frac{d^3\sigma^{\leftarrow\Leftarrow}}{dx_Bdyd\phi} = \frac{4\alpha^2}{Q^2}\left[\left(2-y-\frac{\gamma^2y^2}{2}\right)g_1 - \gamma^2yg_2\right]. \tag{1.20}$$

[1]The F_1 and F_2 structure function notations, due to Bjorken, should not be confused with the Pauli and Dirac electromagnetic Form Factors.

Here, ϕ is the angle between the lepton scattering plane and the plane of the nucleon spin. One should note that g_2 is suppressed by a factor of M^2/Q^2 with respect to the leading terms, thus g_2 is largely inaccessible.

If the target nucleon is transversely polarized ($\Uparrow, \Downarrow$) the differential cross-section difference becomes [85]:

$$\frac{d^3\sigma^{\leftarrow\Uparrow}}{dx_B dy d\phi} - \frac{d^3\sigma^{\leftarrow\Downarrow}}{dx_B dy d\phi} = \frac{4\alpha^2}{Q^2}\gamma\sqrt{1-y-\gamma^2y^2/4}\times[yg_1+2g_2]\cos\phi. \tag{1.21}$$

Here, g_2 is not suppressed, so using the results on g_1 from longitudinal polarized targets, g_2 can be determined.

1.2 | The Quark-Parton model

The quark-parton model (QPM) stands as a crucial theoretical framework within particle physics, unifying the understandings derived from two pivotal historical models: the quark model and the parton model.

1.2.1 | The Quark model

The quark model emerged in the early 1960s in response to the proliferation of newly discovered particles. These included the "mesons" (such as the pion (π), kaon (K), and rho (ρ)), which had masses between that of the electron and proton, and the "baryons" (such as the proton (p), neutron (n) and lambda (Λ)) which were significantly heavier than the mesons. With so many new particles being discovered, it was suggested that they couldn't all be elementary particles, and so there must be some deeper structure to these particles that can be used to describe them. Researchers began seeking underlying principles that could provide order to what was then referred to as the "particle zoo". This led to many attempts to order the mesons and baryons into groups based on their properties, such as charge, isospin, strangeness and mass. In 1961, Gell-Mann [86] and Ne'eman [87] independently proposed the *Eightfold Way* which organized the baryons and mesons with the same spin and parity J^P, according to their charge and strangeness into octets, nonets and decuplets, in the sort of diagrams represented in Figure 1.5, using the SU(3) symmetry [88]. The confirmation of SU(3) group by the discovery of the Ω^- baryon in 1963 led to wide acceptance of the 'Eightfold Way'. It was the regularity of these multiplet groupings that in 1964 led independently Gell-Mann and Zweig to conjecture that this classification scheme could be built up as bound states of a

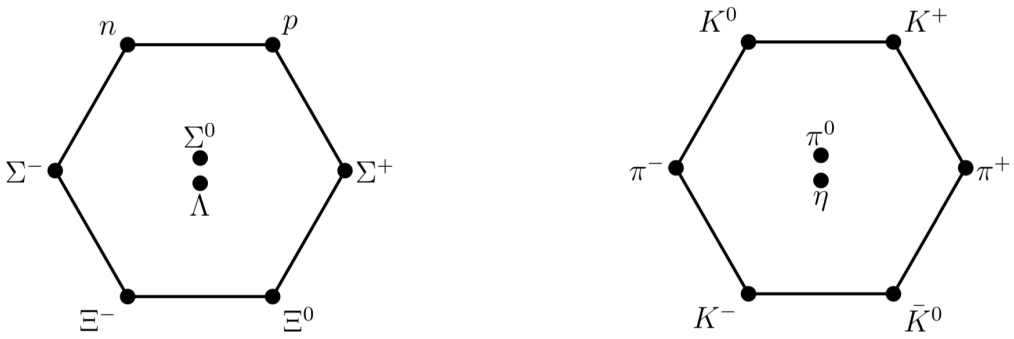

Figure 1.5: Baryon (left) and pseudo-scalar meson (right) octets, $\frac{1}{2}^+$ and 0^- respectively. Horizontal lines associate particles of the same strangeness while left-leaning diagonal lines are for the same charge.

few fundamental spin 1/2 constituents called *quarks* that exist in six different types or 'flavors'. Their conjecture is the basis of the quark model [89, 90]. The quarks were at this time, theoretical constructs with no experimental observation of their existence. The mesons and baryons would eventually be collectively referred to as hadrons. Hadrons are composite particles of quarks bound together by the strong force, with mesons containing bound states of valence quark (q) and an antiquark ($\bar{q}$), while baryons are constructed from three valence quarks qqq (antibaryons are made out of three antiquarks $\bar{q}\bar{q}\bar{q}$). The mesons and baryons so constructed should have an integer electric charge, even though their constituent quarks carry a fractional charge. Using these simple rules one can build all the observed hadrons out of quarks.

An apparent violation of Pauli's exclusion principle was obtained in the low-lying baryon spectrum when quarks were considered fermions. As quarks have spin 1/2, they should obey Fermi statistics, that is all quantum states should be anti-symmetric (change sign) under the interchange of two identical quarks. However, this expectation seemed to be violated by the lowest energy baryons. For example, the Ω^- is made up of three spin 1/2 strange quarks; so according to Fermi statistics, its wave function should be antisymmetric under the interchange of any two of these quarks. But the Ω^-has total spin 3/2 so the spin part is symmetric; and as it is the lowest energy state of three s quarks, they ought to have zero orbital angular momentum relative to one another, thereby implying that the spatial part of the wave function is also symmetric. However, the total wave function is then symmetric under quark interchange in violation of Fermi statistics. This apparent inconsistency is overcome by giving each of the quarks an additional degree of freedom called 'color' [91–93]. Then antisymmetrizing the state in the quarks'

color variables renders the Ω^- overall antisymmetric and resolves the problem. This additional quantum number describes the fact that the observed hadrons do not carry this new quantum number, they must be colorless. It is equivalent to the mathematical statement that each quark flavor transforms as a triplet representation under an internal $SU(3)_c$ color symmetry, but physical hadron states are all singlets. The color property ultimately completes the foundation of the quark model.

The quark model has been very successful in predicting new hadronic states and correctly describing their properties. It is one of the cornerstones of elementary particle physics. However, some critical questions remained. The most prominent among these is why are free quarks or any other colored hadronic states not observed in nature. All of our knowledge regarding quarks has been obtained indirectly from the properties of hadrons, as an isolated quark has never been observed.

1.2.2 | Deep inelastic scattering and the Quark Parton model

The first results on inelastic electron-proton scattering [71, 72] , obtained by the MIT-SLAC collaboration and presented at the 14th International Conference on High Energy Physics, 1968 in Vienna, hint at the structure of the proton. If the proton's electric charge were diffused throughout the internal structure, then at very high energies the inelastic scattering cross-section would be expected to decrease very rapidly. That was not observed. Instead, the cross-section decreased slowly in a manner that suggested the proton's electric charge was concentrated in point-like constituents, (see Figure 1.6).

The groundbreaking inelastic electron-proton scattering experiment revealed the independence of the spin-averaged structure functions on $q^2 = -Q^2$ predicted by Bjorken [94] in the limit of large Q^2 and finite x_B, known as scaling invariance, i.e. in the Bjorken limit the structure functions tend to depend on x_B only :

$$\begin{aligned} MW_1(\nu, Q^2) &= F_1(x_B), \\ \nu W_2(\nu, Q^2) &= F_2(x_B). \end{aligned} \tag{1.22}$$

This feature is expected for scattering from a point-like object. It came as a surprise to observe this scale invariance at such small values of Q^2. Despite the fact, that the assumptions taken by Bjorken were questionable and his arguments turned out to be flawed, the idea of scaling still served well for Feynman's interpretation of the experimental results.

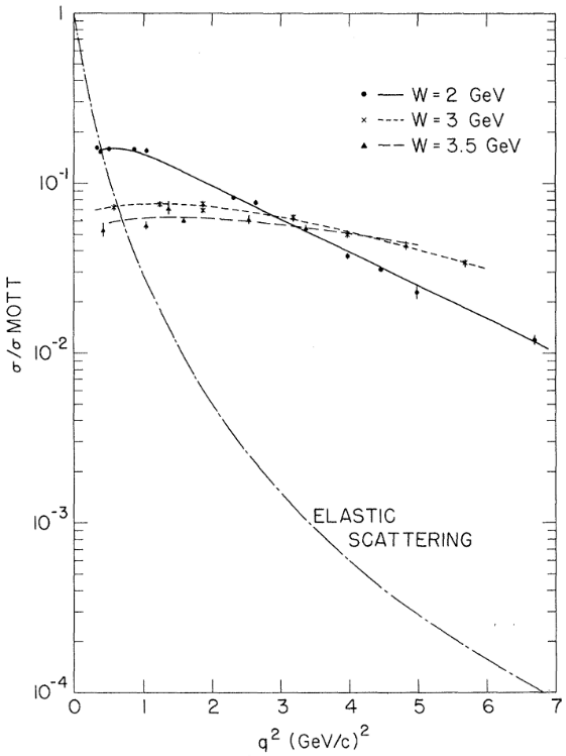

Figure 1.6: Measured differential cross section for inelastic proton-electron scattering divided by the Mott cross section as a function of q^2 for different values of W. The data was taken at SLAC with incident electron energies between 7 GeV and 17 GeV and scattering angles of 6°and 10°. As a reference, the expected behavior for elastic scattering is drawn. The observed weak dependence on q^2 is characteristic of scattering on point-like particles. Figure taken from [72].

In his interpretation, the proton consists of point-like, spin-1/2 particles, initially termed "partons" in the developed Parton model by Feynman [95] in 1969. Even though the Parton model was mainly developed by Feynman, it was first published by Bjorken and Paschos [96] where the study of the quantum numbers of Feynman's partons allowed identifying them with the Gell-Man's and Zweig's quarks.

In the Parton model, the assumption is taken that the nucleon, in a lepton-nucleon scattering process, can be described as a collinear beam of free-moving, massless and point-like spin-1/2 partons in a reference frame in which the momentum was infinite, the *infinite momentum* frame (IMF). The partons in this frame are considered to be spread far enough apart that the probability of interactions between the partons, after the transfer of the virtual photon, is very small. Time dilation also limits the likelihood of parton-parton interactions occurring in this frame. The hadron would be moving so fast that the duration of any interaction

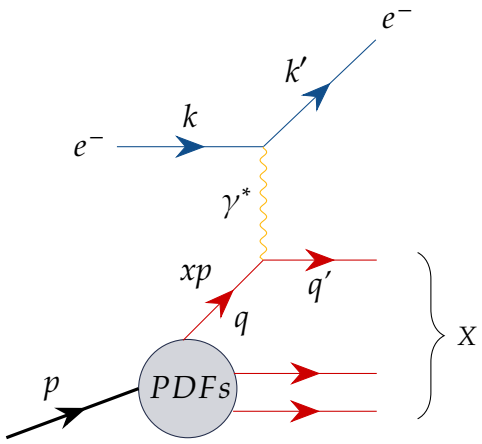

Figure 1.7: Interpretation of the deep inelastic lepton-nucleon scattering in the QPM for the one-photon-exchange approximation.

would be very long inside the hadron, such that the partons would appear to be almost frozen in place within the hadron. For these reasons, any transverse momenta and interactions between partons inside the nucleon can be neglected and the partons considered 'free'. This approach is today known as the naive quark-parton model (QPM).

In the picture of the naive QPM the DIS process is not described as an interaction between the lepton and the nucleon, but as the incoherent sum of the elastic lepton scattering on all possible types of quarks (see Figure 1.7). Under its assumptions, one finds that x_B, can be interpreted as the fraction of the nucleon four-momentum x carried by a quark/antiquark where $0 < x_B < 1$, and $x_B = 1$ corresponds to elastic scattering. Comparing the cross-section of the incoherent sum of elastic lepton-quark scattering to the cross-section for unpolarized inelastic lepton-nucleon scattering allows one to express the structure functions in terms of so-called Parton Distribution Functions (PDFs) as:

$$\begin{aligned} F_1(x_B) &= \frac{1}{2}\sum_q e_q^2 \left(q_q(x_B) + \bar{q}_q(x_B)\right), \\ F_2(x_B) &= x_B \sum_q e_q^2 \left(q_q(x_B) + \bar{q}_q(x_B)\right). \end{aligned} \tag{1.23}$$

Here, e_q is the electric charge of a particular quark of flavor q and $q_q(x_B)/\bar{q}_q(x_B)$ the PDFs of the corresponding quarks/antiquarks. The PDFs, give the probability to find quarks/antiquarks of flavor q carrying a fraction x_B of the total nucleon four-momentum. They have the character of number density functions, so if integrated over the full x_B-range the result corresponds to the number of quarks/antiquarks of a certain flavor in the nucleon. In the case of spin-averaged PDFs, the functions

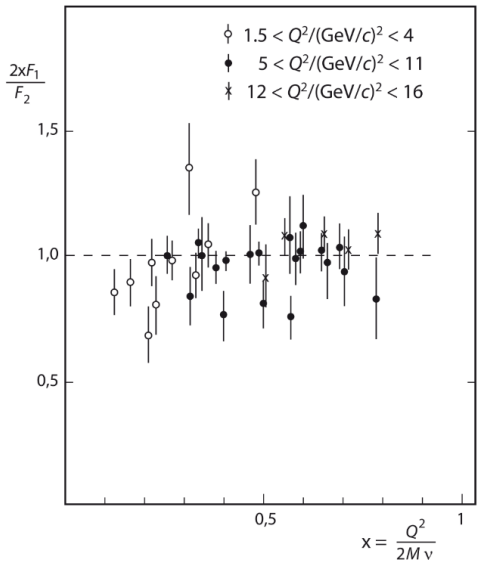

Figure 1.8: Ratio of $2x_B \cdot F_1(x_B)$ to $F_2(x_B)$ as function of x_B as measured by experiments at SLAC. The results confirmed that quarks are spin-1/2 particles. Figure taken from Ref. [97].

are given by the sum of the number densities of quarks/antiquarks, with spins parallel (q^+) or antiparallel (q^-) with respect to the nucleon spin:

$$\begin{aligned} q(x_B) &= q^+(x_B) + q^-(x_B), \\ \bar{q}(x_B) &= \bar{q}^+(x_B) + \bar{q}^-(x_B). \end{aligned} \tag{1.24}$$

The assumption of the quarks/antiquarks being spin- 1/2 particles is confirmed by measurements of the relation between the structure functions:

$$F_2(x_B) = 2x_B \cdot F_1(x_B). \tag{1.25}$$

Equation (1.25) is known as the Callan-Gross relation [98]. As the structure function F_1 is related to the magnetic properties of the nucleon, it is equal to zero for spin- 0 and spin-1 particles. The result of the measurement, shown in Figure 1.8, is in agreement with the expectation for spin-1/2 particles. Similar to the spin-averaged structure functions, the spin-dependent structure functions are expressed via PDFs:

$$\begin{aligned} g_1(x_B) &= \frac{1}{2}\sum_q e_q^2 \left(\Delta q_q(x_B) + \Delta\bar{q}_q(x_B)\right), \\ g_2(x_B) &= 0. \end{aligned} \tag{1.26}$$

While in the spin-averaged case $q_q(x_B)$ and $\bar{q}_q(x_B)$ correspond to the sum over all quark polarizations, the quark and antiquark helicity distributions $\Delta q_q(x_B)$ and

$\Delta\bar{q}_q(x_B)$ are given by the difference between quarks/antiquarks with parallel or antiparallel spins with respect to the one of the nucleon:

$$\begin{aligned}\Delta q_q(x_B) &= q_q^+(x_B) - q_q^-(x_B),\\ \Delta\bar{q}_q(x_B) &= \bar{q}_q^+(x_B) - \bar{q}_q^-(x_B).\end{aligned} \tag{1.27}$$

In the QPM only g_1 is related to the quark helicity distributions of the nucleon. Despite the success of the naive QPM in interpreting the experimental results of earlier DIS measurements, further measurements showed deviations from its predictions. The most important deviations are summarized in the following.

Considering the interpretation of x_B as a four-momentum fraction, the expression $x_B q_q(x_B)$ gives the momentum distribution of quarks of a specific flavor. The first result, hinting at the incomplete picture of the naive QPM was by the measurements on the momentum sum rule. The sum over all types of quarks and antiquarks in the nucleon is given as:

$$\Sigma(x_B) = \sum_q \left(q_q(x_B) + \bar{q}_q(x_B)\right), \tag{1.28}$$

where the functions correspond to the PDF of a certain quark flavor $(u, d, \ldots)$. In the naive QPM, the prediction for the momentum sum rule is:

$$\int_0^1 x_B \Sigma(x_B)\, dx_B = 1. \tag{1.29}$$

Here, it is assumed that the total nucleon four-momentum is carried by the quarks and antiquarks. Considering the relation between the spin-averaged structure function F_2 and the PDFs, as introduced in (1.23), $x_B\Sigma(x_B)$ is equal to the structure function $F_2^N = \frac{1}{2}\left(F_2^p + F_2^n\right)$ of the nucleon. Measurements of F_2 in neutrino-nucleon (νN) and electron-nucleon $(eN$, electron-proton ep and electron-neutron en) scattering, resulted in:

$$\int_0^1 F_2^{\nu N}(x_B) \sim \int_0^1 \frac{18}{5} F_2^{eN}(x_B)\, dx_B \sim 0.5, \tag{1.30}$$

These results imply that there are constituents of the nucleon, which do not interact through the weak or electromagnetic interaction.

Further studies of the nucleon structure finally led to the modern QPM and today's understanding of the strong interactions as a quantum field theory. In the Standard Model (SM) picture, hadrons consist of a constant number of valence quarks of a different flavor. These quarks are constrained by the strong force

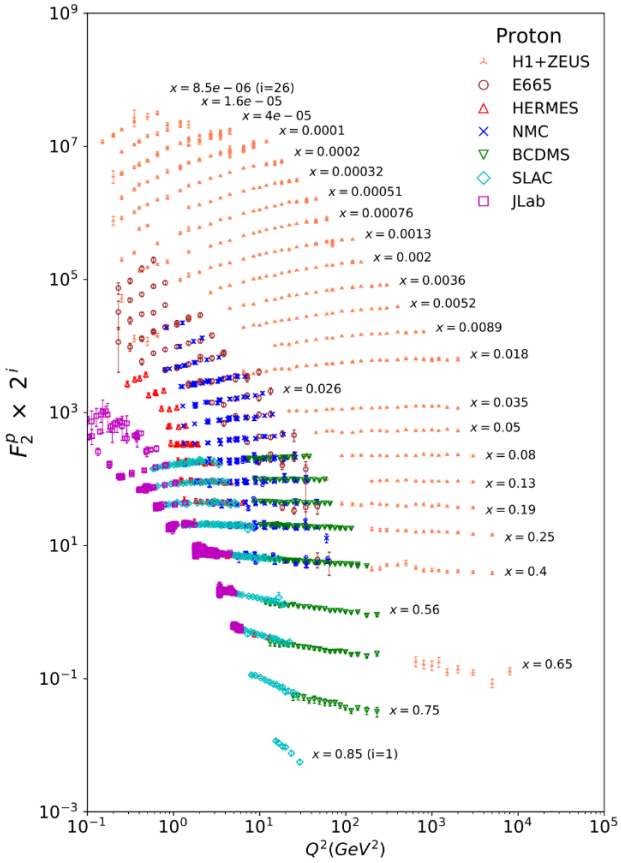

Figure 1.9: Structure function F_2 of the proton from worldwide measurements. The data is plotted as a function of Q^2 in bins of fixed x_B. For the plot, the data in each x_B bin are multiplied by 2^i, where $i \in [1, 26]$ is the number of the corresponding bin. Figure taken from Ref. [82].

and interact through the exchange of gluons. Those gluons also can form quark-antiquark-pairs that again annihilate into gluons. Thus, the valence quarks are surrounded by gluons and quark-antiquark fluctuations. These fluctuations are referred to as *sea quarks*. All these particles, their interactions and fluctuations represent the complex structure of hadrons and give them their properties.

The measurements of spin-averaged structure functions continued and cover today a wide kinematic range. Figure 1.9 shows a compilation of the world data on the proton structure function F_2^p measured in DIS by fixed target experiments using electron (SLAC [99], JLAB [100]), positrons (HERMES [101]) or muon (BCDMS [102], E665 [103], NMC [104]) beams and in electron/positron-proton-collider experiments (H1+ZEUS). The structure function is displayed as a function of Q^2 at different values of x_B and demonstrates that scaling is not exact because the structure functions exhibit a Q^2 dependence, which is most pronounced at small

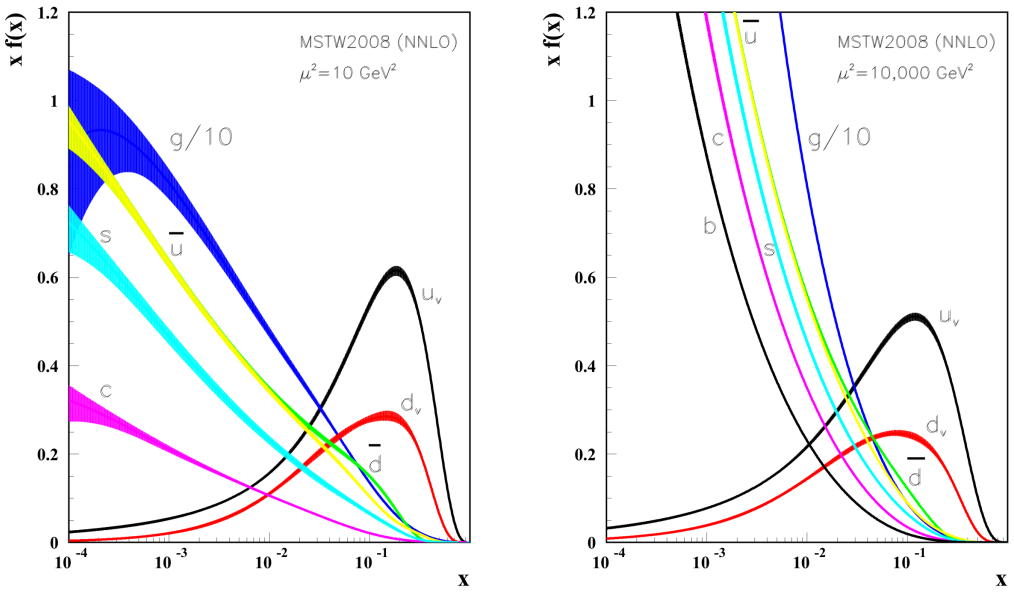

Figure 1.10: Unpolarized PDFs of the proton at two different scales. Figure taken from [105] (Particle Data Group).

and large values of x_B. These observations of a clear logarithmic dependence of F_2^p on Q^2 are in contrast to the predictions of the naive QPM.

In terms of the PDFs, this implies that their x_B-dependence is not completely independent of the resolution scale Q^2 but also evolves with Q^2, which can be seen in Figure 1.10 that shows recent extractions of the PDFs. We can intuitively understand this as follows: a photon with intermediate Q^2 does not resolve the full spatial structure of the proton and mainly sees three interacting quarks, together with parts of the sea. In contrast, a high Q^2 photon can resolve small distances and will reveal more and more of the quark sea which contains short-distance processes such as gluon emission from a quark or gluon splitting into $q\bar{q}$ pairs. As a result, the sea-quark contributions will be more prominent at higher Q^2. On the other hand, since the photon can resolve more partons, momentum conservation implies that each parton carries now a smaller fraction of the total momentum, and hence the PDFs will be shifted to smaller x_B. The resulting structure function $F_2(x_B)$ that sums up the individual quark PDFs will rise with higher Q^2 at small x_B and fall with higher Q^2 at large x_B.

The observed PDFs offer insights into the internal momentum structure of the proton, revealing distinctive patterns that shed light on its composite nature. If the proton were composed of a single quark carrying all its momentum, the PDFs would exhibit a single prominent peak at $x = 1$. Conversely, in a scenario with three non-interacting quarks, each carrying an equal fraction of momentum, the PDFs

would peak at $x = \frac{1}{3}$. However, when these three quarks interact, allowing for momentum exchange, the momentum fraction carried by each quark fluctuates, resulting in a smooth distribution that peaks near $x = \frac{1}{3}$ which is the behavior exhibited in Figure 1.10 for the valence quarks. Additionally, the presence of sea quarks, arising from quantum fluctuations within the proton, contributes to an enhancement at small x. Sea quarks, generated in Bremsstrahlung-like processes, tend to be more prevalent at small momenta, leading to an increase in the PDFs at low x values. The measured PDFs revealed that the sea quarks and mainly gluons are indeed dominant at small x whereas valence up quarks are important at large x.

1.3 | The *spin crisis*

Decades of work spanning many experimental facilities have been aimed at studying and understanding the internal spin structure of the nucleon. The goal is to understand how the spin of the nucleon is determined from the dynamics of the quarks and gluons, separating the orbital angular momentum components from angular momentum and intrinsic spin. The impetus for this work stemmed from the first experiments in the late 1980's by the European Muon Collaboration (EMC) [106] which led to a proton "spin crisis". They measured that, contrary to the naive QPM prediction that the proton spin could be calculated by summing the spins of the quarks that it is composed of, the valence quarks do not contribute much to the spin of the proton.

The proton "spin crisis" is the realization that the QPM is not sufficient enough to explain the spin quantum numbers of the proton. The spin dependent structure function g_1 provides a starting point for determining the contributions to the spin of the proton,

$$g_1(x) = \frac{1}{2}\sum_i e_i^2 \Delta q_i(x). \tag{1.31}$$

The sum here runs over all quark and anti-quark flavors. The "spin crisis" of the proton came about during the measurement of the integral of $g_1(x)$.

$$\int_0^1 dx g_1^p(x) = \frac{1}{9}a_0 + \frac{1}{12}a_3 + \frac{1}{36}a_8 \tag{1.32}$$

where,

$$\begin{aligned} a_0 \equiv \Delta\Sigma &= \Delta u + \Delta d + \Delta s \\ a_3 &= \Delta u - \Delta d \\ a_8 &= \Delta u + \Delta d - 2\Delta s. \end{aligned} \tag{1.33}$$

This reorganization allows for the decomposition into components related to neutron beta decay a_3 and hyperon beta decay a_8.

The integral of $g_1(x)$ was calculated from experimental measurements from the EMC experiment at CERN [106] of the spin asymmetry in DIS of longitudinally polarized muons by longitudinally polarized protons over a large range of x. Their results revealed this integral to be $0.126 \pm 0.01 \pm 0.015$ and using the experimental values of a_3 and a_8 revealed that $\Delta\Sigma = 0.05$. This was a huge problem, it shows that the valence quark contribution to the proton spin is essentially negligible. However, $\Delta\Sigma$ has been more precisely calculated to be now about a third, $\Delta\Sigma \approx (33 \pm 3 \pm 5)\%$ [107, 108]. Nevertheless, calculations in the QPM predict that most of the proton spin should be carried by the valence quarks, meaning that the naive QPM is not sufficient to understand the spin of the proton. These results could have meant that the proton contained a large amount of polarized gluons. However, gluon helicity distributions have been measured to be about $\Delta G \approx 0.20 \pm 0.06$ [109–111], which still does not fully solve this puzzle.

1.4 | Proton spin decomposition

From the failure of the QPM, one would expect that there must be some orbital motion of the quarks and gluons inside of the proton, and through this orbital motion, one can then satisfy the proton spin quantum numbers. The idea of non-negligible contributions to the nucleon spin by the orbital momentum of partons was already discussed by Sehgal in the 1970s [112]. Later Ratcliffe observed that an orbital momentum is also generated by the splitting processes $q \to qg$ and $g \to q\bar{q}$ [113]. The decomposition of the proton spin and momentum in terms of the quark and glue contributions can be defined from the forward matrix elements of the QCD Energy-momentum Tensor (EMT) [114–116]. There are, in principle, infinite ways to define this decomposition. A meaningful one will depend on whether each component in the division can be measured experimentally and it would be desirable that they can be calculated on the lattice with either local or non-local operators.

Two of the different decompositions can be seen in Figure 1.11, one written down by Jaffe and Manohar (JM) [117] in 1990 in which the contributions of the orbital angular momentum and spin of the gluons are separated as:

$$\frac{1}{2} = \frac{\Delta\Sigma}{2} + \mathcal{L}_q + \Delta G + \mathcal{L}_g \tag{1.34}$$

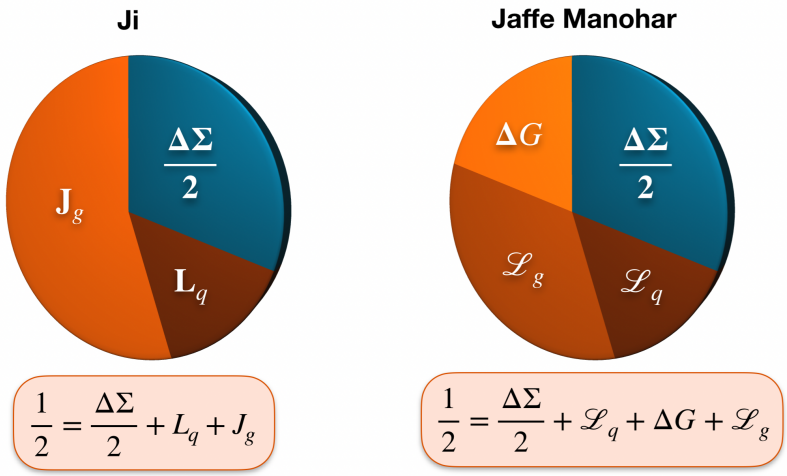

Figure 1.11: Pi charts of proton spin decompositions in two schemes, one written down by Ji in which the gluon AM is whole and the other by Jaffe and Manohar who decomposed the gluon AM into a spin and orbital component. Both schemes can be made gauge invariant and thus observable in experiments.

The other decomposition was written by Xiangdong Ji [2] in which the gluon angular momentum contribution, J_g, remains whole:

$$\frac{1}{2} = \frac{\Delta\Sigma}{2} + L_q + J_g \tag{1.35}$$

Here, $\Delta\Sigma$ is the sum of all helicity contributions by quarks and antiquarks, ΔG the contribution by the gluon helicity and L_q and L_g the contribution by the orbital angular momentum (OAM) of quarks and anti-quarks and by gluons to the spin of the proton respectively. Similarly, $\mathcal{L}_{q,g}$ are canonical quark and gluon OAM.

The JM decomposition is derived from the canonical EMT in the infinite momentum frame. Thus, this is superficially gauge-dependent and is also frame-dependent. Furthermore, while ΔG can be extracted from high-energy experiments, the calculation of the gluon helicity ΔG has not been possible for many years because it is intrinsically a time-dependent light-front quantity. However, a breakthrough in 2013 has finally been made by studying the frame dependence of non-local matrix elements.

Ji's decomposition is derived from the energy-momentum tensor (EMT) in the Belinfante form and each term is gauge invariant and frame-independent and can be calculated on the lattice with local operators.

The intriguing difference between these two decompositions and their respective realization in experiments has perplexed the community for quite a number of years. The partonic picture of the glue spin ΔG from the gluon helicity distribution and OAM are naturally depicted in the light-front formalism with ΔG extractable

from high energy pp collision and OAM from generalized parton distributions (GPDs) and the Wigner functions or distributions [118] i.e, functions that can be obtained through a Fourier transform in the transverse space of the generalized transverse-momentum dependent parton distributions (GTMDs)[119, 120]).

The definition of AM of quarks and gluons was first written down by Xiangdong Ji in terms of GPDs. This connection is made in Ref. [2] through the EMT of QCD where plugging in the matrix element of the EMT in terms of form factors one finds that the total AM carried by each flavor of quarks and gluons for a spin-1/2 hadron is:

$$J_{q,g} = \frac{1}{2}\left[A_{q,g}(0) + B_{q,g}(0)\right] \tag{1.36}$$

In Section 2.5 we will show how the GPDs explicitly enter into the definition of the total angular momentum.

Generalized Parton Distribution functions 2

Hadron structure is non-perturbative in nature due to the large value of the strong coupling at energies of the order of the nucleon mass. A major tool to probe hadron structure while keeping ingredients from perturbation theory is provided by factorization theorems. They decompose processes in a perturbative and a non-perturbative parts. The latter is encoded in a universal object known as parton distribution which contains crucial information on the inner dynamics of the hadron. Parton Distribution Functions (PDFs) are a well-known example and find application in the description of deep inelastic scattering, where they represent the density of partons (quarks and gluons) within a fast-moving hadron, as a function of the fraction of longitudinal momentum they carry, denoted as x. In exclusive processes, such as Deeply Virtual Compton Scattering (DVCS) and Deeply Virtual Meson Production (DVMP), more complex parton distributions called Generalized Parton Distributions (GPDs) become relevant. Unlike PDFs, GPDs can describe scattering amplitudes involving momentum transfers to the target hadron. Consequently, they depend not only on the longitudinal momentum fraction x but also on the longitudinal momentum transfer ξ and the total momentum transfer t. PDFs can be obtained from GPDs in the "forward limit" when no momentum transfer occurs to the target hadron ($\xi = t = 0$). GPDs also extend to elastic form factors, which are derived by integrating GPDs over x.

In addition to the three variables x, ξ and t akin to PDFs, GPDs are contingent on a renormalization scale denoted as μ^2. This scale arises from the necessity to eliminate the ultraviolet (UV) divergences of field operators that formally define GPDs. The dependence of parton distributions on this renormalization scale can be described through perturbation theory, utilizing integro-differential equations known as evolution equations. As an extension of PDFs, GPDs offer a probabilistic interpretation, encapsulating the correlation between the longitudinal momentum fraction x and the transverse position within the hadron. This depiction of the radial distribution of longitudinal momentum is known as "hadron tomography"

and stands as a fundamental motivation behind the study of GPDs. Another significant incentive lies in the remarkable ability to express matrix elements of the energy-momentum tensor in terms of gravitational form factors (GFFs) derived from GPDs. These GFFs, in turn, allow for the definition of energy and pressure distributions within hadronic matter. Through GPDs, it becomes possible to access the transverse spatial distribution of partons, which is a key element in understanding Orbital Angular Momentum (OAM) contributions to the proton's total angular momentum. OAM, which was introduced in Section 1.4, contributes to the proton's overall spin, and GPDs offer a valuable tool for examining this intricate interplay. The study of GPDs is instrumental in addressing the OAM puzzle and advancing our comprehension of the proton's internal structure and the factors that govern its spin properties. Therefore, GPDs have garnered substantial theoretical and experimental interest in recent years, leading to various phenomenological extractions based on different DVCS datasets and modeling assumptions.

In this chapter, we embark on a formal introduction to GPDs and provide an overview of some of their properties. The primary motivation for this study of this thesis is rooted in the extraction of GPD-related observables, namely the Compton Form Factors (CFFs). These observables are central to our research, driving our exploration into the complex and essential realm of GPDs. Through this overview of GPDs and their properties, we aim to shed light on the intricacies of these distributions and their significance in unraveling the mysteries of particle physics.

2.1 | Formal definition

Generalized Parton Distributions were first introduced in the 1990s in the description of two exclusive experimental processes: Deeply Virtual Compton Scattering (DVCS) and Deeply Virtual Meson Production (DVMP). The formal definition of GPDs is conveniently expressed in light-cone coordinates, defined from the usual time-space coordinates:

$\left(z^0, z^1, z^2, z^3\right)$ with Minkowskian metric $\eta^{\mu\nu}$ of signature $(+,-,-,-)$ by

$$z^{\pm} = \frac{1}{\sqrt{2}}\left(z^0 \pm z^3\right) \text{ and } z_{\perp} = \left(0, z^1, z^2, 0\right). \tag{2.1}$$

where the notations of the review [14] have been followed.

GPDs are formally defined as integral transforms of bilocal matrix elements, where a light-like distance separates the quark and gluon fields composing the operator. They are dimensionless quantities and for a spin-$\frac{1}{2}$ hadron, quark GPDs

H^q and E^q are necessary in order to parameterize the off-forward matrix element of the nucleon:

$$\begin{aligned}\frac{1}{2}\int \frac{\mathrm{d}z^-}{2\pi} e^{ixP^+z^-} \left\langle p_2 \left| \bar{\psi}^q\left(-\frac{z}{2}\right)\gamma^+\psi^q\left(\frac{z}{2}\right)\right| p_1\right\rangle_{z_\perp=0,z^+=0} \\ = \frac{1}{2P^+}\left(H^q(x,\xi,t)\bar{u}\left(p_2\right)\gamma^+ u\left(p_1\right) + E^q(x,\xi,t)\bar{u}\left(p_2\right)\frac{i\sigma^{+\mu}\Delta_\mu}{2M}u\left(p_1\right)\right)\end{aligned} \tag{2.2}$$

where p_1 and p_2 denote the incoming and outgoing hadron four-momenta, and we define

$$\begin{aligned} P &\equiv \tfrac{1}{2}\left(p_1+p_2\right), & \Delta &\equiv p_2 - p_1 \\ t &\equiv \Delta^2, & \xi &\equiv -\tfrac{\Delta^+}{2P^+}. \end{aligned} \tag{2.3}$$

Working in the light-cone gauge collapses to unity the Wilson line which ensures that the GPD definition is gauge invariant. ψ^q is a quark field of flavour q and the Dirac matrices are defined by $\gamma^\mu\gamma^\nu + \gamma^\nu\gamma^\mu = 2\eta^{\mu\nu}$, and $\gamma^+ = \left(\gamma^0+\gamma^3\right)/\sqrt{2}.\sigma^{\mu\nu} = \frac{i}{2}\left(\gamma^\mu\gamma^\nu - \gamma^\mu\gamma^\nu\right)$. The normalization of the spinors is taken as $\bar{u}\left(p_2\right)u\left(p_1\right) = 2M\delta\left(\lambda_1,\lambda_2\right)$ where $\lambda_{1,2}$ are the respective helicities of the incoming and outgoing hadron states and M the hadron mass. The gluon GPDs H^g and E^g are likewise defined as:

$$\begin{aligned}\frac{1}{P^+}\int \frac{\mathrm{d}z^-}{2\pi} e^{ixP^+z^-} \left\langle p_2 \left| G^{+\mu}\left(-\frac{z}{2}\right)G^+_\mu\left(\frac{z}{2}\right)\right| p_1\right\rangle_{z_\perp=0,z^+=0} \\ = \frac{1}{2P^+}\left(H^g(x,\xi,t)\bar{u}\left(p_2\right)\gamma^+ u\left(p_1\right) + E^g(x,\xi,t)\bar{u}\left(p_2\right)\frac{i\sigma^{+\mu}\Delta_\mu}{2M}u\left(p_1\right)\right),\end{aligned} \tag{2.4}$$

where $G^{\mu\nu}$ the gluon field strength. It is also possible to define polarised proton GPDs $\widetilde{H}$ and $\widetilde{E}$ by introducing a γ_5 operator in the matrix element. For instance for quarks,

$$\begin{aligned}\frac{1}{2}\int \frac{\mathrm{d}z^-}{2\pi} e^{ixP^+z^-} \left\langle p_2 \left| \bar{\psi}^q\left(-\frac{z}{2}\right)\gamma^+\gamma_5\psi^q\left(\frac{z}{2}\right)\right| p_1\right\rangle_{z_\perp=0,z^+=0} \\ = \frac{1}{2P^+}\left(\widetilde{H}^q(x,\xi,t)\bar{u}\left(p_2\right)\gamma^+\gamma_5 u\left(p_1\right) + \widetilde{E}^q(x,\xi,t)\bar{u}\left(p_2\right)\frac{\gamma_5\Delta^+}{2M}u\left(p_1\right)\right).\end{aligned} \tag{2.5}$$

For a spin-0 hadron, the situation is simplified since only the GPDs H and $\widetilde{H}$ are necessary to parameterize the Fourier transform of the non-local matrix element, giving immediately

$$H^q_{\text{spin0}}(x,\xi,t) = \frac{1}{2}\int \frac{\mathrm{d}z^-}{2\pi} e^{ixP^+z^-} \left\langle p_2 \left| \bar{\psi}^q\left(-\frac{z}{2}\right)\gamma^+\psi^q\left(\frac{z}{2}\right)\right| p_1\right\rangle_{z_\perp=0,z^+=0}. \tag{2.6}$$

For completeness, let us notice that all four GPDs we have presented here are twist-2 GPDs which are chiral-even, in the sense that the struck parton helicity is

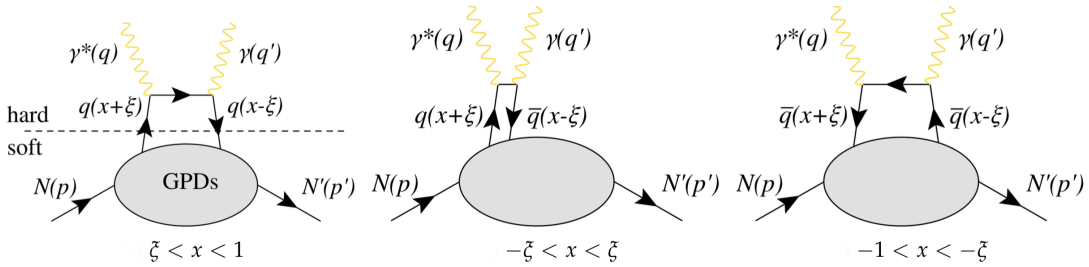

Figure 2.1: Handbag diagram for DVCS. Depending on the x-intervals, the GPD is interpreted as either an emission and re-absorption of a quark (left), of a quark-antiquark pair (center), or of an antiquark (right). Figure taken from [122].

conserved. There exist higher twist GPDs and also chiral-odd that are often coined as transversity GPDs. Chiral-odd GPDs appear in the description of exclusive processes with several produced particles in the final state (see for instance [121]).

2.2 | GPDs interpretation

GPDs are functions of x, ξ and t. The latter two variables are defined in Eq. (2.3). We notice that t is the traditional Mandelstam variable equal to the square of the total transfer of four-momentum to the hadron, while ξ characterizes the transfer of plus-momentum. In a frame where the hadron travels almost at light-speed, the plus-momentum p^+ becomes proportional to the forward momentum p^3 and to the energy p^0. It is therefore common to denote the plus-momentum as "longitudinal momentum" or "forward momentum" with an implicit reference to this frame. On the other hand, x is only indirectly defined in (2.2) as a factor preceding P^+in the exponential weight $e^{ixP^+z^-}$of the integral transform.

In the context of exclusive processes, it is possible to give a partonic interpretation to GPDs. xP^+ is then shown to be the average plus-momentum of the struck parton, whereas $\Delta^+ = -2\xi P^+$ is the plus-momentum transfer to the struck parton, or equivalently the hadron. We deduce then that $(x+\xi)P^+$ is the plus-momentum of the struck parton before interacting with the virtual photon, and $(x-\xi)P^+$its plus-momentum before re-absorption in the hadron. It is shown in Ref. [14] that GPDs are defined for $(x, \xi) \in [-1, 1]$. Depending on the relative values of x and ξ, the GPDs are divided into two distinct regions, each carrying entirely different physical interpretations:

- For $x \in [\xi, 1]$ ($x \in [-1, -\xi]$) referred to as DGLAP [16–19] region, Figure 2.1 (left and right), can be attributed to the amplitude of hitting a quark (antiquark)

in the nucleon with momentum fraction $x + \xi$ ($\xi - x$) and putting it back with a different momentum fraction $x - \xi$ ($-\xi - x$) at a given transverse distance, relative to the transverse center of mass, in the nucleon.

- In the ERBL [20, 21] region, Figure 2.1 (center), $x \in [-\xi, \xi]$ the GPD resembles distribution amplitudes governing the emission or absorption of a quark-antiquark or gluon pair with squared momentum t.

Since gluons are their own anti-particles, the same reasoning shows that the gluon GPD is even in the variable x.

2.3 | General properties

This Section gives a brief excerpt of the general properties of GPDs and their relations to ordinary PDFs and elastic form factors. For a more detailed discussion see for e.g. the reviews [14, 123, 124].

2.3.1 | Link to PDFs

The fact that a non-vanishing four-momentum transfer t is received by the hadron target in DVCS and DVMP makes it necessary to describe the soft part of the interaction thanks to GPDs, and not ordinary PDFs. The link between the two distributions can be observed formally by setting $\Delta = 0$ ($\xi = 0, t = 0$), known as forward limit, the nucleon has the same momentum and helicity configuration in its initial and final state and the GPDs reduce to the ordinary parton densities:

$$\begin{aligned} H^q(x,0,0) &= q_q(x), & \tilde{H}^q(x,0,0) &= \Delta q_q(x) & \text{for } x > 0, \\ H^q(x,0,0) &= -\overline{q}_q(-x), & \tilde{H}^q(x,0,0) &= \Delta \overline{q}_q(-x) & \text{for } x < 0, \\ H^g(x,0,0) &= x g(x), & \tilde{H}^g(x,0,0) &= x \Delta g(x) & \text{for } x > 0, \end{aligned} \tag{2.7}$$

where $q_q(x)(\overline{q}_q(x))$ and $\Delta q_q(x)(\Delta \overline{q}_q(x))$ are respectively the quark (antiquark) unpolarized and polarized PDFs for flavor q. Since PDFs are well-known from a wealth of experimental data, notably thanks to inclusive processes like DIS, the fact that they are the forward limit of GPDs is a crucial aspect of the modeling of the latter.

For the remaining GPDs E and $\tilde{E}$, there exist no corresponding relations as they are multiplied by factors proportional to Δ, (see Eq. (2.2)). Therefore, the forward limit, does not bring any constraint on E or $\widetilde{E}$. Nonetheless, values of E in this limit unaccessible from DIS play an important role in the determination of the spin decomposition of hadrons. They only appear at finite momentum transfers to the nucleon, where a spin flip is possible. The GPDs E^q and E^g carry information

on the nucleon spin contributions by the angular momenta of quarks and gluons, which makes them of particular importance for studying the nucleon spin.

2.3.2 | Link to FFs

GPDs also generalize the usual elastic form factors (FFs) F_1^q and F_2^q which parameterize the matrix element of the electromagnetic current at $z = 0$:

$$\left\langle p_2 \left| \bar{\psi}^q(z)\gamma^\mu \psi^q(z) \right| p_1 \right\rangle = \bar{u}\left(p_2\right)\left[F_1^q(t)\gamma^\mu + F_2^q(t)\frac{i\sigma^{\mu\nu}\Delta_\nu}{2M}\right] u\left(p_1\right). \tag{2.8}$$

From $F_1^q(t)$ and $F_2^q(t)$ are defined the Dirac and Pauli form factors $F_1(t)$ and $F_2(t)$ defined by:

$$F_1(t) = \sum_q e_q F_1^q(t) \quad \text{and} \quad F_2(t) = \sum_q e_q F_2^q(t), \tag{2.9}$$

where e_q is the electric charge of the quark of flavor q. At $t = 0, F_1(0)$ gives the total electric charge of the hadron, and $F_2(0)$ its anomalous magnetic moment.

The link between GPDs and FFs is obtained by taking the limit $z^- = 0$ in Eq. (2.2), which can be achieved by integrating H^q and E^q over their dependence on x, giving their first moment in x [14]:

$$\begin{aligned} \int_{-1}^{1} dx H^q(x,\xi,t) &= F_1^q(t), \quad \int_{-1}^{1} dx E^q(x,\xi,t) = F_2^q(t), \\ \int_{-1}^{1} dx \tilde{H}^q(x,\xi,t) &= g_A^q(t), \quad \int_{-1}^{1} dx \tilde{E}^q(x,\xi,t) = g_P^q(t). \end{aligned} \tag{2.10}$$

Here, g_A^q and g_P^q are the corresponding axial-vector and pseudo-scalar form factors. This relation has been extensively used to describe the t-dependence of GPDs. It should be pointed out that the results are ξ-independent. The integration over x removes all reference to the longitudinal direction, which defines ξ, hence the result must be independent of ξ [14]. The dependence of the form factors on t is characterized by the scale dependence of the strong coupling, which also controls the t-dependence of the GPDs [123].

The nomenclature of "generalized" Parton Distributions (GPDs) becomes evident as these distributions encapsulate various well-established sources of non-perturbative insights into hadron structure. GPDs represent a higher-order generalization of parton distributions, offering a more comprehensive description of hadron properties. Beyond GPDs, there exists another level of generalization known as Generalized Transverse Momentum Dependent Distributions (GTMDs)

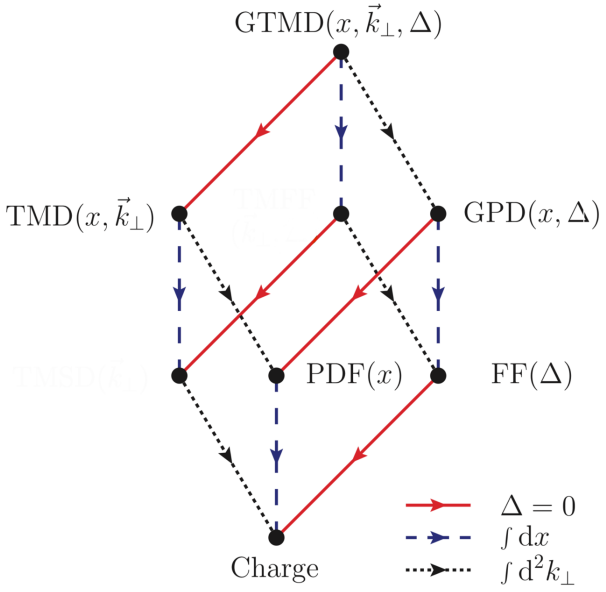

Figure 2.2: Family tree of parton distributions. The link from GPDs to FFs is obtained by integrating the x dependence, whereas the link from GPDs to PDFs is obtained thanks to the limit $\Delta = 0$. Figure taken from [125].

[119, 120]. These distributions, as depicted in the "family tree" of parton distributions in Figure 2.2, involve the unintegrated GPDs over the parton's transverse momentum, denoted as $k_\perp$. In practical terms, integrating GTMDs over the transverse momentum $k_\perp$ is equivalent to setting $z_\perp = 0$ for GPDs, which, is implicitly done in (2.2) by only considering z^- in the definition of the matrix element. This hierarchical structure of parton distributions, from PDFs to GPDs and ultimately to GTMDs, provides a comprehensive framework for understanding the increasingly intricate facets of hadron structure and the wealth of information these distributions offer in the realm of particle physics.

2.3.3 | Polinomiality

Higher moments in x introduce higher-order corrections to the form factors, which appear as polynomials in ξ. For the quark GPDs H^q and E^q, these higher moments are given as [14]:

$$\int_{-1}^{1} dx x^n H^q(x,\xi,t) = \begin{cases} a_0(t) + a_2(t)\xi^2 + a_4(t)\xi^4 + \ldots + a_n\xi^n & \text{even } n \\ a_0(t) + a_2(t)\xi^2 + a_4(t)\xi^4 + \ldots + c_{n+1}\xi^{(n+1)} & \text{odd } n \end{cases}$$
$$\int_{-1}^{1} dx x^n E^q(x,\xi,t) = \begin{cases} b_0(t) + b_2(t)\xi^2 + b_4(t)\xi^4 + \ldots + b_n\xi^n & \text{even } n \\ b_0(t) + b_2(t)\xi^2 + b_4(t)\xi^4 + \ldots - c_{n+1}\xi^{(n+1)} & \text{odd } n \end{cases} \tag{2.11}$$

This property of GPDs is called the polynomiality [14]. Similar Equations also exist for the quark GPDs $\tilde{H}$ and $\tilde{E}$, as well as for the gluons. The fact that only even powers of ξ appear is due to the time reversal invariance: $H(x,\xi,t) = H(x,-\xi,t)$.

2.4 | The hadron tomography

Usual PDFs $a(x)$ possess a probabilistic interpretation as the number density of partons of type a carrying a fraction x of the plus-momentum of the hadron. As generalizations of PDFs, GPDs have an even more appealing probabilistic interpretation when transforming GPDs from momentum space to position space, in the so-called impact parameter representation. At zero skewness $\xi = 0$, the Fourier transform of a GPD with respect to $\Delta_\perp$ is called an impact parameter distribution (IPD) [7, 8]:

$$q(x, b_\perp) = \int \frac{\mathrm{d}^2\Delta_\perp}{(2\pi)^2} e^{-ib_\perp\cdot\Delta_\perp} H^q\left(x, 0, t = -\Delta_\perp^2\right) \tag{2.12}$$

$b_\perp$ is the Fourier conjugate variable of the transverse momentum transfer $\Delta_\perp$.

When $\xi = 0$, Eq. (2.12) gives the number density of quarks with flavor q and longitudinal four-momentum fraction x at the transverse distance $b_\perp$ (impact parameter) with respect to the transverse center of the nucleon momentum $R_\perp$. In the parton representation $R_\perp$ is given by the sum of the transverse positions $r_{\perp,i}$ of all partons i, weighted by their corresponding momentum fraction x_i :

$$R_\perp = \sum_i x_i r_{\perp,i} \tag{2.13}$$

A similar probabilistic interpretation can be found for GPD $\widetilde{H}$, which describes the polarized impact parameter dependent probability density. In a less intuitive form, an interpretation for the Fourier transformation of the GPD E exists.

By experiments, it is not possible to perform measurements at $\xi = 0$. As for $\xi \neq 0$ when the longitudinal momentum of the parton/nucleon changes, the

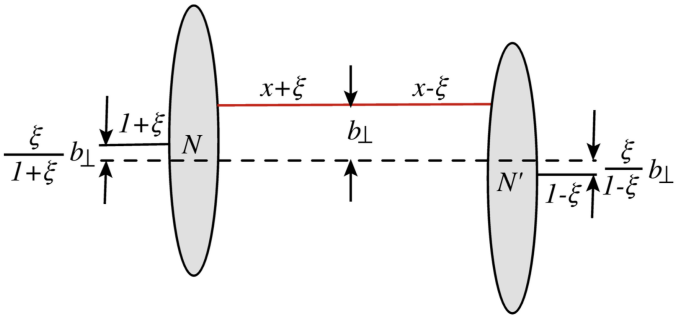

Figure 2.3: Illustration of the shift of center of transverse momentum for GPDs represented in the impact parameter space in the region $x \in [\xi, 1]$. The struck quark is indicated as a red line. Figure taken from [122].

probabilistic interpretation does not hold. Nevertheless, since the incoming hadron carries a plus-momentum $(1+\xi)P^+$whereas the outgoing one carries $(1-\xi)P^+$, it implies a shift of the transverse center of momentum during the interaction if ξ is non zero [14].

An illustration of this shift is shown in Figure 2.3. The transverse center of momenta of the nucleon before and after the scattering process, as well as the average, are indicated by the horizontal solid black lines and the dashed black line, respectively. The shift in the transverse center of momenta with respect to its average is proportional to $b_\perp$. The horizontal red line illustrates the struck quark.

The practical extraction of IPDs faces the challenges of accessing a large range of values in t to perform the Fourier transform. However, factorization theorems are only valid for $|t|$ small with respect to Q^2, which restricts considerably the access to moderate values of $|t|$ of the order of several GeV^2 which introduces model-dependent extrapolations. In addition, since the experimental data are accessible only at non-vanishing ξ, an extrapolation to $\xi = 0$ is necessary.

Although the probabilistic interpretation is lost, the measurements of exclusive reactions still allow us to study the GPDs as a function of the longitudinal parton momentum at small momentum transfer to the nucleon, which provides important information on the transverse parton distribution. Commonly this is referred to as 'nucleon tomography'. For instance, we reproduce in Figure 2.4 the result of the fit of IPDs led in [126].

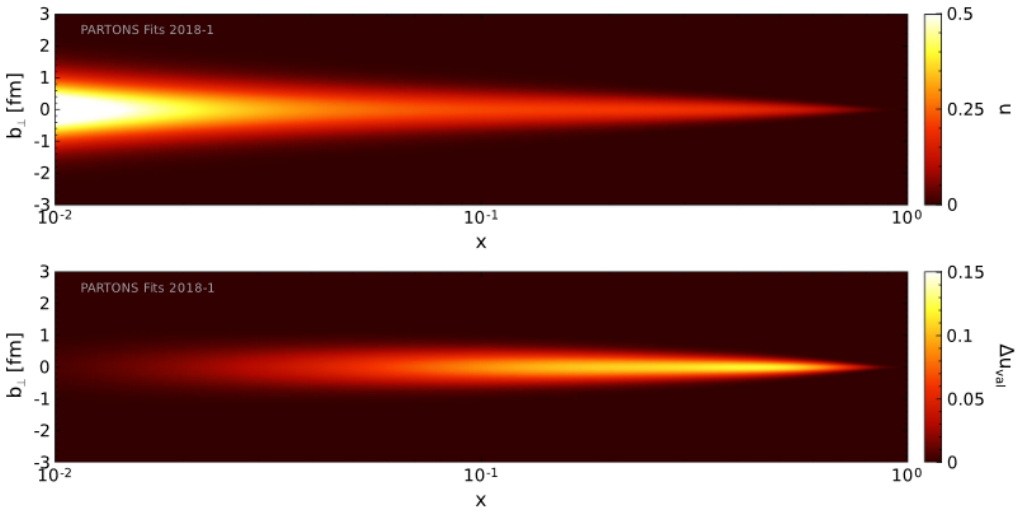

Figure 2.4: Number density of u quarks as a function of x and $b_\perp$ in an unpolarised proton (top) and a longitudinally polarized proton (bottom). For the lower plot, only the valence contribution is shown. Figure taken from [126].

2.5 | Energy-momentum tensor

One of the remarkable features of GPDs is their inherent connection to the QCD Energy-Momentum Tensor (EMT). This connection serves a dual purpose in our understanding of hadron physics. Firstly, it helps elucidate the longstanding enigma of nucleon spin decomposition, a puzzle that originated three decades ago with the pioneering European Muon Collaboration (EMC) measurements [127]. Secondly, it enables the exploration of the mechanical characteristics of hadrons, such as the distribution of pressure within the nucleon [11, 128]. The potential to investigate the mechanical properties of partonic matter was initially emphasized in [10]. This profound link between GPDs and the QCD EMT offers a rich avenue for exploring fundamental aspects of hadron structure and properties, addressing questions that have intrigued physicists for many years.

In the case of a spin-$\frac{1}{2}$ hadron, the matrix element of the local gauge-invariant EMT operator can be parameterized in terms of five gravitational form factors (GFFs) $A^a(t)$, $B^a(t)$, $C^a(t)$, $\bar{C}^a(t)$ and $D^a_{GFF}(t)$[5] as [114–116]

$$\left\langle p_2 \left| T_a^{\mu\nu}(0) \right| p_1 \right\rangle = \bar{u}(p_2) \Big\{ \frac{P^\mu P^\nu}{M} A^a(t) + \frac{\Delta^\mu \Delta^\nu - \eta^{\mu\nu}\Delta^2}{M} C^a(t) + M\eta^{\mu\nu}\bar{C}^a(t) + \frac{P^{\{\mu} i\sigma^{\nu\}\rho}\Delta_\rho}{4M}\left[A^a(t) + B^a(t)\right] + \frac{P^{[\mu} i\sigma^{\nu]\rho}\Delta_\rho}{4M} D^a_{GFF}(t) \Big\} u(p_1), \tag{2.14}$$

where $a^{\{\mu}b^{\nu\}} = a^\mu b^\nu + a^\nu b^\mu$ and $a^{[\mu}b^{\nu]} = a^\mu b^\nu - a^\nu b^\mu$. The connection between

GPDs and GFFs are given for quarks by [14]:

$$\begin{aligned}\int_{-1}^{1} \mathrm{d}x x H^q(x,\xi,t) &= A^q(t) + 4\xi^2 C^q(t),\\ \int_{-1}^{1} \mathrm{d}x x E^q(x,\xi,t) &= B^q(t) - 4\xi^2 C^q(t),\\ \sum_q \int_{-1}^{1} \mathrm{d}x \widetilde{H}^q(x,\xi,t) &= -\sum_q D^q_{GFF}(t),\end{aligned} \tag{2.15}$$

and for gluons by

$$\begin{aligned}\int_{-1}^{1} \mathrm{d}x H^g(x,\xi,t) &= A^g(t) + 4\xi^2 C^g(t),\\ \int_{-1}^{1} \mathrm{d}x E^g(x,\xi,t) &= B^g(t) - 4\xi^2 C^g(t),\\ D^g_{GFF}(t) &= 0.\end{aligned} \tag{2.16}$$

Access to the GFF $\bar{C}^q$ is more intricate since it involves higher twist GPDs [115].

2.5.1 | Disentangling the nucleon spin

The initial measurements of the proton's spin-dependent structure function denoted as g_1^p, were conducted at SLAC and by the European Muon Collaboration (EMC). The findings from the EMC experiments indicated that the role of quark spins in determining the proton's spin was minimal. This was a stark contrast to the prevailing expectation that the spin of the nucleon primarily arises from the spins of its valence quarks. These results triggered what became known as the "spin crisis." Subsequent measurements, conducted more recently, have estimated the contribution of quark spins to be approximately 30%. Additionally, the introduction of gluons through the QCD extension of the Quark-Parton Model (QPM) has added to the complexity of understanding the nucleon's spin composition. Despite these developments, the precise composition of the nucleon's spin remains unresolved and continues to be the subject of intensive research efforts.

It can be shown that the total angular momentum carried by each flavor of quark J^q and gluons J^g for a spin-1/2 hadron is given by [2]:

$$J^q = \frac{1}{2}\left(A^q(0) + B^q(0)\right), J^g = \frac{1}{2}\left(A^g(0) + B^g(0)\right). \tag{2.17}$$

From Eqs. (2.15)-(2.16) the decomposition of the total spin of the hadron, known as Ji's sum rule (see Section 1.4) is deduced as a function of the GPDs:

$$\begin{aligned}\frac{1}{2} &= \sum_q J^q + J^g \\ &= \sum_q \frac{1}{2}\int_{-1}^{1} \mathrm{d}x\, x\,(H^q(x,\xi,0) + E^q(x,\xi,0)) + \frac{1}{2}\int_{-1}^{1} \mathrm{d}x H^g(x,\xi,0) + E^g(x,\xi,0).\end{aligned} \tag{2.18}$$

This sum rule reminds us of the one observed by usual PDFs:

$$1 = \sum_{a=q,\bar{q},g} \int_0^1 \mathrm{d}x\, x a(x). \tag{2.19}$$

Thanks to the probabilistic interpretation of PDFs, this sum rule merely states that when adding the fractional plus-momentum over all partons, we obtain the full plus-momentum of the hadron.

2.5.2 | Mechanical properties

In the Breit frame where spatial three-vectors of $\boldsymbol{P} = \mathbf{0}$ and $t = -\boldsymbol{\Delta}^2$, Fourier transforms of GFFs with respect to $\boldsymbol{\Delta}$ allow us to measure how energy and momentum are distributed inside the hadron [10, 11, 128]. Denoting by $r = |\boldsymbol{r}|$ the radial coordinate, one can define for instance the radial energy $\varepsilon_a(r)$ distribution in the Breit frame as a Fourier transform of the GFFs $A^a(t), B^a(t), C^a(t)$ and $\bar{C}^a(t)$:

$$\varepsilon_a(r) = M \int \frac{\mathrm{d}^3\boldsymbol{\Delta}}{(2\pi)^3} e^{-i\boldsymbol{\Delta}\cdot\boldsymbol{r}} \left\{ A^a(t) + \bar{C}^a(t) + \frac{t}{4M^2}\left[B^a(t) - 4C^a(t)\right]\right\}.$$

Among several distributions of radial mechanical properties that can be defined, the pressure anisotropy $s_a(r)$ has attracted attention due to the fact that it does not depend on $\bar{C}a(t)$. In theory, it can therefore be completely extracted from leading twist GPDs:

$$s_a(r) = -\frac{4M}{r^2} \int \frac{\mathrm{d}^3\boldsymbol{\Delta}}{(2\pi)^3} e^{-i\boldsymbol{\Delta}\cdot\boldsymbol{r}} \frac{t^{-1/2}}{M^2} \frac{\mathrm{d}^2}{\mathrm{d}t^2}\left[t^{5/2} C^a(t)\right]. \tag{2.20}$$

The first determination of the shear forces and the pressure distribution experienced by the quarks inside the proton from DVCS data exploiting the connection between GPDs and GFFs was performed in Refs. [129, 130] Their results are reproduced in Figure 2.5. A strong repulsive pressure near the center of the proton (up to 0.6 fm) and a binding pressure at greater distances were found. The maximum shear force of 40 ± 20 MeV fm^{-1} occurs near 0.6 fm from the proton center, indicating where confinement forces may be strongest. The shear forces in the proton reverse direction at r ≈ 0.45 fm from the center.

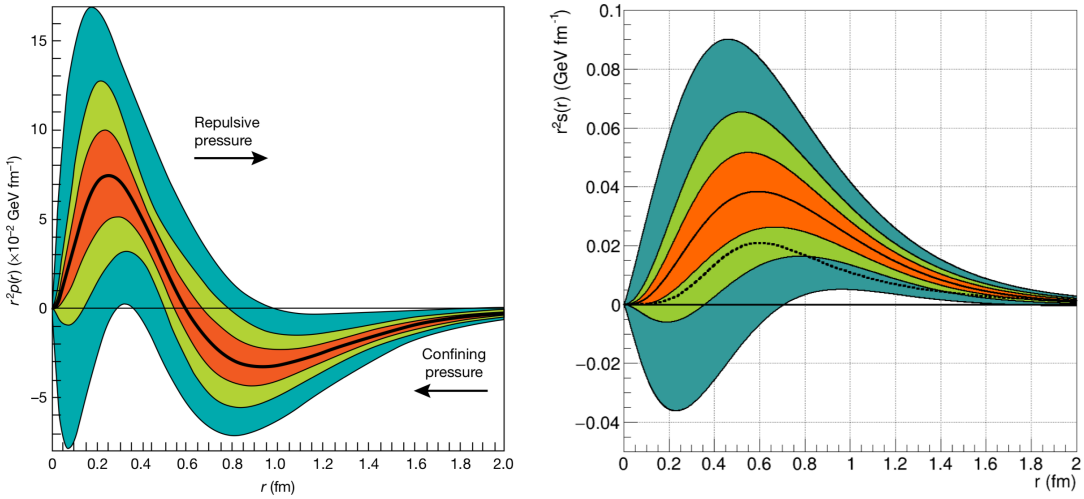

Figure 2.5: (left) Radial pressure distribution in the proton versus the radial distance r from the center of the proton. Figure from [129]. (right) Distribution of the shear forces in the proton. Figure from [130]. The middle solid line represents the fit result. The outer blue-shaded area marks the range of uncertainties when only data prior to the CLAS data are included. The middle (light-green) areas are based on the CLAS data, and the inner (red) area represents projections when expected results from the ongoing and planned experiments are included in the fits. The dashed black curve is a model prediction.

2.6 | Modelling of GPDs

The parametrization of Generalized Parton Distributions (GPDs) through specific models plays a vital role in understanding nucleon structure. Three distinct model families are commonly used: Double Distributions (DDs), dual parametrization, and Mellin-Barnes integrals.

The DDs model is equivalent to satisfying the requirements of Lorentz covariance on the polynomiality of Mellin moments of GPDs. It was initially introduced by A. Radyushkin [131, 132] and D. Müller et al. [1] and they offer a framework to parameterize the (x, ξ)-dependence and inherently satisfy polynomiality. This approach enables the decoupling of the longitudinal component of the transferred momentum to the nucleon (Δ) from its initial momentum by introducing two new variables, making the dependence on x and ξ more manageable. As DD-ansatz only supports polynomials of ξ up to a power of n, the introduction of the so-called D-term, proposed by C. Weiss and M. Polyakov [133], facilitates the inclusion of the highest power of ξ for odd $n(n+1)$ in the moments of the GPDs H and E, see Eq. (2.11)

Two notable models that employ DDs for parameterization are the VGG [56] and

GK [55] models. The VGG model was developed through a series of publications spanning from 1999 to 2005. The GK model's parameterization evolved while fitting data from DVMP by S.V. Goloskokov and P. Kroll [55, 134, 135] that shares the same GPDs as DVCS.

The study of GPDs in the impact parameter space suggests that GPD $H^q(x, 0, -\Delta_\perp^2)$ should become independent of t as x approaches 1. In this scenario, the active quark carries all the nucleon's four-momentum, which according to (2.13) brings it closer to the transverse center of momentum. This results in a small impact parameter $b_\perp$. As $b_\perp$ is the Fourier conjugated to $\Delta_\perp$, and $\Delta_\perp$ related to t, hence GPD H should not depend on t anymore. For $x \to 0$ one expects an increasing contribution by the quark-antiquark sea, resulting in a diverging behavior of the GPD. This should translate to an increase of the nucleon's transverse size like $\alpha \ln \frac{1}{x}$ [7]. An ansatz of this kind is based on Regge theory, which arose from the study of the analytic properties of scattering amplitudes in strong interaction processes [136]. In this theory, the high energy behavior of amplitudes is described by $(s/s_0)^{\alpha(t)}$, where s is the squared center of mass energy, $\alpha(t)$ a so-called Regge trajectory and s_0 a scale factor, usually taken to be 1 GeV^2. In the sea and gluon regime (small x_B, x) this trajectory is the Pomeron trajectory and has the quantum number of the vacuum [124].

Considering the mentioned constraints due to the expected behaviour of $b_\perp(x)$, an ansatz for e.g. of the form:

$$H^q\left(x, 0, -\Delta_\perp^2\right) = q^q(x) e^{-a(1-x)\ln\frac{1}{x}\cdot\Delta_\perp^2} \tag{2.21}$$

can be chosen to parameterize the t-dependence of the GPD H^q [7]. Here, $q^q(x)$ denotes the corresponding quark distribution. The t-dependence of GPD H is of particular interest when investigating the correlation of the slope parameter of the DVCS cross-section to the transverse extension of parton distributions in the proton.

Accessing GPDs in exclusive processes 3

Experimental observables play a crucial role in gaining access to Generalized Parton Distributions (GPDs) in the real world. While the contributions of parton spins can be probed through their polarized Parton Distribution Functions (PDFs), their orbital motions, which are equally vital for understanding the internal dynamics of hadrons, are described by their quantum phase space distributions, essentially encapsulated in their GPDs.

For instance, the quark and gluon angular momentum (AM) densities can be expressed as [2],

$$J_{q,g}(x) = \frac{x}{2}\left(H_{q,g}(x,0,0) + E_{q,g}(x,0,0)\right) \tag{3.1}$$

where $H_{q,g}(x,\xi,t)$ and $E_{q,g}(x,\xi,t)$ are two different types of GPDs. Hence, experiments capable of accessing GPDs are pivotal for measuring the spin structures of nucleons. GPDs are naturally probed by the Deep Exclusive Processes (DEPs), namely the exclusive productions of particles off nucleons with deeply virtual photons, including Deeply Virtual Compton Scattering (DVCS) [2, 3] and Deeply Virtual Meson Production (DVMP) [4, 22] via the collinear factorization of QCD.

Among these processes, DVCS has garnered significant theoretical and experimental attention in recent years. This is due to its advantageous characteristics, including a substantial cross-section, which is crucial when considering its interference with the Bethe-Heitler process, and a relatively clean theoretical description. In contrast, other processes like DVMP offer increased sensitivity to gluons but involve additional non-perturbative functions, such as distribution amplitudes, making them more complex to analyze.

In the following Sections, the general cross-section for exclusive photon production and in particular the contribution by DVCS, namely the process of leptoproduction of a photon off the nucleon with the virtual photon momentum square, or the virtuality, $Q^2 = -q^2$ much larger than the momentum transfer square t, are discussed. The DVCS contribution provides GPD-related observables, named Compton Form Factors (CFFs). Therefore, the DVCS measurements that allow us

to measure the CFFs and reconstruct the GPDs play an important role in studying the internal structure of the nucleon. In the last section, we give an overview of the current experimental landscape regarding DVCS and GPDs measurements and detail the experiments of interest in this thesis used for the extraction of the CFFs.

3.1 | Compton Form Factors

The DVCS cross-section, which provides insights into the parton structure of nucleons, is indirectly dependent on GPDs. Instead of GPDs, the cross-section is parametrized in terms of CFFs. These CFFs have a linear influence on the description of the interference between the Bethe-Heitler (BH) and DVCS processes and a quadratic influence on the pure DVCS term.

Factorization theorems [4, 22] enable us to express CFFs as convolutions of GPDs with coefficient functions. These coefficient functions are calculable at any order of perturbative Quantum Chromodynamics (pQCD). Consequently, retrieving GPDs from CFFs is a significant challenge within the field, often referred to as the deconvolution problem. It involves determining the underlying GPDs from the experimentally accessible CFFs, and its solution is a fundamental goal in understanding the partonic structure of nucleons.

In detail, the CFFs read as [49]:

$$
\begin{aligned}
[\mathcal{H},\mathcal{E},\mathcal{H}^3_+,\mathcal{E}^3_+,\widetilde{\mathcal{H}}^3_-,\widetilde{\mathcal{E}}^3_-](\xi,t) &= \sum_q \int_{-1}^{1} dx C^{q[-]}(x,\xi)[H^q,E^q,H^{q3}_+,E^{q3}_+,\widetilde{H}^{q3}_-,\widetilde{E}^{q3}_-](x,\xi,t),\\
[\widetilde{\mathcal{H}},\widetilde{\mathcal{E}},\widetilde{\mathcal{H}}^3_+,\widetilde{\mathcal{E}}^3_+,\mathcal{H}^3_-,\mathcal{E}^3_-](\xi,t) &= \sum_q \int_{-1}^{1} dx C^{q[+]}(x,\xi)[\widetilde{H}^q,\widetilde{E}^q,\widetilde{H}^{q3}_+,\widetilde{E}^{q3}_+,H^{q3}_-,E^{q3}_-](x,\xi,t),
\end{aligned}
\tag{3.2}
$$

summing over all the quark flavors. Here $C^{q[\pm]}$ is a coefficient function related to the hard scattering part and it is convoluted with twist-2 or leading twist (LT) GPDs, i.e., $H, E, \widetilde{H}, \widetilde{E}$, and twist-3 GPDs, i.e., H^3_+, E^3_+, $\widetilde{H}^3_-$, $\widetilde{E}^3_-$, $\widetilde{H}^3_+$, $\widetilde{E}^3_+$, H^{q3}_-, E^{q3}_-. These convolution integrals arise in the vector and axial vector decomposition of the DVCS amplitude. In pQCD these coefficient functions are calculated as:

$$
C^{q[\pm]} = C^{q[\pm]}_{(0)} + \frac{\alpha_s}{2\pi} C^{q[\pm]}_{(1)} + O\left(\alpha_s^2\right), \tag{3.3}
$$

At leading order (LO), the coefficient function has no scale dependence and reads:

$$
C^{q[\pm]}_{(0)} = e_q^2 \left(\frac{1}{\xi - x - i0} \pm \frac{1}{\xi + x - i0} \right), \tag{3.4}
$$

where e_q^2 is the charge of the quarks in the unit of proton charge. Using the Sokhotski-Plemelj theorem, it is possible to decompose integrals of the form given in Eq. 3.2 into a real and an imaginary part. For any arbitrary GPD F and corresponding CFF $\mathcal{F}$, at LO, this results yields for the imaginary part:

$$\begin{aligned}\Im\mathrm{m}\mathcal{F}^q(\xi,t) &= \pi\sum_q e_q^2\left[F^q(\xi,\xi,t) \mp F^q(-\xi,\xi,t)\right] \\ &= \pi\sum_q e_q^2 F^{q(\pm)}(\xi,\xi,t)\,,\end{aligned} \tag{3.5}$$

and for the real part,

$$\begin{aligned}\Re\mathrm{e}\mathcal{F}^q(\xi,t) &= \sum_q e_q^2\mathcal{P}\int_{-1}^{1}\mathrm{d}x\left(\frac{1}{\xi-x}\mp\frac{1}{\xi+x}\right)F^q(x,\xi,t) \\ &= \sum_q e_q^2\mathcal{P}\int_{0}^{1}\mathrm{d}x\left(\frac{1}{\xi-x}\mp\frac{1}{\xi+x}\right)F^{q(\pm)}(x,\xi,t)\,,\end{aligned} \tag{3.6}$$

where $\mathcal{P}$ denotes Cauchy's principal value. We have used the explicit x parity of the DVCS coefficient function to restrict integration on $[0,1]$. The top sign applies for the unpolarized GPDs (H, E) and the the bottom sign is for the polarized GPDs ($\widetilde{H},\widetilde{E}$). Equations (3.5) and (3.6) show that in case an experimental observable is sensitive to the imaginary part of the CFFs, it will only contain information along the line $x=\pm\xi$, whereas the real part probes GPD integrals over the momentum fraction x. The maximum model-independent information that can be extracted from the DVCS reaction at the leading twist is eight CFFs, which depend on two variables, ξ and t, at QCD leading order. There is an additional Q^2 dependence in the CFFs (and in the GPDs) if QCD evolution is taken into account.

The connection between CFFs and GPDs (3.2) holds profound significance in the realm of nuclear and particle physics acting as a bridge, linking the observable outcomes of experiments with the underlying dynamics of quarks and gluons within hadrons. This relationship provides a unique window into the intricate subatomic world, offering insights into the spatial distribution, momentum, and spin of partons.

The majority of studies on DVCS have traditionally been conducted at LO in the context of pQCD. This choice is driven by the remarkable ability to directly access the diagonal elements of the GPDs through the imaginary part of the LO coefficient function (3.5). Furthermore, the limited range of Q^2 values covered by current experimental DVCS datasets has allowed for a simplified treatment of the Q^2 dependence. However, the extraction of CFFs from experimental data

presents formidable challenges. The process involves disentangling these form factors from complex experimental measurements, often mired in uncertainties and systematic errors. The non-perturbative nature of strong interactions poses a significant challenge, as CFFs are intimately tied to the behavior of quarks and gluons under extreme conditions. This necessitates advanced theoretical models and precise measurements that can distinguish between various hadron structures and quark-gluon interactions. Moreover, the multiplicity of CFFs, each with real and imaginary components, increases the complexity of the extraction process. To access these elusive form factors, continuous innovation in theoretical, experimental, and analysis techniques is necessary. The extraction of CFFs is the main subject of this thesis making use of sophisticated analysis methods.

3.2 | DVCS cross-section

Before we can extract the twist-2 Compton form factors (CFFs), we must have a thorough understanding of the relevant cross sections that have been and can be measured. DVCS is considered the golden channel for the measurements of quark GPDs with its clean final state. The DVCS is an exclusive process where a virtual photon γ^* with large space-like squared four-momentum $q^2 \ll -M^2$ is exchanged usually from an incoming lepton beam with a hadron target of mass M. Contrary to inclusive processes where any final state of the interaction is considered, exclusive processes require that the hadron remains intact in the final state. Providing that the struck nucleon is not broken, part of the incoming energy is re-emitted through a real photon.

The computation of the first Deeply Virtual Compton Scattering (DVCS) cross-section in terms of the leading twist CFFs was presented in the works from Ji [3], which marked a significant milestone in the field of high-energy physics. This pioneering work established a clear connection between the proton's Generalized Parton Distributions (GPDs) and experimentally measurable observables. Subsequently, Belitsky, Müller, and Kirchner (BKM) [49], significantly advanced the field of DVCS by extending their computations beyond the leading-order Generalized Parton Distributions (GPDs). They provided explicit formulas for DVCS cross-sections in terms of laboratory frame kinematic variables. Notably, in their work, they introduced the azimuthal dependence of DVCS cross-sections through the use of harmonic functions. Furthermore, they proposed methods for the extraction of CFFs, which are essential for understanding the internal structure of hadrons. To

enhance the accuracy and precision of their calculations, the same authors revisited their study in a subsequent work, referred to in this thesis as BKM10 formulation, published in [61]. This updated formulation offered more refined and kinematically accurate formulas, which have become a key reference in the field of DVCS research. Throughout our work, we have utilized the BKM10 formulation as the basis for the CFFs extraction from the DVCS proccess, benefiting from its improved accuracy and reliability.

Following or extending the work in [49, 61], Belitsky, Müller, and Ji (BMJ) [137] suggested a new decomposition of the Compton hadronic tensor in terms of photon helicity-dependent CFFs that are free from kinematical singularities at the edges of the available phase space. The main motivation for this study has been to establish the connection between large-Q^2 description in terms of GPDs and small-Q^2 description in terms of generalized polarizabilities, the BMJ basis seems to be well suited for the study of higher twist effects.

The parameterization of the DVCS amplitude by the expressions that arise from a leading-twist QCD calculation at leading order accuracy in terms of GPDs is however incomplete and in fact, convention-dependent, as it violates the required symmetries which are restored by contributions that are formally suppressed by powers of 1/Q, dubbed higher-twist corrections. There are other available DVCS calculations using distinct conventions in the literature. The Braun, Manashov, and Pirnay (BMP) formulation, is known for its calculations of finite-t and target-mass corrections to DVCS. Their work, found in references [138, 139], addresses specific corrections related to the kinematic variables involved in DVCS. A more recent calculation, referred to as UVa [140], has been performed with full inclusion of the twist-3 GPDs using the helicity amplitudes formalism. However, the UVa formulation provides results that differ quantitatively from those of BKM, as highlighted in reference [141].

Another original computation of the DVCS cross-section was conducted and detailed in reference [62]. This work undertook a comprehensive examination of higher-order kinematic effects associated with twist-2 CFFs. The results of this calculation offered insights into the impact of factors such as light cone choices and gauge dependence and provided a comprehensive comparison of the various DVCS calculations based on their convention choices. It also demonstrated that the results of BKM and UVa could be reconciled with appropriate coordinate choices, with some exceptions, such as an additional source of phase dependence claimed by the UVa authors.

In this section, we provide an overview of many of the important observables

needed to extract leading twist CFFs, with many detailed formulas given in Appendices A and B. Specifically, we introduce the kinematics of the DVCS process, the factorization, and the general cross-section for exclusive photon production and in particular, the contribution by DVCS using the BKM10 formulation.

3.2.1 | DVCS kinematics

A handbag diagram illustrating DVCS in electron-proton scattering at leading order and leading twist is shown in left panel of Figure 3.1. Its event topology is summarized as:

$$e + p \rightarrow e' + p' + \gamma. \tag{3.7}$$

The angular dependence of the DVCS in the laboratory frame, where the target is at rest, is defined in the right panel of Figure 3.1: ϕ is the azimuthal angle between the leptonic and hadronic planes, and ϕ_s is the angle between the leptonic plane and the transverse polarisation of the hadron in the case of a polarised target. In this frame, the four momenta of the participating particles in the process are denoted as k and k' for the incoming and scattered lepton, p and p' for the proton before and after the interaction, with q and q' for the virtual and real photon respectively:

$$k = (E, \vec{k}), \quad k' = (E', \vec{k}'), \quad p = (M, \vec{0}) \quad \text{and} \quad q = (k - k') = (\nu, \vec{q}). \tag{3.8}$$

Here, M is the mass of the nucleon. The energy of the virtual photon and the so-called photon virtuality Q^2 are Lorentz invariants given by:

$$\nu = \frac{pq}{M} \overset{\text{lab}}{=} E - E', \tag{3.9}$$

$$Q^2 = -q^2 = -(k - k')^2, \tag{3.10}$$

As ν is not dimensionless, a frequently used variable is the lepton energy loss:

$$y = \frac{qp}{pk} \overset{\text{lab}}{=} \frac{\nu}{E}. \tag{3.11}$$

In the laboratory frame, y is given by the difference between the lepton energies divided by the energy of the incoming lepton.

Another commonly used quantity is the Lorentz invariant Bjorken scaling variable:

$$x_B = \frac{Q^2}{2pq} = \frac{Q^2}{2M\nu}. \tag{3.12}$$

In the case of elastic lepton-nucleon scattering, x_B is equal to one, while in the inelastic case $x_B < 1$.

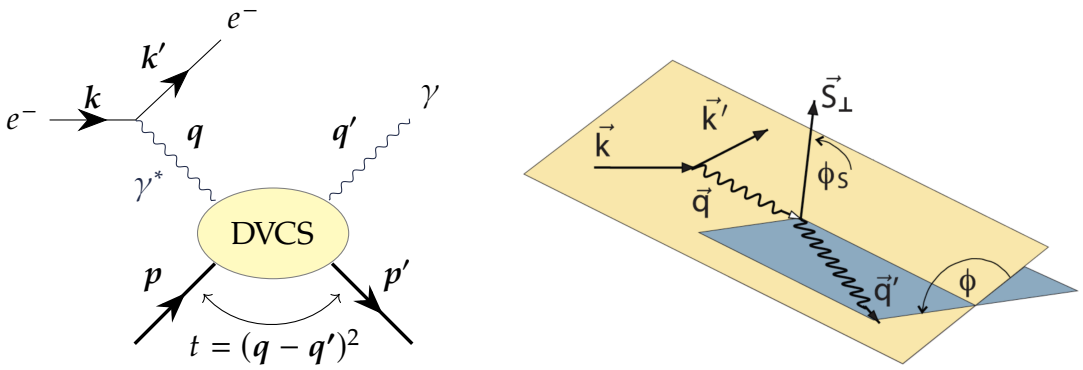

Figure 3.1: (left) Handbag diagram for DVCS in lepton-nucleon scattering at leading order and leading twist. (right) Kinematics of a photon lepto-production event in the hadron rest frame (Trento notations [142]). The incoming and outgoing leptons are denoted by $\vec{k}$ and $\vec{k}'$, the exchanged photon by $\vec{q}$ and the real photon in the final state by $\vec{q}'$. The incoming and outgoing lepton trajectories define the leptonic plane, and the recoil hadron and real photon define the hadronic plane. In this reference system, ϕ is the angle between the leptonic and hadronic planes. ϕ_S is the angle between the leptonic plane and the transverse polarisation of the hadron in the case of a polarised target Figure taken from Ref [143].

In the DVCS process, the virtual photon of mass Q^2 is absorbed and transfers a four-momentum q to the quark. This four-momentum transfer is partly re-emitted in the form of a real photon and partly absorbed by the quark, resulting in a recoil momentum of the nucleon. The four-momentum transfer to the nucleon is denoted as $\Delta = p' - p$, and the square of the total four-momentum transfer to the hadron is given by the variable t:

$$t = \Delta^2 = (p' - p)^2 . \tag{3.13}$$

In the literature at least two parametrizations of the longitudinal momentum fraction carried by the quark are common. This fraction relates to the average nucleon momentum $P = \frac{1}{2}(p + p')$. In this thesis, the symmetric parametrization is used, which was introduced by Ji [144]. In this parametrization, the difference in the momentum fraction of the quark before absorbing the virtual photon and after the emission of the real photon is denoted as 2ξ. Hence, the corresponding momentum fractions carried by the quark are $x+\xi$ and $x-\xi$. The variable x denotes the average longitudinal momentum fraction of the nucleon carried by the struck quark. When using the symmetric parametrization, the skewness ξ is related to the common Bjorken variable x_B by [14]:

$$\xi = x_B \frac{1 + \frac{t}{2Q^2}}{2 - x_B + x_B \frac{t}{Q^2}} \overset{\text{small}}{\approx} \frac{x_B}{2 - x_B}. \tag{3.14}$$

It is therefore also called generalized Bjorken variable. For small values of Δ, ξ can be approximated by $x_B/(2-x_B)$. In an alternative parametrization, introduced by Radyushkin [5], the difference in the momentum fraction is not symmetric but only accounts for the quark after the emission of the real photon. For more details on both notations see Ref. [14]. The longitudinal momentum fractions of both parametrizations are related by [14]:

$$X = \frac{x+\xi}{1+\xi}, \zeta = \frac{2\xi}{1+\xi}. \tag{3.15}$$

A detailed discussion of DVCS cross section is given in Section 3.2.3.

3.2.2 | Factorization of the DVCS

Factorization is a central idea in QCD that simplifies the description of complex scattering processes like DVCS. It separates the process into two distinct stages: the hard scattering process at short distances, which can be calculated using perturbative QCD, and the non-perturbative, long-distance GPDs that describe the internal structure of hadrons. In the case of DVCS, factorization allows us to isolate the hard interaction between the virtual photon, electron, and quarks from the soft interaction that characterizes the distribution of quarks and gluons within the target hadron. This separation simplifies the theoretical description and enables the use of perturbation theory to calculate the hard scattering amplitudes, while the GPDs describe the quark and gluon content of the hadron.

The theoretical foundation of studying the DVCS process is the collinear factorization proven in QCD to the leading power accuracy of Q [5, 23, 145]. In this approach, the DVCS amplitudes are written as convolutions of perturbatively calculable coefficient functions and nonperturbative GPDs that represent the nontrivial nucleon structure. The DVCS coefficient functions have been calculated including the next-to-leading-order (NLO) corrections of the strong coupling constant $O(\alpha_s)$ and the scale-dependence of GPDs is known to the two-loop accuracy so that the complete NLO renormalization- group improved calculation of the amplitudes is possible . This collinear factorization is valid only at values of t such that $-t \ll Q^2$. Reference [146] provides a clear picture of the physical content of factorization for inclusive processes and the interpretation of usual parton distribution functions (PDFs) as probability distributions. We also refer to the introduction of Ref. [147] for a very nice intuitive introduction to factorization.

When a deeply virtual photon interacts with a parton inside a hadron, the struck parton receives a large four-momentum transfer and the interaction of the

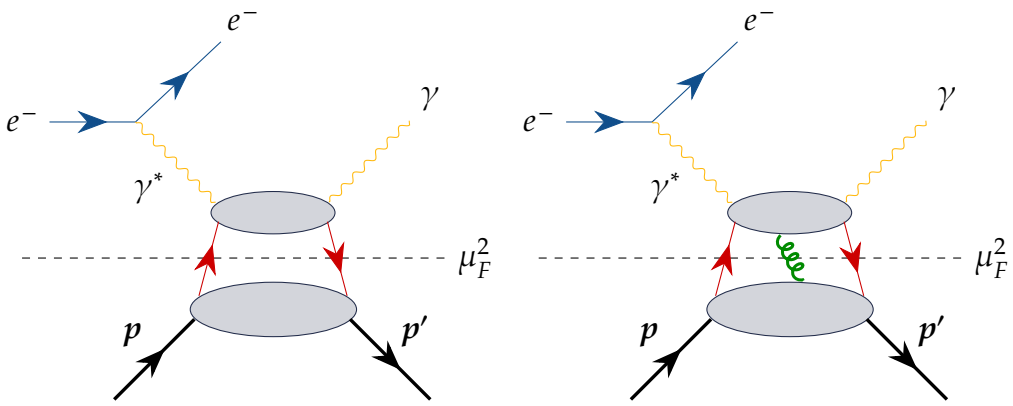

Figure 3.2: Quark contributions to the factorization of DVCS in the leading twist (left panel) and next-to-leading twist approximations (right panel). μ_F^2 is the factorization scale.

struck parton with the rest of the hadron can be viewed diagrammatically as the exchange of partons of virtuality of the order of Q^2. Their contribution to the cross-section of the process is suppressed by powers of $1/Q$ as the number of exchanged partons increases. This gives rise to a so-called twist expansion of the process (see for instance Ref [148] for a precise definition of twist). In the left part of Figure 3.2, we present a diagram that illustrates the leading twist (LT) contribution, i.e., twist-2, in the context of DVCS. This representation depicts the interaction between the virtual photon and the struck parton, shown in the upper grey area, separated from the remaining constituents of the hadron on the lower grey area, as long as substantial virtuality Q^2, where the collinear factorization stands, is transferred to the struck parton. The right panel of Figure 3.2 illustrates a higher twist contribution, wherein the interaction between the struck parton, carrying significant four-momentum, and the other components of the hadron is mediated by the involvement of a gluon.

The separation between the hard part, where large virtuality flows thanks to the interaction with the deeply virtual photon, and the soft part, given only by small virtuality, is somewhat arbitrary and fixed by the choice of a factorization scale μ_F^2. The factorization scale can be thought of as an upper limit on the transverse momentum, denoted as $k_\perp$, carried by partons within the hadron, (see Ref. [146, 149] for instance for more details). Intuitively, it can be understood as the energy resolution at which the system is being described. As this scale increases, partons are treated as being further subdivided into radiatively generated constituents.

The remarkable property of asymptotic freedom in Quantum Chromodynamics (QCD) allows us to describe the hard part of scattering processes using a pertur-

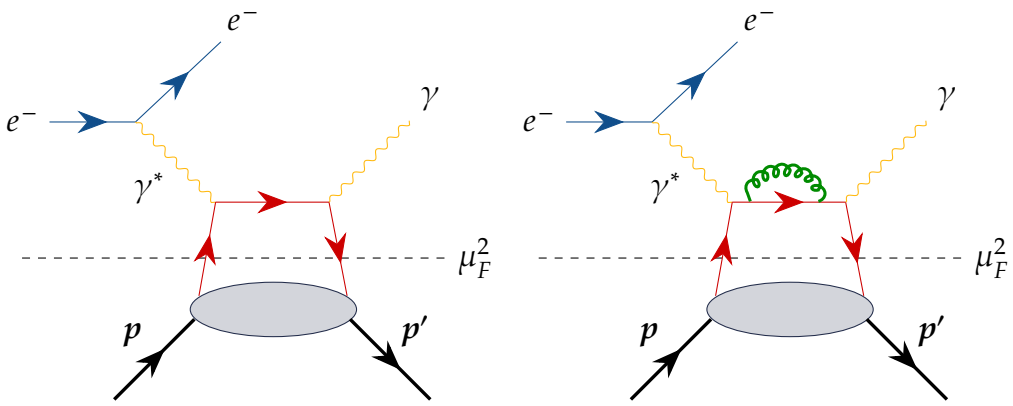

Figure 3.3: Factorization of DVCS in the leading twist description at leading order (left panel) and an example of a next-to-leading order contribution (right panel).

bative expansion in increasing orders of the strong coupling constant, denoted as $\alpha_s\left(\mu_R^2\right)$, where μ_R^2 represents the renormalization scale. It is generally recommended to set the renormalization/factorization scale to be in close proximity to the actual virtuality involved in the specific QCD process. This choice minimizes the need for resuming large logarithmic corrections that arise due to the disparity between the theoretical description's resolution and the experimental probing resolution. Figure 3.3 illustrates the leading order (LO) and an example of a next-to-leading order (NLO) contribution to the hard part description, where the struck quark emits a gluon loop. This perturbative expression of the hard part in the scattering process is known as the coefficient function. Different processes, such as DVCS and DVMP, are characterized by distinct coefficient functions. The coefficient functions must rely on the factorization scale to absorb, at least up to the defined perturbative order, the effects of arbitrary scale variations.

In contrast, the soft part of the interaction, which encompasses the dynamics of low-energy QCD interactions within the hadron, cannot be effectively described within the perturbative framework. This soft part is characterized by non-perturbative parton distributions. In the case of DIS processes, conventional PDFs are sufficient for description. However, for processes like DVCS and DVMP, a more refined description is required, involving GPDs. This refinement is necessary due to the more intricate kinematic structure of DVCS and DVMP. While the structure functions in DIS solely depend on variables like Bjorken's variable x_B, Q^2, and lepton trajectory angles, the measurement of the final state in exclusive processes introduces a dependence on the transfer of four-momentum to the target GPDs extend the information provided by PDFs, which only describe the distribution of forward momentum x within the struck hadron. GPDs also depend on

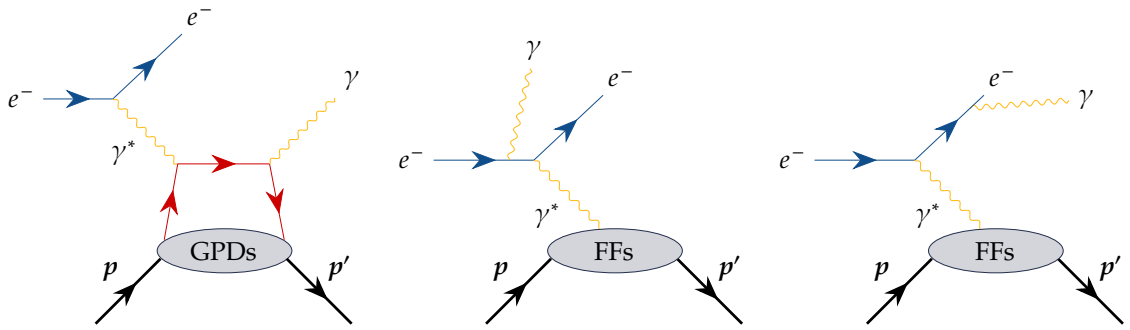

Figure 3.4: Handbag diagram of the DVCS process at leading order and leading twist (left). Diagram of the Bethe-Heitler process at leading order where the real photon is emitted by the lepton either before (center) or after (right) the scattering off the nucleon.

the total four-momentum transfer t and its longitudinal component ξ, often called skewness.

It's important to note that unlike coefficient functions, which are process-specific, parton distributions are universal objects. They play a consistent role in describing various processes, providing a unified framework for understanding the internal structure of hadrons across a range of high-energy scattering processes.

3.2.3 | Photon leptoproduction cross-section

As depicted on the handbag diagram on the left panel of Figure 3.4, in the case of an electron, DVCS corresponds to the initial and final states $lh \rightarrow l\gamma h$, where l is a lepton, γ a real photon and h the hadron target DVCS is therefore measured thanks to photon leptoproduction events. There exists however another process with the same initial and final states which can not be distinguished experimentally from the DVCS, known as Bethe-Heitler (BH). A diagrammatic representation of the BH contribution is given in Figure 3.4. The incoming electron is elastically scattered by the hadron target and a photon is radiated by the electron instead of the struck quark of the nucleon either before (center panel) or after (right panel) the scattering off the nucleon. The description of this process involves only elastic form factors (FFs).

DVCS and BH interfere coherently, so the cross-section of leptoproduction of a photon is written as the sum of the squared amplitudes of the two processes $|\mathcal{T}_{DVCS}|^2$ and $|\mathcal{T}_{BH}|^2$ with the addition of an interference term $\mathcal{I}$. As a consequence,

the four-fold cross section can be expressed as [49]:

$$\frac{d^4\sigma}{dQ^2 dx_B dt d\phi} = \frac{\alpha^3 x_B y^2}{8\pi Q^4 \sqrt{1+\epsilon^2}} \frac{1}{e^6} |\mathcal{T}|^2, \tag{3.16}$$

where $\epsilon = 2x_B \frac{M}{Q}$, and e is the elementary charge. The amplitude $\mathcal{T}$ is decomposed into the contributions from the DVCS, BH, and interference terms:

$$|\mathcal{T}|^2 = |\mathcal{T}_{BH}|^2 + |\mathcal{T}_{DVCS}|^2 + \mathcal{I}, \tag{3.17}$$

with the interference term $\mathcal{I}$ being:

$$\mathcal{I} = \mathcal{T}_{DVCS}\mathcal{T}^*_{BH} + \mathcal{T}^*_{DVCS}\mathcal{T}_{BH}. \tag{3.18}$$

Here * denotes complex conjugation.

The BKM formulations performed a harmonic expansion of the DVCS, BH, and Interference terms as a function of ϕ up to twist-3 including gluon transversity. The development from [49] will be used for the BH, while the parametrization from the BKM10 [61] will be applied for the DVCS and Interference terms[1].

3.2.3.1 | BH term

The Bethe-Heitler amplitude is computed using pure QED and can be expressed as a function of the elastic Form Factors. By using the FFs parametrization proposed by Kelly in [150], the BH term can be computed with a precision better than 1% in the kinematic settings of this experiment. $|\mathcal{T}_{BH}|^2$ is given by the expression:

$$|\mathcal{T}_{BH}|^2 = \frac{e^6}{x_B^2 y^2 (1+\epsilon^2)^2 t \mathcal{P}_1(\phi)\mathcal{P}_2(\phi)} \left\{ c_0^{BH} + \sum_{n=1}^{2} c_n^{BH} \cos(n\phi) + s_1^{BH} \sin(\phi) \right\},$$

where $\mathcal{P}_1(\phi)$ and $\mathcal{P}_2(\phi)$ are the lepton propagators. The full set of the harmonic coefficients c_i^{BH} and s_1^{BH}, are given in [49]. In the case of an unpolarized target , $s_1^{BH} = 0$. The expressions of $\mathcal{P}_1(\phi)$ and $\mathcal{P}_2(\phi)$ and the harmonic coefficients for the unpolarized case which is the main interest of this thesis are given in Appendix A.1.

3.2.3.2 | DVCS term

The DVCS amplitude is parametrized by bi-linear combinations of CFFs. The term $|\mathcal{T}_{DVCS}|^2$ is given by the expression:

$$\left|\mathcal{T}^{\text{DVCS}}\right|^2 = \frac{e^6}{y^2 Q^2} \left\{ c_0^{\text{DVCS}} + \sum_{n=1}^{2} \left[c_n^{\text{DVCS}} \cos(n\phi) + s_n^{\text{DVCS}} \sin(n\phi) \right] \right\}, \tag{3.19}$$

[1]The definition of ϕ used by BKM formulations is not the same as the one from the Trento convention [142]. The transformation $\phi_{BKM} = \pi - \phi_{Trento}$ must be applied.

and the harmonic coefficients c_n^{DVCS} and s_n^{DVCS} are detailed in Appendix A.2. The first term of c_0^{DVCS} contains twist-2 quark and gluon transversity CFFs while the second term involves twist-3 quark CFFs, c_1^{DVCS} and s_1^{DVCS} encompass twist-2 and twist-3 quark CFFs, and c_2^{DVCS} encloses twist-2 gluon transversity CFFs. Furthermore, the coefficient s_1^{DVCS} depends on the beam helicity, and $s_2^{DVCS} = 0$ in the case of an unpolarized target.

3.2.3.3 | Interference term

The Interference amplitude is parametrized by linear combinations of CFFs. $\mathcal{I}$ is given by the expression:

$$\mathcal{I} = \frac{\pm e^6}{x_B y^3 t \mathcal{P}_1(\phi)\mathcal{P}_2(\phi)} \left\{ c_0^{\mathcal{I}} + \sum_{n=1}^{3} \left[c_n^{\mathcal{I}} \cos(n\phi) + s_n^{\mathcal{I}} \sin(n\phi) \right] \right\},$$

where the $+(-)$ case stands for a negatively (positively) charged lepton beam.

Each harmonic coefficient is a mixture of twist-2 and twist- 3 quarks CFFs and twist-2 gluon transversity CFFs. Nevertheless, $c_0^{\mathcal{I}}$, $c_1^{\mathcal{I}}$ and $s_1^{\mathcal{I}}$ have a twist-2 quark dominant term, while $c_2^{\mathcal{I}}$ and $s_2^{\mathcal{I}}$ have a twist-3 quark dominant term, and $c_3^{\mathcal{I}}$ has a twist-2 gluon transversity dominant term. Furthermore, the coefficients $s_1^{\mathcal{I}}$ and $s_2^{\mathcal{I}}$ depend on the beam helicity, and $s_3^{\mathcal{I}} = 0$ in the case of an unpolarized target.

The helicity conserving components of the harmonic coefficients $c_n^{\mathcal{I}}$ and $s_n^{\mathcal{I}}$ where no twist-3 contributions are included, are detailed for the unpolarized case in the Appendix A.3.

3.3 | Experimental observables

The total cross-section for exclusive photon leptoproduction, both unpolarized and polarized, are primary observables. For all possible combinations of beam and target polarizations, it is given by [151]:

$$\begin{aligned} \mathrm{d}\sigma \sim\ & \mathrm{d}\sigma_{UU}^{\mathrm{BH}} + e_\ell \mathrm{d}\sigma_{UU}^{\mathrm{I}} + \mathrm{d}\sigma_{UU}^{\mathrm{DVCS}} \\ & + e_\ell P_\ell \mathrm{d}\sigma_{LU}^{\mathrm{I}} + P_\ell \mathrm{d}\sigma_{LU}^{\mathrm{DVCS}} \\ & + e_\ell S_L\, \mathrm{d}\sigma_{UL}^{\mathrm{I}} + S_L\, \mathrm{d}\sigma_{UL}^{\mathrm{DVCS}} \\ & + e_\ell S_\perp \mathrm{d}\sigma_{UT}^{\mathrm{I}} + S_\perp \mathrm{d}\sigma_{UT}^{\mathrm{DVCS}} \\ + P_\ell S_L\, \mathrm{d}\sigma_{LL}^{\mathrm{BH}} & + e_\ell P_\ell S_L\, \mathrm{d}\sigma_{LL}^{\mathrm{I}} + P_\ell S_L\, \mathrm{d}\sigma_{LL}^{\mathrm{DVCS}} \\ & + P_\ell S_\perp \mathrm{d}\sigma_{LT}^{\mathrm{BH}} + e_\ell P_\ell S_\perp \mathrm{d}\sigma_{LT}^{\mathrm{I}} + P_\ell S_\perp \mathrm{d}\sigma_{LT}^{\mathrm{DVCS}}. \end{aligned} \tag{3.20}$$

This equation follows from the explicit BKM formulae in [49, 61, 137]. Note that for simplicity $d\sigma$ is used instead of fourfold differential $d^4\sigma/dx_B\, dQ^2\, d|t|d\phi$ or, in case of the transversely polarized target, instead of fivefold differential $d^5\sigma/dx_B\, dQ^2\, d|t|d\phi d\phi_S$.

The first subscript of the cross-section σ_{XY} refers to the beam polarization state while the second refers to the target polarization state. U stands for unpolarized, L for longitudinal and T for transverse polarizations. P_ℓ and e_ℓ are the helicity and the charge of the lepton beam, respectively, and S_L is the component of the target polarization vector that is parallel to $\vec{q}$. Equation (3.20) consists of three parts, representing the contributions of BH (first column), the DVCS process (third column), and their interference (I, the second column). The first row of (3.20) represents the spin-independent cross sections, rows 2-4 the singlespin-dependent cross sections, and rows 5-6 the doublespin-dependent cross sections. In the case of a transversely polarized target, the UT and LT cross sections can be further divided into 2 sub-components. Each beam and target polarization combination gives a different observable. This will indeed ensure we have a sufficiently constrained system of equations that is required to extract the many multiplicity of twist-2 and twist-3 CFFs.

Besides absolute cross sections, another way to access CFFs is through the measurement of asymmetries. They involve specific linear combinations of polarized cross-sections in a rational expression. Consequently, one can think of cross sections (and all their polarization combinations) as the independent experimental inputs, while regarding asymmetries as non-independent experimental inputs. Nonetheless, they offer an intrinsic advantage since some systematic uncertainties linked to the normalization of the cross-sections cancel out because of the numerator over denominator ratio. They represent a large fraction of the available worldwide data on GPDs.

One of the typical asymmetries measured is, for instance, the beam charge asymmetry (BCA) which is defined as:

$$A_C = \frac{d\sigma^+ - d\sigma^-}{d\sigma^+ + d\sigma^-},$$

where $d\sigma^+$and $d\sigma^-$refer to cross-sections with lepton beams of opposite charge. Another example is the beam spin asymmetry (BSA), measured for longitudinally polarised electrons and unpolarised hadrons defined by:

$$A_{LU} = \frac{d\sigma^{\rightarrow} - d\sigma^{\leftarrow}}{d\sigma^{\rightarrow} + d\sigma^{\leftarrow}}$$

where $d\sigma^{\rightarrow}$ and $d\sigma^{\leftarrow}$ designate cross sections with opposite lepton beam helicity.

Different observables - including different Fourier harmonics of the same asymmetry are sensitive to different combinations of CFFs and provide therefore various handles to perform CFF extraction from experimental data. Reference [151] summarises expressions of various observables in terms of CFFs. The question of determining which observables to measure in which kinematic regions is central to increasing the experimental knowledge on CFFs.

3.4 | Experimental status

While Deeply Virtual Compton Scattering (DVCS) represents a highly precise means to probe Generalized Parton Distributions (GPDs), its measurement poses formidable challenges. Achieving accurate measurements demands a substantial increase in luminosity due to the inherently small DVCS cross sections. Additionally, experiments necessitate detectors capable of ensuring the exclusive occurrence of the DVCS process, filtering out other inelastic interactions. Furthermore, a wide array of experimental configurations is indispensable to capture the full range of observables required for the extraction of Compton Form Factors (CFFs) and GPDs. This entails conducting DVCS experiments on both protons and neutrons, utilizing lepton beams with varying polarizations and charges (positive or negative), and employing targets with different polarization states (unpolarized, longitudinally polarized, or transversely polarized), while also covering a spectrum of beam energies and kinematic scenarios. To amass these diverse datasets, the exploration of GPD physics involves collaborative efforts across multiple experimental programs which are summarized in Figure 3.5

Approximately two decades ago, the pioneering measurements of DVCS commenced at two prominent facilities, HERA in Germany and JLab (Jefferson Lab) in the United States. The H1 [24, 25] and ZEUS [26] collaborations at HERA employed a collider setup, allowing them to access the smallest values of the x_B and the highest values Q^2 in DVCS measurements. Their work probed remarkably low values of x_B (around 10^{-4}) and high Q^2 values (approximately 100GeV^2), as illustrated in Figure 3.5. Regrettably, these measurements suffered from relatively low statistics. These experiments were conducted using both electron and positron beams, leading to publications on beam charge asymmetries and DVCS cross-sections, particularly emphasizing the pure DVCS contribution at low x_B.

Additionally, at HERA, the HERMES collaboration [27–33] used a fixed target approach, offering longitudinal or transverse polarization. They provided a com-

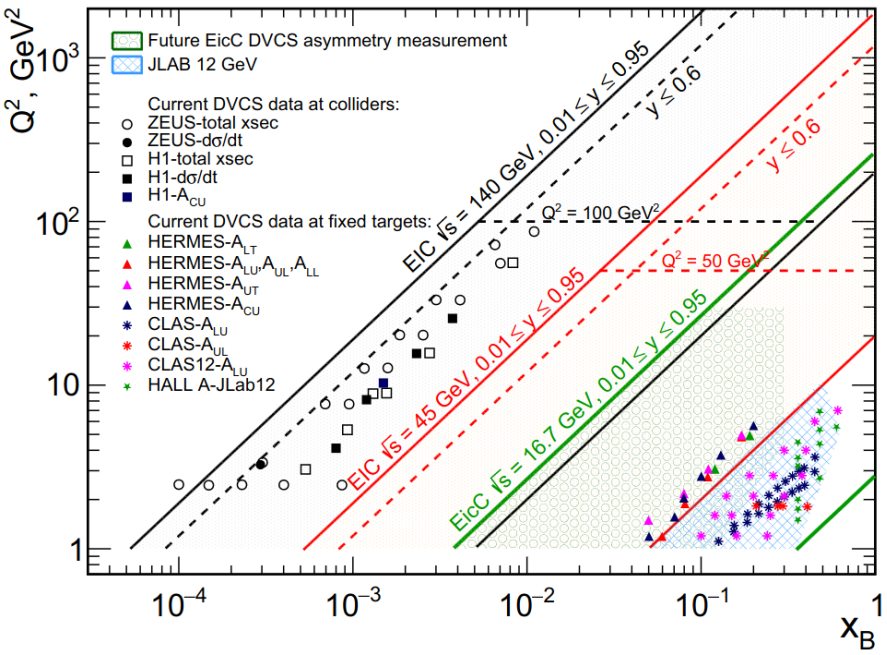

Figure 3.5: Kinematic coverage of the available and future DVCS measurements. The points are the current DVCS world data at HERA (H1, ZEUS, HERMES) and JLab 6 GeV and 12 GeV (CLAS, CLAS12 (Hall-B) and Hall A). Figure taken from [152].

prehensive dataset of asymmetries for x_B values ranging from 0.04 to 0.1, with Q^2 extending up to approximately 7 GeV^2.

At JLab [34–40], the Hall-A and Hall-B collaborations also employed a fixed target setup, focusing on a higher range of x_B (around 0.1 to 0.6) and lower Q^2 values (up to about 8 GeV^2). There are new Hall-A data with the upgrade of JLab to 12 GeV already published which is also used in this analysis. As more data taken after the upgrade is available, an extended kinematic region with improved experimental precision is achievable.

CERN's COMPASS collaboration [41], using a fixed target, occupies an intermediate position in the x_B range, falling between HERMES and H1/ZEUS data. Notably, COMPASS has the capacity to employ both positively and negatively charged muons in their experiments. COMPASS has completed its last run and the next-generation successor of the COMPASS experiment, AMBER, will build on COMPASS's legacy and take it to the next level.

Presently, a significant portion of the data utilized for global fits of DVCS primarily covers low Q^2 values, with the majority of data points spanning from 1.5 to 4 GeV^2. It is widely recognized that obtaining data across a broader range of

Q^2 values is of paramount importance. Additionally, new proposals are in preparation to utilize a future positron beam at JLab. Future electron-ion colliders like EIC[45, 46], EicC [47], and LHeC [48], are at the center of a lot of attention thanks to their promise of a high luminosity coverage over an extended region at relatively small x_B and large Q^2 that will probe the gluon rich environment.

3.5 | DVCS experiments at Jefferson Lab

Following the initial publication by CLAS (CEBAF Large Acceptance Spectrometer) in 2001, a sequence of high-statistics experiments dedicated to Deeply Virtual Compton Scattering (DVCS) ensued at Jefferson Lab. These experiments were conducted at moderate values of the momentum transfer, Q^2 (ranging from 1 to 3 GeV^2), and centered around x_B, approximately equal to 0.3, which corresponds to the valence-quark region. The polarized and unpolarized cross sections measured at Jefferson Lab in Hall A, through a Q^2-scaling test, have indicated the validity of factorization and the leading-twist dominance hypothesis, even at relatively low Q^2 (around 1-2 GeV^2). In Hall-B, CLAS conducted experiments with high statistics, and finely binned fourfold beam-spin asymmetries, providing significant constraints for the study of the GPD H across a wide kinematic range.

These initial datasets are now being expanded and complemented by results from more recent JLab experiments and analyses focused on DVCS with proton targets. These experiments aim to measure fully differential beam-polarized cross-section differences, unpolarized cross-sections, longitudinally polarized target-spin asymmetries, along with double polarization observables. The CEBAF accelerator at JLab underwent an energy upgrade to 12 GeV in 2014, and the detector capabilities in Halls A, B, and C have been enhanced to accommodate the new experimental program. This program places a particular emphasis on the study of GPDs. With coverage in x_B ranging from 0.1 to 0.7 and Q^2 from 1 to 10 GeV^2, the upgraded JLab is well-suited for investigating GPDs in the valence regime.

The first experiment of the 12 GeV era has already been published in Hall A and concentrates on proton DVCS [39]. We will give further details on this experiment in the following section as it was part of the data used to extract and study the kinematic behavior of the CFFs in this analysis. The experimental program for the initial five years of operation of CLAS12 (the new Hall-B detector) is already undergoing. It will primarily focus on GPD measurements in exclusive processes. This includes measurements of beam-spin asymmetries, unpolarized and polarized

proton-DVCS cross sections, as well as target-spin asymmetries and double-spin asymmetries on both longitudinally and transversely polarized targets. In Hall-B, the first measurement of the DVCS beam spin asymmetry using the CLAS12 spectrometer with a 10.2 and 10.6 GeV electron beam scattering from unpolarized protons has also been reported [44]. The results greatly extend the Q^2 and x_B phase space beyond the existing data in the valence region and provide 1600 new data points measured with unprecedented statistical uncertainty.

A similar experimental program is in development for DVCS studies on the neutron. Hall-A has also used liquid deuterium targets, providing the first experimental data to study DVCS on the neutron [153]. Neutrons are sensitive to E, the least known GPD, which is required to access quark orbital angular momentum through Ji's sum rule. Neutron data also allow quark-flavor separation, making neutron experiments invaluable. However, limited statistical precision was obtained because of the inherent difficulty of experiments on the neutron. Recently, Hall-B has also provided preliminary beam spin asymmetries for neutron DVCS extracted using the upgraded CEBAF 12 GeV polarized electron beam and the Hall-B CLAS12 detector [154].

We have also taken part in the eight months of operation time of data-taking of the Hall-B experiment E12-06-119(b) recently completed in the Spring of 2023. This experiment measures DVCS cross-sections and asymmetries on a longitudinally polarized proton target giving access to a larger number of observables.

In the following sections, we particularly focus on the DVCS experiments taken at Jefferson Lab that are used in the analysis performed in this thesis.

3.5.1 | Hall-A E00-110 experiment

The Jefferson Lab Hall A experiments are characterized by a small acceptance, but a very high luminosity for high precision results. In 2004, E00-110 was the very first experiment specifically dedicated to the measurement of DVCS cross sections. By sending a polarized electron beam on a liquid hydrogen target, the E00-110 experiment measured both unpolarized and beam helicity-dependent DVCS cross sections at $x_{Bj} = 0.36$ with Q^2 ranging from 1.5GeV^2 to 2.3GeV^2, in the valence quark region. The results published in 2006 have recently been re-analyzed and the new results now supersede the previous ones [37].

The exclusivity of the $ep\gamma$ final state was ensured by detecting the scattered electrons in the High-Resolution Spectrometer, the DVCS/BH photons in a custom-built PbF_2 electromagnetic calorimeter, and reconstructing the recoil protons via

Setting	k' (GeV/c)	θ_e ($^\circ$)	Q^2 (GeV^2)	x_B
Kin1	3.53	15.6	1.5	0.36
Kin2	2.94	19.3	1.9	0.36
Kin3	2.34	23.8	2.3	0.36
KinX2	2.94	20.1	2.06	0.39
KinX3	2.36	23.1	2.17	0.34

Table 3.1: Kinematic settings of the Hall-A E00-110 experiment.

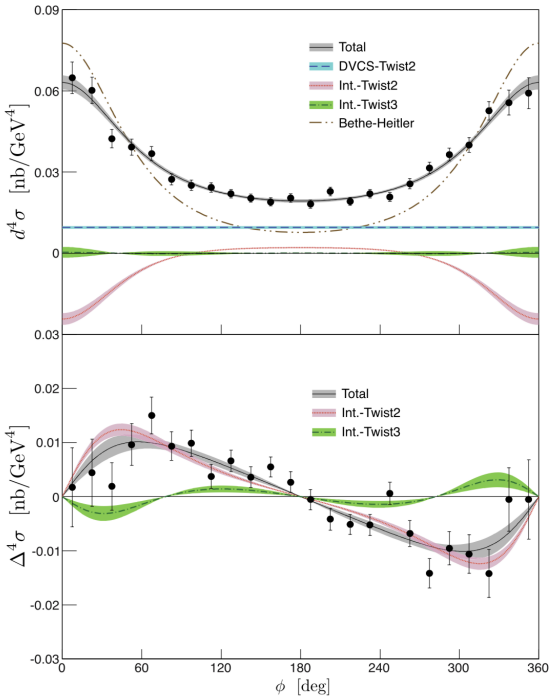

Figure 3.6: Hall-A results, for Kin3, t = -0.32 GeV^2 : unpolarized (top) and helicity-dependent (bottom) cross-section as a function of ϕ. The error bars on the data points are statistical only. The shaded areas represent the statistical uncertainty for each contribution. This figure is taken from [37].

the $ep \rightarrow e\gamma X$ missing mass. $ep\gamma$ events were collected for five different (Q^2, x_B) kinematics bins shown in Table 3.1. Each of these five (Q^2, x_B) kinematics was further differentiated in $5 - t$ bins and 24ϕ bins, and fourfold unpolarized and beam-polarized cross sections were extracted.

Figure 3.6 shows the obtained results for the $-t = 0.32\text{GeV}^2$ bin of Kin3. The unpolarized cross sections peak towards $\phi = 0^\circ$ due to the BH process (dot-dashed gray curves). The different contributions to the cross-section (DVCS, Bethe-Heitler, Interference), shown in color, were separated, up to twist three for the interference

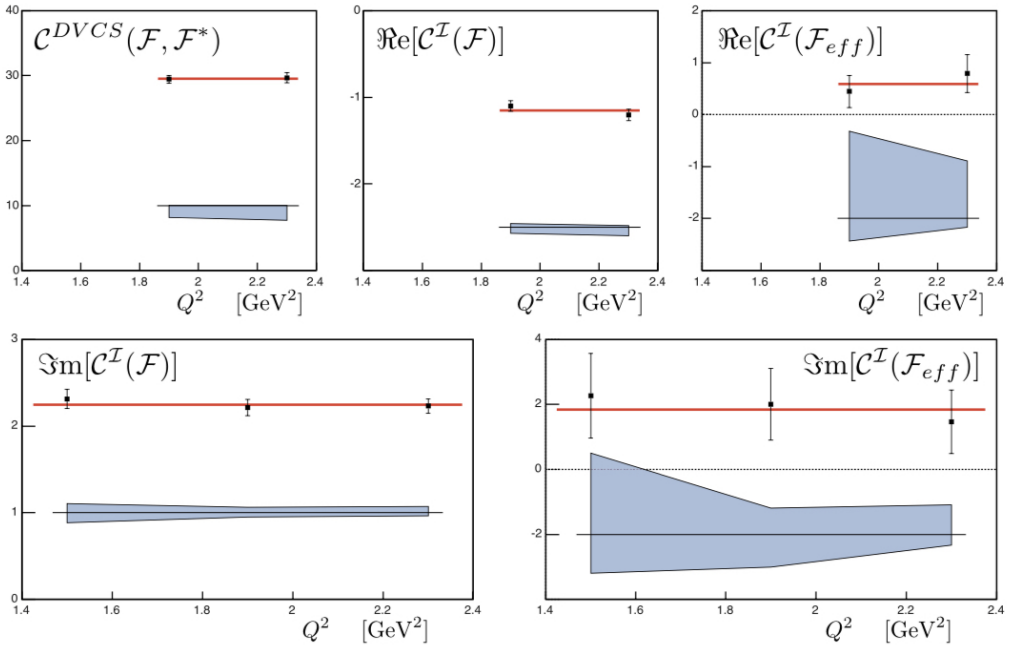

Figure 3.7: Combinations CFFs extracted from the Hall-A E00-110 data using the BKM10 formalism [61], integrated over t and plotted as a function of Q^2. The top three plots show the effective CFFs resulting from the unpolarized cross-section fit (Kin2 and Kin3), whereas the bottom plots show the effective CFFs resulting from the helicity-dependent cross-section fit (Kin1–3). The shaded areas represent systematic errors. This figure is taken from [37].

term, using the BMK formalism [61]. This method also allowed the extraction of five observables linked to combinations of real and imaginary parts of CFFs. The real combinations $C^{\mathrm{DVCS}}(\mathcal{F},\mathcal{F}^*)$ (bilinear in the CFFs, obtained from the $c^{\mathrm{DVCS}}_{0,\mathrm{unp}}$ harmonic), $\Re\mathrm{e}\left[C^{\mathrm{I}}(\mathcal{F})\right]$ (linear in the CFFs, obtained from $c^{\mathrm{I}}_{1,\mathrm{unp}}$), and $\Re\mathrm{e}\left[C^{\mathrm{I}}(\mathcal{F}_{\mathrm{eff}})\right]$ (twist-3 term) are extracted from the unpolarized cross section. These combinations are explicitly written in the Appendix A for the twist-2 CFFs. The helicity-dependent cross section is fitted using the $\Im\mathrm{m}\left[C^{\mathrm{I}}(\mathcal{F})\right]$ (linear in the CFFs) and $\Im\mathrm{m}\left[C^{\mathrm{I}}(\mathcal{F}_{\mathrm{eff}})\right]$ (twist-3 term, from $s^{\mathrm{I}}_{2,\mathrm{unp}}$ [61]). The constant Q^2-dependence of the five observables (Figure 3.7) confirms that the factorization and leading-twist approximations for DVCS are valid already at these relatively low Q^2 (~ 1–2 GeV^2). We will compare with these results in Section 5.5.4.

3.5.2 | Hall-A E07-007 experiment

In experiment E07-007 a unpolarized or longitudinally polarized electron beam impinged on a 15 – cm-long liquid H_2 target. Beam polarization was continuously

Q^2 (GeV^2)	x_B	E^{beam} (GeV)	$-t$ (GeV^2)
1.50	0.36	3.355 5.55	0.18, 0.24, 0.30
1.75	0.36	4.455 5.55	0.18, 0.24, 0.30, 0.36
2.00	0.36	4.455 5.55	0.18, 0.24, 0.30, 0.36

Table 3.2: Kinematic settings of the Hall-A E07-007 experiment.

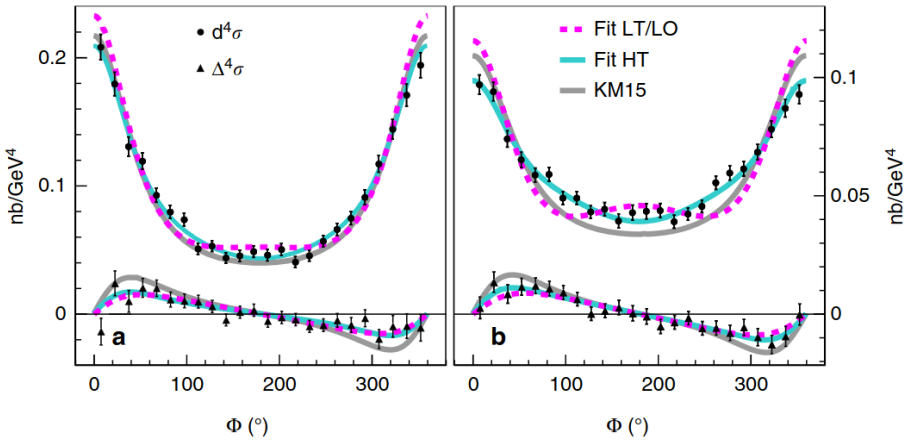

Figure 3.8: Beam helicity-dependent and helicity-independent cross sections. Unpolarized cross sections are represented with black circles and polarized cross sections with black triangles. The kinematic setting shown corresponds to Q^2 = 1.75 GeV^2, x_B = 0.36, and t = -0.30 GeV^2 . The beam energies are E^{beam} = 4.455 GeV (left) and Ebeam = 5.55 GeV (right). This figure is taken from [38].

measured by the Hall A Compton polarimeter and found to be 72 ± 2%$_{\text{sys}}$ on average. Scattered electrons were detected in the left high-resolution spectrometer (HRS) and the tracking efficiency was known to 0.5%. The final state photon was detected in an electromagnetic calorimeter consisting on an 16 × 13 array of PbF_2 crystals. Its energy resolution was measured to be 2.4% at 4.2GeV, with ~ 3 mm spatial resolution.

Results from the E07-007 experiment were available in 2017 [38]. This experiment performed measurements of helicity-dependent and helicity-independent photon electroproduction cross-sections with high statistical accuracy in Hall A of Jefferson Lab, as shown in Figure 3.8 for two different kinematic bins. The H $(\vec{e}, e'\gamma)\, p$ cross section was measured at x_B = 0.36 for three Q^2-settings. Data for each Q^2-value were taken with two incident beam energies and binned in $-t$. The kinematics setting is summarized in Table 3.3. The aim of this experiment was

Setting	Kin-36-1	Kin-36-2	Kin-36-3	Kin-48-1	Kin-48-2	Kin-48-3	Kin-48-4	Kin-60-1	Kin-60-3
x_B		0.36			0.48			0.60	
E_b (GeV)	7.38	8.52	10.59	4.49	8.85	8.85	10.99	8.52	10.59
Q^2 (GeV^2)	3.20	3.60	4.47	2.70	4.37	5.33	6.90	5.54	8.40
E_γ (GeV)	4.7	5.2	6.5	2.8	4.7	5.7	7.5	4.6	7.1
$-t_{\min}$ (GeV^2)	0.16	0.17	0.17	0.32	0.34	0.35	0.36	0.66	0.70

Table 3.3: Kinematic settings of the Hall-A E12-06-114 experiment. E_b is the incident electron energy. Table taken from [39].

to separate the DVCS-BH interference and DVCS contributions to the $ep \to ep\gamma$ cross-section, by exploiting the different energy dependences of the BH and DVCS amplitudes. Their results indicated a sensitivity of high-precision DVCS data to twist-3 (HT) and/or higher-order (NLO) contributions through a phenomenological study including kinematical power corrections. Within either a pure HT or a pure NLO scenario, at moderate values of Q^2, a statistically significant experimental separation of the pure DVCS and DVCS-BH interference terms are achieved.

3.5.3 | Hall-A E12-06-114 experiment

E12-06-114 is the 3rd generation dedicated DVCS experiment at Hall-A of Jefferson Lab. The experiment ran in 2014 and 2016 as a high-energy extension of the previous Hall A experiments. Similarly, a polarized electron beam and unpolarized LH2 target were used to extract absolute polarized and unpolarized DVCS cross-sections in a range of (x_B, Q^2, t). It is the first experiment run after the 12GeV upgrade of Hall-A using an electron beam of 7 -11 GeV/c and accumulated data in 9 of the originally planned 11 different kinematic settings which are listed in Table.

This experiment expands the kinematic coverage of previous measurements and extracts the squared-DVCS and interference terms of the cross-section which were fitted simultaneously using the BMMP formalism [155]. They present the first complete extraction of all four helicity-conserving CFFs as a function of x_B averaged over t appearing in the DVCS cross-section, Figure. We compare with their CFFs results in Section 5.5.3 and perform a scaling test, now at larger Q^2, and investigate leading twist dominance, see Section 5.5.4.

3.5.4 | Hall-B e1-DVCS1 experiment

The Hall-B e1-dvcs1 experiment [36] measured unpolarized and beam-polarized cross sections over a wide phase space in the valence-quark region, with 110 (Q^2, x_B, t) bins covering: $1.0 < Q^2 < 4.6\text{GeV}^2, 0.10 < x_B < 0.58$, and $0.09 <$

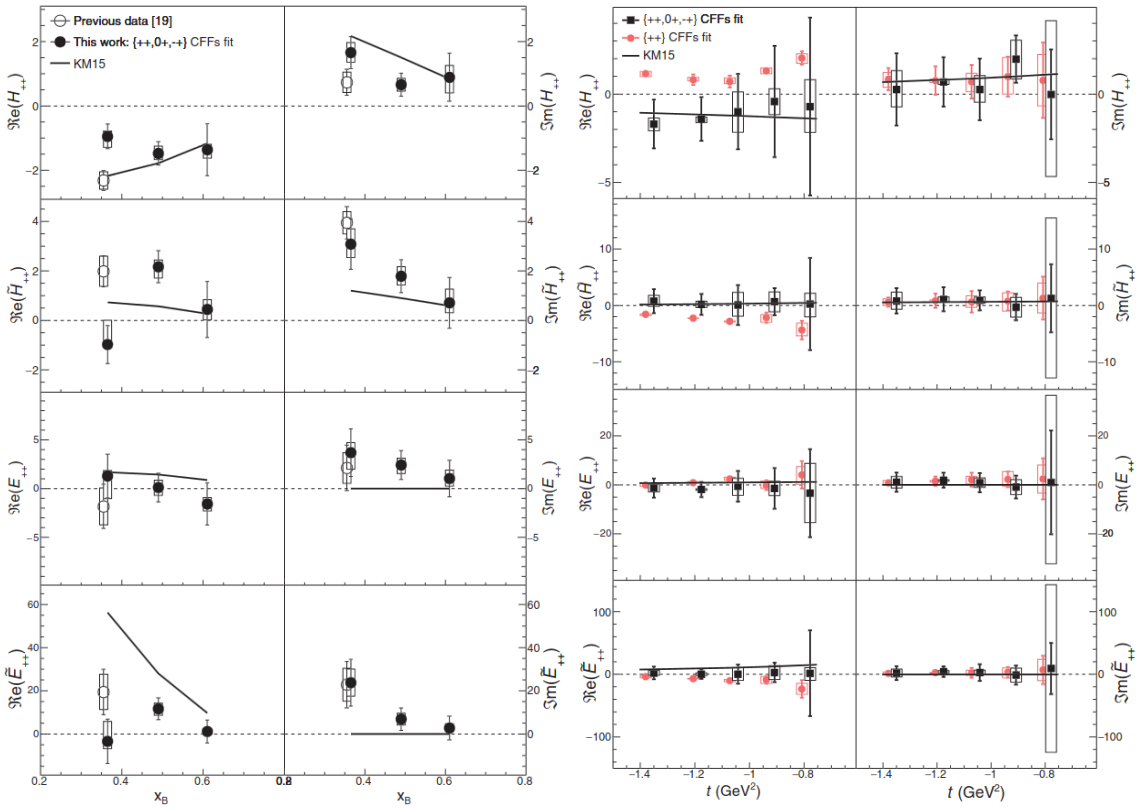

Figure 3.9: Values of the helicity-conserving CFFs, averaged over t, as a function of x_B (left) and as a function of t at $x_B = 0.60$ (right) obtained from a fit including only the helicity-conserving CFFs (red) and a fit including both helicity-conserving and helicity-flip CFFs (black). This figure is taken from [39].

$-t < 0.52\text{GeV}^2$. The experiment took place at JLab for three months in 2005, using the 5.75 GeV polarized electron beam (79.4% polarization), a 2.5 -cm-long liquid-hydrogen target, and the Hall-B large-acceptance CLAS spectrometer, operating at a luminosity of 2×10^{34} cm^{-2} s^{-1}. A specially designed electromagnetic calorimeter was added to the CLAS detector and allowed the detection of photons for polar angles from about 5° to 16°, with full azimuthal coverage. Figure 3.10 shows the resulting (Q^2, x_B) and ($-t, x_B$) kinematic coverages of the data and the adopted binning i.e., 21 (Q^2, x_B) bins and 6 t bins. Note that the bins and results are limited to the $|t|$ region below 0.52GeV^2 while the actual coverage of the data goes beyond 1GeV^2.

The measured cross-sections showed that three well-known GPD models, VGG, KMS, and the KM10a version of the KM model, describe the data well without additional inputs which reinforces the expectation of the H-dominance in the unpolarized cross-section. Two of the CFFs, $\Re e\mathcal{H}$ and $\Im m\mathcal{H}$ were able to be extracted from this data by fitting simultaneously both cross-section observables,

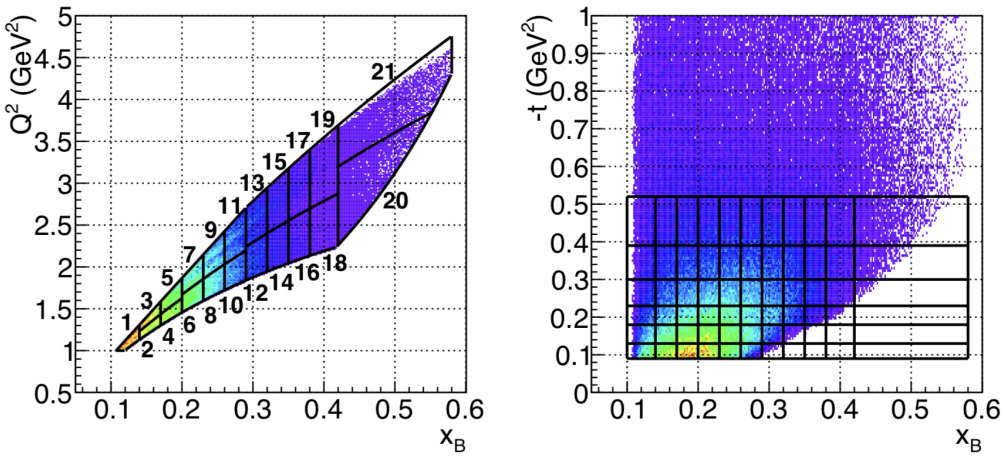

Figure 3.10: Kinematic coverage of the Hall-B e1-DVCS1 experiment with the corresponding binning. This figure is taken from [36].

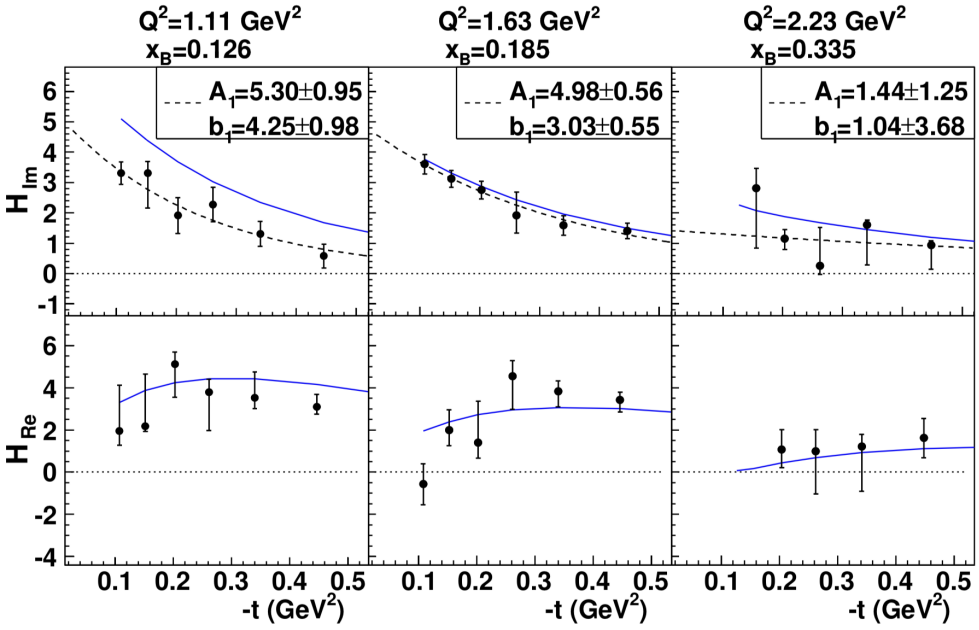

Figure 3.11: Results of the CFF fits of the e1-DVCS1 experiment for $H_{Im} = -\Im\mathfrak{m}\mathcal{H}$ (upper panel) and $H_{Re} = -\Re\mathfrak{e}\mathcal{H}$ (lower panel), for three (Q^2, x_B) bins, as a function of t. The blue solid curves are the predictions of the VGG model. The black dashed curves show the fit of the results by the function Ae^{bt}. This figure is taken from [36].

see Figure 3.11. The t-dependence of $\Im\mathfrak{m}\mathcal{H}$ was fitted by the function Ae^{bt} with the normalization A and the slope b as free parameters. Under the hypothesis of neglecting Q^2 higher-twist and evolution effects as well as deskewing effects, these behaviors reveal the transverse size of the nucleon. The data suggest, over the x_B range explored in this experiment, that the size of the nucleon increases as lower

momentum fractions (proportional to x_B) are probed.

Generation of pseudodata 4

This chapter presents the details of the simulated data, often referred to as pseudodata, that have been generated for the purpose of testing and demonstrating the reliability and robustness of the extraction methods. The generated pseudodata is also used for the evaluation of systematic errors and uncertainties in the analysis pipeline.

The simulation of the total leptoproduction cross-section includes contributions from both DVCS and the competing BH processes that can not be disentangled experimentally in the kinematic range of the data studied. These two processes and their interference are generated for the least constrained and most challenging observable case, lying in the presence of 8 CFFs, when there is no polarization of the initial or final-state particles involved in the scattering process: the unpolarized cross section σ_{UU}.

4.1 | Theoretical GPD model

For a given kinematic set (k, Q^2, x_B, t), the only inputs needed to generate the cross sections as a function of the azimuthal angle ϕ, are the 8 CFFs entering the DVCS amplitude, see Appendix A.2, where the CFFs $\mathfrak{Re}\mathcal{H}$, $\mathfrak{Re}\mathcal{E}$, and $\mathfrak{Re}\widetilde{\mathcal{H}}$ also appear in the interference term for the unpolarized beam and target configuration (5.7). To keep the problem realistic, given that GPDs have to fulfill a certain number of normalization constraints, see Section 2.3, the CFFs are generated by using a version of the KM model [52] originally developed by K. Kumericki and D. Mueller. In this version, the valence and sea components are described by the simpler modeling of just the GPD on the crossover line $x = \xi$, discussed in Section 4.1.2 , and the dispersion relation technique, shown in Section 4.1.1, is used to recover the remaining needed part. A similar modeling was used in the reference [156] model dependent least-squares fit to the data.

Overall, this approach allows to generate pseudodata that closely resemble the complexities and challenges of experimental data, where DVCS and BH processes

are entangled, and GPDs must adhere to certain constraints. This synthetic data is then used for testing and validating our analysis techniques, as well as for systematic studies.

The details of obtaining the 8 CFFs starting from the employed GPD model are shown in the following sections.

4.1.1 | Dispersion relation technique

As has been discussed in Section 3.1, the observables entering DVCS are the CFFs, which depend on the GPDs. The CFFs are in general complex valued with the real and imaginary parts given by (3.6) and (3.5). The dispersion relation (DR) [157–160] is a remarkable description of CFFs inherited from the study of their general analytical properties of scattering amplitudes, notably causality, and unitarity. The dispersion relation in equation (4.1) allows us to relate the ξ dependences of the real and imaginary parts of CFFs, containing the same information up to a subtraction constant $C_{\mathcal{F}}(t)$ independent of ξ. In particular, it does not depend on the formalism of perturbative QCD and the development of dispersion relations applied to hadron scattering dating back to the 1950 s.

$$\Re e\mathcal{F}(\xi,t) = \frac{1}{\pi}\mathcal{P}\int_0^1 \mathrm{d}x \left(\frac{1}{\xi - x} \mp \frac{1}{\xi + x}\right) \Im m\mathcal{F}(x,t) + C_{\mathcal{F}}(t)\,. \tag{4.1}$$

The top (bottom) sign of the r.h.s of equation (4.1) refers to the CFFs $\mathcal{F} = \{\mathcal{H}, \mathcal{E}\}$ ($\mathcal{F} = \{\widetilde{\mathcal{H}}, \widetilde{\mathcal{E}}\}$). The subtraction constant $C_{\mathcal{F}}(t)$ is up to an opposite sign the same for $\mathcal{H}$ and $\mathcal{E}$, while it vanishes for the CFFs $\widetilde{\mathcal{H}}$ and $\widetilde{\mathcal{E}}$, and is perturbatively predicted to be zero for the combination $\mathcal{H} + \mathcal{E}$, see Ref. [159]:

$$C_{\mathcal{H}} = -C_{\mathcal{E}}; \quad C_{\tilde{\mathcal{H}}} = C_{\tilde{\mathcal{E}}} = 0. \tag{4.2}$$

The imaginary part of the CFF, e.g., for H is,

$$\Im m\mathcal{H}(\xi,t) \overset{\text{LO}}{=} \pi \sum_q e_q^2 \left[H_q(\xi,\xi,t) - H_q(-\xi,\xi,t)\right]. \tag{4.3}$$

Note that in contrast to the convolution integral in (1), where the GPD enters for unequal values of its first and second argument, the integrand in the DR (spectral function) corresponds to the GPD where its first and second arguments are equal (cross-over line $x = \xi$). Therefore, for example, instead of $H(x,\xi,t)$ one can model the simpler functions $H(x,x,t)$ and $C_{\mathcal{H}}(t)$, in a LO and leading-twist approximation, ignoring the effects of GPD evolution, which are all acceptable approximations when trying to describe presently available data in fixed-target kinematics.

It is worth mentioning that the real part of the CFF contains information on the imaginary part integrated from $x = 0$ to the upper kinematic bound, which represents an opportunity to constrain the imaginary part at small values of ξ which are difficult to reach in experiments.

4.1.2 | GPDs parametrization

A version of the KM model [52] was adopted for which the partonic decomposition of $\Im\mathrm{m}\mathcal{H}$ is:

$$\Im m\mathcal{H}(\xi,t) = \pi\left[\left(2\frac{4}{9}+\frac{1}{9}\right)H^{\mathrm{val}}(\xi,\xi,t)+\frac{2}{9}H^{\mathrm{sea}}(\xi,\xi,t)\right]. \tag{4.4}$$

In the fixed target kinematics region and to LO accuracy, where the Q^2 virtuality is rather limited, the so-called scaling hypothesis is assumed i.e., on the assumption that the GPD does not evolve under the change of the photon virtuality. The functional form of the GPD H for both, the sea and the valence contributions at the cross-over line, is motivated by a generic ansatz based on the double distribution (DD) [1, 131, 132] representation and a t-dependence inspired by a quark spectator model [161]:

$$H(\xi,\xi,t) = \frac{nr}{1+\xi}\left(\frac{2\xi}{1+\xi}\right)^{-\alpha(t)}\left(\frac{1-\xi}{1+\xi}\right)^{b}\frac{1}{\left(1-\frac{1-\xi}{1+\xi}\frac{t}{M^2}\right)^{p}} \tag{4.5}$$

Here n is the residual normalization of PDF $q(x) = H(x,0,0)$ taken from PDF fits, r is the skewness ratio at small x, i.e. the ratio of a GPD at some point on the cross-over trajectory and the corresponding PDF, $\alpha(t)$ is the "Regge trajectory" borrowed from Regge phenomenology [136], b controls the large-x behavior, and M and p control the t-dependence.

A similar ansatz to equation (4.5) is used for $\widetilde{H}$ which introduces three additional parameters $\widetilde{M}$, $\widetilde{b}$ and $\widetilde{r}$:

$$\Im\mathrm{m}\widetilde{\mathcal{H}}(\xi,t) = \pi\left(2\frac{4}{9}+\frac{1}{9}\right)\frac{\widetilde{n}^{\mathrm{val}}\,\widetilde{r}^{\mathrm{val}}}{1+\xi}\left(\frac{2\xi}{1+\xi}\right)^{-\alpha^{\mathrm{val}}(t)}\frac{1}{\left(1-\frac{1-\xi}{1+\xi}\frac{t}{\left(\widetilde{M}^{\mathrm{val}}\right)^2}\right)^{\widetilde{p}^{\mathrm{val}}}}\left(\frac{1-\xi}{1+\xi}\right)^{\widetilde{b}^{\mathrm{val}}} \tag{4.6}$$

The valence quark parameters $n^{\mathrm{val}} = 1.35$, $\widetilde{n}^{\mathrm{val}} = 0.6$ and $p^{\mathrm{val}} = \widetilde{p}^{\mathrm{val}} = 1$ are deduced from standard PDF parameterizations. For $\alpha^{val}(t)$ in the valence case,

$\rho - \omega$ Regge trajectory is used,

$$\alpha^{val}(t) = 0.43 + 0.85t/\text{GeV}^2. \tag{4.7}$$

The remaining valence quark free parameters are taken from the state-of-the-art KM15 [53] GPD parametrization version of the KM model that reproduces worldwide DVCS data.

The parameters of the sea-quark GPD H^{sea} were taken to be as in [52] where the parameterization (4.5) is requested to reproduce their small x_B fits from H1/ZEUS data in the Mellin-Barnes representation [52, 162] described within the parameters:

$$\begin{gathered}\alpha^{\text{sea}}(t) = 1.13 + 0.15t/\text{GeV}^2, n^{\text{sea}} = 1.5, r^{\text{sea}} = 1, b^{\text{sea}} = 4.6, \\ (M^{\text{sea}})^2 = 0.5\text{GeV}^2, p^{\text{sea}} = 2.\end{gathered} \tag{4.8}$$

These GPDs give the imaginary part of the CFFs $\Im\mathrm{m}\mathcal{H}$ and $\Im m\widetilde{\mathcal{H}}$ which allows us to obtain $\Re e\mathcal{H}$ and $\Re e\widetilde{\mathcal{H}}$ from the dispersion relation (4.1) that correlates them. The non-vanishing subtraction constant of the DR is normalized by C and M_C controls the t-dependence:

$$C_{\mathcal{E}}(t) = -C_{\mathcal{H}}(t) = \frac{C}{\left(1 - \frac{t}{M_C^2}\right)^2}, \tag{4.9}$$

giving two additional free parameters. In [52] GPD E is modeled solely in terms of this subtraction constant, $\mathcal{E} = C_{\mathcal{E}}$, i.e., the E contribution is only through the D-term [133] and therefore vanishes at $x = \xi$, resulting in $\Im\mathrm{m}\mathcal{E} = 0$. The contribution of GPD $\tilde{E}$ is described using pion-pole [163] inspired effective ansatz and thus the amplitude in this channel is also purely real.

$$\begin{aligned}\Re\mathrm{e}\widetilde{\mathcal{E}}(\xi, t) &= \frac{r_\pi}{\xi} \frac{2.164}{\left(0.0196 - \frac{t}{\text{GeV}^2}\right)\left(1 - \frac{t}{M_\pi^2}\right)^2}, \\ \Im\mathrm{m}\widetilde{\mathcal{E}}(\xi, t) &= 0,\end{aligned} \tag{4.10}$$

where $m_\pi^2 = 0.0196\text{GeV}^2$, while M_π and r_π are free parameters.

A summary of the GPD model free parameters taken from the global DVCS fit KM15 is shown in Table 4.1. For the rest of this work, we will refer to the described GPD parametrization in this section as KM15* model unless otherwise specified.

The resulting model parametrization of the GPDs, achieves a relatively good description of all helicity-independent JLab DVCS available data (Table 4.2) with an overall normalized χ^2 of ≈ 1.43 for 195 data points. This is illustrated in Figure 4.1

M^{val}	r^{val}	b^{val}	C	M_C	$\tilde{M}^{\text{val}}$	$\tilde{r}^{\text{val}}$	$\tilde{b}^{\text{val}}$	r_π	M_π
0.789	0.918	0.4	2.768	1.204	3.993	0.881	0.4	2.646	4.

Table 4.1: Model parameters obtained by the global DVCS fit KM15 [53].

for two different kinematic sets, where the total cross-section obtained with the BKM10 cross-section formulation evaluating the CFFs using this model is shown to represent the experimental unpolarized cross-section data.

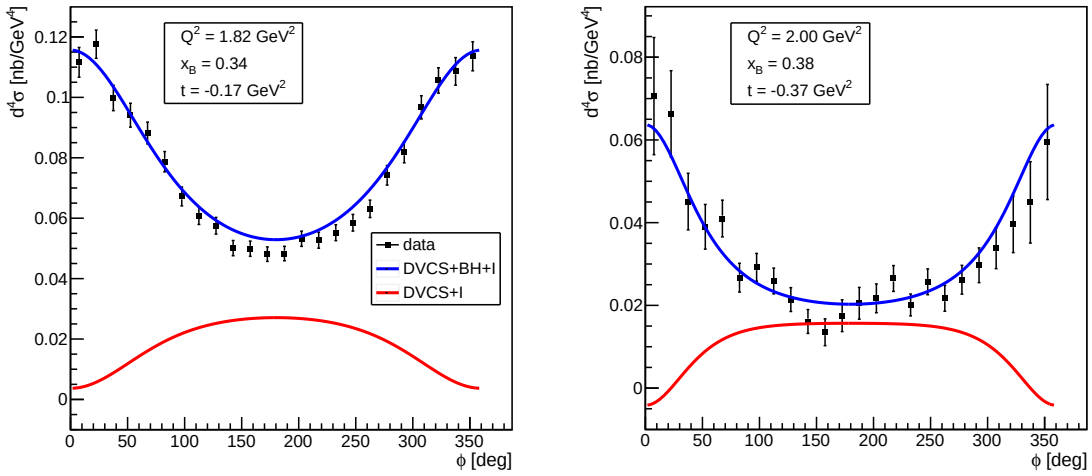

Figure 4.1: Helicity-independent cross-section at $k = 5.75$ GeV in two different kinematic sets (left and right) from the HallA $E00-110$ experiment (black squares). There are also shown the total cross-section (blue) and the DVCS cross-section including the BH-DVCS interference (red) obtained with the BKM10 cross-section formulation evaluating the CFFs from the KM model GPDs parametrization.

In Figure 4.2, the obtained CFFs with the described KM15* model are shown as a function of x_B and t in the kinematic range of the HallA experiment.

4.2 | Pseudodata production

In this section, some examples and specific information about the simulated data are provided. The BH and the DVCS cross-section as well as the interference between these two processes are computed using the BKM10 DVCS formulation at twist-2 for fixed values of k, Q^2, x_B and t (kinematic set). In this approximation, the DVCS observables receive contributions from 8 CFFs which are strongly correlated. For each kinematic set, the CFFs required to calculate the cross-section

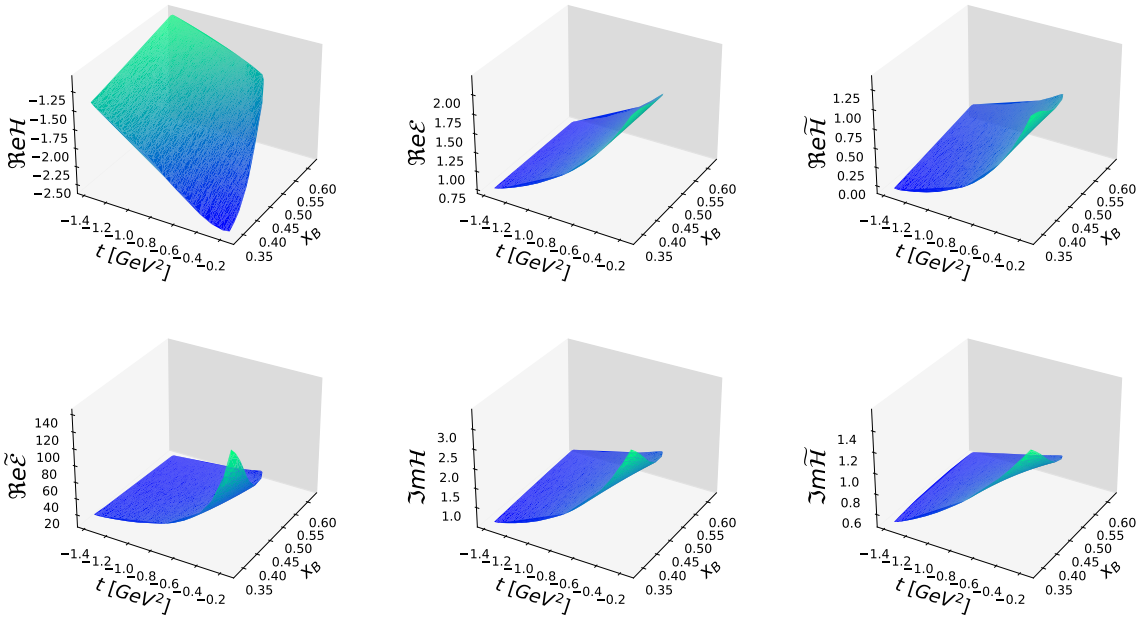

Figure 4.2: CFFs obtained from KM model parametrizations in Hall-A kinematics range.

are obtained from the KM15* model (Section 4.1.2). The total cross-section of the lepto-production process is then modeled as a function of the azimuthal angle ϕ in every set of kinematics.

4.2.1 | Kinematic coverage

The pseudodata produced mimics the kinematics of the experimental data used in this analysis. The total helicity-independent cross-section as a function of the azimuthal angle is simulated at every 195 kinematic sets of the Jefferson Lab (JLab) DVCS data.

This analysis is based on the fixed target experimental DVCS data collected from Hall A [37–39] and Hall B [36] at JLab, summarized in Table 4.2. The dataset comprises both helicity-independent and helicity-dependent cross-section measurements. However, for this specific analysis, the focus is solely on the least constrained helicity-independent or unpolarized cross-sections.

The data is finely binned into a fourfold differential cross-section format, characterized by the variables Q^2, x_B, t, and ϕ. There is a total of 195 distinct kinematic

Hall A Collaboration				
Experiment	E_{beam} (GeV)	Q^2 (GeV^2)	x_B	$-t$ (GeV^2)
E00-110 (2015) [37]	5.75	1.82 - 2.37	0.336 - 0.401	0.171 - 0.372
E07-007 (2017) [38]	3.355 - 5.55	1.49 - 2.00	0.356 - 0.361	0.177 - 0.363
E12-06-114 (2022) [39]	4.487 - 10.992	2.71 - 8.51	0.363 - 0.617	0.204 - 1.373
Hall B Collaboration				
Experiment	E_{beam} (GeV)	Q^2 (GeV^2)	x_B	$-t$ (GeV^2)
e1-DVCS1 (2015) [36]	5.75	1.11 - 3.77	0.126 - 0.475	0.11 - 0.45

Table 4.2: Summary of the DVCS data from JLAB used in this analysis. The table includes information on the data source and the kinematic range covered by the data.

conditions available for use in this analysis defined by Q^2, x_B and t. It's worth noting that the measurements cover the moderate to high x_B range which primarily pertains to the valence-quark region. Within this specific fixed-target kinematics range, and considering only LO accuracy, the virtuality Q^2 is relatively limited. Consequently, in this analysis, it is assumed that the GPDs do not evolve when the photon virtuality changes. However, this assumption will be further scrutinized in Section 5.5.4.

Figure 4.3 provides a visualization of the kinematic region covered by the utilized data. This data is a combination of results obtained from Jefferson Lab's 6GeV and 12GeV eras. Notably, the 12GeV JLab data extends to higher values of Q^2, reaching up to 8.5 GeV^2.

4.2.2 | DVCS cross-section pseudodata

The unpolarized cross-section of the $ep \to ep\gamma$ process is generated as a function of ϕ for a given (x_B, Q^2, t) kinematic bin and a given beam energy of the experimental data (see Section 4.2.1). The calculation of the DVCS+BH amplitudes is based on the BKM10 formulation [61] at leading-twist i.e, the dominant contribution in terms of the twist expansion in QCD, and leading-order approximation i.e. the dominant contribution in terms of the perturbative expansion in QCD. Then, the only inputs needed to generate the cross sections are the 8 CFFs entering the DVCS amplitude. The CFFs are computed at each x_B and t values from the GPD model parametrization described in Section 4.1.2, based on the well-known and widely used KM models which obey most of the model-independent GPD normalization constraints and reproduces the general trends of the experimental DVCS data used

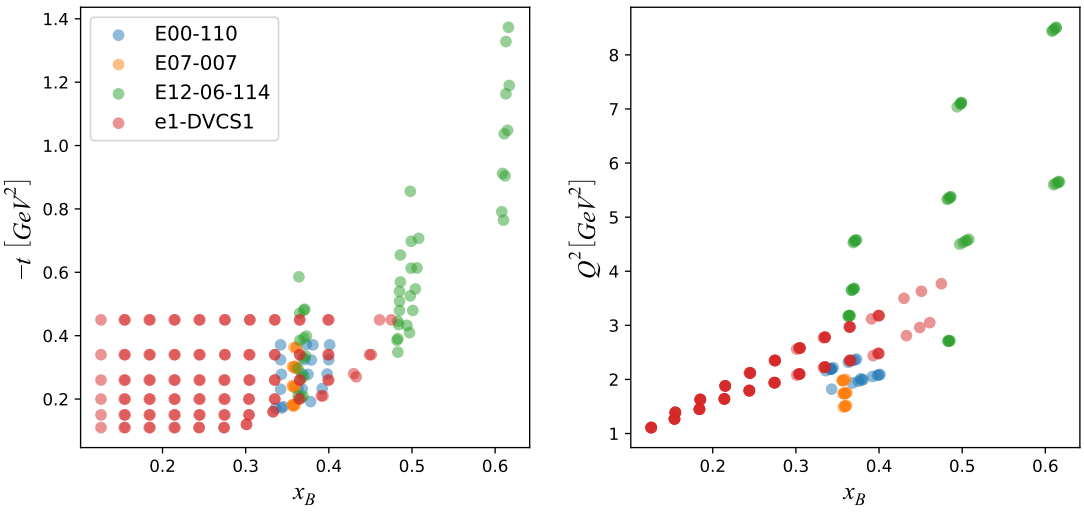

Figure 4.3: Kinematical coverage of the experimental data listed in Table 4.2 in t vs x_B (left) and Q^2 vs x_B (right) space.

in this analysis.

For each particular kinematic bin, the number of generated ϕ points is the same as in the corresponding experimental data in order to account for the available data statistics effects. Figure 4.4 shows the number of ϕ points on each kinematic set of the experimental data used that were replicated. The majority of Hall-A experiments have 24 ϕ points per set, while the number of points in the Hall-B experiment is more variable and the two sets with 2 and 4 points will not be considered to construct the global CFFs model in Section 6.3.

In the first example (Figure 4.5), the pseudodata for the particular kinematics $(x_B, Q^2, t) = (0.34, 1.82GeV^2, -0.17GeV^2)$ is taken with a 5.75 GeV beam energy. This corresponds to a kinematic bin measured by the Hall-A E00-110 experiment. The 24 generated points, corresponding to the ϕ binning of the experimental data, are superimposed on the theoretical curves. On the left panel of Figure 4.5, the unpolarized cross-section pseudodata is shown unsmeared while the right panel makes use of smearing which is meant to mimic real data.

The uncertainties and the accessible ϕ regions vary for each (x_B, Q^2, t) bin, and differ for the Hall-A and Hall-B experiments. The error bars added on the pseudodata correspond to the published experimental uncertainties of the JLab data and they average to about 5 % for the unpolarized DVCS cross-section.

The smearing of the pseudodata has been done via a Gaussian distribution, centered at the theoretically computed value, with a standard deviation corresponding

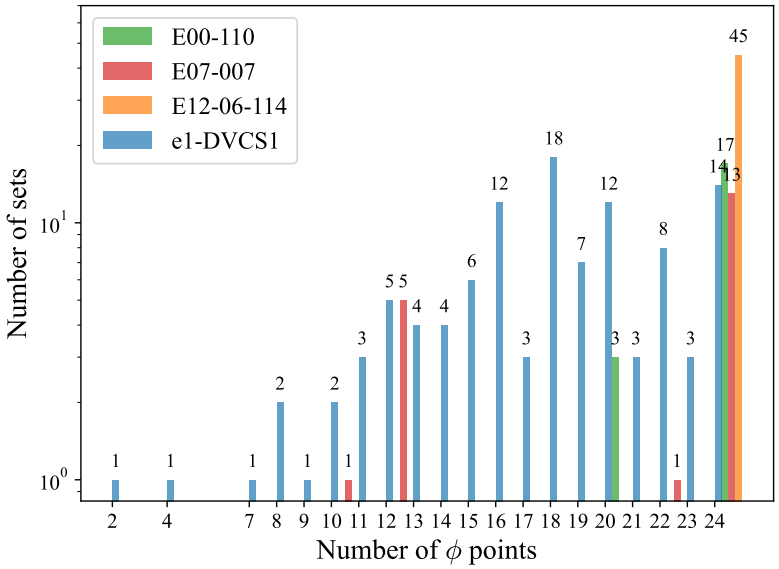

Figure 4.4: Frequency of the ϕ points on the 195 experimental kinematics sets from the DVCS data.

to the experimental uncertainties. Each ϕ point was smeared independently of the other ϕ points. The smeared pseudodata replicate the real-world experimental conditions that could influence the measured quantities. Through a comparative analysis of results derived from smeared and non-smeared pseudodata, one can shed light on potential biases arising from the experimental setup. Comprehending how these uncertainties affect the deduced CFFs is essential for accurately interpreting experimental outcomes. The use of smeared pseudodata facilitates the assessment of how sensitive extraction algorithms are to these experimental conditions, offering valuable insights into optimizing the experiment for maximal CFF sensitivity.

Under these conditions, we deem that in the following we will perform the CFFs extraction in rather realistic conditions, taking into account the ϕ-coverage of the data, their dispersion, and their uncertainties. By comparing the results from the pseudodata to the known input (theoretical predictions or actual CFFs), the accuracy and reliability of the analysis procedures can be accessed. This is essential for ensuring the robustness of the extraction process and enhancing the depth of understanding regarding systematic errors inherent in both the experimental procedures and analysis methodologies.

In summary, the generated pseudodata is crucial for validating the analysis process, assessing systematic errors, optimizing experimental designs, and improving theoretical models, ultimately enhancing the reliability and accuracy of

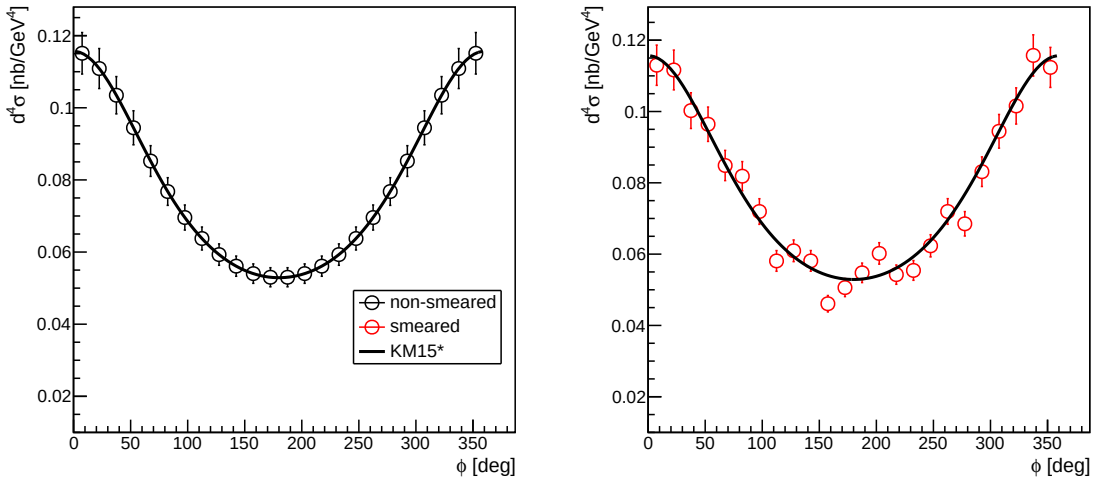

Figure 4.5: Generated pseudodata for the kinematics $(x_B, Q^2, t) = (0.34, 1.82GeV^2, -0.17GeV^2)$ corresponding to one set measured by the E00-100 HallA experiment. The unpolarized cross-sections are shown unsmeared (left) and smeared (right). The solid line corresponds to the generated distribution with the KM model CFFs parametrization.

the extracted CFFs.

Extraction of Compton Form Factors 5

Any attempt to extract GPDs from DVCS experimental data starts with the extraction of CFFs. The complete and precise extraction of CFFs has been one of the major activities in the study of GPD-related processes in the past decade, both on the theoretical and phenomenological side. One of the major challenges in extracting CFFs from exclusive measurements is the higher dimensionality of the problem, as discussed in the nice review [164], for example. Traditionally, the CFFs extraction technique falls into either a local fit (see Ref. [9, 39, 165–171]) or a global fit (see Ref. [52, 159]) strategy. The analytical fit function is defined by the helicity amplitudes so the results can be specific to a particular DVCS formalism.

Global fits assume a parametrized analytical shape of the CFFs and adjust it using experimental data on all available kinematics simultaneously. The model may be built at the level of the CFF, or directly at the level of the GPD using available phenomenological models, like GK [55], VGG [56] and KM [52–54, 156] . Such a model dependency suffers from initial biases built into the framework and its severity on e.g. the extraction of orbital angular momentum, has never been studied in a systematic way. The global fit method allows the prediction of measurements in unprobed kinematics at the cost of introducing some level of model dependence. Efforts to reduce this bias have been led, notably by introducing artificial neural network (ANN) techniques incorporating known properties of GPDs but without assuming any particular parameterized model [54, 156, 172, 173].

At present, the only known way to model-independently extract CFFs is locally in the kinematical points (x_B, t, Q) at which the CFFs are fitted as free parameters on the experimental data. Therefore, this method introduces no bias on the general form of the CFF apart from the chosen framework of general approximation, like twist truncation, neglection, and dominance of some CFFs,... Local fits have however no ability to predict the result of measurements in previously unexplored kinematics with the shortcoming that GPDs can not be fitted themselves. Nonetheless, we introduce in Chapter 6, a novel local multivariate fit (LMI) using a deep neural network (DNN) technique at many fixed kinematics across the independent

variable ϕ that results in a CFF model that can be interpolated and extrapolated to unavailable experimental kinematic regions similar to a global fit. This schema is still considered a local fit as it requires no additional information beyond what is used in a standard local fit.

We choose to adopt an approach by exploiting the χ^2 distribution of randomly generated CFFs. As a matter of priority, this study is confined to the goal of locally extracting twist-2 CFFs directly from the least constraining and most challenging DVCS unpolarized observable in a model-independent way. Additional observables can of course only improve the situation, and their inclusion is reserved for future study. The extraction of eight CFFs from only one observable, with finite experimental uncertainties, is an underconstrained problem. Without the necessary constraints using multiple observables in simultaneous fitting, there is a lack of uniqueness leading to large systematic errors in the extraction. However, we show in this analysis that the extraction of the CFFs $\mathfrak{Re}\mathcal{H}$, $\mathfrak{Re}\mathcal{E}$ and $\mathfrak{Re}\widetilde{\mathcal{H}}$ is achievable with reasonable accuracy and precision.

To progress in this underconstrained problem, LO and LT approximations were taken at the expense of higher accuracy reducing the fitting problem from eight to four parameters (Section 5.1). With this novel approach, we will show that the CFFs $\mathfrak{Re}\mathcal{H}$, $\mathfrak{Re}\mathcal{E}$, $\mathfrak{Re}\widetilde{\mathcal{H}}$, and the pure DVCS cross-section can, in fact, be constrained with a finite uncertainty with some insight into its t and x_B-dependence, at Hall-A kinematics and at Hall-B kinematics limited by the data smearing in the least constrained case observable and with minimum model dependence. Indeed, it is crucial to give both a best-fit value and an estimation of the uncertainty associated with the extraction.

Generically, no information can be reliably extracted from any CFFs unless several different observables measured at the same kinematics are studied simultaneously. Despite the limitations and approximation of this extraction method, having an extraction procedure capable of effectively constraining three of the CFFs out of one observable is a valuable contribution. In fact, it was observed in the pioneering local least squares minimization extraction [165] at LO and LT that fitted two observables, unpolarized and beam-polarized Hall-A cross sections, resulted in a convergence of the fits for $\mathfrak{Re}\mathcal{H}$ and $\mathfrak{Im}\mathcal{H}$ only while the other CFFs are left undetermined.

The available data from JLab used in this analysis, Table 4.2, is limited to the valence region. This gives much more constraint on the CFF $\mathcal{H}$ than the other CFFs, as recognized by GPD models [52, 55, 56]. While the CFF $\mathcal{E}$ suffers from scarcity and sizable statistical uncertainties. This is seen for example in Figure 5.1 obtained

from the generated pseudodata, where good least-squares fits of unpolarized cross sections with small normalized χ^2 values, less than 1.6, and represented in the figure by a red band, give a large range of values of the CFFs extracted which is larger for $\Re e\mathcal{E}$ and more constraining for $\Re e\mathcal{H}$ as seen on the right panel. The generating function of the pseudo-data cross-section (red line) is produced with the true values of the CFFs $\Re e\mathcal{H}$ (orange), $\Re e\mathcal{E}$ (red) and $\Re e\widetilde{\mathcal{H}}$ (green) shown on the right plot as solid lines. This will be further discussed in Section 5.2 where an optimized χ^2 fit will be used for comparison with the new extraction method (Section 5.3). The obtained local extraction results are then used to train a DNN and construct a CFFs global model for any kinematic region, see Section 6.3.

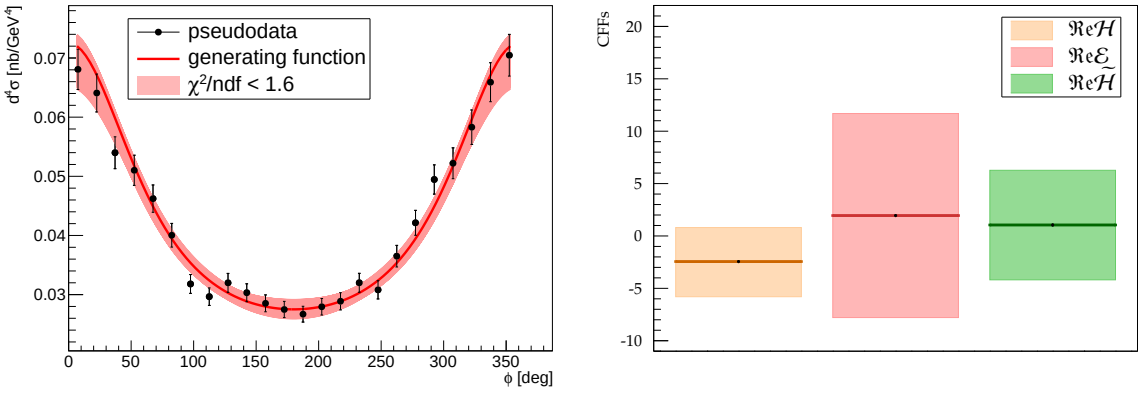

Figure 5.1: Fits of the pseudodata cross-section with χ^2/ndf values less than 1.6 (left) and the corresponding range of $\Re e\mathcal{H}$, $\Re e\mathcal{H}$ and $\Re e\widetilde{\mathcal{H}}$ that generated them (right) at the kinematic bin k = 5.75 GeV, $Q^2 = 1.96\ \text{GeV}^2$, $x_B = 0.37$, $t = -0.23\ \text{GeV}^2$. The true values generating the cross-section distribution are represented by solid lines.

Kinematical twist-4 and quantum loop corrections [23, 149] that are α_S suppressed, like the target mass and finite t corrections [155], are omitted. Those corrections are related to leading-twist GPDs but involve different perturbative coefficients [49] that get convoluted. Therefore, they lead to a different set of CFFs that can be considered independent of the twist-2 CFFs discussed here.

The generated pseudodata, Chapter 4, is used for optimizing and testing the goodness of the extraction, Section 5.4.1, as well as for the evaluation of systematic errors in Section 5.4.3.

5.1 | The fit function: $ep \to e'p'\gamma$ cross-section

The photon electroproduction cross-section has been discussed in detail in Chapter 3. Here we show the specifics of the unpolarized observable case in the BKM10 formulation at leading order in perturbative QCD and at leading twist approximations used to describe the (pseudo-) data. For this observable, a virtual photon scatters from an unpolarized electron beam of energy k off an unpolarized proton leading to the $ep \to e'p'\gamma$ 4-fold differential cross-section which constitutes the local fit function (5.1). The cross-section comprises not only the contributions of the DVCS amplitude $\mathcal{T}_{UU}^{DVCS}$ and the BH amplitude $\mathcal{T}_{UU}^{BH}$ that contain the same final state particles and cannot be distinguished experimentally but also that from their interference denoted by $\mathcal{I}_{UU}$.

$$\frac{d^4\sigma_{UU}}{dx_{Bj}dQ^2d|t|d\phi} = \frac{\alpha^3 x_B y^2}{8\pi Q^4\sqrt{1+\epsilon^2}}\frac{1}{e^6}\left(\left|\mathcal{T}_{UU}^{BH}\right|^2 + \left|\mathcal{T}_{UU}^{DVCS}\right|^2 + \mathcal{I}_{UU}\right) . \tag{5.1}$$

The phase space of this process is parameterized by the Bjorken variable, $x_B = \frac{Q^2}{2pq}$, in terms of the momentum $q = k - k'$ carried by the virtual photon of mass $Q^2 = -q^2 = -(k-k')^2$, the squared momentum transfer between the initial and final protons $t = \Delta^2$ with $\Delta = p' - p$ and the lepton energy loss $y = (p\cdot q)/(p\cdot k)$. The azimuthal angle ϕ between the leptonic and hadronic planes is defined in the Trento convention [142], $\alpha = e^2/(4\pi)$ is the fine structure constant, and $\epsilon = 2x_B M/Q^2$ where M is the proton mass.

The BH contribution is an undesirable contamination that is fully calculable in quantum electrodynamics with the nucleon form factors (FFs) within 1% uncertainty. The unpolarized BH amplitude is given by:

$$\left|\mathcal{T}_{UU}^{BH}\right|^2 = \frac{e^6}{x_B^2 y^2(1+\epsilon^2)^2 t\mathcal{P}_1(\phi)\mathcal{P}_2(\phi)}\sum_{n=0}^{2} c_{n,UU}^{BH}\cos(n\phi). \tag{5.2}$$

The harmonic terms $c_{n,UU}^{BH}$ of the BH amplitude squared are given in Appendix A.1 and they only depend upon bilinear combinations of the Dirac and Pauli FFs i.e., $F_1(t)$ and $F_2(t)$, which are computed using Kelly's parametrization [150]. The factors $P_1(\phi)$ and $P_2(\phi)$ are the electron propagators in the BH amplitude.

At sufficiently large values of Q^2 and small values of $|t|$, the azimuthal dependences of the unpolarized DVCS amplitude and of the interference term including twist-3 contributions read as follows:

$$\left|\mathcal{T}_{UU}^{DVCS}\right|^2 = \frac{e^6}{y^2Q^2}\left(c_{0,UU}^{DVCS} + \sum_{n=1}^{2} c_{n,UU}^{DVCS}\cos(n\phi)\right) \tag{5.3}$$

$$\mathcal{I}_{UU} = \frac{e^6}{x_B y^3 t P_1(\phi) P_2(\phi)} \sum_{n=0}^{3} c^{\mathcal{I}}_{n,UU} \cos(n\phi) \tag{5.4}$$

At leading order in the strong coupling constant α_S and considering twist-2 CFFs alone enter the cross-section, only the terms containing $c^{DVCS}_{0,UU}$ remain in (5.3). In this case, the squared DVCS amplitude is independent of the angle ϕ and a bilinear combination of the CFFs is contained in the coefficient $C^{DVCS}_{UU}(\mathcal{F}, \mathcal{F}^*)$ given explicitly in Appendix A.2 with $\mathcal{F} = \{\mathcal{H}, \mathcal{E}, \widetilde{\mathcal{H}}, \widetilde{\mathcal{E}}\}$:

$$|\mathcal{T}^{DVCS}_{UU}|^2 = \frac{e^6}{y^2 Q^2} \left\{ 2 \frac{2 - 2y + y^2 + \frac{\epsilon^2}{2} y^2}{1 + \epsilon^2} C^{DVCS}_{UU}(\mathcal{F}, \mathcal{F}^*) \right\}. \tag{5.5}$$

The DVCS amplitude is contingent on the four twist-2 CFFs. These CFFs are complex-valued, consisting of two real magnitudes – $\Re e\mathcal{F}$ and $\Im m\mathcal{F}$ – each, leading to the emergence of eight distinct CFF parameters. This intricate multiplicity of parameters underscores the complexity involved in their extraction process. A noteworthy aspect in this context is that, under this approximation, the pure DVCS cross-section is taken as a free parameter in the fit function as it lacks dependence on the azimuthal angle.

In this framework, LO and LT, the Fourier coefficients in the harmonic structure of the unpolarized interference term (5.4) only contain helicity-conserving amplitudes given by:

$$c^{\mathcal{I}}_{n,UU} = C^{n}_{++,UU} \mathrm{ReC}^{\mathcal{I}}_{UU}(\mathcal{F}) + C^{V,n}_{++,UU} \mathrm{ReC}^{\mathcal{I},V}_{UU}(\mathcal{F}) + C^{A,n}_{++,UU} \mathrm{ReC}^{\mathcal{I},A}_{UU}(\mathcal{F}). \tag{5.6}$$

The complete expressions of the kinematic coefficients $C^{n}_{++,UU}$, $C^{V,n}_{++,UU}$ and $C^{A,n}_{++,UU}$ are given in Appendix A.3. The $C^{\mathcal{I}}_{UU}$, $C^{\mathcal{I},V}_{UU}$ and $C^{\mathcal{I},A}_{UU}$ terms are a linear combination of the CFFs $\mathcal{H}$, $\mathcal{E}$ and $\widetilde{\mathcal{H}}$:

$$\mathrm{ReC}^{\mathcal{I}}_{UU}(\mathcal{F}) = F_1 \Re e\mathcal{H} + \xi(F_1 + F_2) \Re e\widetilde{\mathcal{H}} - \frac{t}{4M^2} F_2 \Re e\mathcal{E}, \tag{5.7}$$

$$\mathrm{ReC}^{\mathcal{I},V}_{UU}(\mathcal{F}) = \frac{x_B}{2 - x_B + x_B \frac{t}{Q^2}} (F_1 + F_2)(\Re e\mathcal{H} + \Re e\mathcal{E}), \tag{5.8}$$

$$\mathrm{ReC}^{\mathcal{I},A}_{UU}(\mathcal{F}) = \frac{x_B}{2 - x_B + x_B \frac{t}{Q^2}} (F_1 + F_2) \Re e\widetilde{\mathcal{H}}. \tag{5.9}$$

Therefore, in this scenario, the interference amplitude becomes reliant solely on three real-valued Compton Form Factors: $\Re e\mathcal{H}$, $\Re e\mathcal{E}$ and $\Re e\widetilde{\mathcal{H}}$. Additionally, accounting for the constant nature of the pure DVCS cross-section in terms

of the azimuthal angle, the total number of free parameters in the fit function that need to be extracted is streamlined to four. The reduction in the parameter count simplifies the extraction process relative to the full eight-parameter scenario, while still capturing significant aspects of the DVCS amplitude's complexity. This streamlined parameter space facilitates more manageable data analysis and model-fitting endeavors, enhancing the feasibility of accurately deducing these essential parameters from experimental data.

From the perspective that the real Compton form factors at leading twist are relevant to hadron tomography and helpful in the interpretation of the phenomenology of the DVCS process, we focus on an extraction schema that prioritizes both high accuracy and precision that is minimally biased. Any bias in the application of the helicity amplitudes will certainly carry over to the CFF.

5.2 | Least squares extraction

We compare our results with an optimized local least squares fit using the smeared generated pseudodata (Section 4.2.2). In this procedure, the best-fit value is found at each kinematic set by minimizing, with the least squares method, the χ^2 defined as:

$$\chi^2 = \sum_{i=1}^{n} \frac{(\sigma_i^{fit} - \sigma_i^{data})^2}{(\delta\sigma_i^{data})^2}, \tag{5.10}$$

where σ^{fit} is the fit function given by the theoretical DVCS +BH cross-section (Section 5.1), which depends on the 4 free parameters: $\Re e\mathcal{H}$, $\Re e\mathcal{E}$, $\Re e\widetilde{\mathcal{H}}$, and the pure DVCS cross-section. In the interest of comparison, these parameters are limited to the same range used to generate the χ^2 maps, see Section 5.3.1.1. The quantities σ^{data} and $\delta\sigma^{\text{data}}$ are, respectively, the values and the uncertainties of the pseudo- or experimental data. The index i runs over all the available ϕ-points for a given (x_B, Q^2, t) bin.

5.2.1 | Algorithm optimization

We use the well-known MINUIT2 code from CERN [31] with the MIGRAD minimization algorithm which is the best minimizer for generic functions. There are some parameters that can be modified to optimize the fit. A systematic study with the smeared pseudodata allowed us to set the algorithm parameters to the values that gave the CFFs and the DVCS cross-section closer to the true values at which the pseudodata was generated. In Figure 5.2 the extracted values for 5 different

	Strategy	Tolerance
default value	1	0.01
best fit	0	10

Table 5.1: MIGRAD minimization parameters.

kinematic sets are shown with the default MINUIT2 parameters and the optimized ones. The deviation from the true values (red line) is significantly reduced after the optimization. The two most relevant parameters tuned are listed in Table 5.1.

The `Strategy` parameter can take the integer values (0, 1, 2), and the optimal fit was obtained at 0, which is intended for cases where there are many variable correlated parameters but it yields non-reliable errors as seen for example Figure 5.2 where the errors have no physical meaning. The proper estimation of the error is discussed in the next section. Selecting a looser `Tolerance` related to the minimization stopping criteria also yields more accurate results. Optimizing these parameters takes particular improvement on the extraction of $\mathfrak{Re}\mathcal{E}$.

5.2.2 | Error estimation

When the problem is not linear and when the χ^2 shape is not a simple parabola or a simple function, as in our case, MINOS error calculations are needed in order to indicate the correct parameter errors. For proper error calculation, MINOS actually follows the function out from the minimum to find where it crosses the function value i.e., minimum χ^2 (χ^2_{min}) + 1, instead of using the curvature at the minimum and assuming a parabolic shape. Consequently, the uncertainty on a given parameter corresponds to the value of this parameter for $\Delta\chi^2 = +1$ above χ^2_{min}. With MINOS error option, MINUIT2 calculates χ^2 at multiple points of the multi-dimensional hyperspace of the free parameters and will retain a smaller function value if they stumble on one, reducing the risk of falling into local minima. MINOS errors are costly to calculate but are very reliable since they take account of non-linearities in the problem and parameter correlations, and are generally asymmetric. However, there were some kinematic sets where the minimization failed when running MINOS for some parameters, caused by intrinsic instability of the obtained fit e.g., very correlated parameters as in this case. Alternatively, when MINOS fails, the HESSE error matrix which calculates the full second–derivative matrix at the minimal point by finite differences and inverts it, is used:

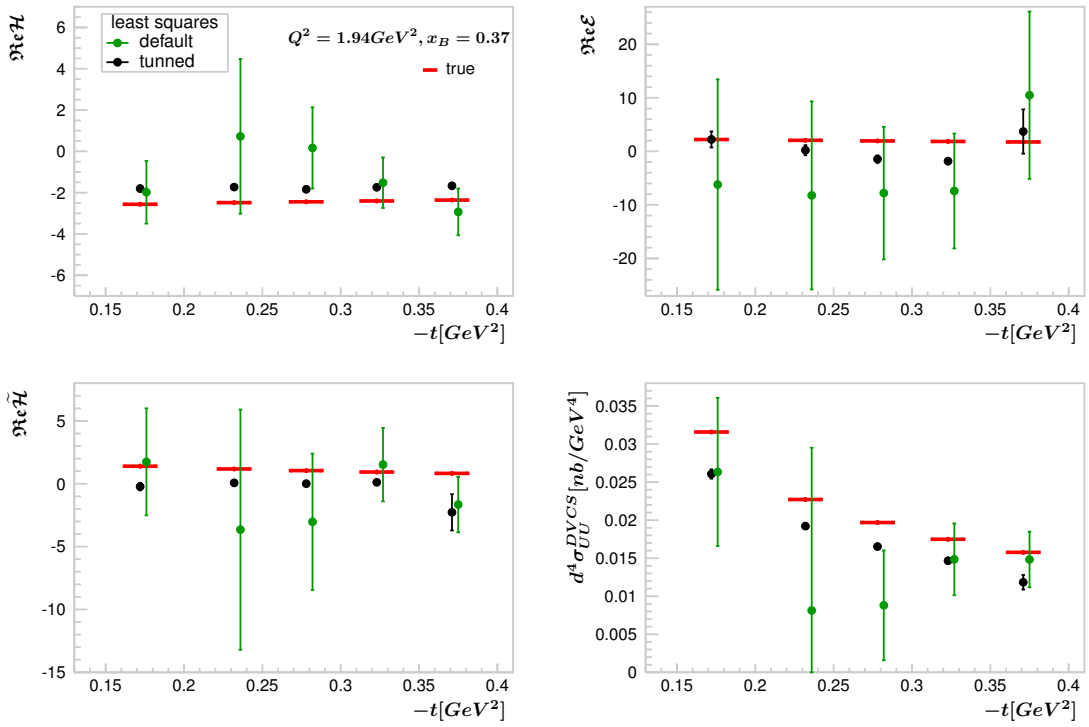

Figure 5.2: Least squares extraction with MINUIT default parameters (green) and with the optimized algorithm parameters (black). The smeared pseudodata from 5 kinematic points correspond to Hall-A experimental data with average $Q^2 = 1.94\ GeV^2$ and $x_B = 0.37$. The parameters used to generate the pseudodata are shown in red, centered at the data t value with an arbitrary bin width. The green points have been slightly shifted in t for clarity on the visualization.

$$H_{ij} = \frac{1}{2}\frac{\partial^2}{\partial\alpha_i\partial\alpha_j}\chi^2\Big|_{\alpha=\alpha^0}. \tag{5.11}$$

Then, the uncertainty can be propagated to a function $\mathcal{F}$ which depends on the fit parameters, by

$$\sigma_{\mathcal{F}} = T\left(\sum_{i,j=1}^{n}\frac{\partial\mathcal{F}}{\partial\alpha_i}H^{-1}\frac{\partial\mathcal{F}}{\partial\alpha_j}\right)^{1/2}, \tag{5.12}$$

where $T = \sqrt{\Delta\chi^2}$ is the tolerance factor. Taking 1 should give the usual 68% confidence interval.

The least squares extraction after tunning the minimization algorithm and calculating the HESSE or the MINOS errors when available, is shown in Figure 5.3 for kinematics corresponding to 5 t-bins of the Hall-A E00-110 experiment. We find that we get better estimates of $\Re e\mathcal{H}$ and the DVCS cross-section while $\Re e\widetilde{\mathcal{H}}$ and

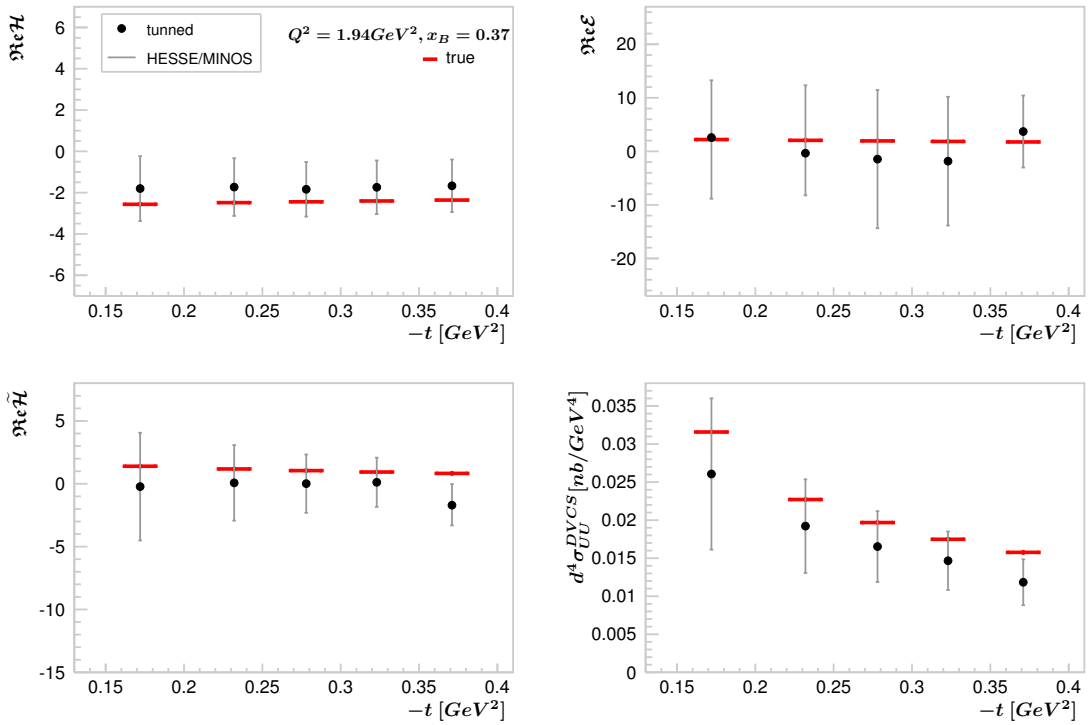

Figure 5.3: Least squares extraction with the optimized algorithm parameters (black) and HESSE/MINOS error option. The smeared pseudodata from 5 kinematic points correspond to Hall-A experimental data with average $Q^2 = 1.94\ GeV^2$ and $x_B = 0.37$. The parameters used to generate the pseudodata are shown in red, centered at the data t value with an arbitrary bin width.

$\Re e\mathcal{E}$ are harder to constrain and the true values are generally contained within the errors.

5.3 | Extraction from χ^2 maps

DVCS observables receive contributions from several CFFs, which are strongly correlated, and therefore their extraction is an unconstrained problem. It is easy to obtain a good fit of the experimental data, but many combinations of the real and imaginary parts of the CFFs can provide an equally good fit as seen in Figure 5.1. In this Section, we will describe a novel extraction method that employs χ^2 maps, allowing us to effectively constrain 3 CFFs and the DVCS cross-section in the helicity-independent case. The extraction of the CFFs through the χ^2 maps analysis is outlined in Section 5.3.1 along with the systematic studies in Section 5.4.3. The final results with the Hall-A and Hall-B experimental data are shown in Section 5.5. We will refer to this method as χ^2 Maps Inference (χMI).

5.3.1 | Weighted χ^2 analysis

In the following, we will focus on a method that calculates χ^2 at multiple points of the multi-dimensional hyperspace of the free parameters by creating Monte Carlo simulation replicas of the 8 CFFs. Thus, the full phase space of the free parameters is explored, and χ^2 maps i.e., the number density of χ^2 vs. each parameter are constructed, Section 5.3.1.1. After applying selections given the topology of the maps, see Section 5.3.1.2, the best-extracted values of the three CFFs and the DVCS cross-section is obtained as a weighted average of the χ^2 confidence level (CL) for the distribution of parameters. For example, the extracted $\mathfrak{Re}\mathcal{H}$ value at a fixed kinematic set is given by:

$$\overline{\mathfrak{Re}\mathcal{H}} = \frac{\sum_{n=1}^{N} \mathfrak{Re}\mathcal{H}_n \cdot D_n(\chi^2_n, r)}{\sum_{n=1}^{N} D_n(\chi^2_n, r)}, \tag{5.13}$$

and similarly for the rest of the parameters. Here, n runs over every randomly generated CFFs set and $D(\chi^2, r)$ is the complement of the cumulative distribution function of the χ^2 distribution with r degrees of freedom (ndf), called in statistic, survival function. $D(\chi^2, r)$ is shown Eq. (5.14) where Γ is the incomplete gamma function. It corresponds to the upper tail integral of the probability density function between x and +infinity giving the probability of having a χ^2 value larger than what you observed. If this probability is very small, it means that the hypothesis that your extraction is a good representation of your data is very unlikely.

$$D(\chi^2, r) = \int_{\chi^2}^{+\infty} \frac{1}{\Gamma(r/2)2^{r/2}} x'^{r/2-1} e^{-x'/2} dx'. \tag{5.14}$$

This method can be applied without assuming that the χ^2 is quadratic in the vicinity of its minimum but demands computing power and time.

5.3.1.1 | Generation of χ^2 maps

In the first stage, we generate the unpolarized cross-sections of the $ep \to ep\gamma$ process at the level of the eight twist-2 CFFs as a function of ϕ. This generation is specific to a given kinematic bin characterized by (Q^2, x_B, t) and a specific energy bin corresponding to the available experimental data kinematic points. For every uniform randomly generated CFFs set the χ^2 is computed as:

$$\chi^2 = \sum_{i=1}^{n} \frac{(\sigma_i^{theo} - \sigma_i^{data})^2}{(\delta\sigma_i^{data})^2}, \tag{5.15}$$

where σ_i^{theo} is the cross-section at the point ϕ_i for a given CFFs replica set. This calculation is based on the leading-twist and leading-order amplitudes for the DVCS process combined with BH process (Section 5.1). The quantities σ^{data} and $\delta\sigma^{\text{data}}$ are, respectively, the values and the uncertainties of the pseudo- or experimental data.

To keep the problem realistic, it was decided to limit, in a conservative and educated way, the range of variation of the CFFs while reducing the computing time and resources. The CFFs are confined within a bounded 8-fold hypervolume, with boundaries set at ±5 times the CFFs predicted by the KM15* model (described in Section 4.1.2), which obeys most of the model-independent GPD normalization constraints (see Section 2.3). Centering the 8-CFFs hypervolume around the KM15* model and restricting it to a ±5 factor prevents us from exploring too unlikely cases. Generated values exceeding 3 times the KM15* model's value probably correspond to quite unrealistic CFFs. Given that GPDs have to fulfill a certain number of normalization constraints, such a strong deviation from the KM15* reference value is quite unlikely. However, the exploration of such a broad range of values enhances the robustness and credibility of the study. The only model-dependent input of this approach is the definition of the range of variation of the CFFs.

As a result, we can construct χ^2 maps for each of the parameters to be extracted. In the case of the pure DVCS cross-section parameter, it is calculated from the Monte-Carlo simulated CFFs using the theoretical calculation on Eq. (5.5).

Examples of the obtained maps are shown in Figure 5.4. We take the particular kinematics $(x_B, Q^2, t) = (0.34, 2.22GeV^2, -0.176GeV^2)$ and $(x_B, Q^2, t) = (0.13, 1.11GeV^2, -0.34GeV^2)$ with a 5.75 GeV^2 beam energy. This corresponds to a kinematic bin measured by the Hall-A and Hall-B experiments respectively. The red point represents the true χ^2 value obtained with the CFFs at which the smeared pseudo data was generated and the magenta point is at the extracted value from Eq. (5.13) and the χ^2 with the obtained parameters. We can see that several combinations of CFFs can give lower χ^2 than the true one and therefore minimizing χ^2 can lead to inaccurate results. There is a more striking limitation of the least-squares fit observed on the maps, given the almost flat behavior of χ^2 near its minimum, particularly for $\Re\mathrm{e}\mathcal{E}$ and $\Re\mathrm{e}\widetilde{\mathcal{H}}$ giving the large uncertainty on the extraction seen for example in Figure 5.3.

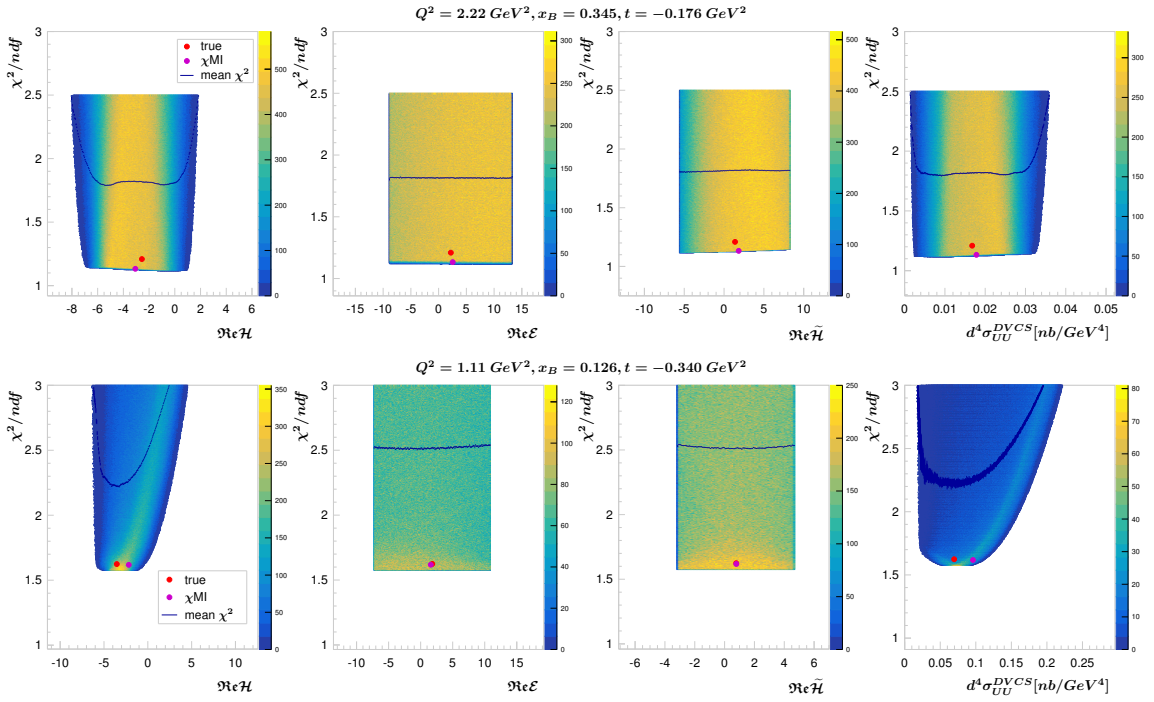

Figure 5.4: Pseudodata χ^2 maps at a fixed kinetic bin of Hall-A (top) and Hall-B (bottom) data.

A threshold is set at the maximum χ^2 value of 50. This choice is informed by the observation that opting for higher χ^2 values does not yield extra informative value as seen in Figure 5.4. The relevant topology primarily resides in the lower spectrum of normalized χ^2, denoted as χ^2/ndf, specifically those less than 2. Here, ndf represents the degrees of freedom calculated by subtracting the number of free parameters i.e., four, from the number of points in ϕ for a given kinematic configuration.

5.3.1.2 | Selections cuts on χ^2 maps

Studying the χ^2 maps topology in this 4-dimensional parameter space is a potential source of information on the CFFs correlations that can constrain the extraction of these parameters. The pseudodata mimicking the real data is a powerful tool to optimize and test the extraction method. We use the smeared pseudodata to fine-tune the selection cuts applied on the χ^2 maps to select the strongest χ^2 values which allow of to reduce the background from very unlikely parameters while finding more constrained high-density χ^2 regions as a function of the parameters. This is of particular importance for the CFFs $\Re e\mathcal{E}$ and $\Re e\widetilde{\mathcal{H}}$ that pertain to a large homogeneous flat distribution.

The selection of the high-density areas is performed iteratively and the weighted average from Eq. (5.13) is calculated at every step. Iterations are performed while the selected map region statistics is greater than 10000 points and the true value is within 1 standard deviation (σ) from the weighted average. In general, 2 iterations are performed on every kinematic set. The optimized selection is applied to the experimental data at the corresponding kinematic bin.

Contour cuts are applied on the maps based on a 70% confidence level from the 2D map's highest density bin. Figure 5.5 for example, shows confidence level contours at 70 (green), and 80% (orange) for $\mathfrak{Re}\mathcal{E}$after the first iteration. In this case, the next step will select only the region contained within the 70% contour level and recalculate the value of $\mathfrak{Re}\mathcal{E}$weighted average as in Eq. (5.13). Several trials showed that varying the number of iterations and the contour cuts ± 10% around 70% yield similar extracted parameter results. The main differences are related to the precision which is limited by the iteration contour statistics and the deviation from the true values in less than one standard deviation.

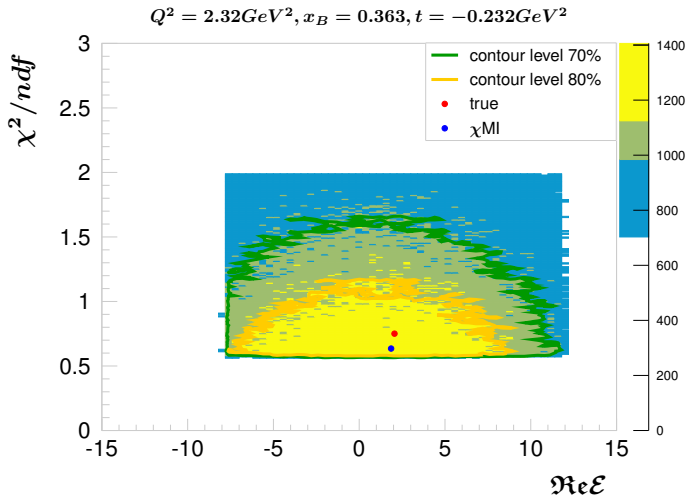

Figure 5.5: $\mathfrak{Re}\mathcal{E}$ contour levels at the first iteration.

Figure 5.6 shows the contour cuts for two iterations after applying simultaneous selections on the strongest χ^2 zones on all the parameters. This selection method on the 2D map allows the calculation of the weighted averages in the most likely regions containing the true (best) values, reducing the uncertainties on the extracted parameters. Noticeably, $\mathfrak{Re}\mathcal{E}$ and $\mathfrak{Re}\widetilde{\mathcal{H}}$ concentrate the most likely χ^2 values in regions closer to the true value after repeated iterations in contrast to the flat homogeneous initial distribution.

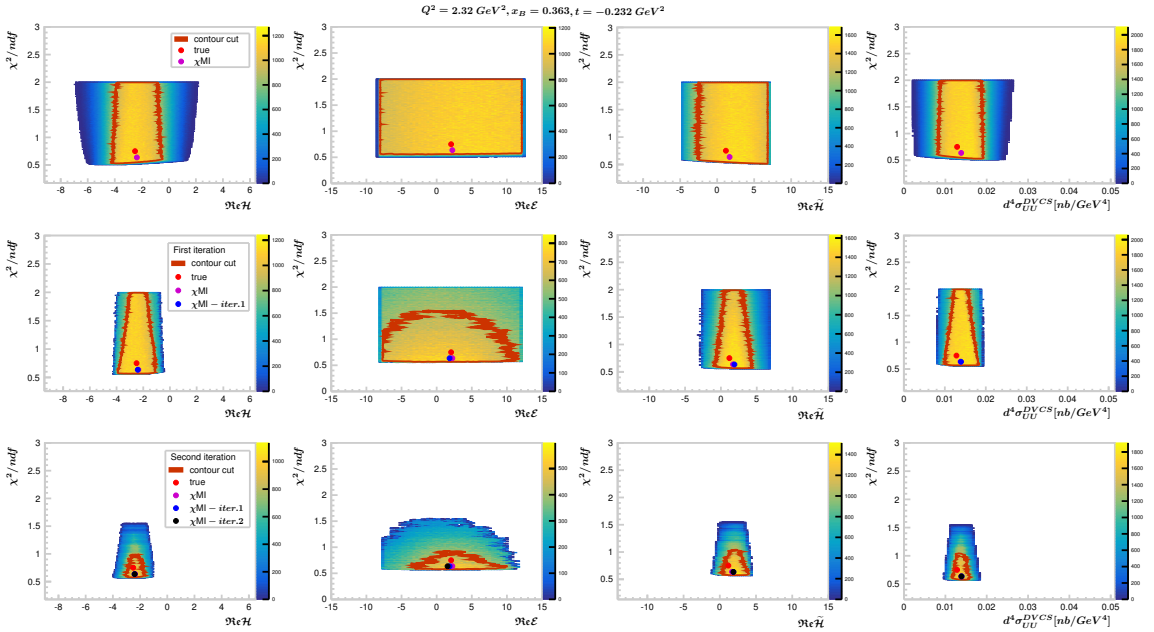

Figure 5.6: Selections on χ^2 maps for the pseudodata at a fixed kinetic bin of Hall-A for all parameters. The top row shows the 2D maps without any selection cuts, in the center row the maps are shown after applying the contour cut (red, top) and the second iteration of selections is at the bottom after applying the contour cut (red, middle).

5.3.2 | Uncertainty estimation

As mentioned before, we recover the intuitive notion that if the likelihood is almost flat near its maximum the uncertainty on the parameter extraction is large. Applying selections on the 2D χ^2 maps we can significantly increase the precision of the extracted parameters, particularly for $\Re e\mathcal{E}$ and $\Re e\widetilde{\mathcal{H}}$ while still containing the true value within. After iterative selections, the extracted value of the CFFs and the DVCS cross section is given by the weighted average, and the uncertainty is obtained by the standard deviation of the final map, for example, for $\Re e\mathcal{H}$:

$$\sigma_{\Re e\mathcal{H}}(x_B, t, Q^2) = \sqrt{\frac{\sum_n \left(\Re e\mathcal{H}_n - \overline{\Re e\mathcal{H}}\right)^2}{N}}, \tag{5.16}$$

where n runs over the number of points in the map, N, and $\overline{\Re e\mathcal{H}}$ is the weighted average obtained from Eq. (5.13).

The uncertainties and the extracted values after every iteration associated with each parameter for one kinematic corresponding to the Hall-A data are summarized in Table 5.2, along with the normalized χ^2. In this kinematic bin, at the third iteration, the precision for the extracted values of $\Re e\mathcal{H}$, $\Re e\mathcal{E}$, $\Re e\widetilde{\mathcal{H}}$ and the DVCS

	$\Re e\mathcal{H}$	$\Re e\mathcal{E}$	$\Re e\widetilde{\mathcal{H}}$	$\sigma_{UU}^{DVCS}(nb/GeV^4)$	χ^2/ndf
true	-2.38	1.75	0.82	$9.11 \cdot 10^{-3}$	1.224
no cuts	-2.27 ± 1.15	1.10 ± 4.85	1.45 ± 2.20	$(9.36 \pm 2.35) \cdot 10^{-3}$	0.975
iter. 1	-2.20 ± 0.67	0.97 ± 4.52	1.34 ± 1.64	$(9.22 \pm 1.33) \cdot 10^{-3}$	0.978
iter. 2	-2.14 ± 0.32	1.04 ± 3.43	1.13 ± 0.83	$(9.03 \pm 0.83) \cdot 10^{-3}$	0.986
iter. 3	-2.11 ± 0.28	1.07 ± 2.21	1.03 ± 0.66	$(8.92 \pm 0.37) \cdot 10^{-3}$	0.990

Table 5.2: Extracted values of $\Re e\mathcal{H}$, $\Re e\mathcal{E}$, $\Re e\widetilde{\mathcal{H}}$ and the DVCS cross-section from the smeared pseudodata at $k = 5.75\ GeV$, $Q^2 = 2.375\ GeV^2$, $x_B = 0.373$ and $t = -0.372\ GeV^2$ corresponding to a Hall-A kinematic set.

cross-section was increased by 75, 54, 70 and 84% respectively, in comparison with the extraction without contour cuts, while still overlapping with the true values.

5.4 | Pseudodata studies

The goal of this study is to find out if, by fitting the generated ϕ pseudo-data distribution, we are able to retrieve, or constrain, the 8 original randomly generated CFFs, at the level of the CFFs $\Re e\mathcal{H}$, $\Re e\mathcal{E}$, $\Re e\widetilde{\mathcal{H}}$ and the DVCS cross-section, under realistic experimental conditions (Section 5.4.1). For the latter, we smear the theoretically calculated cross sections according to the experimental uncertainties of the Hall-A and Hall-B experiments, listed in Table 4.2, which allow us to evaluate the effects of the experimental resolution in the extraction, see Section 5.4.2. Figure 4.5 shows the ϕ dependence of the $ep \to ep\gamma$ unpolarized cross section, un-smeared and smeared (left and right panels respectively), generated with the 8 random CFFs. The systematic uncertainties associated with deviations from the model choice used to generate the pseudodata, are quantified in Section 5.4.3.

5.4.1 | Evaluation of the χMI method

Through our testing phase, the accuracy and precision is estimated through the use of pseudodata generated at the same kinematics as the experimental data and with a smearing mimicking the experimental error. The accuracy (proximity of the weighted average parameter extracted with the χMI method to the *true* CFF) is

	$\Re e\mathcal{H}$	$\Re e\mathcal{E}$	$\Re e\widetilde{\mathcal{H}}$	$\sigma_{UU}^{DVCS}(nb/GeV^4)$
Hall-A E00-110	91(0.5)	68(4.1)	60(1.2)	$96(1.9 \cdot 10^{-3})$
Hall-A E07-007	87(0.4)	24(2.2)	48(0.7)	$94(0.2 \cdot 10^{-3})$
Hall-A E12-06-114	85(0.3)	58(2.8)	30(0.7)	$94(1.7 \cdot 10^{-3})$
Hall-B e1-DVCS1	60(0.5)	42(3.7)	21(1.1)	$60(6.5 \cdot 10^{-3})$

Table 5.3: Average accuracy and precision of the χMI method using the smeared pseudodata. The accuracy, Eq. (5.17) is given in percentage and the precision, in parenthesis, is the standard deviation of the final iteration map, Eq. (5.16).

defined for the CFF $\Re e\mathcal{H}$as,

$$\epsilon_{\Re e\mathcal{H}}(x_B, t, Q^2) = \left(1 - \left|\frac{\Re e\mathcal{H}_{true} - \Re e\mathcal{H}_{\chi\text{MI}}}{\Re e\mathcal{H}_{true}}\right|\right) \times 100\%, \tag{5.17}$$

and similarly for the rest of the parameters. The precision (standard deviation at the final iteration), is given in Eq. 5.16.

The χMI extraction method allows constraining the CFFs with increased precision compared to the regular least-squares fitting, particularly for the CFFs $\Re e\mathcal{E}$ and $\Re e\widetilde{\mathcal{H}}$ which normally carry significant uncertainties given their almost flat likelihood distribution near their maximum - so with a small second derivative - the uncertainty on the parameter extraction is large with the Hessian method as well as with the MINOS method. A comparison between the least-squares fit with HESSE/MINOS errors and the χMI method for the smeared pseudodata in Hall-A and Hall-B data kinematic bins appears in Figure 5.7. This novel method gives the best achievable accuracy and precision for a local χ^2 extraction technique in the least constrained DVCS observable scenario for the kinematic region covered by Hall-A and Hall-B experiments.

Table 5.3 presents the average accuracy given by Eq. (5.17), for the kinematics sets corresponding to each experimental data using the smeared pseudodata. The average standard deviation is also shown in parentheses. The CFF $\Re e\mathcal{H}$ and the DVCS cross-section are extracted with a high accuracy greater than 85% and 94% respectively at Hall-A kinematics. $\Re e\mathcal{E}$ and $\Re e\widetilde{\mathcal{H}}$ are the parameters harder to constrain with the best accuracy obtained at the Hall-A E00-110 experimental kinematic region which yields accuracies above 60%. The accuracies for the Hall-B data are lower; this is given by a stronger smearing effect at these kinematics, particularly, the lower x_B range, as will be seen in the next section.

The percentage difference from the *true* values for each kinematic bin of the Hall-A experiments is presented in Figure 5.8. The gray band represents the average

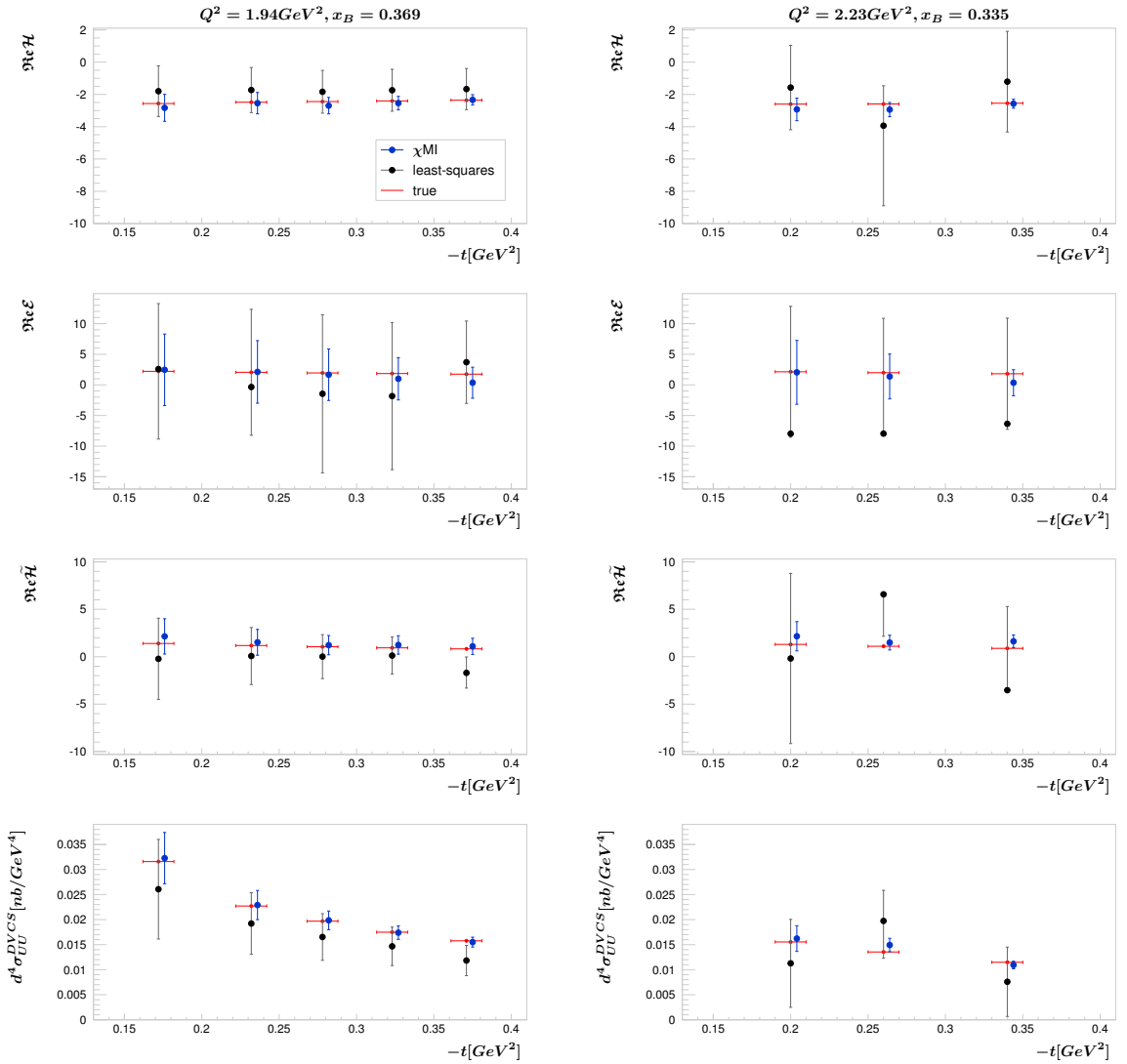

Figure 5.7: Extracted pseudodata parameters corresponding to Hall-A (left) and Hall-B (right) kinematics with average $Q^2 = 1.94\,\text{GeV}^2, x_B = 0.369$ and $Q^2 = 2.23\,\text{GeV}^2, x_B = 0.335$ respectively. The true values used to generate the smeared pseudodata are represented with a red line centered at the experimental t values with an arbitrary bin width. The results from the least-squares fit using the HESSE/MINOS technique are shown in black and the χMI method is shown in blue where the points have been slightly shifted for visualization purposes.

percent difference at each *true* value that is obtained from fitting the extracted parameters $\pm\sigma$ as a function of the *true* values, e.g. for $\mathfrak{Re}\mathcal{H}$ at a given kinematic set:

$$\Delta_{\mathfrak{Re}\mathcal{H}}(\%\text{diff.}) = \frac{(\mathfrak{Re}\mathcal{H} \pm \sigma_{\mathfrak{Re}\mathcal{H}})_{\chi\text{MI}} - \mathfrak{Re}\mathcal{H}_{\text{true}}}{\mathfrak{Re}\mathcal{H}_{\text{true}}}, \tag{5.18}$$

notice that the values have not been multiplied by 100.

Out of the four parameters, $\mathfrak{Re}\mathcal{H}$ and the DVCS cross-section emerge with a

quite well-nailed extraction and finite error bars in the order of ≈ 20% and ≈ 10% respectively for all the Hall-A kinematic range. $\mathfrak{Re}\widetilde{\mathcal{H}}$ is extracted with differences from the *true* values below ≈ 50% for most of the kinematic points. The CFF $\mathfrak{Re}\mathcal{E}$ is extracted with deviations from the *true* values below ≈ 50% in the Hall-A experiments E00-110 and E07-007 kinematics. $\mathfrak{Re}\mathcal{E}$ and $\mathfrak{Re}\widetilde{\mathcal{H}}$ vs χ^2 maps had a very homogeneous topology which makes these parameters harder to constrain compared to $\mathfrak{Re}\mathcal{H}$ and the DVCS cross-section parameters. The deviations of $\mathfrak{Re}\mathcal{E}$ are larger as this CFF value decreases. This is consistent with the $\mathfrak{Re}\mathcal{E}$ values in kinematic regions covered by the E12-06-114 experiment.

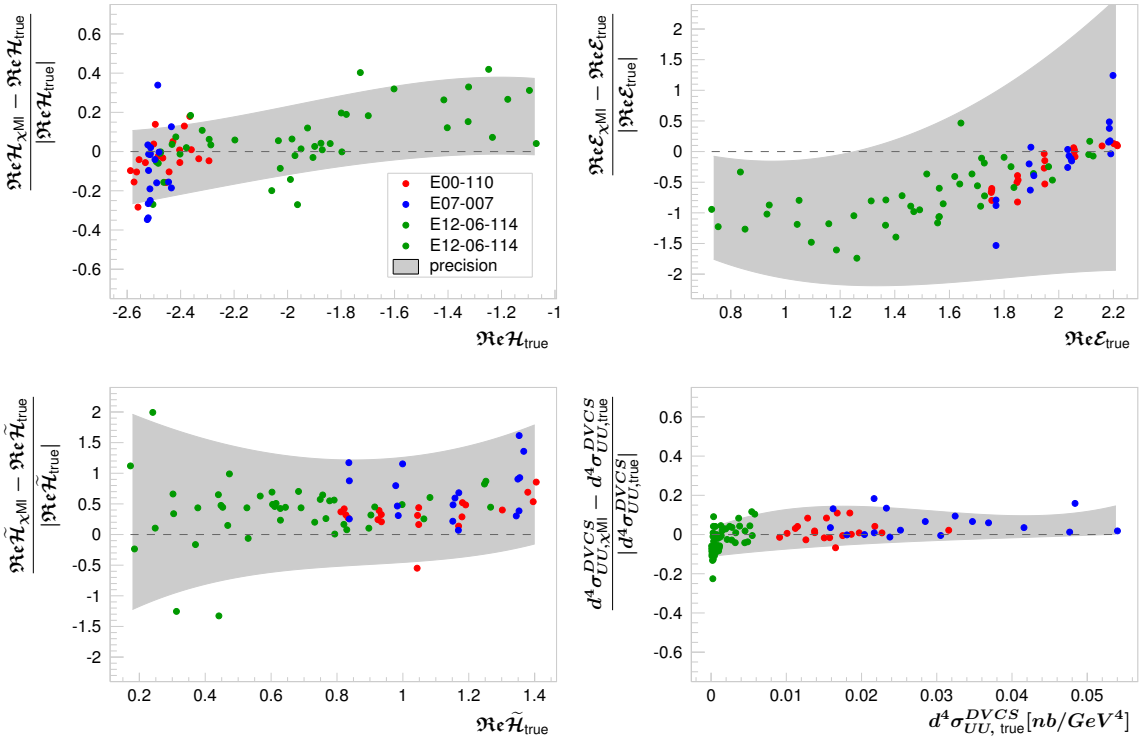

Figure 5.8: Pseudodata percentage difference of the extracted values (dots) and of their average error (gray band) from the *true* parameters used to generate the pseudodata.

5.4.2 | Smearing effects

The pseudodata has been smeared by deliberately introducing random uncertainties simulating the actual experimental errors given by the JLab data used in this work, at the corresponding kinematic bin. This is done to evaluate the robustness and reliability of this analysis technique in the face of real experimental conditions and to understand how these uncertainties might affect the extraction of the CFFs

$\Re e\mathcal{H}$, $\Re e\mathcal{E}$, $\Re e\widetilde{\mathcal{H}}$, and the DVCS cross-section. By contrasting the smeared with non-smeared pseudodata, which represents the true, unaltered dataset, we can estimate the deviations from the actual parameters induced by the experimental accuracy.

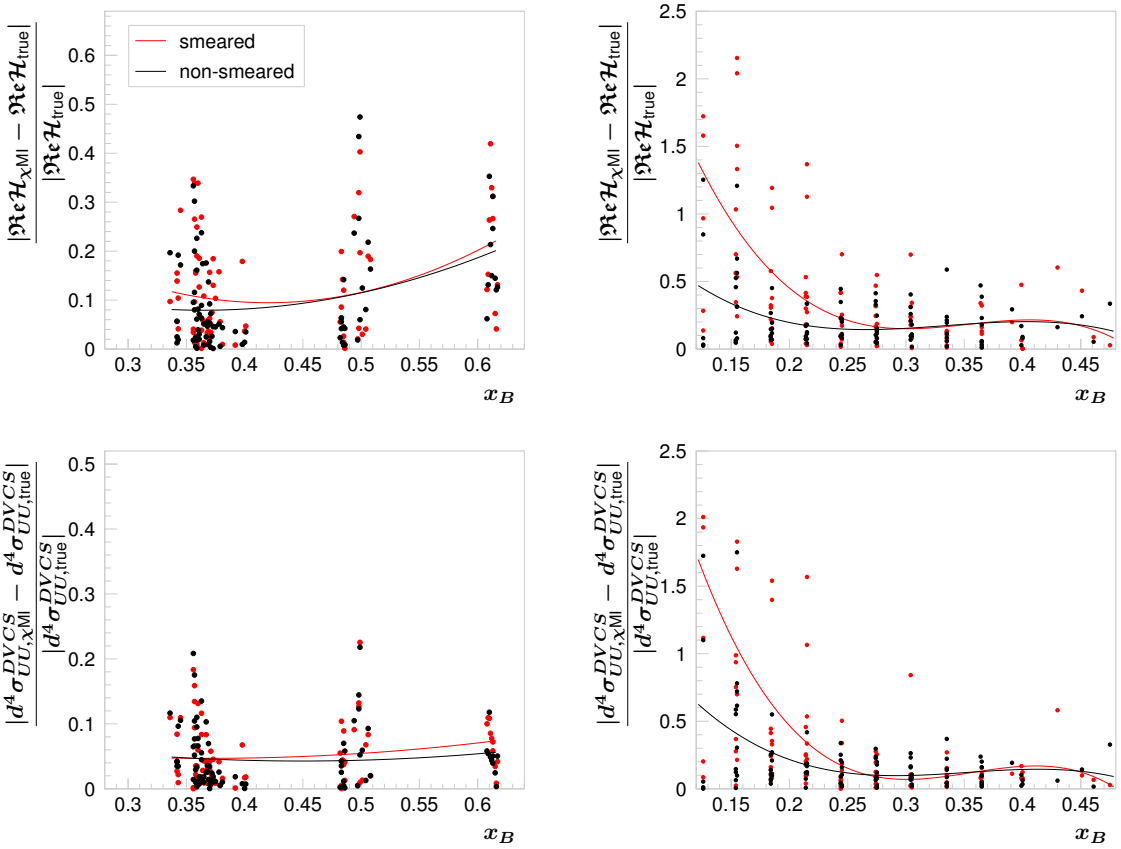

Figure 5.9: Smeared (red) and non-smeared (black) pseudodata percentage difference of the extracted values (dots) for the Hall-A experiments E00-110, E07-007 and E12-06-114 (left panel) and for the Hall-B experiment e1-DVCS1 (right panel) kinematics. Their average deviations from the *true* parameters as a function of x_B are given by a polynomial fit to these values (lines). The percentage difference has not been multiplied by 100.

We have observed that for the datasets in the Hall-A experimental kinematic range, there are no significant changes in the parameters extraction at the level of their experimental uncertainties for the unpolarized photon leptoproduction cross-section measurements which on average is about 5% for both, Hall-A and Hall-B experiments. The left panel of Figure 5.9, shows the absolute value of the percentage difference from the *true* value using the smeared (red) and the non-smeared (black) pseudodata for two parameters $\Re e\mathcal{H}$(top) and the DVCS cross-

section (bottom) for all Hall-A kinematics. The difference between the smeared and non-smeared pseudodata in Hall-A kinematics is bellow 4%. The percentage difference for each experimental kinematic set (dots) is given in Figure 5.9 as a function of x_B and their average deviations (line) are given by a polynomial fit to these values.

We show these two parameters since they are the ones found to be most affected by the experimental uncertainties at the Hall-B experiment kinematics (Figure 5.9, right panel). We had foreseen in Table 5.3 that the averaged accuracy of the extraction of the parameters $\Re e\mathcal{H}$ and the DVCS cross-section was reduced by about 30% compared to the Hall-A kinematics accuracy. It is seen in this figure that the deviations from the true values for these two parameters are very significant for the lower x_B range covered by this dataset, which is not explored in the Hall-A experiments kinematics. The Hall-B experiment expands in $x_B = (0.126 - 0.475)$ while HAll-A covers the $x_B = (0.336 - 0.617)$ region, accounting for the three Hall-A experiments. The effects of the experimental limitations appear for kinematic bins below $x_B \approx 0.25$, increasing quadratically as x_B decreases, for both parameters. The deviations from the true parameters at the lowest achievable x_B value at Hall-B are increased by about 60% when the experimental uncertainties are taken into account. These findings evidence the need for experimental setups able to measure the DVCS cross-sections with uncertainties below 5% for the lower x_B kinematic spectrum, i.e., $x_B \lesssim 0.25$.

In essence, this comparative analysis provides insights into how uncertainties and limitations in the experimental measurements affect the significance and implications of the obtained results in a real experimental context.

5.4.3 | Systematics

To generalize the systematic uncertainty in the extraction method, it is imperative to modify the generated pseudodata to encompass all feasible effects of the deviations of the parameters from the values employed in the evaluation and optimization of the extraction of the CFFs and the DVCS cross-section with the χMI method. This process yields numerous samples of this kinematically dependent deviation. Aggregating all such samples provides a direct means of estimating the systematic uncertainty associated with the extraction method itself. Incorporating this *cumulative accuracy* measure into the quality metrics also ensures the robustness of the method, demonstrating its ability to consistently obtain extractions across a wide range of CFF studies.

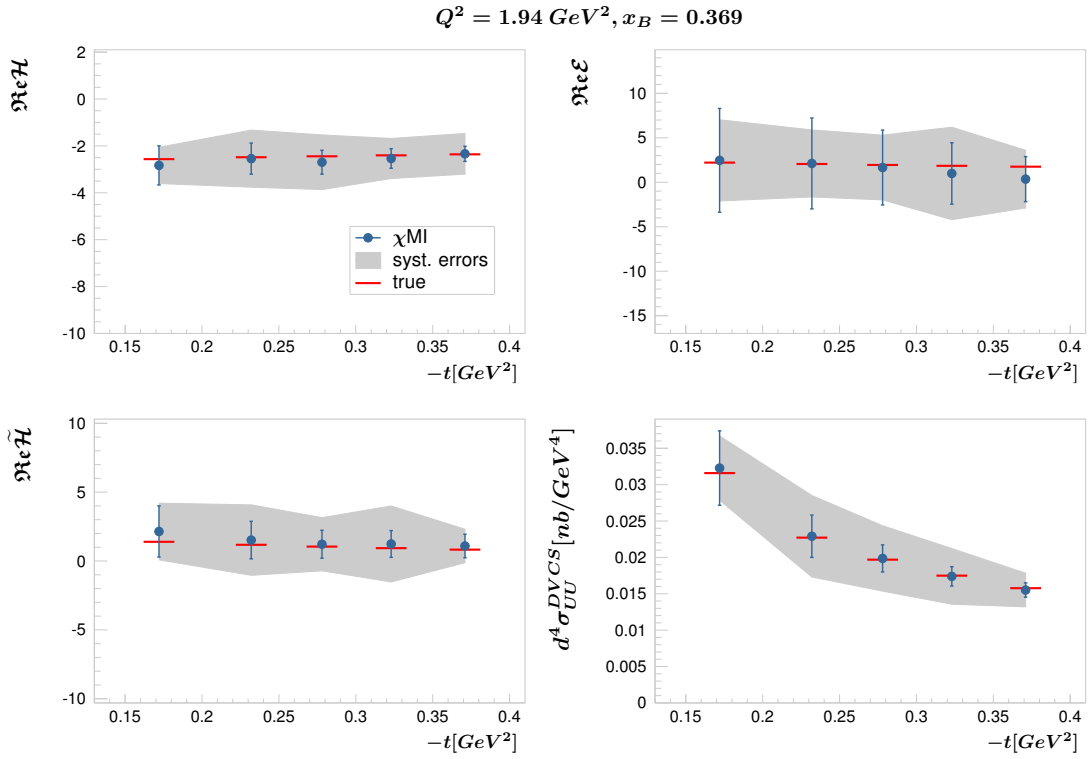

Figure 5.10: Systematic errors on the extraction parameters at kinematics bins corresponding to the Hall-A E00-110 experiment with average Q^2 = 1.94 GeV^2 and x_B = 0.369.

In this methodology, we generate multiple pseudodata samples by randomly generating sets of the eight CFFs within a defined region that spans up to 2 times the values predicted by the $KM15^*$ model. The purpose of this is to simulate a diverse range of possible scenarios and configurations of CFFs that are within a reasonable deviation from the $KM15^*$ model's predictions. The full extraction process with the χMI method is then reperformed on each sample to deduce the kinematic deviation given by the largest difference between the extracted and the true value among all the pseudodata samples. An example of the obtained systematic errors in the extracted parameters is shown in Figure 5.10, as a function of t with average Q^2 = 1.94 GeV^2 and x_B = 0.369 corresponding to the Hall-A E00-110 experiment. The red lines are centered on the true values and the extracted values with the statistical errors bar are shown in blue. The obtained systematic error appears as a gray band.

This step is crucial in assessing the systematic error of the CFF extraction from experimental data, as the uncertainty is contingent on both the kinematics and the magnitude of the CFFs. The experimental error in the cross-section data is a combination of statistical (see Section 5.3.2) and systematic errors.

5.5 | Results

We have evaluated the performance of the χMI method and identified the optimal iterations and contour selections on the 2D χ^2 maps on each kinematic set, as well as the expected effects of the experimental data resolution on the extraction accuracy and the systematic errors. Subsequently, we determine the CFFs $\mathfrak{Re}\mathcal{H}$, $\mathfrak{Re}\mathcal{E}$, and $\mathfrak{Re}\widetilde{\mathcal{H}}$, along with the DVCS unpolarized cross-section and their kinematical dependence using the described χMI method at LO and LT approximations. We use the helicity-independent photon electroproduction cross-section data from the Hall-A and Hall-B experiments presented in Table 4.2, including the new Hall-A data after the 12 GeV JLab upgrade. Details of the kinematic set-up and running conditions of these datasets were discussed in Section 3.5.

The description of the measured photon electroproduction cross-section by the χMI method after extracting the CFFs and the pure DVCS cross-section that parametrizes it is discussed in the next section and compared with the published cross-section fits of the experimental datasets used. We show that with our χMI method we can extract the CFFs $\mathfrak{Re}\mathcal{H}$, $\mathfrak{Re}\mathcal{E}$, and $\mathfrak{Re}\widetilde{\mathcal{H}}$, along with the DVCS unpolarized cross-section unambiguously in the least constrained observable case. The sensitivity to the CFF $\mathfrak{Re}\mathcal{E}$ and $\mathfrak{Re}\widetilde{\mathcal{H}}$ with this approach is of great significance since they are much less well known experimentally. The distribution of the extracted parameters as a function of the squared transverse momentum t is shown in Section 5.5.2 and compared with results from other references when available. Their t-dependence provides access to the transverse profile of the proton. The x_B dependence and the Q^2 evolution are also discussed in Sections 5.5.3 and 5.5.4 respectively. The latter allows us to verify the applicability of the assumption that the GPDs do not evolve under the change of the photon virtuality i.e., Q^2-scaling hypothesis. The full set of extracted parameters for all the experimental data used in every kinematic bin is listed in the Appendix B.

5.5.1 | Photon electroproduction cross-sections

The total cross-section distributions obtained as a function of the azimuthal angle ϕ after substituting the extracted parameters with the χMI method in Eq. (5.1) are shown in Figure 5.11 at one example kinematic set of each experimental dataset used in this work. The contribution of the BH process is shown on each plot as a dashed magenta line. Notice that for the kinematic sets shown on the bottom panel of this figure, the BH contribution is large, and therefore the cross-sections

are given in log-scale. Theoretical curves, including the KM15* model used to generate the pseudo-data, and results from other references, are shown alongside for comparison.

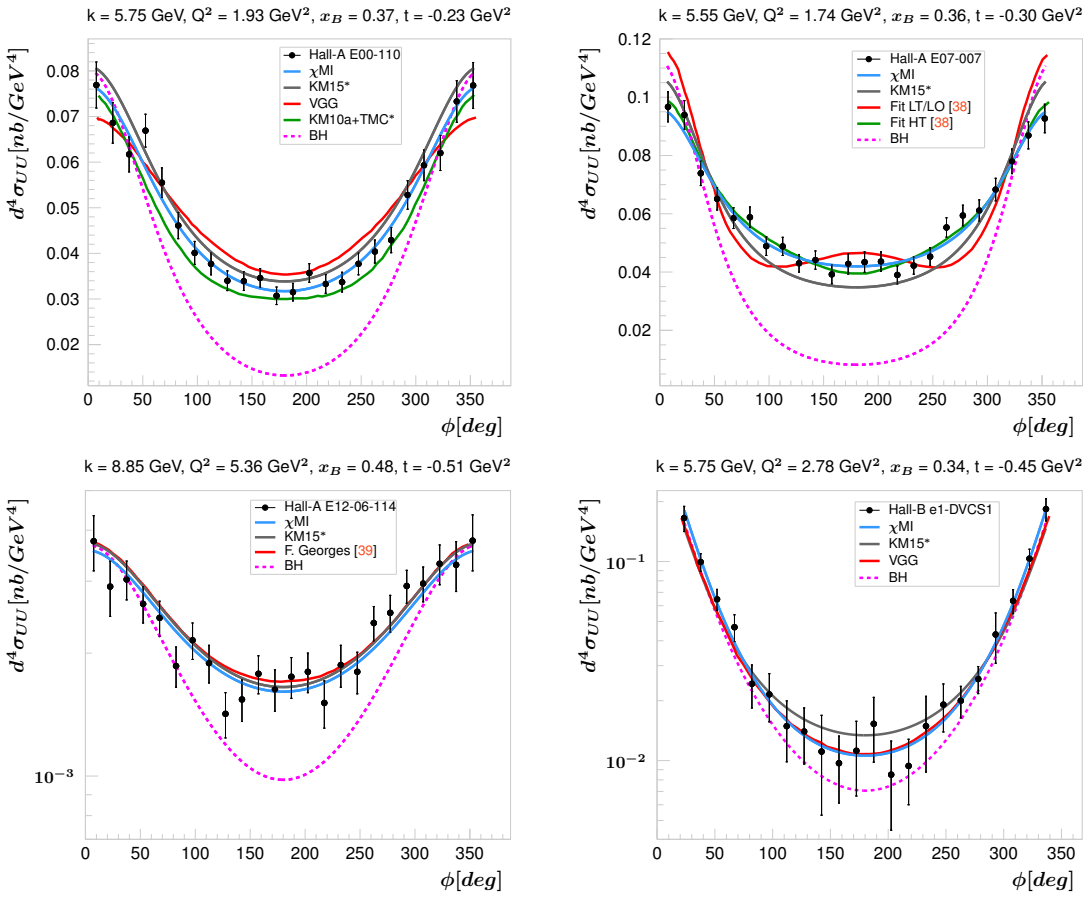

Figure 5.11: Helicity-independent photon electroproduction cross-sections (dots) for one kinematic set of the Hall-A experiments E00-110 (top-left), E07-007 (top-right), E12-06-114 (bottom-left) and of the Hall-B e1-DVCS1 (bottom-right) experiment. The contribution of the BH process is shown on each plot as a dashed magenta line. The cyan line corresponds to the resulting cross-section distribution with the extracted parameters with the χMI method. The theoretical KM15* model that was used to generate the pseudo-data is shown in black.

Hall-A E00-110 experiment

In Figure 5.11 (top-left), we show the experimental data from the E00-110 [37] experiment carried out in Hall-A at Jefferson Lab for the Kin2 setting at $t = -0.23$ GeV^2 along with our χMI predicted results (cyan) and the theoretical models KM15* (black), VGG [56] (red) and KM10a [52] (green) with target mass corrections (TMC) taken from [37]. The χMI result is clearly very close to the helicity-independent data when compared to the other models considered. The information published

Settings	Fit [37]	χMI
Kin2	1.16	0.89
Kin3	0.99	0.84
KinX2	0.82	0.61
KinX3	1.28	1.21

Table 5.4: Values of χ^2/ndf for all the kinematic settings of the Hall-A E00-110 experiment resulting from the extraction on [37] and from the χMI method.

in [37] for the experiment E00-110 are the imaginary and real parts of CFF combinations, without a direct measurement of any of the CFFs independently. These combinations were extracted simultaneously using a combined data-Monte Carlo χ^2 minimization fit to determine the values that give the best agreement between the Monte Carlo predictions and the experimental data using the BKM formalism. The χ^2/ndf values they have obtained from the cross-section fits and the values resulting from the χMI extraction method are given in Table 5.4 for the different kinematic settings of the E00-110 experiment. The χMI extraction method offers improved accuracy with smaller χ^2/ndf values when compared to the Hall-A E00-110 cross-section fits from [37].

Hall-A E07-007 experiment

The E07-007 [38] experiment conducted at Hall-A, had the specific aim of isolating DVCS and DVCS-BH contributions to cross sections and demonstrating the sensitivity of high-precision DVCS data to twist-3 and/or higher-order contributions through a phenomenological study including kinematical power corrections. There are no direct values of the CFFs reported though. This experiment measured cross-sections for three Q^2-values ranging from 1.5 to 2 GeV^2 at $x_B = 0.36$. Each kinematic setting was measured at two incident beam energies. The data were then fitted using a combined fit of two observables, the helicity-independent and the helicity-dependent cross-sections, using the BMMP [155] formalism which incorporates leading-twist and leading-order contributions (LT/LO), higher twist contributions (HT), and next-to-leading order contributions (NLO). Those fits, along with our χMI results, and the KM15* prediction are shown for one kinematic setting at $t = -0.30$ GeV^2 in the top of the right panel of Figure 5.11. The summary of χ^2/ndf values for the Hall-A E07-007 fits utilizing the BMMP formalism from [38] and the χMI method, at three different t settings, are presented in Table 5.5. The χ^2/ndf values indicate that the χMI method provides an improved description of the data when compared to the Hall-A E07-007 fit with BMMP formalism from [38]

$-t$ [GeV^2]	LO/LT	HT	NLO	χMI
0.18	1.20	0.98	0.99	0.77
0.24	1.76	0.99	1.0	0.99
0.30	2.00	0.91	0.91	0.96

Table 5.5: Values of χ^2/ndf for three t bins of the Hall-A E07-007 experiment resulting from the extraction on [38] at LO/LT, HT, NLO and from the χMI method.

Settings	χMI	Settings	χMI	Settings	χMI
Kin-36-1	1.27	Kin-48-1	1.07	Kin-60-1	1.78
Kin-36-2	1.30	Kin-48-2	1.38	Kin-60-2	1.30
Kin-36-3	1.31	Kin-48-3	1.15		
		Kin-48-4	0.97		

Table 5.6: Values of χ^2/ndf resulting from the E12-06-114 helicity-independent cross-section fit with the χMI method for the nine different kinematic settings averaged over t.

in the LO/LT approximations and it is comparable to their fits with HT and NLO corrections.

Hall-A E12-06-114 experiment

The E12-06-114 [39] experiment ran in Hall-A at Jefferson Lab after the 12 GeV upgrade. This experiment measured cross sections at fixed x_B values over a broad range of Q^2, spanning from 2.7 GeV^2 to 8.4 GeV^2, using three distinct electron-energy settings. The aim of the Q^2-dependence measurements was to investigate the contribution of higher-twist terms relative to the leading-twist amplitudes. The cross sections were reported in nine different (Q^2,x_B) kinematic settings, with each setting comprising measurements at 3 to 5 different values of t. The cross sections reported in [39] were fitted simultaneously using the BMMP formalism. They present the first complete extraction of all 4 helicity-conserving CFFs as a function of x_B averaged over t appearing in the DVCS cross-section. We compare with their CFFs results in Section 5.5.3. Figure 5.11, left-bottom plot, displays their fits (red) alongside our fit using the χMI method (cyan) for the specific kinematic setting Kin-48-3 at $t = -0.51$ GeV^2, shown for comparison. They both provide a good description of the data. Table 5.6 shows the obtained χ^2/ndf values of the E12-06-114 helicity-independent cross-section fit with our χMI method for the nine different kinematic settings averaged over t.

VGG	KMS	KM10a	KM10	KM15*	χMI
1.91	1.85	1.46	3.92	1.17	0.76

Table 5.7: Average χ^2/ndf over 110 kinematic bins of the Hall-B e1-DVCS1 helicity-independent experimental data resulting from the theoretical models VGG, KMS, KM10a, KM10 taken from [36] and the KM15* model and our χMI method.

Hall-B e1-DVCS1 experiment

The e1-DVCS1 [36] experiment ran in Hall-B at Jefferson Lab, with 110 finely bins in (Q^2, x_B and t), nevertheless in the same (Q^2, xB, t) bin limits as those used for the Hall-A E00-110 analysis (Q^2 = 2.3 GeV^2, xB = 0.36, and $-t$ = 0.17, 0.23, 0.28 and 0.33 GeV^2) there are larger statistical uncertainties and lack of ϕ-coverage around ϕ = 180°. The e1-DVCS1 experiment accesses the lowest x_B region of all Jefferson Lab data with $0.12 < x_B < 0.47$. Pseudo-data studies (see Section 5.4.2) predict that high precision data with < 5% error is needed to obtain an accurate extraction with the χMI method for their lower x_B spectrum data, i.e., $x_B \lessapprox 0.25$. In [36], well-defined minimizing values for $\Im\mathfrak{m}\mathcal{H}$ and $\Re\mathfrak{e}\mathcal{H}$ are found. We compare their results for $\Re\mathfrak{e}\mathcal{H}$ in Section 5.5.2. They use the local-fitting procedure at leading-twist and leading-order where the two observables, unpolarized and beam-polarized cross sections, are fitted simultaneously. Figure 5.11 (right-bottom) shows the χMI fit to the cross sections for fixed values of Q^2 = 2.78 GeV^2 and x_B = 0.34 at t = -0.45 GeV^2. The BH contribution in this kinematic set is significantly large and the total cross-section is best described by the χMI method. Over the 110 Hall-B data kinematic bins, the average χ^2 per degree of freedom was the smallest for the χMI method (0.76) compared to the theoretical models listed in Table 5.7.

Overall, the χMI method provides the best description of the photon electro-production unpolarized cross-sections for the analyzed experimental data from Hall-A and Hall-B experiments, with the smallest χ^2 per degree of freedom, giving the confidence that the extracted CFFs are realistic. This is remarkable for a local extraction with only one observable, the least constrained one, which brings high expectations on the extraction of CFFs with this technique when further observables are included or its implementation with an ANN approach. Though we take notice of that, as pointed out in Figure 5.1, a good fit of the cross-section data is not sufficient for a reliable extraction of the CFFs. Therefore, in the following sections, we show the direct values of the extracted parameters as a function of the kinematics with the statistical and systematic uncertainties of the extraction obtained as shown in Sections 5.3.2 and 5.4.3. We compare the extracted CFFs $\Re\mathfrak{e}\mathcal{H}$, $\Re\mathfrak{e}\mathcal{E}$,

and $\Re e\widetilde{\mathcal{H}}$ with the results obtained in other references when available.

5.5.2 | $|t|$-dependence

Studying the t-dependence of the CFFs is of great importance since it provides access to the transverse profile of the proton. Figure 5.12 shows the CFFs ReH, $\Re e\mathcal{E}$, and $\Re e\widetilde{\mathcal{H}}$ and the unpolarized DVCS cross-section as a function of t for the Kin3 kinematic setting of the Hall-A E00-110 experiment (left) and for the Hall-B e1-DVCS1 experiment (right) at $Q^2 = 2.10$ GeV^2 and $x_B = 0.30$. The predicted behavior as a function of t by the KM15* model is given by a black line. The statistical errors are given by a line and the systematic errors are represented with a box around the extracted values.

The KM15* that has shown to reproduce the DVCS data, has a reasonable agreement with our extracted parameters using the χMI method. Particularly, we have been able to predict the CFF $\Re e\widetilde{\mathcal{H}}$ and $\Re e\mathcal{E}$ which to the best of our knowledge has not been measured before locally without ANN techniques in the kinematic range accessed by the Jefferson Lab DVCS data, except for the works by F. Georges et. al. [39]. The lack of sensitivity, marked for $\Re e\mathcal{E}$ is given by the H dominance of the DVCS cross-section that is seen in the 2D χ^2 maps of $\Re e\widetilde{\mathcal{H}}$ and $\Re e\mathcal{E}$ as a flat distribution which we are able to constrain after applying the contour cuts.

We compare the extracted CFF $\Re e\mathcal{H}$ with other available local fit results. Kumerički and Müller [53], performed a local fit of the Kin3 kinematic of the Hall-A E00-110 data (black squares). Their extracted values are supported by the extraction with the χMI method within the errors.

Dupré et. al. [9] extracted the CFFs $\Re e\mathcal{H}$ and $\Im m\mathcal{H}$ based on a simultaneous least-squared fitting of the unpolarized and beam-polarized observables by generating an ensemble of fits with randomly distributed start values of CFFs' multipliers. We can determine the CFF $\Re e\mathcal{H}$ on the entire t range of the Hall-A data (left panel) compared to their results (green triangles) that could constrain $\Re e\mathcal{H}$ only at $t = -0.32$ GeV^2 which agrees with our extracted value with the χMI method. On the Hall-B data (right panel) $\Re e\mathcal{H}$ is constrained in the entire t range and they are consistent with the χMI values except for the lowest $t = -0.12$ GeV^2.

Moutarde [171] also provides $\Re e\mathcal{H}$ values extracted with the earlier E00-110 [35] data that contained four t bins (red triangles) between -0.33 and -0.17 GeV^2. Their local fit results are reproduced by the χMI method excluding the low $t = -0.17$ GeV^2 although, the systematic errors of Moutarde's extraction have not been plotted. The same previous experimental data was used in the work of Boër and Guidal [169]

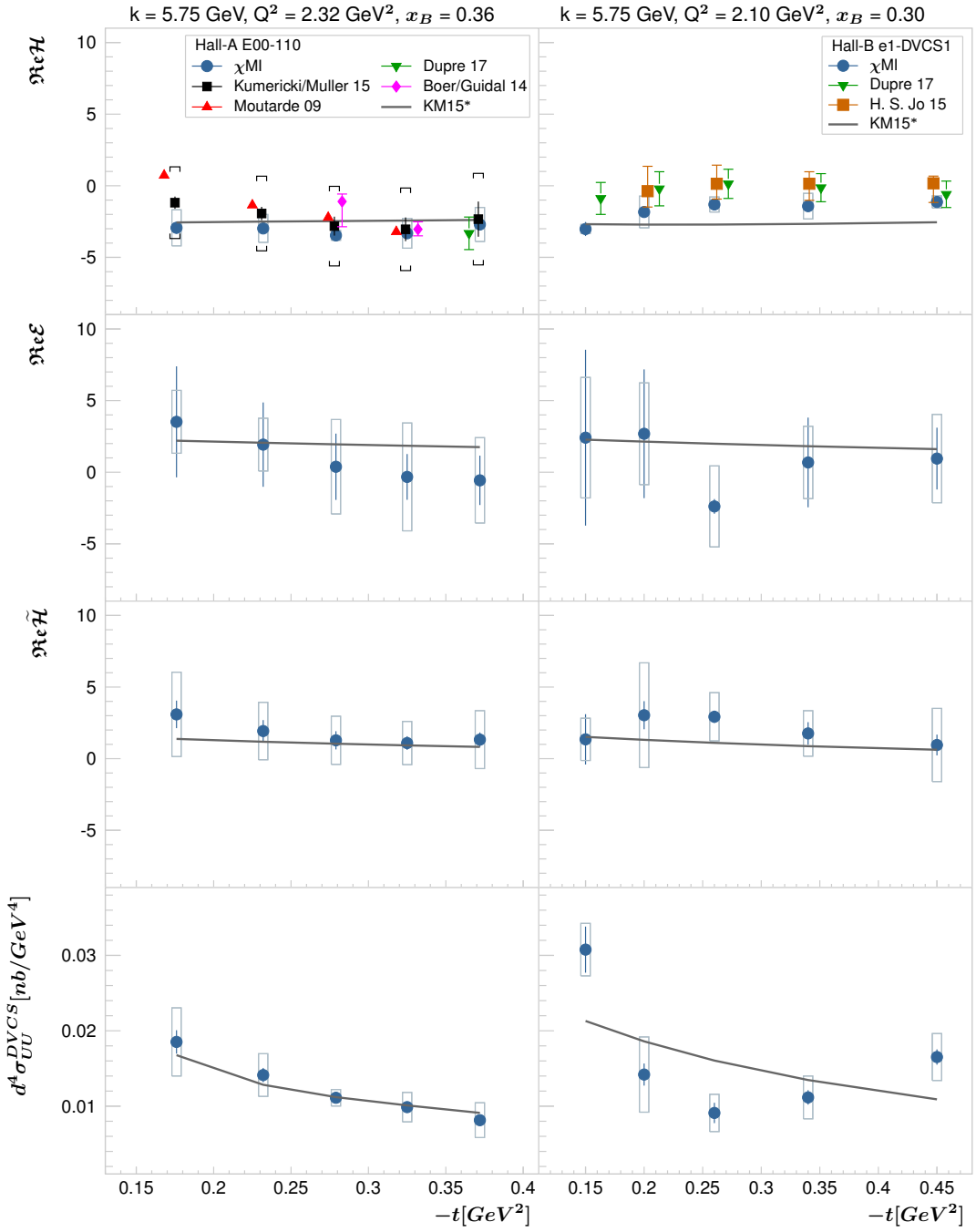

Figure 5.12: Extracted CFFs $\mathfrak{Re}\mathcal{H}$, $\mathfrak{Re}\mathcal{E}$, $\mathfrak{Re}\widetilde{\mathcal{H}}$ and the DVCS cross-section as a function of t for the experiments Hall-A E00-110 (left panel) at Q^2 = 2.32 GeV^2, x_B = 0.36 and Hall-B e1-DVCS1 (right panel) at Q^2 = 2.10 GeV^2, x_B = 0.30. The KM15* model is shown by a black line. The results from Kumerički and Müller [53], Moutarde [171], Boër and Guidal [169], Dupré et. al. [9] and H. S. Jo et. al. [36] are presented for comparison. Some points have been slightly shifted for visibility.

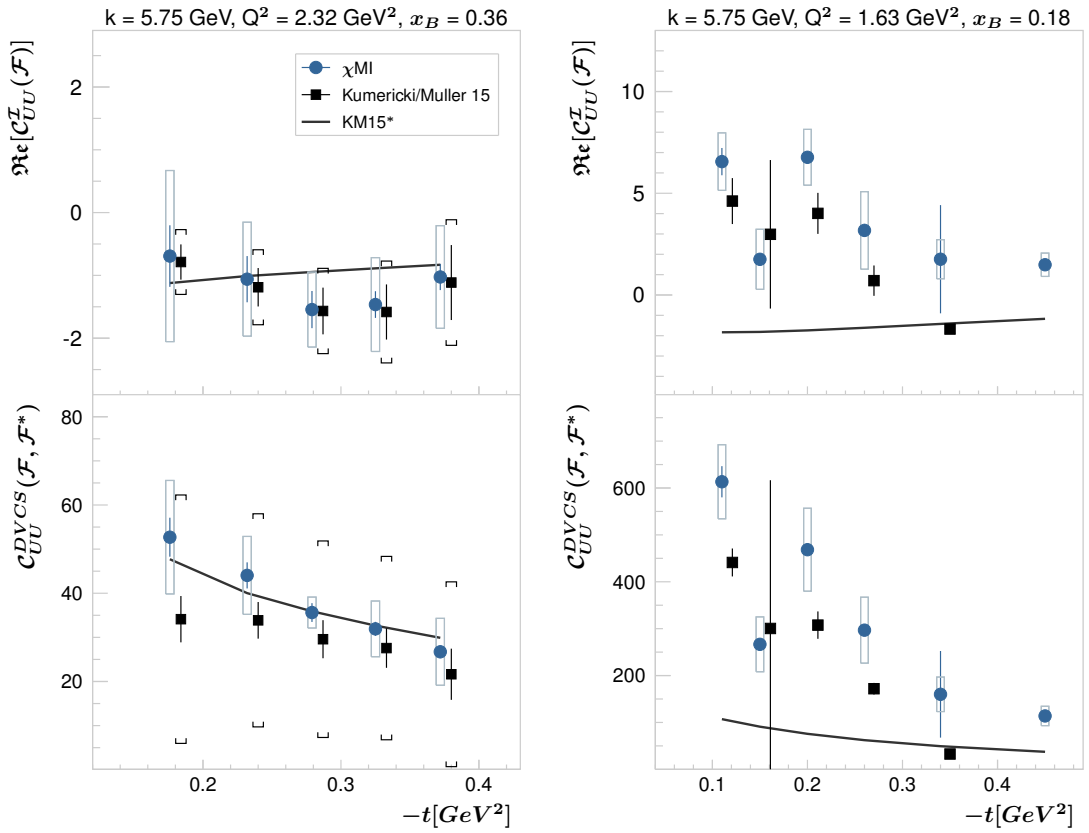

Figure 5.13: Combination of CFFs $\mathfrak{Re}C^{\mathcal{I}}_{UU}(\mathcal{F})$ (top panel), Eq. (5.7), and $C^{DVCS}_{UU}(\mathcal{F},\mathcal{F}^*)$ (bottom panel), Eq. (5.5), as a function of t for the experiments Hall-A E00-110 (left) at $Q^2 = 2.32$ GeV^2, $x_B = 0.36$ and the Hall-B e1-DVCS1 (right) at $Q^2 = 1.63$ GeV^2, $x_B = 0.18$. The results from Kumerički and Müller [53] (black squares) have been slightly shifted for visibility. The KM15* is shown alongside (black line).

with a similar least-squared method followed by Dupré et. al. In [169], they were able to constrain $\mathfrak{Re}\mathcal{H}$ at two kinematic sets (magenta diamonds) that are in agreement with the values we obtained with the χMI method. They were not able to constrain though $\mathfrak{Re}\mathcal{H}$ with the Hall-B dataset.

Within the errors, the results from the Hall-B e1-DVCS1 publication [36] (orange squares) for the CFF $\mathfrak{Re}\mathcal{H}$ that simultaneously fits the unpolarized and beam-polarized cross-sections, are also in agreement with our extraction.

In Figure 5.12, we selected similar kinematics for the Hall-A and the HAll-B experiments as an example to show that no unexpected discrepancies between Halls A and B measurements are found which is consistent along their common kinematic range. This exercise implies that both sets of data are consistent and can be used in a global fit.

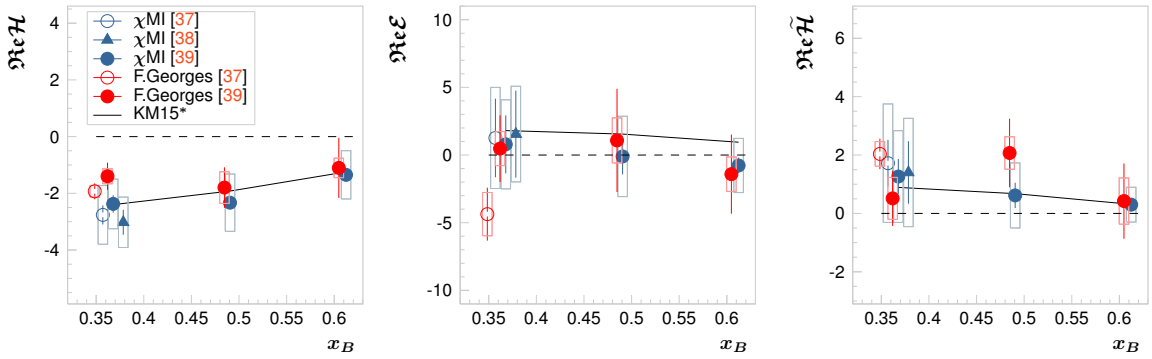

Figure 5.14: Extraction of the CFFs $\mathfrak{Re}\mathcal{H}$ (left), $\mathfrak{Re}\mathcal{E}$ (center) and $\mathfrak{Re}\widetilde{\mathcal{H}}$ (right) from the χMI method (blue) and from F. Georges et.al. [39] (red) as a function of x_B averaged over t and Q^2. The results are extracted from the Hall-A datasets E00-110 [37] (empty circle), E07-007 [38] (triangle) and E12-06-114 [39] (circle) with the χMI method and from the Hall-A datasets E00-110 [37] (empty circle) and E12-06-114 (circle) [39] in F.Georges et. al. The average t values are -0.281 and -0.258 GeV^2 for the experiments E00-110 and E07-007 respectively at $x_B = 0.36$. The average t values for the experiment E12-06-114 are -0.345, -0.702, -1.050 GeV^2 at $x_B = 0.36$, 0.48, 0.60, respectively. Some points have been slightly shifted for visibility.

Since determining all the CFFs is an underconstrained problem, it is also useful to extract the imaginary and real parts of the CFF combinations $C^{\mathcal{I}}(\mathcal{F})$ and the bilinear form $C^{DVCS}(\mathcal{F},\mathcal{F}^*)$. In the unpolarized case, we compute $\mathfrak{Re}C^{\mathcal{I}}_{UU}(\mathcal{F})$ from Eq. (5.7) substituting the extracted CFFs $\mathfrak{Re}\mathcal{H}$, $\mathfrak{Re}\mathcal{E}$ and $\mathfrak{Re}\widetilde{\mathcal{H}}$ and compare it with the results from Kumerički and Müller [53] on the top panel of Figure 5.13 for the Kin3 setting of the Hall-A E00-110 (left) and for the Hall-B e1-DVCS1 experiment (right) at $Q^2 = 1.63$ GeV^2 and $x_B = 0.18$. With the extracted unpolarized DVCS cross-section parameter, e.g. see the bottom panel of Figure 5.12, we can compute $C^{DVCS}_{UU}(\mathcal{F},\mathcal{F}^*)$ from Eq. (5.5) that is shown on the bottom panel of Figure 5.13 for Hall-A (left) and Hall-B (right) at the same kinematics as the top panels. Our results for the CFFs combination forms are consistent in the Hall-A kinematic shown (left). There are larger deviations between our results with [53] for the Hall-B kinematic set (right) however they mention these fit results on the Hall-B data are underestimated.

5.5.3 | x_B-dependence

The first complete extraction of all helicity-conserving CFFs appearing in the DVCS cross-section was done in the Hall-A E12-06-114 publication from F. Georges et. al. [39]. Two observables are fit in F. Georges et. al. work, the unpolarized

and beam-polarized cross-section using the BMMP formalism [155] that included target mass corrections. All kinematic bins in Q^2 and ϕ at constant (x_B, t) are fit simultaneously. Given the larger Q^2 coverage of the E12-06-114 experiment, the sensitivity to the CFFs $\mathcal{E}$ and $\widetilde{\mathcal{E}}$ arises from the Q^2-dependent kinematic factors weighting these terms relative to the contribution of $\mathcal{H}$ and $\widetilde{\mathcal{H}}$. They provide the only source of comparison for the CFFs $\Re\mathrm{e}\mathcal{E}$ and $\Re\mathrm{e}\widetilde{\mathcal{H}}$ from a local least-squares fit at the Hall-A kinematics.

In Figure 5.14, we compare our extracted parameters (blue) with the results from F. Georges et. al. [39] (red) as a function of x_B averaged in t, including the poorly known $\Re\mathrm{e}\mathcal{E}$. The theoretical prediction from the KM15* model is shown as a black line, which shows a reasonable agreement with both results. The resulting CFFs with the Hall-A E00-110 [37] were also calculated at the available $x_B = 0.36$ with average $t = -0.281$ GeV^2 (empty circles). We have also included the results using the Hall-A E07-007 [38] that was also measured at $x_B = 0.36$ with an average $t = -0.258$ GeV^2 (triangles). We find the extracted CFFs $\Re\mathrm{e}\mathcal{H}$, $\Re\mathrm{e}\mathcal{E}$ and $\Re\mathrm{e}\widetilde{\mathcal{H}}$ to be consistent with their results. These measurements therefore demonstrate that the full extraction of the CFFs $\Re\mathrm{e}\mathcal{H}$, $\Re\mathrm{e}\mathcal{E}$ and $\Re\mathrm{e}\widetilde{\mathcal{H}}$ is within reach with the χMI method at leading order and leading twist in the least constrained helicity-independent cross-section observable.

The first moment sum rules relate the GPD $\widetilde{H}$ (summed over quark flavor q) to the axial form factors G_A of the proton:

$$\sum_q \int_{-1}^{1} \widetilde{H}_q(x, \xi, t) dx = G_A(-t). \tag{5.19}$$

GPD $\widetilde{H}$ can be described as momentum decompositions of the corresponding form factor $\widetilde{\mathcal{H}}$, see Eq. (1). Therefore, the present measurement of the CFF $\Re\mathrm{e}\widetilde{\mathcal{H}}$ in this study can complement other measurements on the form factor G_A, which is less well known experimentally than the usual electromagnetic form factors $G_{E,M}$ and therefore provide constraints on the quark momentum distribution support of the corresponding form factors within this x_B range.

5.5.4 | Q^2 evolution

For fixed target kinematics, where Q^2 lever arm is rather limited, the Q^2 evolution on the GPDs is generally dropped since one may rely on the so-called scaling hypothesis, i.e., on the assumption that the GPD does not evolve under the change of the photon virtuality. Here we check the veracity of this assumption in the

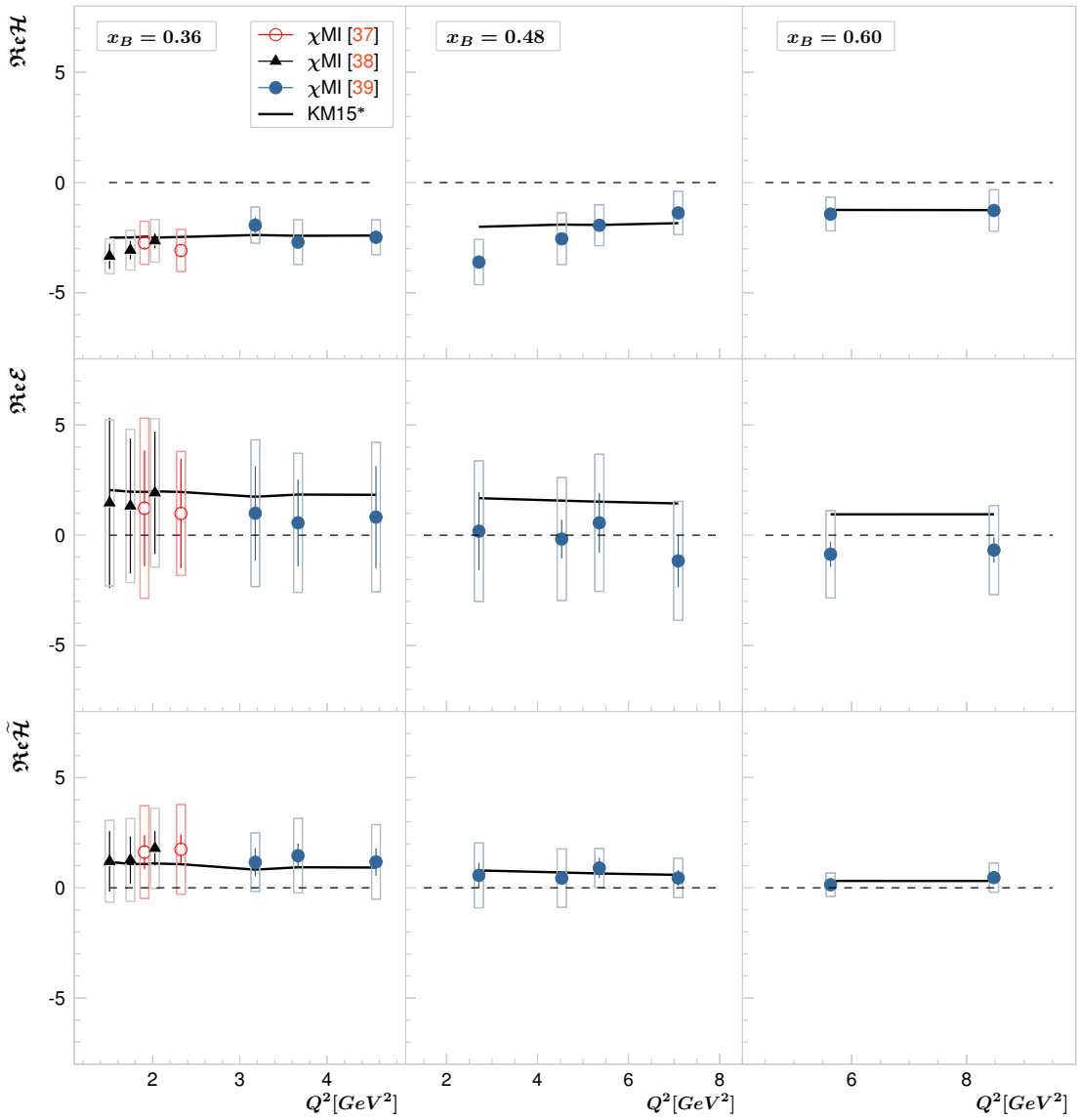

Figure 5.15: Q^2 dependence of the extracted CFFs with the χMI method averaged in t for the Hall-A experiments E00-110 (red), E07-007 (black) and E12-06-114 (blue) for the x_B values 0.36 (left), 0.48 (center) and 0.60 (right).

Hall-A kinematics. Figure 5.15, displays the Q^2 dependence of the extracted CFFs averaged in t for the Hall-A experiments E00-110 (red), E07-007 (black) and E12-06-114 (blue) for the x_B values 0.36 (left), 0.48 (center) and 0.60 (right). Additionally, with the new Hall-A data after the Jefferson Lab 12 GeV upgrade, we can gain insight into the Q^2 dependence in a larger region. The KM15* model which does not include Q^2 evolution on the GPDs is shown alongside for reference and it is computed for each experimental Q^2 value at the corresponding average t.

Overall, the extracted CFFs exhibit little or no dependence on Q^2 within the

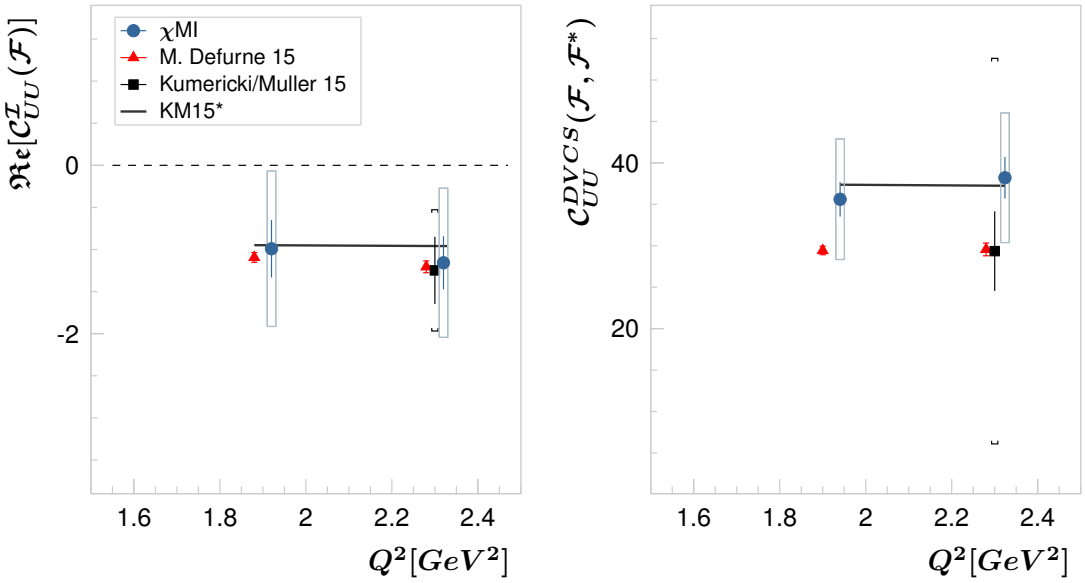

Figure 5.16: CFFs combinations $\Re eC^{\mathcal{I}}_{UU}(\mathcal{F})$ (left) and $C^{DVCS}_{UU}(\mathcal{F},\mathcal{F}^*)$ (right) as a function of Q^2 at xB = 0.36 and integrated over t with the χMI method (blue). For comparison, the results from M. Defurne et. al. [37] (red triangles), Kumerički and Müller [53] (black squares), which have been slightly shifted for visibility, and the KM15* (black line) model prediction are shown alongside. Here the systematic error from [37] is left out.

range of Q^2 values shown in the figure. This slow Q^2-evolution of the extracted CFFs indicates that this kinematic region is suitable for an analysis under the scaling hypothesis. Nevertheless, we observe a sizeable scaling deviation on $\Re e\mathcal{H}$ extracted from the HAll-A E12-06-114 data for $x_B = 0.48$ which expands the largest Q^2 range but is compatible with the scaling hypothesis within the errors.

For comparison with the results from M. Defurne et. al. [37], we show in Figure 5.16, the CFFs combinations $\Re eC^{\mathcal{I}}_{UU}(\mathcal{F})$ and $C^{DVCS}_{UU}(\mathcal{F},\mathcal{F}^*)$ as a function of Q^2 at xB = 0.36 and integrated over t. The result from Kumerički and Müller [53] for the Kin3 setting of the Hall-A E00-110 experiment is also shown along with the KM15* model prediction. No Q^2 dependence is observed for these CFFs combinations and the logarithmic Q^2–evolution can safely be neglected within this Q^2 lever arm at this x_B.

DNN extraction techniques 6

We have extracted the CFFs from unpolarized photon leptoproduction cross-sections from Halls A and B experiments using a novel χ^2 mapping, the χMI method. This novel method describes the experimental helicity-independent data and shows that accessing the CFFs $\mathfrak{Re}\mathcal{H}$, $\mathfrak{Re}\mathcal{E}$ and $\mathfrak{Re}\widetilde{\mathcal{H}}$ in the least constrained observable case is possible at LO and LT. In this Chapter, we introduce an improved Deep-Neural Technique for the extraction of the CFFs.

Neural networks, specifically Deep-Neural Networks (DNNs), are ideal for function approximation which can be rigorously provable through, the Universal Approximation Theorem [174, 175]. The extraordinary capacity of DNNs to approximate complicated functions so well is why they are preferred over other machine learning (ML) approaches for information extraction and modeling. The existence of a function implies that DNNs can be used to represent it and work with it without actually knowing the function form. With such a high level of abstraction, one can use data and make assessments not otherwise possible, even given an arbitrary degree of complexity. The approach we use, like others, [156, 172], uses the BKM10 formalism (see Section 5.1) in the loss function during the process of backpropagation of error. However, our method connects data from different kinematics within the same DNN model, unlike traditional local fits. This builds a representation of the CFFs as a function of the kinematics across the phase space of the data in the fit providing the ability of interpolation while also reducing extraction error and increasing accuracy. Experimental error is propagated using the common bootstrap approach leading to a generalized multivariate inference over the local fitting domain.

In this chapter, we perform a traditional ANN local fit, Section 6.1, and then focus on the new extraction method, a local multivariate inference (LMI) using DNNs, and demonstrate its utility, Section 6.2. Another critical advancement in the extraction process is the use of an iteratively improved generating function to produce the pseudodata in the testing phase, Section 6.2.1. As this generating function is improved by the information extracted from the experimental data it

can be used to successively enhance the DNN optimization to then improve the DNN fit to experimental data. A global CFFs model is illustrated in Section 6.3, where a DNN is trained using the extracted parameters from the χMI technique to predict the CFFs at any kinematic set.

6.1 | Standard local fitting with DNNs

The objective of the local fit is to determine the CFFs for specific kinematic settings (Q^2, x_B, t) without relying on information or correlations from any other part of phase space. This approach establishes a direct relationship between the CFFs and observables, circumventing the need for a GPD model. In this section, we will only focus on a standard local DNN extraction of CFFs. As in the χMI method, the first step is to use the generated pseudo-data, Chapter 4, to estimate the accuracy and precision expected when applying the same steps to the real experimental data. We will refer to the generated pseudo-data as *pseudo-data 1*.

For the best representation of the propagated uncertainty, a high number of replicas must be used. For the initial test, 1,000 replicas are generated by randomly sampling within the experimental errors of the calculated pseudodata cross-section at each experimental data point across ϕ. The experimental errors on the pseudodata reproduce the reported uncertainties of the Halls A and B experiments used in this work [36–39], on each kinematic set of the experiments mimicked by the pseudodata. The distribution of the error is approximated as a Gaussian with variance based on the combination of both statistical and systematic experimental uncertainty. Each replica data set is then fitted independently resulting in 1,000 sets of CFFs. The mean of these distributions provides the extracted CFFs, with the difference between the mean and the true value from the pseudodata generator indicating the accuracy, Eq. (6.1). The standard deviation of the extracted CFF distributions provides the precision, Eq. (6.2), and is a combination of propagated experimental uncertainty and the additional algorithmic (fitting) error.

$$\epsilon(x_B, t, Q^2) = \left(1 - \left|\frac{CFF_{true} - CFF_{DNN}}{CFF_{true}}\right|\right) \times 100\%, \tag{6.1}$$

$$\sigma(x_B, t, Q^2) = \sqrt{\frac{\sum_i \left(CFF^i_{DNN} - \overline{CFF}_{DNN}\right)^2}{N}}. \tag{6.2}$$

This definition for accuracy, ϵ, is only meaningful if the difference between the DNN distribution of extracted Compton form factors, CFF_{DNN}, and the true Compton form factor, CFF_{true} is less than 1. For very poor accuracy where this difference is large, we use multiples of the precision, σ to indicate the proximity to the true value.

A basic feed-forward neural network architecture is used which reads in three normalized kinematic variables. The initial kinematic variables are $v = (Q^2, x_B, t)$ which are normalized using:

$$v' = -1 + 2\frac{v - v_{min}}{v_{max} - v_{min}}, \tag{6.3}$$

such that $v' = (Q'^2, x'_B, t')$. The values of v_{min} and v_{max} for each variable are listed in Table 6.1. Normalizing the data ensures that the features have a similar scale which can help the optimization algorithm converge faster during training. This also helps to prevent vanishing or exploding gradients, which can hinder the training process. Normalizing the data makes the model more independent of the units used for the input features by keeping the features within a specific range which helps prevent large weights from dominating the learning process.

Kinematics (v)	v_{min}	v_{max}
Q^2	0	10.0
x_B	0	0.8
t	-2.0	0

Table 6.1: The v_{min} and v_{max} values used for normalizing three input variables (Q^2, x_B, t).

Each hidden layer is comprised of 100 neurons with a select activation function used at each layer determined by analyzing the model and validation loss during the training process. The activation functions used are *Linear* (hidden-layer 1), *Tanhshrink* (hidden-layers 2 and 3), and *Tanh* (hidden-layer 4). The activation function Tanhshrink has been previously determined to enhance network performance for similar architectures [176]. The Tanhshrink function is defined as,

$$\text{Tanhshrink}(x) = x - \tanh(x). \tag{6.4}$$

Additionally, our own testing indicates that Tanhshrink accelerates the minimization of the loss function significantly. Each activation, number of layers, and nodes are ultimately determined through a systematic process of trial and error.

The loss function is denoted as $L(v', \theta)$, where v' represents the normalized-input kinematics and θ denotes the output variables, which include $\Re e\mathcal{H}$, $\Re e\mathcal{E}$, $\Re e\widetilde{\mathcal{H}}$, and the DVCS cross-section. This function is calculated by taking the square of the differences between the inferred unpolarized photon leptoproduction cross-section (σ^{DNN}), see Section 5.1, and the sampled (pseudo-) data cross-section (σ^{data}), and deciding by the square of the experimental uncertainty (δ) for that ϕ bin i, and averaged over the number of total ϕ bins N for each kinematic setting,

$$L(v', \theta) = \frac{1}{N}\sum_{i=1}^{N}\frac{(\sigma_i^{DNN} - \sigma_i^{data})^2}{\delta_i^2}. \tag{6.5}$$

The experimental sampled cross-section, (σ^{data}), is replaced by the sampled pseudo-data points when testing the DNN fitting technique with the generated pseudo-data based on the BKM10 DVCS formulation and the KM15* GPD model, as described in Chapter 4.

A standard optimizer with adaptive moment estimation was employed, Adam [177], to adjust the weights through backpropagation during each epoch with an initial learning rate of $\alpha = 0.00025$. Adam uses an efficient stochastic optimization that only requires first-order gradients with little memory demand. Adam adjusts the learning rate automatically, but such ability is limited so careful prototyping is required and the initial learning rate remains a key hyperparameter. A maximum of 1500 epochs were used with a batch size of 30.

The three CFFs and the DVCS cross-section are extracted for all kinematic points used in the data set to test the extraction method. Figure 6.1 shows an example of the local fit for the extracted $\Re e\mathcal{H}$ values from the pseudo-data for the 1000 replicas. The left plot shows the cross-section fitted for $Q^2 = 1.96$ GeV^2, $x_B = 0.38$, and $t = -0.28$ GeV^2, represented by solid lines. The light-colored error bands surrounding the fitted curves correspond to the 68% confidence level. In the right plot, the distributions of $\Re e\mathcal{H}$ resulting from each replica fit on the aforementioned kinematic setting are shown. The mean of each distribution, depicted as the red vertical line, represents the extracted value of $\Re e\mathcal{H}$, while the true value is denoted by the blue vertical line. This example is representative of the overall results of the DNN local fits. For most of the pseudodata fit results, the true values are within 2σ.

Preliminary pseudo-data investigations have shown that while the DNN local fit method allows for satisfactory extraction, achieving highly accurate extraction remains a challenge, notably for $\Re e\widetilde{\mathcal{H}}$ and $\Re e\mathcal{E}$ where the deviations are up to 2σ even when the fit visually seems excellent across the ϕ distribution of data points.

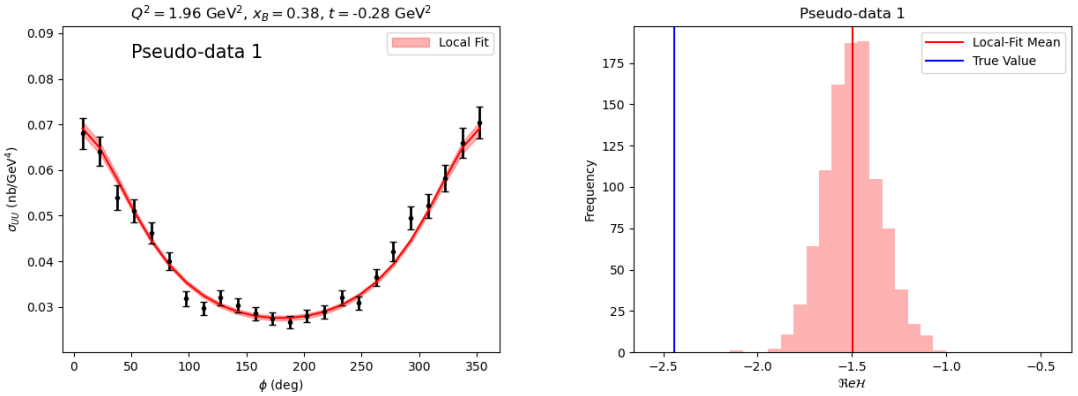

Figure 6.1: An example of the local fit result from pseudodata 1 (generated using the KM15* model): cross-section fit represented by the solid line surrounded by light-colored error bands correspond to the 68% confidence level (left), the distributions of $\Re e\mathcal{H}$ resulting from each replica fit (right).

This underscores our previous well-documented limitation of local fitting methods, see Figure 5.1, which is that a visually good fit in ϕ does not ensure the accurate extraction of CFFs. This can be attributed to issues like local minima and the absence of uniqueness, problems that can arise in both DNN and χ^2 minimization fitting.

To check the consistency of the DNN extraction method, we have generated a second pseudo-data set (pseudo-data 2) using the following *basic* model-generating function:

$$G(x_B, t) = (ax_B^2 + bx_B)e^{ct^2+dt+e} + f, \tag{6.6}$$

where $G(x,t)$ represent the CFF and the DVCS cross sections ($\Re e\mathcal{H}$, $\Re e\mathcal{E}$, $\Re e\widetilde{\mathcal{H}}$, σ_{UU}^{DVCS}), with parameters $\{a, b, c, d, e, f\}$ for each case shown in Table 6.2. The *basic* model for each CFF is parameterized using fits to real experimental data.

The precision obtained with pseudo-data 2 is comparable to pseudo-data 1 but the accuracy is better for the extraction with the *basic* model pseudodata where the true values are on average within 1σ for 80% of the data compared to the KM15* model pseudodata that resulted in most of the true values within 2σ. The DNN models have the same architecture and similar hyperparameters including the number of epochs.

These studies shed light on an important aspect: an extraction method and DNN architecture that excels with one pseudodata set might not perform as well with another, even under identical kinematics. This is particularly true when these datasets represent different scales of CFFs. Consequently, assessing a method's efficacy across multiple pseudodata sets becomes paramount. This ensures not just

CFFs	a	b	c	d	e	f
$\Re e\mathcal{H}$	-4.41	1.68	-9.14	-3.57	1.54	-1.37
$\Re e\mathcal{E}$	144.56	149.99	0.32	-1.09	-148.49	-0.31
$\Re e\widetilde{\mathcal{H}}$	-1.86	1.50	-0.29	-1.33	0.46	-0.98
σ_{UU}^{DVCS}	0.50	-0.41	0.05	-0.25	0.55	0.166

Table 6.2: The parameters used in equation 6.6 to generate the second pseudodata data set.

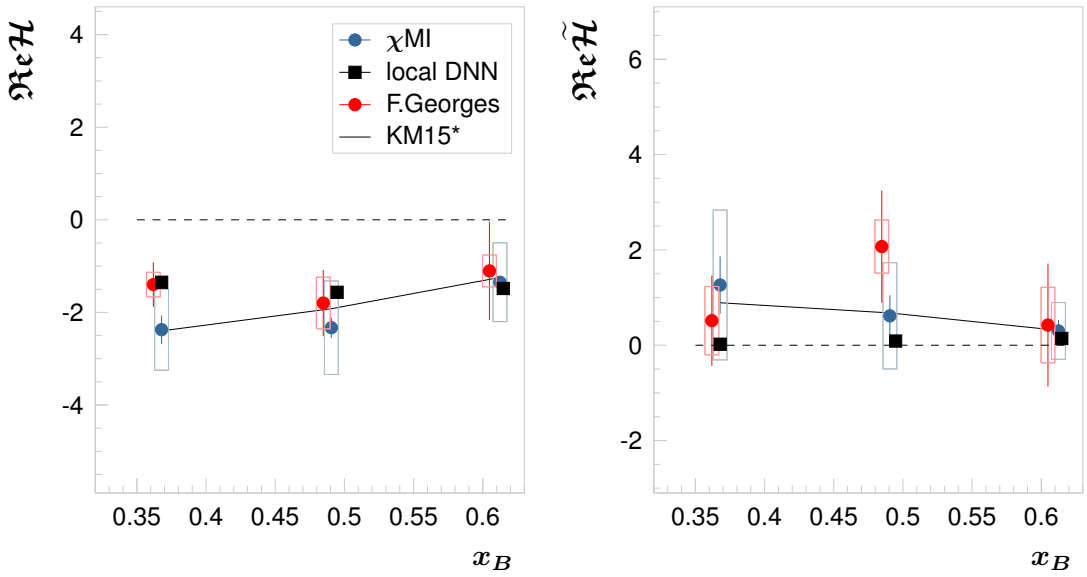

Figure 6.2: Extraction of the CFFs $\Re e\mathcal{H}$ (left) and $\Re e\widetilde{\mathcal{H}}$ (right) from the local DNN fit (black), the χMI method (blue) and from F. Georges et.al. (red) as a function of x_B averaged over t and Q^2. The results are extracted from the Hall-A dataset E12-06-114. The average t values are -0.345, -0.702, -1.050 GeV^2 at x_B = 0.36, 0.48, 0.60, respectively.

its consistency but also robustness. It provides a better estimate of the expected systematic uncertainties inherent in the extraction procedure. Lastly, employing pseudodata that closely mimics the actual experimental data is imperative, as deviations can lead to successful extraction from well-tested pseudodata but suboptimal results when applied to the genuine experimental dataset using the same extraction steps.

The extracted results using the standard local DNN fit for the Hall-A E12-06-114 experimental cross-sections as a function of x_B averaged in t are shown in Figure 6.2 for $\Re e\mathcal{H}$ (left) and $\Re e\widetilde{\mathcal{H}}$ (right). The theoretical prediction from the KM15* model is shown as a black line. The results from F. Georges et. al. [39] (red) and from

our χMI method (blue) are shown alongside for comparison. The error is reduced from the local DNN fit and it is still consistent with the previous Hall-A fits [39] and with the χMI extraction.

Further refinement can be made with careful tuning and optimization of the DNN architecture and hyperparameters. However, only slight improvements are possible without additional information, data, or constraints when using this standard local fitting method. We now turn our attention to the Local Multivariate Inference (LMI).

6.2 | Local Multivariate Inference with DNNs

One of the major differences between the local fit and LMI is the range of kinematics and as a result, the number of data points used in the fitting process, indicated by N in Eq. (6.5). In the standard local-fit method, the CFFs are extracted for each (Q^2, x_B, t) bin independently, with N representing the number of ϕ bins at a fixed Q^2, t, and x_B. In contrast, with LMI the CFFs are extracted for all data points simultaneously utilizing all ϕ bins across all kinematics, with N representing the total number of ϕ data points in the entire data compilation. The data compilation may include multiple data sets from multiple experiments. The LMI method better leverages the DNN technology reducing model error and providing interpolation by combining isolated kinematics as a collection of data with phase space sensitivity rather than a collection of local fits that are analyzed separately at fixed kinematics. The level of information that is possible to extract from traditional local fits will always be limited due to data sparsity and the binning choice. The LMI method has a distinct advantage when using sparse data by training with the full data available resulting in multidimensional generative feature inference between the fixed kinematic points. Obviously, more information could be obtained with this method if the raw data is available and the data could be iteratively rebinned to progressively enhance the model and the resulting inference.

To demonstrate the utility of LMI, we employ the same DNN architecture and hyperparameters used in the local-fit approach, Section 6.1, such that only the data input scheme and training process are changed. A comparison is made between the resulting CFFs and the cross-section with the true values used to generate the pseudo-data 1, i.e. KM15* GPD model. The results for $\mathfrak{Re}\mathcal{H}$ are shown in Figure 6.3 (left). Just by changing this training process to the LMI method, there is a significant improvement. A comprehensive comparison of the local versus the

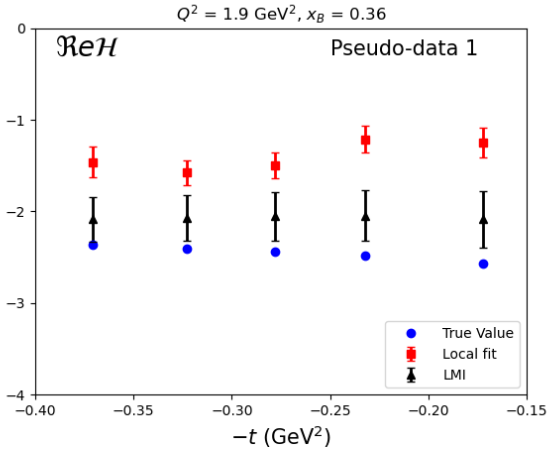

Figure 6.3: The $\Re e\mathcal{H}$ results from the standard local DNN fit (red) and the LMI (black) for the Kin3 setting of the Hall-A E00-110 experiment. The *true* values of the generated pseudo-data 1 are shown with blue markers.

LMI extraction using the generated pseudo-data sets showed that roughly 50% of the kinematic bins increase in accuracy for each CFF. In some cases for pseudo-data 1, the distribution of the CFFs gets broader as no special consideration is given to tuning for a better fit so that a direct systematic comparison can be made for the training style alone. With additional hyperparameter optimization precision also increases by about 10% for pseudo-data 1.

The LMI training method demonstrates a clear advantage by leveraging the collective information from the entire phase space simultaneously. The LMI method has considerable flexibility and is well-suited for further optimization and extraction enhancement which will be discussed in detail in the subsequent section.

6.2.1 | Generating function improvement

To more broadly demonstrate LMI effectiveness, we use it as part of a multi-step extraction schema tested on a third pseudodata set, designed to closely mimic real experimental data. This necessitates the development of an iteratively improved generating function for producing quality pseudodata to help better optimize the DNN architecture and hyperparameters. This crucial step ensures that the hyperparameters are appropriately tuned for optimal extraction specific to this specialized pseudodata, which is ultimately near indistinguishable from the real experimental data it is based on. The schema also provides a means to quantify the expected accuracy of the extraction when performed on the real experimental data in the final step.

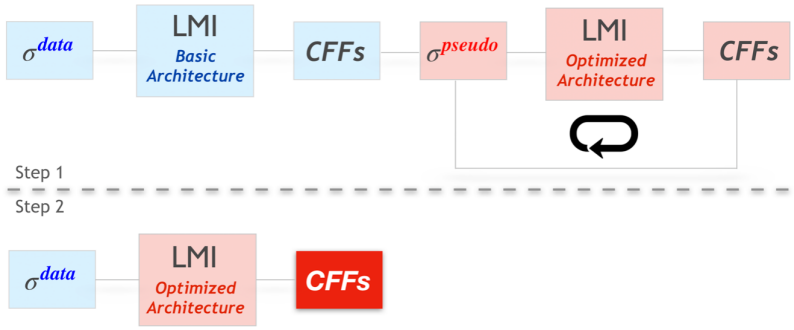

Figure 6.4: Schematic representation of the R-LMI method.

The process of refining the generating function can be described as two distinct steps that can be subsequently iterated for successive improvement. The first step is using an LMI fit to the experimental data then taking the central value of the resulting model as the generating function to produce pseudodata. The next step is to use that new pseudodata to optimize the LMI DNN for the best extraction, and then refit the experimental data. This optimization could be changing the architecture completely or just re-tuning some or all of the hyperparameters. These steps are schematically illustrated in Figure 6.4.

In the first fit to the full data set, we apply the LMI method to the experimental data using the same basic architecture as employed during the standard local extraction described in Section 6.1. The resulting model is then used to generate the pseudodata needed to redesign the architecture and tune the hyperparameters of the new DNN to achieve the best accuracy, Eq. (6.1), and precision, Eq. (6.2) of the extraction. Next, we employ the enhanced architecture and hyperparameters that were optimized during the first fit and perform another LMI fit to the experimental data to achieve an improved fit. Again, the central value of the distribution of resulting CFFs is used to generate a set of new and improved pseudodata which is a better representative of the experimental data. This improved pseudodata data will hold features and trends across phase space that the previous iteration of pseudodata did not. To optimally enhance the sensitivity of the extraction to these changes the architecture should be redesigned and the hyperparameters reoptimized to further improve both the accuracy and precision.

The process of LMI fitting, improving the generating function and using the results to improve the fit again is done recursively until no further change is seen in the resulting mean and width of the CFFs distributions. We refer to this technique as *recursive* LMI (R-LMI).

The R-LMI schema ensures that the hyperparameters are finely tuned to op-

timally extract information from the real experimental data while progressively improving the generating function to better test the extraction quality for the specialized DNN. At each stage of DNN improvement, there is necessarily a degree of variation required to re-tune the architecture and hyperparameters to improve the quality metrics. Some minor variations in the number of layers and neurons are studied through fast prototyping by hand and then automated to explore a larger possible hyperparameter space. This schema coincides with the premise that once information is extracted from the experimental data, it should be incorporated into the pseudodata generator used for testing and optimizing the extraction tools. DNN's in general are so highly tunable that once a better representation of the experimental data is available the architecture and hyperparameters can and should be optimized again to better implicitly capture all salient features resulting in a better fit but also a better generator to produce pseudodata for more rigorous testing. With each successive iteration, the CFFs shift closer to the true values until they stabilize at which point no further incremental improvement can be achieved and the CFF means of the different families of models will oscillate around a limit that defines the scale of the systematic error in the extraction. This limit is typically on the scale of the propagated experimental error so once the difference between the two iterations is smaller than the Gaussian width of the CFF distribution little improvement can be expected and the iteration process can stop.

We first demonstrate this technique by going through the complete schema using pseudodata produced using KM15* so we can clearly show its functionality using a concrete model with the clear goal of extracting the CFF values that were put into producing the data. The steps in this regard use KM15* to produce pseudodata for a set of bins over the kinematic range of the experimental data. Then an initial LMI DNN fit is performed using the same architecture described for the standard local fit and the results are used to generate the pseudodata that will be used to improve the architecture and hyperparameters. This sequence is performed recursively until the generator values no longer change and the extracted CFFs are stable. In this example, only the number of epochs and the batch size are changing. These final CFFs are then compared to the original true CFFs from KM15* for those kinematics. The resulting R-LMI model of the interpolated phase space is also compared to the original KM15* model. This is shown in Figure 6.5, where we present the LMI fit for kinematic bins corresponding to the experimental data of the Hall-B e1-DVCS1 experiment. The extracted CFFs for the pseudodata 1 (KM15*) are obtained after five iterations of the R-LMI schema.

Having identified the optimal DNN architecture and parameterization through

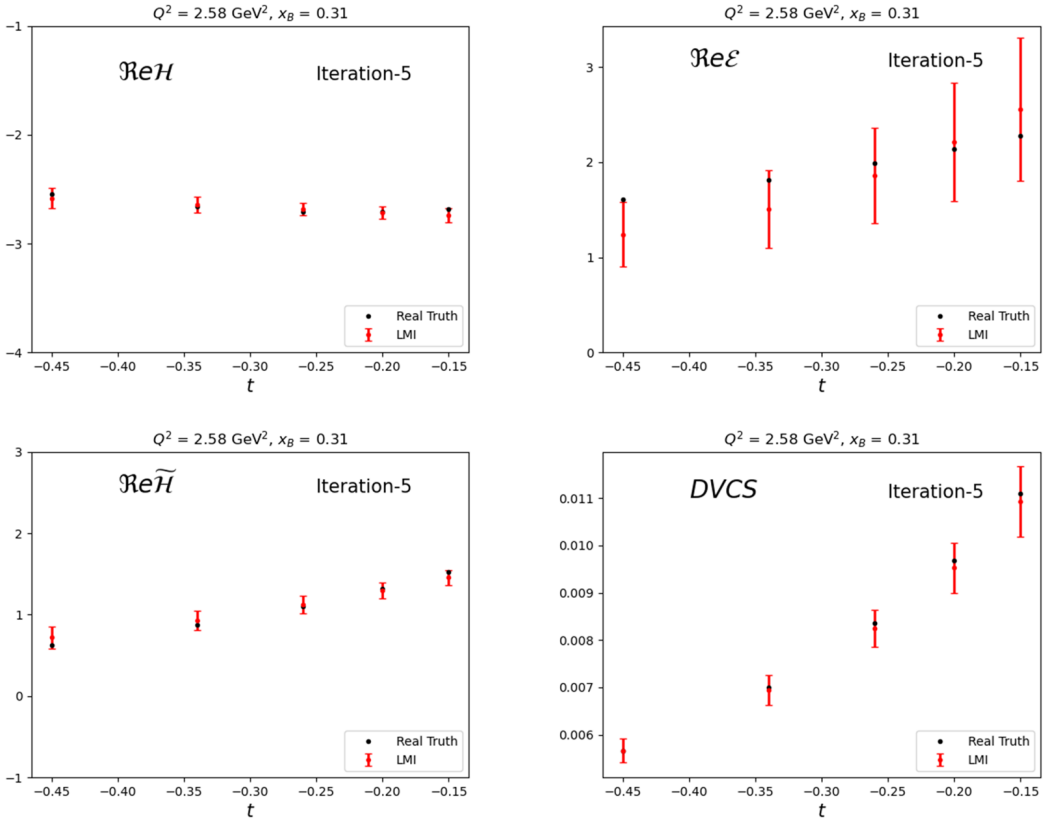

Figure 6.5: The R-LMI extracted values of $\Re e\mathcal{H}$(top left), $\Re e\mathcal{E}$(top right), and $\Re e\widetilde{\mathcal{H}}$(bottom left) and the DVCS cross-section (bottom right) are presented for pseudodata 1 (KM15*). These results are based on the pseudodata generated specifically for Hall-B kinematics.

the R-LMI schema, we subsequently deploy the same architecture to extract the CFFs from the experimental data presented in Table 4.2. After the R-LMI extraction process and successive pseudodata generator improvements, the resulting pseudodata will have very similar CFFs as the real experimental data so estimating the expected accuracy of extraction on the experimental data becomes feasible using the final version of the generator. The difference between the penultimate CFFs and final iteration CFFs is one sample of the systematic deviation. A comparison of the obtained results with the R-LMI and the χMI techniques along with the results from F. Georges et al. [39] are shown in Figure 6.6 where these novel techniques consistently extracted the CFFs within the errors.

Figure 6.7, shows an example of the extracted CFF $\Re e\mathcal{H}$ with the R-LMI from the Halls A and B experimental data and extrapolated to the HERMES [30] kinematics over ξ at $t = -0.2$ Gev^2 (left) and $t = -0.02$ Gev^2 (right), in order to compare with the results from Kumerički et. at. [156] that were obtained from HERMES

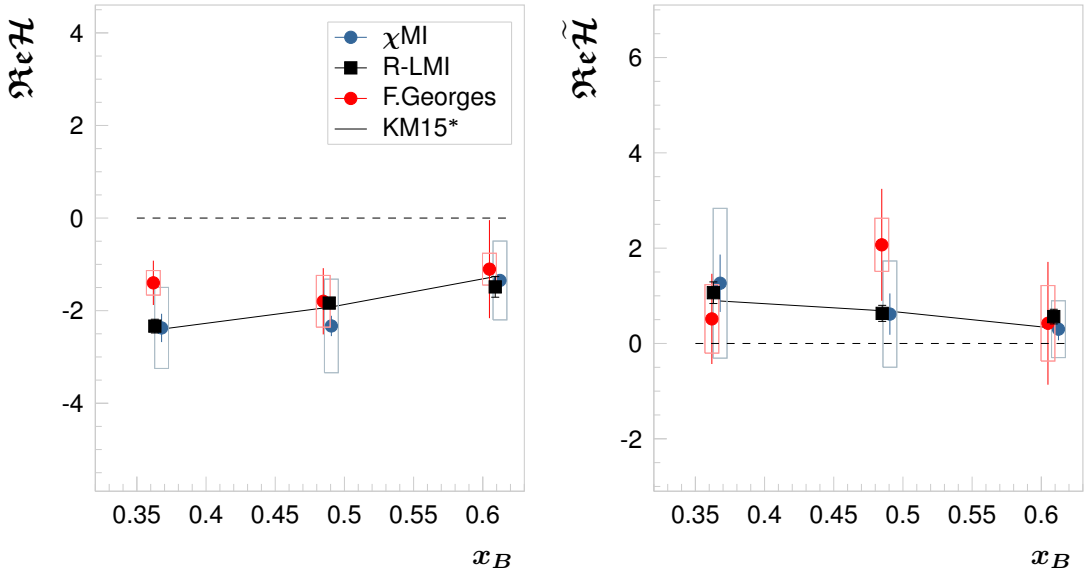

Figure 6.6: Extraction of the CFFs $\Re e\mathcal{H}$ (left) and $\Re e\widetilde{\mathcal{H}}$ (right) from the R-LMI fit (black), the χMI method (blue) and from F. Georges et.al. (red) as a function of x_B averaged over t and Q^2. The results are extracted from the Hall-A dataset E12-06-114. The average t values are -0.345, -0.702, -1.050 GeV^2 at x_B = 0.36, 0.48, 0.60, respectively.

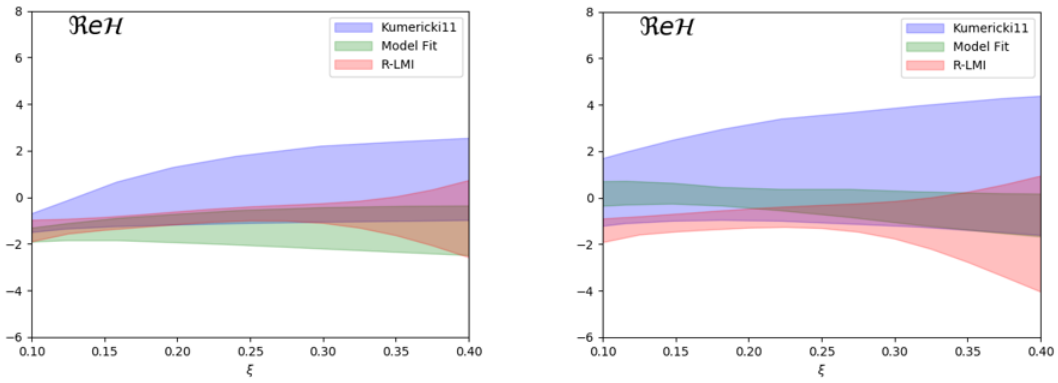

Figure 6.7: DNN extraction of $\Re e\mathcal{H}$ from the R-LMI (red band), in comparison to Kumericky11 extraction (blue band) and GPD-model fit (green band), as a function of ξ at $t = -0.2$ Gev^2 (top plot) and $t = -0.02$ Gev^2 (bottom plot).

data with the assumption of $\mathcal{H}$ dominance. The handling of experimental errors is similar however so the striking difference comes from the method itself. The results from [156], labeled as Kumericky11, are shown along with the R-LMI fit results and a GPD global model fit taken also from the same reference. The GPD model fit shown in the figure used a similar parametrization as in [52]. The DNN

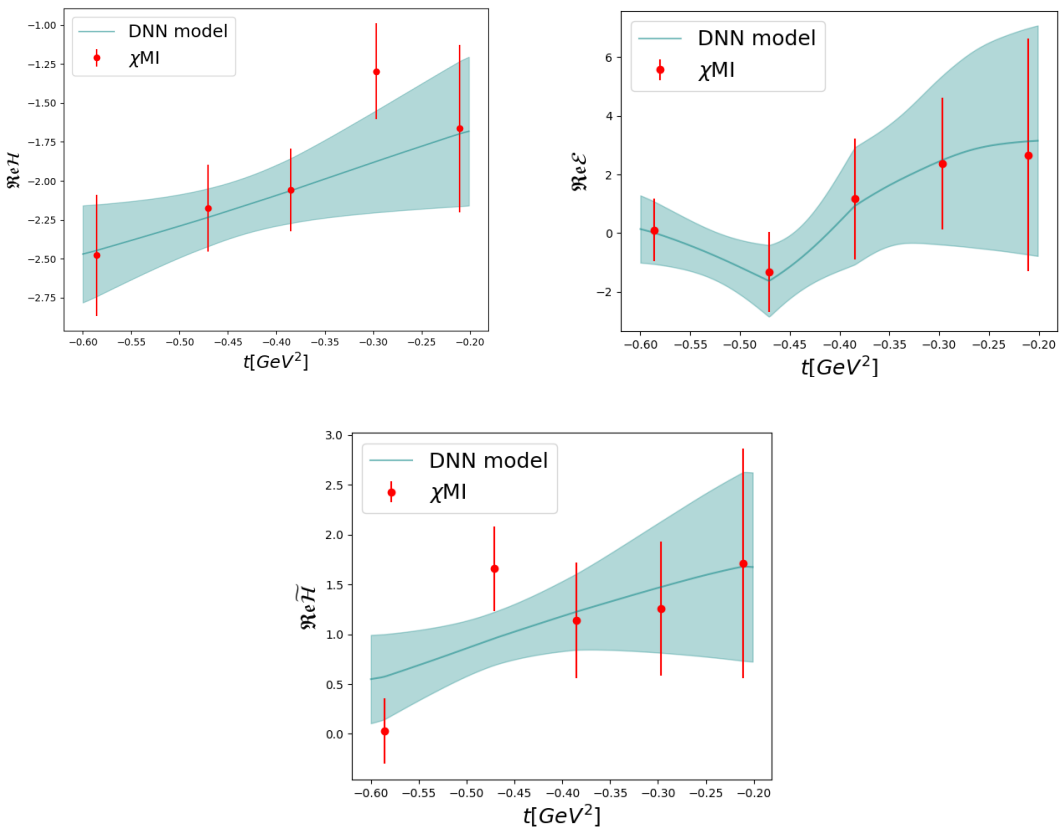

Figure 6.8: DNN model for the CFFs as a function of t for $x_B = 0.36$ corresponding to the Hall-A E12-06-114 kin-36-1 kinematic setting.

extraction of $\mathfrak{Re}\mathcal{H}$ from the R-LMI is shown with a red band, while the results from [156] for the DNN fit, i.e., Kumericky11, are shown with a blue band and for GPD-model fit with a green band.

6.3 | CFFs modeling with DNNs

Compton form factors are intricate functions of energy and momentum transfer. DNNs can approximate these complex functions, making them useful for modeling and predicting form factors since they can learn patterns that can capture nonlinear relationships in the data, without actually knowing the function form. Well-trained DNNs can generalize from the data they were trained on to make predictions for new, unseen data points, which can be useful for predicting form factors in unexplored kinematic regions.

In order to predict the values of the extracted CFFs $\mathfrak{Re}\mathcal{H}$, $\mathfrak{Re}\mathcal{E}$ and $\mathfrak{Re}\widetilde{\mathcal{H}}$ for any kinematic point, we perform a global fit of the extracted CFFs obtained from the

$\Re e\mathcal{H}$		$\Re e\mathcal{E}$		$\Re e\widetilde{\mathcal{H}}$	
batch size					
5		6		1	
hidden layers					
neurons	activation	neurons	activation	neurons	activation
20	*relu*	140	*tanh*	100	*relu*
40	*tanh*	140	*tanh*	20	*relu*
180	*sigmoid*	70	*relu*	20	*relu*
130	*relu*	200	*sigmoid*	20	*relu*
20	*relu*	120	*tanh*	20	*relu*
		170	*relu*		

Table 6.3: DNN architecture parameters for the global fit.

χMI method by training a DNN with these values for the given kinematic bins. The training is repeated for 1000 replicas of the CFFs created at each kinematic set by sampling with a Gaussian distribution about the extracted values with a standard deviation equal to the χMI extraction error. The final distribution of the CFFs as a function of the kinematics is then given by the mean of the CFFs models obtained for each replica and the precision is given by the standard deviation of models which at a fixed kinematic point, is defined by Eq. (6.2) The precision is a combination of the extraction uncertainty and the additional algorithmic (fitting) error.

The success of this approach depends on the quality and quantity of data, the architecture of the neural network, and the quality of the training process. The loss function is given by:

$$L(v', \theta) = \frac{1}{N} \sum_{i=1}^{N} \left(CFF_i^{DNN} - CFF_i^{\chi MI} \right)^2 \tag{6.7}$$

where v' represents the input kinematics and θ denotes the output variables, which include either $\Re e\mathcal{H}$, $\Re e\mathcal{E}$ or $\Re e\widetilde{\mathcal{H}}$. This function is calculated by taking the square of the differences between the inferred CFF (CFF^{DNN}), and the extracted CFF with the χMI method ($CFF^{\chi\text{MI}}$) averaged over the number of total kinematic bins N.

In Figure 6.8, an example of the constructed DNN model for the CFFs is shown as a function of t for $x_B = 0.36$ corresponding to the Hall-A E12-06-114 kin-36-1 kinematic setting. The neural network training used the standard Adam optimizer with a starting learning rate of 0.0001 and a maximum number of epochs set to 1000. The optimal architecture was tuned with the built-in random search algorithm of

the KerasTuner hyperparameter optimization framework [178]. The resulting DNN architecture used for each CFF model is listed in Table 6.3.

Summary

The proton, a fundamental particle in the Standard Model of particle physics, has been a subject of extensive research for decades. Despite our comprehensive knowledge of its basic properties, several intriguing questions remain open, fueling ongoing investigations. One of the foremost enigmas pertains to the proton's internal structure. While we understand that protons are composed of three quarks—two "up" quarks and one "down" quark—held together by gluons, the exact distribution and dynamics of quarks and gluons within the proton remain elusive. Researchers seek to unveil the spatial arrangement of these constituents in three dimensions, as well as their transverse momentum distributions, intrinsic transverse momentum, and their role in chiral symmetry breaking.

Another pressing issue revolves around the proton's spin structure. Although we know that quarks carry a fraction of the proton's spin, there is an ongoing debate about how this spin is distributed among quarks, gluons, and orbital angular momentum. Unraveling this complexity is vital to comprehending the proton's intricate internal dynamics. Generalized parton distribution functions allow us to obtain a 3D description of the proton while resolving many of these open questions like the orbital angular momentum contribution of the proton constituents. These questions are not only essential for advancing our understanding of the proton's structure but also for deepening our insights into the strong force and the nature of matter itself.

Accessing these functions is among the other key challenges that continue to captivate the scientific community. They appear in the physics observables convoluted with perturbative coefficients, the so-called Compton Form Factors. Therefore, the CFFs provide valuable insights into the internal structure of nucleons and have been a crucial focus of this research. The extraction of the CFFs themself from experimental data presents a formidable challenge in the field of hadronic physics. Precise measurements of CFFs require high-energy, high-luminosity experiments, and sophisticated theoretical models that can account for QCD effects, factorization violations, and higher-order corrections. Additionally, given that eight leading twist CFFs appear in the exclusive process and twenty-four at next

to leading twist; a large number of experimental observables need to be measured in order to constrain the CFFs. Overcoming these obstacles in CFF extraction is essential for advancing our understanding of nucleon structure and QCD in the non-perturbative regime.

In this work, we developed a novel extraction technique of the Compton form factors from experimental data by applying selections to the topology of the 2D χ^2 maps locally, which reduces model biases. We were able to extract three of the CFFs with reasonable accuracy using only one observable, the least-constrained one, which is the unpolarized photon leptoproduction cross-section. This is very remarkable since other local extraction works in the literature could only constrain two of the CFFs from simultaneously fitting two observables; like [9] for example. Particularly relevant, we were able to measure the CFF $\Re\mathrm{e}\mathcal{E}$ whose extraction is very lacking and given its connexion to GPD E, is of its own importance in the sense of its involvement to the parton orbital angular momenta (OAM), which plays an important role in the proton spin decomposition as seen in Section 2.5. A thoroughly systematic study with generated pseudodata mimicking the real data showed the efficacy of this method. We also compared the available values of CFFs extracted in other references that employed more the one observable with our results. The χMI extraction method was able to reproduce their results within the errors using only the unpolarized cross-section observable. This shows the great potential of this method when adding constraints using further observables. It is also expected significant improvements when applying advanced techniques like Convolutional Neural Networks (CNN) with this method. Our study also emphasizes some of the limitations in traditional least-squares local fitting.

Another revolutionary method to extract CFFs using of neural networks (DNNs) was introduced, the Local Multivariate Inference (LMI), which differs from standard local fitting by utilizing all ϕ data points across all kinematics simultaneously. This approach leverages the full data available, resulting in more accurate and reliable extraction capable of interpolation and interpolation. Additionally, the Recursive LMI (R-LMI) schema is also introduced, which iteratively improves the DNN optimization by using information extracted from experimental data to enhance the generating function during testing and optimization. The work presents this novel methodology using pseudodata generated from various models, demonstrating its effectiveness in accurately recovering the input CFF values. We also present a clear and concise handling of the uncertainty estimates in the method ensuring a degree of confidence in the extraction that can be well quantified so that the final R-LMI model from the experimental data provides significantly more predictive power

than many current models available.

Though all these CFF extraction techniques were applied specifically to the BKM formalism, this formalism is just used as an example and the methodology here can be applied to any formalism. Also what is presented here is specific to the unpolarized cross-section but these techniques can be easily expanded into multiple observables which can be fitted in a simultaneous DNN extraction. We expect to explore this in subsequent work.

Overall, this study presents a promising approach to extracting CFFs from experimental data, utilizing advanced techniques like the χ^2 map contour selections (i.e. χMI) and DNN-driven R-LMI to help overcome the challenges associated with model dependence, sparse data, and limited observables. Lastly, the proposed R-LMI methodology also shows potential for improving the accuracy, precision, and reliability of future CFF extractions.

Harmonic Coefficients A

A.1 | Bethe-Heitler coefficients

Here we reproduce explicitly the BH harmonic coefficients from [49] for the unpolarized cross-section.

The following parametrization is introduced for the lepton propagators:

$$\mathcal{P}_1 = -\frac{1}{y\,(1+\epsilon^2)}\{J + 2K\cos(\phi)\}, \quad \mathcal{P}_2 = 1 + \frac{\Delta^2}{Q^2} + \frac{1}{y\,(1+\epsilon^2)}\{J + 2K\cos(\phi)\}, \tag{A.1}$$

where

$$J = \left(1 - y - \frac{y\epsilon^2}{2}\right)\left(1 + \frac{\Delta^2}{Q^2}\right) - (1-x)(2-y)\frac{\Delta^2}{Q^2} \tag{A.2}$$

and,

$$K^2 = -\frac{\Delta^2}{Q^2}(1-x_B)\left(1 - y - \frac{y^2\epsilon^2}{4}\right)\left(1 - \frac{\Delta^2_{\text{min}}}{\Delta^2}\right)\left\{\sqrt{1+\epsilon^2} + \frac{4x_B\,(1-x_B) + \epsilon^2}{4\,(1-x_B)}\frac{\Delta^2 - \Delta^2_{\text{min}}}{Q^2}\right\} \tag{A.3}$$

The unpolarized harmonics are:

$$\begin{aligned} c^{\text{BH}}_{0,\,\text{unp}} &= 8K^2\left\{\left(2+3\epsilon^2\right)\frac{Q^2}{\Delta^2}\left(F_1^2 - \frac{\Delta^2}{4M^2}F_2^2\right) + 2x_B^2\,(F_1+F_2)^2\right\} \\ &+ (2-y)^2\left\{\left(2+\epsilon^2\right)\left[\frac{4x_B^2M^2}{\Delta^2}\left(1+\frac{\Delta^2}{Q^2}\right)^2 + 4\,(1-x_B)\left(1 + x_B\frac{\Delta^2}{Q^2}\right)\right]\left(F_1^2 - \frac{\Delta^2}{4M^2}F_2^2\right)\right. \\ &\left. +4x_B^2\left[x_B + \left(1 - x_B + \frac{\epsilon^2}{2}\right)\left(1 - \frac{\Delta^2}{Q^2}\right)^2 - x_B\,(1-2x_B)\,\frac{\Delta^4}{Q^4}\right](F_1+F_2)^2\right\} \\ &+ 8\left(1+\epsilon^2\right)\left(1 - y - \frac{\epsilon^2y^2}{4}\right)\left\{2\epsilon^2\left(1 - \frac{\Delta^2}{4M^2}\right)\left(F_1^2 - \frac{\Delta^2}{4M^2}F_2^2\right) - -x_B^2\left(1 - \frac{\Delta^2}{Q^2}\right)^2(F_1+F_2)^2\right\}, \end{aligned} \tag{A.4}$$

$$c^{\text{BH}}_{1,\,\text{unp}} = 8K(2-y)\left\{\left(\frac{4x_B^2M^2}{\Delta^2} - 2x_B - \epsilon^2\right)\left(F_1^2 - \frac{\Delta^2}{4M^2}F_2^2\right) + 2x_B^2\left(1 - (1-2x_B)\,\frac{\Delta^2}{Q^2}\right)(F_1+F_2)^2\right\}, \tag{A.5}$$

$$c_{2,\,\mathrm{unp}}^{\mathrm{BH}} = 8x_{\mathrm{B}}^2K^2\left\{\frac{4M^2}{\Delta^2}\left(F_1^2-\frac{\Delta^2}{4M^2}F_2^2\right)+2\left(F_1+F_2\right)^2\right\}. \tag{A.6}$$

A.2 | Pure DVCS cross-section

$$\left|\mathcal{T}^{\mathrm{DVCS}}\right|^2=\frac{e^6}{y^2Q^2}\left\{c_0^{\mathrm{DVCS}}+\sum_{n=1}^{2}\left[c_n^{\mathrm{DVCS}}\cos(n\phi)+s_n^{\mathrm{DVCS}}\sin(n\phi)\right]\right\}$$

for an unpolarized target:

$$c_{0,\,\mathrm{unp}}^{\mathrm{DVCS}} = 2\frac{2-2y+y^2+\frac{\epsilon^2}{2}y^2}{1+\epsilon^2}\mathcal{C}_{\mathrm{unp}}^{\mathrm{DVCS}}\left(\mathcal{F},\mathcal{F}^*\right)+\frac{16K^2}{\left(2-x_{\mathrm{B}}\right)^2\left(1+\epsilon^2\right)}\mathcal{C}_{\mathrm{unp}}^{\mathrm{DVCS}}\left(\mathcal{F}_{\mathrm{eff}},\mathcal{F}_{\mathrm{eff}}^*\right),$$

$$\begin{Bmatrix} c_{1,\,\mathrm{unp}}^{\mathrm{DVCS}} \\ s_{1,\,\mathrm{unp}}^{\mathrm{DVCS}} \end{Bmatrix} = \frac{8K}{\left(2-x_{\mathrm{B}}\right)\left(1+\epsilon^2\right)}\begin{Bmatrix} (2-y) \\ -\lambda y\sqrt{1+\epsilon^2} \end{Bmatrix}\begin{Bmatrix} \Re\mathrm{e} \\ \Im\mathrm{m} \end{Bmatrix}\mathcal{C}_{\mathrm{unp}}^{\mathrm{DVCS}}\left(\mathcal{F}_{\mathrm{eff}},\mathcal{F}^*\right)$$

where,

$$\begin{aligned}\mathcal{C}_{\mathrm{unp}}^{\mathrm{DVCS}} =& \frac{Q^2\left(Q^2+x_{\mathrm{B}}t\right)}{\left(\left(2-x_{\mathrm{B}}\right)Q^2+x_{\mathrm{B}}t\right)^2}\left\{4\left(1-x_{\mathrm{B}}\right)\mathcal{H}\mathcal{H}^*+4\left(1-x_{\mathrm{B}}+\frac{2Q^2+t}{Q^2+x_{\mathrm{B}}t}\frac{\epsilon^2}{4}\right)\widetilde{\mathcal{H}}\widetilde{\mathcal{H}}^*\right.\\ &-\frac{x_{\mathrm{B}}^2\left(Q^2+t\right)^2}{Q^2\left(Q^2+x_{\mathrm{B}}t\right)}\left(\mathcal{H}\mathcal{E}^*+\mathcal{E}\mathcal{H}^*\right)-\frac{x_{\mathrm{B}}^2Q^2}{Q^2+x_{\mathrm{B}}t}\left(\widetilde{\mathcal{H}}\widetilde{\mathcal{E}}^*+\widetilde{\mathcal{E}}\widetilde{\mathcal{H}}^*\right)\\ &\left.-\left(\frac{x_{\mathrm{B}}^2\left(Q^2+t\right)^2}{Q^2\left(Q^2+x_{\mathrm{B}}t\right)}+\frac{\left(\left(2-x_{\mathrm{B}}\right)Q^2+x_{\mathrm{B}}t\right)^2}{Q^2\left(Q^2+x_{\mathrm{B}}t\right)}\frac{t}{4M^2}\right)\mathcal{E}\mathcal{E}^*-\frac{x_{\mathrm{B}}^2Q^2}{Q^2+x_{\mathrm{B}}t}\frac{t}{4M^2}\widetilde{\mathcal{E}}\widetilde{\mathcal{E}}^*\right\}\end{aligned}$$

We emphasize that the squared twist-three contribution in $\mathcal{F}_{eff}$ is a $1/Q^2$ suppressed contribution and that the transversity contribution $\mathcal{F}_T$ is set to zero.

A.3 | Interference

$$\mathcal{I}=\frac{\pm e^6}{x_{\mathrm{B}}y^3t\mathcal{P}_1(\phi)\mathcal{P}_2(\phi)}\left\{c_0^{\mathcal{I}}+\sum_{n=1}^{3}\left[c_n^{\mathcal{I}}\cos(n\phi)+s_n^{\mathcal{I}}\sin(n\phi)\right]\right\}$$

with kinematically power-suppressed contributions exactly accounted for,

$$\begin{aligned}c_n^{\mathcal{I}} &= C_{++}(n)\Re\mathrm{e}\mathcal{C}_{++}^{\mathcal{I}}(n\mid\mathcal{F})+C_{0+}(n)\Re\mathrm{e}\mathcal{C}_{0+}^{\mathcal{I}}\left(n\mid\mathcal{F}_{\mathrm{eff}}\right)+C_{-+}(n)\Re\mathrm{e}\mathcal{C}_{-+}^{\mathcal{I}}\left(n\mid\mathcal{F}_T\right),\\ s_n^{\mathcal{I}} &= S_{++}(n)\Im\mathrm{m}\mathcal{S}_{++}^{\mathcal{I}}(n\mid\mathcal{F})+S_{0+}(n)\Im\mathrm{m}\mathcal{S}_{0+}^{\mathcal{I}}\left(n\mid\mathcal{F}_{\mathrm{eff}}\right)+S_{-+}(n)\Im\mathrm{m}\mathcal{S}_{-+}^{\mathcal{I}}\left(n\mid\mathcal{F}_T\right).\end{aligned}$$

The above coefficients are defined in terms of the photon helicity-conserving

$$\begin{aligned}\mathcal{C}_{++}^{\mathcal{I}}(n\mid\mathcal{F}) &= \mathcal{C}^{\mathcal{I}}(\mathcal{F})+\frac{C_{++}^V(n)}{C_{++}(n)}\mathcal{C}^{\mathcal{I},V}(\mathcal{F})+\frac{C_{++}^A(n)}{C_{++}(n)}\mathcal{C}^{\mathcal{I},A}(\mathcal{F})\\ \mathcal{S}_{++}^{\mathcal{I}}(n\mid\mathcal{F}) &= \mathcal{C}^{\mathcal{I}}(\mathcal{F})+\frac{S_{++}^V(n)}{S_{++}(n)}\mathcal{C}^{\mathcal{I},V}(\mathcal{F})+\frac{S_{++}^A(n)}{S_{++}(n)}\mathcal{C}^{\mathcal{I},A}(\mathcal{F})\end{aligned}$$

and helicity-changing amplitudes

$$C^{\mathcal{I}}_{0+}(n \mid \mathcal{F}_{\text{eff}}) = \frac{\sqrt{2}}{2-x_{\text{B}}}\frac{\widetilde{K}}{Q}\left[C^{\mathcal{I}}(\mathcal{F}_{\text{eff}}) + \frac{C^{V}_{0+}(n)}{C_{0+}(n)}C^{\mathcal{I},V}(\mathcal{F}_{\text{eff}}) + \frac{C^{A}_{0+}(n)}{C_{0+}(n)}C^{\mathcal{I},A}(\mathcal{F}_{\text{eff}})\right]$$
$$S^{\mathcal{I}}_{0+}(n \mid \mathcal{F}_{\text{eff}}) = \frac{\sqrt{2}}{2-x_{\text{B}}}\frac{\widetilde{K}}{Q}\left[C^{\mathcal{I}}(\mathcal{F}_{\text{eff}}) + \frac{S^{V}_{0+}(n)}{S_{0+}(n)}C^{\mathcal{I},V}(\mathcal{F}_{\text{eff}}) + \frac{S^{A}_{0+}(n)}{S_{0+}(n)}C^{\mathcal{I},A}(\mathcal{F}_{\text{eff}})\right]$$

where the combination of CFFs are:

$$C^{\mathcal{I}}_{\text{unp}}(\mathcal{F}) = F_1\mathcal{H} - \frac{t}{4M^2}F_2\mathcal{E} + \frac{x_{\text{B}}}{2-x_{\text{B}}+x_{\text{B}}\frac{t}{Q^2}}(F_1+F_2)\widetilde{\mathcal{H}}$$
$$C^{\mathcal{I},V}_{\text{unp}}(\mathcal{F}) = \frac{x_{\text{B}}}{2-x_{\text{B}}+x_{\text{B}}\frac{t}{Q^2}}(F_1+F_2)(\mathcal{H}+\mathcal{E}),$$
$$C^{\mathcal{I},A}_{\text{unp}}(\mathcal{F}) = \frac{x_{\text{B}}}{2-x_{\text{B}}+x_{\text{B}}\frac{t}{Q^2}}(F_1+F_2)\widetilde{\mathcal{H}}$$

The third odd harmonics vanishes, i.e.,

$$S^{\text{unp}}_{ab}(n=3) = S^{\text{unp},V}_{ab}(n=3) = S^{\text{unp},A}_{ab}(n=3) = 0,$$

Only the conserved photon-helicity coefficients, where no twist-3 effects are present, are listed here for the unpolarized case:

$$C^{\text{unp}}_{++}(n=0) = -\frac{4(2-y)\left(1+\sqrt{1+\epsilon^2}\right)}{(1+\epsilon^2)^2}\left\{\frac{\widetilde{K}^2}{Q^2}\frac{(2-y)^2}{\sqrt{1+\epsilon^2}}\right.$$
$$\left.+\frac{t}{Q^2}\left(1-y-\frac{\epsilon^2}{4}y^2\right)(2-x_{\text{B}})\left(1+\frac{2x_{\text{B}}\left(2-x_{\text{B}}+\frac{\sqrt{1+\epsilon^2}-1}{2}+\frac{\epsilon^2}{2x_{\text{B}}}\right)\frac{t}{Q^2}+\epsilon^2}{(2-x_{\text{B}})\left(1+\sqrt{1+\epsilon^2}\right)}\right)\right\}$$

$$C^{\text{unp},V}_{++}(n=0) = \frac{8(2-y)}{(1+\epsilon^2)^2}\frac{x_{\text{B}}t}{Q^2}\left\{\frac{(2-y)^2K^2}{\sqrt{1+\epsilon^2}Q^2}+\left(1-y-\frac{\epsilon^2}{4}y^2\right)\frac{1+\sqrt{1+\epsilon^2}}{2}\right.$$
$$\left.\times\left(1+\frac{t}{Q^2}\right)\left(1+\frac{\sqrt{1+\epsilon^2}-1+2x_{\text{B}}}{1+\sqrt{1+\epsilon^2}}\frac{t}{Q^2}\right)\right\},$$
$$C^{\text{unp},A}_{++}(n=0) = \frac{8(2-y)}{(1+\epsilon^2)^2}\frac{t}{Q^2}\left\{\frac{(2-y)^2\widetilde{K}^2}{\sqrt{1+\epsilon^2}Q^2}\frac{1+\sqrt{1+\epsilon^2}-2x_{\text{B}}}{2}+\left(1-y-\frac{\epsilon^2}{4}y^2\right)\left[\frac{1+\sqrt{1+\epsilon^2}}{2}\right.\right.$$
$$\left.\left.\times\left(1+\sqrt{1+\epsilon^2}-x_{\text{B}}+\left(\sqrt{1+\epsilon^2}-1+x_{\text{B}}\frac{3+\sqrt{1+\epsilon^2}-2x_{\text{B}}}{1+\sqrt{1+\epsilon^2}}\right)\frac{t}{Q^2}\right)-\frac{2\widetilde{K}^2}{Q^2}\right]\right\}$$

$$C_{++}^{\mathrm{unp}}(n=1)=\frac{-16K\left(1-y-\frac{\epsilon^2}{4}y^2\right)}{\left(1+\epsilon^2\right)^{5/2}}\left\{\left(1+\left(1-x_{\mathrm{B}}\right)\frac{\sqrt{\epsilon^2+1}-1}{2x_{\mathrm{B}}}+\frac{\epsilon^2}{4x_{\mathrm{B}}}\right)\frac{x_{\mathrm{B}}t}{Q^2}-\frac{3\epsilon^2}{4}\right\}$$

$$-4K\left(2-2y+y^2+\frac{\epsilon^2}{2}y^2\right)\frac{1+\sqrt{1+\epsilon^2}-\epsilon^2}{\left(1+\epsilon^2\right)^{5/2}}\left\{1-\left(1-3x_{\mathrm{B}}\right)\frac{t}{Q^2}\right.$$

$$\left.+\frac{1-\sqrt{1+\epsilon^2}+3\epsilon^2}{1+\sqrt{1+\epsilon^2}-\epsilon^2}\frac{x_{\mathrm{B}}t}{Q^2}\right\}$$

$$C_{++}^{\mathrm{unp},V}(n=1)=\frac{16K}{\left(1+\epsilon^2\right)^{5/2}}\frac{x_{\mathrm{B}}t}{Q^2}\left\{(2-y)^2\left(1-\left(1-2x_{\mathrm{B}}\right)\frac{t}{Q^2}\right)+\left(1-y-\frac{\epsilon^2}{4}y^2\right)\right.$$

$$\left.\times\frac{1+\sqrt{1+\epsilon^2}-2x_{\mathrm{B}}}{2}\frac{t'}{Q^2}\right\}$$

$$C_{++}^{\mathrm{unp},A}(n=1)=\frac{-16K}{\left(1+\epsilon^2\right)^2}\frac{t}{Q^2}\left\{\left(1-y-\frac{\epsilon^2}{4}y^2\right)\left(1-\left(1-2x_{\mathrm{B}}\right)\frac{t}{Q^2}+\frac{4x_{\mathrm{B}}\left(1-x_{\mathrm{B}}\right)+\epsilon^2}{4\sqrt{1+\epsilon^2}}\frac{t'}{Q^2}\right)\right.$$

$$\left.-(2-y)^2\left(1-\frac{x_{\mathrm{B}}}{2}+\frac{1+\sqrt{1+\epsilon^2}-2x_{\mathrm{B}}}{4}\left(1-\frac{t}{Q^2}\right)+\frac{4x_{\mathrm{B}}\left(1-x_{\mathrm{B}}\right)+\epsilon^2}{2\sqrt{1+\epsilon^2}}\frac{t'}{Q^2}\right)\right\}$$

$$C_{++}^{\mathrm{unp}}(n=2)=\frac{8(2-y)\left(1-y-\frac{\epsilon^2}{4}y^2\right)}{\left(1+\epsilon^2\right)^2}\left\{\frac{2\epsilon^2}{\sqrt{1+\epsilon^2}\left(1+\sqrt{1+\epsilon^2}\right)}\frac{\widetilde{K}^2}{Q^2}\right.$$

$$\left.+\frac{x_{\mathrm{B}}tt'}{Q^4}\left(1-x_{\mathrm{B}}-\frac{\sqrt{1+\epsilon^2}-1}{2}+\frac{\epsilon^2}{2x_{\mathrm{B}}}\right)\right\}$$

$$C_{++}^{\mathrm{unp},V}(n=2)=\frac{8(2-y)\left(1-y-\frac{\epsilon^2}{4}y^2\right)}{\left(1+\epsilon^2\right)^2}\frac{x_{\mathrm{B}}t}{Q^2}\left\{\frac{4\widetilde{K}^2}{\sqrt{1+\epsilon^2}Q^2}+\frac{1+\sqrt{1+\epsilon^2}-2x_{\mathrm{B}}}{2}\left(1+\frac{t}{Q^2}\right)\frac{t'}{Q^2}\right\}$$

$$C_{++}^{\mathrm{unp},A}(n=2)=\frac{4(2-y)\left(1-y-\frac{\epsilon^2}{4}y^2\right)}{\left(1+\epsilon^2\right)^2}\frac{t}{Q^2}\left\{\frac{4\left(1-2x_{\mathrm{B}}\right)\widetilde{K}^2}{\sqrt{1+\epsilon^2}Q^2}-\left(3-\sqrt{1+\epsilon^2}-2x_{\mathrm{B}}+\frac{\epsilon^2}{x_{\mathrm{B}}}\right)\frac{x_{\mathrm{B}}t'}{Q^2}\right\}$$

$$C_{++}^{\mathrm{unp}}(n=3)=-8K\left(1-y-\frac{\epsilon^2}{4}y^2\right)\frac{\sqrt{1+\epsilon^2}-1}{\left(1+\epsilon^2\right)^{5/2}}\left\{\left(1-x_{\mathrm{B}}\right)\frac{t}{Q^2}+\frac{\sqrt{1+\epsilon^2}-1}{2}\left(1+\frac{t}{Q^2}\right)\right\},$$

$$C_{++}^{\mathrm{unp},V}(n=3)=-\frac{8K\left(1-y-\frac{\epsilon^2}{4}y^2\right)}{\left(1+\epsilon^2\right)^{5/2}}\frac{x_{\mathrm{B}}t}{Q^2}\left\{\sqrt{1+\epsilon^2}-1+\left(1+\sqrt{1+\epsilon^2}-2x_{\mathrm{B}}\right)\frac{t}{Q^2}\right\},$$

$$C_{++}^{\mathrm{unp},A}(n=3)=\frac{16K\left(1-y-\frac{\epsilon^2}{4}y^2\right)}{\left(1+\epsilon^2\right)^{5/2}}\frac{tt'}{Q^4}\left\{x_{\mathrm{B}}\left(1-x_{\mathrm{B}}\right)+\frac{\epsilon^2}{4}\right\}$$

$$S_{++}^{\mathrm{unp}}(n=1) = \frac{8\lambda K(2-y)y}{1+\epsilon^2}\left\{1+\frac{1-x_{\mathrm{B}}+\frac{\sqrt{1+\epsilon^2}-1}{2}}{1+\epsilon^2}\frac{t'}{Q^2}\right\},$$

$$S_{++}^{\mathrm{unp},V}(n=1) = -\frac{8\lambda K(2-y)y}{\left(1+\epsilon^2\right)^2}\frac{x_{\mathrm{B}}t}{Q^2}\left\{\sqrt{1+\epsilon^2}-1+\left(1+\sqrt{1+\epsilon^2}-2x_{\mathrm{B}}\right)\frac{t}{Q^2}\right\},$$

$$S_{++}^{\mathrm{unp},A}(n=1) = \frac{8\lambda K(2-y)y}{\left(1+\epsilon^2\right)}\frac{t}{Q^2}\left\{1-\left(1-2x_{\mathrm{B}}\right)\frac{1+\sqrt{1+\epsilon^2}-2x_{\mathrm{B}}}{2\sqrt{1+\epsilon^2}}\frac{t'}{Q^2}\right\},$$

$$S_{++}^{\mathrm{unp}}(n=2) - \frac{4\lambda\left(1-y-\frac{\epsilon^2}{4}y^2\right)y}{\left(1+\epsilon^2\right)^{3/2}}\left(1+\sqrt{1+\epsilon^2}-2x_{\mathrm{B}}\right)\frac{t'}{Q^2}\left\{\frac{\epsilon^2-x_{\mathrm{B}}\left(\sqrt{1+\epsilon^2}-1\right)}{1+\sqrt{\epsilon^2+1}-2x_{\mathrm{B}}}-\frac{2x_{\mathrm{B}}+\epsilon^2}{2\sqrt{1+\epsilon^2}}\frac{t'}{Q^2}\right\}$$

$$S_{++}^{\mathrm{unp},V}(n=2) = -\frac{4\lambda\left(1-y-\frac{\epsilon^2}{4}y^2\right)y}{\left(1+\epsilon^2\right)^2}\frac{x_{\mathrm{B}}t}{Q^2}$$
$$\times\left(1-\left(1-2x_{\mathrm{B}}\right)\frac{t}{Q^2}\right)\left\{\sqrt{1+\epsilon^2}-1+\left(1+\sqrt{1+\epsilon^2}-2x_{\mathrm{B}}\right)\frac{t}{Q^2}\right\},$$

$$S_{++}^{\mathrm{unp},A}(n=2) = -\frac{8\lambda\left(1-y-\frac{\epsilon^2}{4}y^2\right)y}{\left(1+\epsilon^2\right)^2}\frac{tt'}{Q^4}$$
$$\times\left(1+\sqrt{1+\epsilon^2}-2x_{\mathrm{B}}\right)\left(1+\frac{4\left(1-x_{\mathrm{B}}\right)x_{\mathrm{B}}+\epsilon^2}{4-2x_{\mathrm{B}}+3\epsilon^2}\frac{t}{Q^2}\right).$$

Extracted CFFs B

Extracted values of the CFFs with the χMI method

k	$Q^2[GeV^2]$	x_B	$t[GeV^2]$	$\Re e\mathcal{H}$	$\Re e\mathcal{E}$	$\Re e\widetilde{\mathcal{H}}$
5.75	1.82	0.343	-0.172	-2.8956	3.41007	2.9572
5.75	1.933	0.368	-0.232	-2.77019	1.3375	1.56292
5.75	1.964	0.375	-0.278	-2.96729	1.14869	1.12443
5.75	1.986	0.379	-0.323	-2.68067	-0.12473	1.25234
5.75	1.999	0.381	-0.371	-2.3452	0.346873	1.20187
5.75	2.218	0.345	-0.176	-2.93561	3.51748	3.09152
5.75	2.318	0.363	-0.232	-2.97882	1.92657	1.92798
5.75	2.348	0.368	-0.279	-3.46405	0.381411	1.28119
5.75	2.36	0.371	-0.325	-3.3164	-0.32753	1.08996
5.75	2.375	0.373	-0.372	-2.70275	-0.567723	1.32901
5.75	2.012	0.378	-0.192	-2.61855	2.96213	2.4155
5.75	2.054	0.392	-0.233	-2.16777	2.37356	1.63352
5.75	2.074	0.398	-0.279	-2.59757	1.5016	0.973781
5.75	2.084	0.4	-0.324	-2.62256	1.0176	1.15207
5.75	2.091	0.401	-0.371	-2.551	0.493684	1.29341
5.75	2.161	0.336	-0.171	-3.24538	2.95931	4.12955
5.75	2.19	0.342	-0.231	-3.74846	1.41684	1.67532
5.75	2.194	0.343	-0.278	-3.72355	-1.32847	1.31779
5.75	2.191	0.342	-0.324	-2.45902	0.651948	1.52977
5.75	2.193	0.342	-0.371	-0.431453	2.14464	1.48533
7.383	3.17	0.363	-0.21085	-1.66482	2.6576	1.71091
7.383	3.17	0.363	-0.29665	-1.29685	2.37369	1.25688
7.383	3.18	0.365	-0.38488	-2.05709	1.17128	1.13898
7.383	3.18	0.365	-0.47088	-2.17401	-1.32666	1.65889
7.383	3.18	0.364	-0.58578	-2.47817	0.100036	0.02688
8.521	3.65	0.367	-0.20459	-2.9553	2.24927	2.01973
8.521	3.65	0.367	-0.26579	-2.97006	1.94244	1.78407
8.521	3.67	0.369	-0.33034	-2.57712	0.379167	1.24802
8.521	3.68	0.37	-0.39252	-2.51127	-0.0774329	1.15317
8.521	3.68	0.37	-0.48052	-2.50444	-1.69233	1.07617

k	$Q^2[GeV^2]$	x_B	$t[GeV^2]$	$\Re e\mathcal{H}$	$\Re e\mathcal{E}$	$\Re e\widetilde{\mathcal{H}}$
10.591	4.53	0.369	-0.20942	-3.16019	2.62276	1.74569
10.591	4.55	0.37	-0.27194	-2.98064	0.998258	1.13865
10.591	4.57	0.372	-0.33557	-2.50198	0.0972902	1.09995
10.591	4.58	0.373	-0.39879	-1.77486	0.707222	1.15546
10.591	4.57	0.371	-0.48338	-1.98977	-0.322381	0.741225
4.487	2.71	0.483	-0.34812	-4.14854	0.697937	0.641192
4.487	2.71	0.483	-0.39062	-3.28873	0.817852	0.661511
4.487	2.71	0.484	-0.43499	-3.31284	0.38929	0.687117
4.487	2.71	0.485	-0.47967	-3.6829	-1.17895	0.27394
8.851	4.5	0.497	-0.40977	-2.51495	0.266658	0.643724
8.851	4.53	0.501	-0.47956	-2.43988	0.190258	0.476501
8.851	4.56	0.504	-0.54751	-2.69991	-0.982921	0.19079
8.847	5.33	0.482	-0.38537	-1.86835	1.91864	1.17648
8.847	5.34	0.483	-0.44561	-1.85993	2.14715	1.01992
8.847	5.36	0.485	-0.50851	-2.1745	0.345145	1.07317
8.847	5.37	0.486	-0.56958	-2.27407	-0.0661938	0.920326
8.847	5.38	0.486	-0.65465	-1.51053	-1.53759	0.313632
10.992	7.04	0.494	-0.43254	-1.95721	-0.483575	0.70665
10.992	7.09	0.498	-0.52556	-0.783056	-1.84796	0.223082
10.992	7.12	0.499	-0.61292	-1.6359	-0.950857	0.490101
10.992	7.11	0.499	-0.69787	-1.13092	-1.37792	0.362761
8.521	5.6	0.61	-0.76451	-1.39899	0.677896	0.608824
8.521	5.62	0.612	-0.9042	-1.42217	-0.340222	0.482646
8.521	5.64	0.615	-1.0482	-1.78696	-0.674271	0.44966
8.521	5.65	0.617	-1.18956	-0.969414	-1.89008	-0.438886
8.521	5.66	0.616	-1.3732	-1.57301	-2.10856	-0.416163
10.591	8.44	0.608	-0.7911	-1.29047	-0.606574	0.396237
10.591	8.45	0.609	-0.91204	-1.15452	-0.774257	0.513637
10.591	8.48	0.611	-1.03708	-1.25554	-0.604997	0.478022
10.591	8.5	0.613	-1.1631	-1.44837	-0.700223	0.539364
10.591	8.51	0.613	-1.3282	-1.17891	-0.69054	0.387401
5.55	1.51	0.359	-0.18	-3.45572	2.20308	1.29826
5.55	1.51	0.359	-0.237	-3.06768	0.226175	0.225891
5.55	1.52	0.361	-0.298	-3.97427	0.941639	0.775175
5.55	1.74	0.359	-0.183	-2.97439	2.25588	1.42862
5.55	1.74	0.359	-0.242	-2.55548	4.19703	-0.727083
5.55	1.74	0.359	-0.302	-3.24409	-0.797545	1.18743
5.55	1.75	0.361	-0.363	-3.49633	0.811798	0.354246
5.55	1.98	0.357	-0.182	-2.71831	3.82014	2.42472
5.55	1.98	0.356	-0.242	-2.86712	2.00176	1.47262
5.55	1.98	0.356	-0.302	-2.42805	1.23643	1.39239
5.55	1.99	0.358	-0.363	-2.07848	0.484231	1.40412
3.355	1.49	0.357	-0.177	-3.68229	2.19175	1.84603
3.355	1.5	0.359	-0.236	-3.44635	1.91013	1.32651
3.355	1.5	0.36	-0.296	-2.41887	1.33414	1.72988

k	$Q^2[GeV^2]$	x_B	$t[GeV^2]$	$\Re e\mathcal{H}$	$\Re e\mathcal{E}$	$\Re e\widetilde{\mathcal{H}}$
4.455	1.74	0.357	-0.181	-3.19282	2.25381	2.57394
4.455	1.74	0.357	-0.24	-2.75944	1.91453	2.11238
4.455	1.74	0.358	-0.301	-2.91377	1.16717	1.66242
4.455	1.76	0.361	-0.363	-3.40035	-1.17582	1.49872
4.455	1.98	0.356	-0.182	-3.01611	2.96899	2.58751
4.455	2	0.36	-0.304	-2.73722	1.02303	1.47422
5.75	1.11	0.126	-0.11	5.04772	1.92064	-1.33267
5.75	1.11	0.126	-0.15	6.67052	-4.18805	0.624527
5.75	1.11	0.126	-0.2	3.78811	2.22661	1.53852
5.75	1.11	0.126	-0.26	-1.42723	2.63645	1.7085
5.75	1.11	0.126	-0.34	-1.11689	2.31654	0.742452
5.75	1.11	0.126	-0.45	-2.80414	3.86703	0.193773
5.75	1.27	0.154	-0.11	1.04542	2.39766	2.36249
5.75	1.27	0.154	-0.15	4.96676	3.36854	-2.62002
5.75	1.27	0.154	-0.2	4.48462	2.27655	1.63216
5.75	1.27	0.154	-0.26	2.37623	1.41509	1.19054
5.75	1.27	0.154	-0.34	1.28646	1.75005	0.767894
5.75	1.27	0.154	-0.45	0.149155	4.41071	-0.210049
5.75	1.39	0.155	-0.11	-3.38355	5.58996	1.71511
5.75	1.39	0.155	-0.15	0.281899	2.5955	1.48579
5.75	1.39	0.155	-0.2	4.68219	2.30683	1.63843
5.75	1.39	0.155	-0.26	4.01951	1.87155	0.939705
5.75	1.39	0.155	-0.34	-2.29231	2.62173	0.401999
5.75	1.39	0.155	-0.45	-1.66424	3.29454	0.146043
5.75	1.45	0.184	-0.11	-1.97558	2.42264	3.87052
5.75	1.45	0.184	-0.15	0.736357	2.3124	2.95879
5.75	1.45	0.184	-0.2	4.88715	2.19192	0.523219
5.75	1.45	0.184	-0.26	4.0027	-5.00975	2.88384
5.75	1.45	0.184	-0.34	4.3402	2.06048	0.874482
5.75	1.45	0.184	-0.45	2.39804	2.37878	0.249205
5.75	1.62	0.185	-0.11	8.08694	2.42463	1.0487
5.75	1.63	0.185	-0.15	2.42115	-3.90807	1.21085
5.75	1.63	0.185	-0.2	9.46949	-1.82639	4.50986
5.75	1.63	0.185	-0.26	5.16996	-3.47039	2.67219
5.75	1.63	0.185	-0.34	2.95925	1.90652	0.799875
5.75	1.63	0.185	-0.45	2.70882	4.50686	-0.582436

k	$Q^2[GeV^2]$	x_B	$t[GeV^2]$	$\Re e\mathcal{H}$	$\Re e\mathcal{E}$	$\Re e\widetilde{\mathcal{H}}$
5.75	1.64	0.214	-0.11	-2.2489	2.74976	3.75625
5.75	1.64	0.214	-0.15	-2.47726	3.64441	3.22506
5.75	1.64	0.214	-0.2	1.15146	2.55037	-1.88628
5.75	1.64	0.214	-0.26	0.834819	1.64589	1.61204
5.75	1.64	0.214	-0.34	-0.446157	2.54319	1.12108
5.75	1.64	0.214	-0.45	5.04955	1.1213	1.92517
5.75	1.88	0.215	-0.11	2.81598	2.53407	1.43417
5.75	1.88	0.215	-0.15	4.31502	1.93731	0.316696
5.75	1.88	0.215	-0.2	5.93641	-1.43759	1.73004
5.75	1.88	0.215	-0.26	10.8823	4.51102	3.13982
5.75	1.88	0.215	-0.34	6.55356	0.59297	2.31633
5.75	1.88	0.215	-0.45	3.45152	1.07166	1.15171
5.75	1.79	0.244	-0.11	-3.17011	8.01726	3.23985
5.75	1.79	0.244	-0.15	-0.512333	2.71925	3.27245
5.75	1.79	0.244	-0.2	-0.956602	2.40367	2.43893
5.75	1.79	0.244	-0.26	-0.592307	0.942747	2.01426
5.75	1.8	0.244	-0.34	0.319456	2.03678	0.98754
5.75	1.8	0.244	-0.45	0.468607	1.33856	1.04317
5.75	2.12	0.244	-0.11	3.73759	5.56709	3.21128
5.75	2.12	0.245	-0.15	4.9459	2.42105	1.91637
5.75	2.12	0.245	-0.2	6.85584	2.32296	1.69918
5.75	2.12	0.245	-0.26	8.31205	2.20537	1.1392
5.75	2.12	0.245	-0.34	10.034	4.89453	1.23024
5.75	2.12	0.245	-0.45	4.56642	-0.0881904	1.81139
5.75	1.94	0.274	-0.11	-1.40712	3.92933	3.16766
5.75	1.94	0.274	-0.15	-2.70326	2.57311	3.06782
5.75	1.94	0.274	-0.2	-1.29806	1.05529	2.91855
5.75	1.94	0.274	-0.26	-1.51427	0.879443	2.27658
5.75	1.94	0.275	-0.34	-0.59429	1.26947	1.58771
5.75	1.94	0.275	-0.45	0.583555	0.87608	1.16665
5.75	2.35	0.274	-0.11	-4.14818	1.30492	0.12586
5.75	2.35	0.275	-0.15	0.681737	4.40724	3.85334
5.75	2.35	0.275	-0.2	1.85881	3.38809	2.28613
5.75	2.35	0.275	-0.26	5.03944	2.11224	1.3143
5.75	2.35	0.275	-0.34	4.65065	1.80586	1.16216
5.75	2.35	0.275	-0.45	5.82447	0.787198	0.914404
5.75	2.08	0.301	-0.12	-9.1074	2.93374	1.19797
5.75	2.1	0.304	-0.15	-3.02118	2.41159	1.3488
5.75	2.1	0.304	-0.2	-1.83066	2.68374	3.03369
5.75	2.1	0.304	-0.26	-1.30758	-2.38776	2.92434
5.75	2.1	0.304	-0.34	-1.42349	0.681449	1.76132
5.75	2.1	0.305	-0.45	-1.13029	0.951708	0.953793

k	$Q^2[GeV^2]$	x_B	$t[GeV^2]$	$\Re e\mathcal{H}$	$\Re e\mathcal{E}$	$\Re e\widetilde{\mathcal{H}}$
5.75	2.58	0.304	-0.15	-1.36902	2.44624	3.94376
5.75	2.58	0.304	-0.2	-0.455896	4.52629	3.23826
5.75	2.58	0.305	-0.26	2.11614	2.53977	1.61211
5.75	2.58	0.305	-0.34	2.30788	0.470109	1.79221
5.75	2.58	0.305	-0.45	3.81359	0.550976	1.44426
5.75	2.23	0.335	-0.2	-2.45037	2.68578	2.49463
5.75	2.23	0.335	-0.26	-1.83382	1.49881	1.89142
5.75	2.23	0.335	-0.34	-1.37332	1.41016	1.23776
5.75	2.23	0.335	-0.45	-2.28743	-0.458603	1.26144
5.75	2.78	0.335	-0.2	-2.48822	3.73421	2.80538
5.75	2.78	0.335	-0.26	-0.628885	2.02111	2.73905
5.75	2.78	0.335	-0.34	1.02445	2.20713	1.55573
5.75	2.78	0.335	-0.45	1.67708	1.35531	1.13947
5.75	2.35	0.365	-0.2	-4.75459	1.94945	0.43575
5.75	2.35	0.365	-0.26	-2.04903	1.4745	1.63906
5.75	2.35	0.365	-0.34	-1.82319	0.936192	1.33749
5.75	2.35	0.365	-0.45	-0.992191	0.47797	1.79142
5.75	2.97	0.364	-0.2	-3.27901	2.17512	2.14125
5.75	2.97	0.365	-0.26	-0.684387	3.19388	1.88746
5.75	2.97	0.365	-0.34	0.110677	3.03073	2.19363
5.75	2.97	0.365	-0.45	1.02464	2.49008	1.07582
5.75	2.44	0.393	-0.21	-5.28603	1.23638	-0.734679
5.75	2.48	0.4	-0.26	-1.69601	0.842433	2.99937
5.75	2.48	0.399	-0.34	-1.14562	1.11491	1.55756
5.75	2.48	0.399	-0.45	-2.10296	-0.279672	1.07951
5.75	3.12	0.391	-0.21	-10.075	7.02862	1.79455
5.75	3.18	0.399	-0.26	-3.38792	-2.28925	0.867458
5.75	3.18	0.4	-0.34	-1.41884	2.04261	1.64053
5.75	3.18	0.4	-0.45	-0.112215	1.66275	1.18987
5.75	2.81	0.433	-0.27	-5.39898	-4.21936	-2.0093
5.75	2.96	0.449	-0.34	-1.73262	2.88793	1.00888
5.75	3.05	0.461	-0.45	-1.25093	1.56055	1.42663
5.75	3.5	0.43	-0.28	-8.52117	-5.99621	-3.46157
5.75	3.63	0.451	-0.34	-1.80137	1.87112	1.59771
5.75	3.77	0.475	-0.45	-0.952082	2.35201	0.969479

References

[1] D. Müeller, D. Robaschik, B. Geyer, F-M. Dittes, and J. Hořejši. Wave functions, evolution equations and evolution kernels from light ray operators of QCD. *Fortschr. Phys.*, 42:101, 1994.

[2] X.-D. Ji. Gauge-invariant decomposition of nucleon spin. *Phys. Rev. Lett*, 78:610, 1997.

[3] X.-D. Ji. Deeply virtual compton scattering. *Phys. Rev. D*, 55:7114, 1997.

[4] A. Radyushkin. Asymmetric gluon distributions and hard diffractive electroproduction. *Phys. Lett. B*, 385:333, 1996.

[5] A. Radyushkin. Nonforward parton distributions. *Phys. Rev. D*, 56:5524, 1997.

[6] Christine A. Aidala, Steven D. Bass, Delia Hasch, and Gerhard K. Mallot. The spin structure of the nucleon. *Rev. Mod. Phys.*, 85:655, 2013.

[7] Matthias Burkardt. Impact parameter dependent parton distributions and off-forward parton distributions for $\zeta \to 0$. *Phys. Rev. D*, 62:071503, Sep 2000. doi: 10.1103/PhysRevD.62.071503. URL `https://link.aps.org/doi/10.1103/PhysRevD.62.071503`.

[8] M Diehl. Generalized parton distributions in impact parameter space. *Eur. Phys. J. C*, 25: 223–232, 2002.

[9] Raphaël Dupré, Michel Guidal, Silvia Niccolai, and Marc Vanderhaeghen. Analysis of Deeply Virtual Compton Scattering Data at Jefferson Lab and Proton Tomography. *Eur. Phys. J. A*, 53 (8):171, 2017. doi: 10.1140/epja/i2017-12356-8.

[10] M.V. Polyakov. Generalized parton distributions and strong forces inside nucleons and nuclei. *Physics Letters B*, 555(1):57–62, 2003. ISSN 0370-2693. doi: https://doi.org/10.1016/S0370-2693(03)00036-4. URL `https://www.sciencedirect.com/science/article/pii/S0370269303000364`.

[11] M. V. Polyakov and P. Schweitzer. Forces inside hadrons: Pressure, surface tension, mechanical radius, and all that. *Int. J. Mod. Phys. A*, 33(1):1830025, 2018.

[12] E. Berger, M. Diehl, and B. Pire. Timelike Compton scattering: exclusive photoproduction of lepton pairs. *Eur. Phys. J. C*, 23:675–689, 2002.

[13] M. Guidal and M. Vanderhaeghen. Double Deeply Virtual Compton Scattering off the Nucleon. *Phys. Rev. Lett.*, 90:012001, 2003.

[14] M Diehl. Generalized parton distributions. *Phys. Rep.*, 388:41–277, 2003.

[15] P. Hoodbhoy and X. Ji. Helicity-flip off-forward parton distributions of the nucleon. *Phys. Rev. D*, 58:054006, 1998.

[16] Yuri L. Dokshitzer. Calculation of the Structure Functions for Deep Inelastic Scattering and e+ e- Annihilation by Perturbation Theory in Quantum Chromodynamics. *Sov. Phys. JETP*, 46:641–653, 1977.

[17] V. N. Gribov and L. N. Lipatov. Deep inelastic e p scattering in perturbation theory. *Sov. J. Nucl. Phys.*, 15:438–450, 1972.

[18] L. N. Lipatov. The parton model and perturbation theory. *Yad. Fiz.*, 20:181–198, 1974.

[19] Guido Altarelli and G. Parisi. Asymptotic Freedom in Parton Language. *Nucl. Phys. B*, 126: 298–318, 1977. doi: 10.1016/0550-3213(77)90384-4.

[20] A. V. Efremov and A. V. Radyushkin. Factorization and Asymptotical Behavior of Pion Form-Factor in QCD. *Phys. Lett. B*, 94:245–250, 1980. doi: 10.1016/0370-2693(80)90869-2.

[21] G. Peter Lepage and Stanley J. Brodsky. Exclusive Processes in Perturbative Quantum Chromodynamics. *Phys. Rev. D*, 22:2157, 1980. doi: 10.1103/PhysRevD.22.2157.

[22] John C. Collins, Leonid Frankfurt, , and Mark Strikman. Factorization for hard exclusive electroproduction of mesons in QCD. *Phys. Rev. D*, 56:2982, 1997.

[23] Xiangdong Ji and Jonathan Osborne. One-loop corrections and all order factorization in deeply virtual Compton scattering. *Phys. Rev. D*, 58:094018, 1998.

[24] A. Aktas et al. Measurement of deeply virtual compton scattering at HERA. *Eur. Phys. J. C*, 44:1–11, 2005. doi: 10.1140/epjc/s2005-02345-3.

[25] F. D. Aaron et al. Deeply Virtual Compton Scattering and its beam charge asymmetry in $e \pm p$ collisions at HERA. *Phys. Lett. B*, 681:391–399, 2009. doi: 10.1016/j.physletb.2009.10.035.

[26] S. Chekanov et al. *JHEP*, 05:108 (2009), 2009. ISSN 10298479. doi: 10.1088/1126-6708/2009/05/108.

[27] A. Airapetian et al. Measurement of the beam spin azimuthal asymmetry associated with deeply virtual Compton scattering. *Phys. Rev. Lett.*, 87:182001, 2001. doi: 10.1103/PhysRevLett.87.182001. URL `https://arxiv.org/pdf/hep-ex/0106068.pdf`.

[28] A. Airapetian et al. The Beam-charge azimuthal asymmetry and deeply virtual compton scattering. *Phys. Rev. D*, 75:011103, 2007. doi: 10.1103/PhysRevD.75.011103. URL `https://arxiv.org/pdf/hep-ex/0605108.pdf`.

[29] A. Airapetian et al. Measurement of Azimuthal Asymmetries With Respect To Both Beam Charge and Transverse Target Polarization in Exclusive Electroproduction of Real Photons. *JHEP*, 06:066, 2008. doi: 10.1088/1126-6708/2008/06/066. URL `https://arxiv.org/pdf/0802.2499.pdf`.

[30] A. Airapetian et al. Separation of contributions from deeply virtual Compton scattering and its interference with the Bethe-Heitler process in measurements on a hydrogen target. *JHEP*, 11:083, 2009. doi: 10.1088/1126-6708/2009/11/083. URL https://arxiv.org/pdf/0909.3587.pdf.

[31] A. Airapetian et al. Exclusive Leptoproduction of Real Photons on a Longitudinally Polarised Hydrogen Target. *JHEP*, 06:019, 2010. doi: 10.1007/JHEP06(2010)019. URL https://arxiv.org/pdf/1004.0177.pdf.

[32] A. Airapetian et al. Measurement of double-spin asymmetries associated with deeply virtual Compton scattering on a transversely polarized hydrogen target. *Phys. Lett. B*, 704:15–23, 2011. doi: 10.1016/j.physletb.2011.08.067. URL https://arxiv.org/pdf/1106.2990.pdf.

[33] A. Airapetian et al. Beam-helicity and beam-charge asymmetries associated with deeply virtual Compton scattering on the unpolarised proton. *JHEP*, 07:032, 2012. doi: 10.1007/JHEP07(2012)032. URL https://arxiv.org/pdf/1203.6287.pdf.

[34] S. Stepanyan et al. Observation of exclusive deeply virtual Compton scattering in polarized electron beam asymmetry measurements. *Phys. Rev. Lett.*, 87:182002, 2001. doi: 10.1103/PhysRevLett.87.182002. URL https://arxiv.org/pdf/hep-ex/0107043.pdf.

[35] C. Muñoz Camacho et al. Scaling tests of the cross section for deeply virtual compton scattering. *Phys. Rev. Lett.*, 97:262002, Dec 2006. doi: 10.1103/PhysRevLett.97.262002. URL https://link.aps.org/doi/10.1103/PhysRevLett.97.262002.

[36] H. S. Jo et al. Cross sections for the exclusive photon electroproduction on the proton and generalized parton distributions. *Phys. Rev. Lett.*, 115:212003, Nov 2015. doi: 10.1103/PhysRevLett.115.212003. URL https://link.aps.org/doi/10.1103/PhysRevLett.115.212003.

[37] M. Defurne et al. E00-110 experiment at Jefferson Lab Hall A: Deeply virtual Compton scattering off the proton at 6 GeV. *Phys. Rev. C*, 92:055202, Nov 2015. doi: 10.1103/PhysRevC.92.055202. URL https://link.aps.org/doi/10.1103/PhysRevC.92.055202.

[38] M. Defurne et al. A glimpse of gluons through deeply virtual Compton scattering on the proton. *Phys. Rev. C*, 8:1408, 2017. doi: https://doi.org/10.1038/s41467-017-01819-3. URL https://www.nature.com/articles/s41467-017-01819-3.

[39] F. Georges et al. Deeply Virtual Compton Scattering Cross Section at High Bjorken xB. *Phys. Rev. Lett.*, 128(25):252002, 2022. doi: 10.1103/PhysRevLett.128.252002. URL https://journals.aps.org/prl/abstract/10.1103/PhysRevLett.128.252002.

[40] M. Benali, C. Desnault, M. Mazouz, Z. Ahmed, H. Albataineh, et al. Deeply virtual Compton scattering off the neutron. *Nature Phys.*, 16:191–198, 2020.

[41] R. Akhunzyanov et al. Transverse extension of partons in the proton probed in the sea-quark range by measuring the DVCS cross section. *Phys. Lett. B*, 793:188–194, 2019. doi: 10.1016/j.physletb.2019.04.038. URL https://arxiv.org/pdf/1802.02739.pdf. [Erratum: Phys.Lett.B 800, 135129 (2020)].

[42] F. Gautheron et al. *COMPASS-II Proposal, CERN/SPSC-2010-014, SPSC-P340*, 6 2010. ISSN 03702693.

[43] A. Biselli et al. *E12-06-119 Experiment Proposal: Deeply Virtual Compton Scattering with CLAS at 11 GeV*, 6 2006. ISSN 03702693.

[44] G. Christiaens, M. Defurne, et al. First CLAS12 Measurement of Deeply Virtual Compton Scattering Beam-Spin Asymmetries in the Extended Valence Region. *Phys. Rev. Lett.*, 130: 211902, May 2023. doi: 10.1103/PhysRevLett.130.211902. URL https://link.aps.org/doi/10.1103/PhysRevLett.130.211902.

[45] A. Accardi, J.L. Albacete, M. Anselmino, et al. Electron-Ion Collider: The next QCD frontier. *Eur. Phys. J. A*, 52:268, 2016.

[46] R. Abdul Khalek et al. Requirements and detector concepts for the Electron-Ion Collider: EIC Yellow Report. 2021.

[47] D.P. Anderle, V. Bertone, X. Cao, et al. Electron-ion collider in china. *Front. Phys.*, 16:64701, 2021.

[48] J L Abelleira Fernandez et al. A large hadron electron collider at CERN report on the physics and design concepts for machine and detector. *J. Phys. G*, 39(7):075001, jun 2012. doi: 10.1088/0954-3899/39/7/075001. URL https://dx.doi.org/10.1088/0954-3899/39/7/075001.

[49] A.V. Belitsky, D. Müller, and A. Kirchner. Theory of deeply virtual compton scattering on the nucleon. *Nuclear Physics B*, 629(1):323–392, 2002. ISSN 0550-3213. doi: https://doi.org/10.1016/S0550-3213(02)00144-X. URL https://www.sciencedirect.com/science/article/pii/S055032130200144X.

[50] V. Bertone, H. Dutrieux, C. Mezrag, H. Moutarde, and P. Sznajder. Deconvolution problem of deeply virtual Compton scattering. *Phys. Rev. D*, 103(11):114019, 2021. doi: 10.1103/PhysRevD.103.114019.

[51] Eric Moffat et al. Shedding light on shadow generalized parton distributions. 3 2023.

[52] Kresimir Kumerički and Dieter Mueller. Deeply virtual Compton scattering at small x_B and the access to the GPD H. *Nucl. Phys. B*, 841:1–58, 2010. doi: 10.1016/j.nuclphysb.2010.07.015.

[53] Krešimir Kumerički and Dieter Müller. Description and interpretation of DVCS measurements. *EPJ Web Conf.*, 112:01012, 2016. doi: 10.1051/epjconf/201611201012.

[54] Marija Čuić, Krešimir Kumerički, and Andreas Schäfer. Separation of Quark Flavors Using Deeply Virtual Compton Scattering Data. *Phys. Rev. Lett.*, 125(23):232005, 2020. doi: 10.1103/PhysRevLett.125.232005.

[55] S. V. Goloskokov and P. Kroll. The Role of the quark and gluon GPDs in hard vector-meson electroproduction. *Eur. Phys. J. C*, 53:367–384, 2008. doi: 10.1140/epjc/s10052-007-0466-5.

[56] M. Vanderhaeghen, Pierre A. M. Guichon, and M. Guidal. Deeply virtual electroproduction of photons and mesons on the nucleon. *Nucl. Phys. A*, 663:324–327, 2000. doi: 10.1016/S0375-9474(99)00608-9.

[57] H. Dutrieux, H., O. Grocholski, H. Moutarde, and P. Sznajder. Artificial neural network modelling of generalised parton distributions. *Eur. Phys. J. C*, 82(3):252, 2022. doi: 10.1140/epjc/s10052-022-10211-5. [Erratum: Eur.Phys.J.C 82, 389 (2022)].

[58] Xiangdong Ji. Parton physics on a euclidean lattice. *Phys. Rev. Lett.*, 110:262002, Jun 2013. doi: 10.1103/PhysRevLett.110.262002. URL https://link.aps.org/doi/10.1103/PhysRevLett.110.262002.

[59] Xiangdong Ji. Parton physics from large-momentum effective field theory. *Sci. China. Phys, Mech. & Astron.*, 57:1407–1412, 2014. URL https://api.semanticscholar.org/CorpusID:119208297.

[60] Xiangdong Ji, Yu-Sheng Liu, Yizhuang Liu, Jian-Hui Zhang, and Yong Zhao. Large-momentum effective theory. *Rev. Mod. Phys.*, 93(3):035005, 2021. doi: 10.1103/RevModPhys.93.035005.

[61] A. V. Belitsky and Dieter Mueller. Exclusive electroproduction revisited: treating kinematical effects. *Phys. Rev. D*, 82:074010, 2010. doi: 10.1103/PhysRevD.82.074010.

[62] Yuxun Guo, Xiangdong Ji, and Kyle Shiells. Higher-order kinematical effects in deeply virtual Compton scattering. *JHEP*, 12:103, 2021. doi: 10.1007/JHEP12(2021)103.

[63] E. Rutherford. Liv. collision of particles with light atoms. iv. an anomalous effect in nitrogen. *The London, Edinburgh, and Dublin Philosophical Magazine and Journal of Science*, 37 (222):581–587, 1919. doi: 10.1080/14786440608635919. URL https://doi.org/10.1080/14786440608635919.

[64] David M. Dennison. A note on the specific heat of the hydrogen molecule. *Proceedings of the Royal Society of London. Series A, Containing Papers of a Mathematical and Physical Character*, 115 (771):483–486, 1927. ISSN 09501207. URL http://www.jstor.org/stable/94849.

[65] R. Frisch and Otto Stern. Über die magnetische ablenkung von wasserstoffmolekülen und das magnetische moment des protons. i. *Zeitschrift für Physik*, 85:4–16, 1933. URL https://api.semanticscholar.org/CorpusID:120793548.

[66] I. Estermann and Otto Stern. Über die magnetische ablenkung von wasserstoffmolekülen und das magnetische moment des protons. ii. *Zeitschrift für Physik*, 85:17–24, 1933. URL https://api.semanticscholar.org/CorpusID:186232193.

[67] I. I. Rabi, J. M. B. Kellogg, and J. R. Zacharias. The magnetic moment of the proton. *Phys. Rev.*, 46:157–163, Aug 1934. doi: 10.1103/PhysRev.46.157. URL https://link.aps.org/doi/10.1103/PhysRev.46.157.

[68] I. I. Rabi, J. M. B. Kellogg, and J. R. Zacharias. The magnetic moment of the deuton. *Phys. Rev.*, 46:163–165, Aug 1934. doi: 10.1103/PhysRev.46.163. URL https://link.aps.org/doi/10.1103/PhysRev.46.163.

[69] R. W. McAllister and R. Hofstadter. Elastic scattering of 188-mev electrons from the proton and the alpha particle. *Phys. Rev.*, 102:851–856, May 1956. doi: 10.1103/PhysRev.102.851. URL https://link.aps.org/doi/10.1103/PhysRev.102.851.

[70] Robert Hofstadter. Electron scattering and nuclear structure. *Rev. Mod. Phys.*, 28:214–254, Jul 1956. doi: 10.1103/RevModPhys.28.214. URL https://link.aps.org/doi/10.1103/RevModPhys.28.214.

[71] M. Breidenbach, J. I. Friedman, H. W. Kendall, E. D. Bloom, D. H. Coward, H. DeStaebler, J. Drees, L. W. Mo, and R. E. Taylor. Observed behavior of highly inelastic electron-proton scattering. *Phys. Rev. Lett.*, 23:935–939, Oct 1969. doi: 10.1103/PhysRevLett.23.935. URL https://link.aps.org/doi/10.1103/PhysRevLett.23.935.

[72] E. D. Bloom, D. H. Coward, H. DeStaebler, J. Drees, G. Miller, L. W. Mo, R. E. Taylor, M. Breidenbach, J. I. Friedman, G. C. Hartmann, and H. W. Kendall. High-energy inelastic $e-p$ scattering at 6° and 10°. *Phys. Rev. Lett.*, 23:930–934, Oct 1969. doi: 10.1103/PhysRevLett.23.930. URL https://link.aps.org/doi/10.1103/PhysRevLett.23.930.

[73] L. L. Foldy. The electromagnetic properties of dirac particles. *Phys. Rev.*, 87:688–693, Sep 1952. doi: 10.1103/PhysRev.87.688. URL https://link.aps.org/doi/10.1103/PhysRev.87.688.

[74] F. J. Ernst, R. G. Sachs, and K. C. Wali. Electromagnetic form factors of the nucleon. *Phys. Rev.*, 119:1105–1114, Aug 1960. doi: 10.1103/PhysRev.119.1105. URL https://link.aps.org/doi/10.1103/PhysRev.119.1105.

[75] R. G. Sachs. High-energy behavior of nucleon electromagnetic form factors. *Phys. Rev.*, 126:2256–2260, Jun 1962. doi: 10.1103/PhysRev.126.2256. URL https://link.aps.org/doi/10.1103/PhysRev.126.2256.

[76] Kirill Melnikov and Timo van Ritbergen. Three-loop slope of the dirac form factor and the 1S lamb shift in hydrogen. *Phys. Rev. Lett.*, 84:1673–1676, Feb 2000. doi: 10.1103/PhysRevLett.84.1673. URL https://link.aps.org/doi/10.1103/PhysRevLett.84.1673.

[77] Aldo Antognini, Franz Kottmann, François Biraben, Paul Indelicato, François Nez, and Randolf Pohl. Theory of the 2s–2p lamb shift and 2s hyperfine splitting in muonic hydrogen. *Annals of Physics*, 331:127–145, 2013. ISSN 0003-4916. doi: https://doi.org/10.1016/j.aop.2012.12.003. URL https://www.sciencedirect.com/science/article/pii/S0003491612002102.

[78] Randolf Pohl, Ronald Gilman, Gerald A. Miller, and Krzysztof Pachucki. Muonic hydrogen and the proton radius puzzle. *Annual Review of Nuclear and Particle Science*, 63(1):175–204, 2013. doi: 10.1146/annurev-nucl-102212-170627. URL https://doi.org/10.1146/annurev-nucl-102212-170627.

[79] V. Punjabi, C. F. Perdrisat, M. K. Jones, E. J. Brash, and C. E. Carlson. The Structure of the Nucleon: Elastic Electromagnetic Form Factors. *Eur. Phys. J. A*, 51:79, 2015. doi: 10.1140/epja/i2015-15079-x.

[80] Cédric Lorcé. Charge distributions of moving nucleons. *Phys. Rev. Lett.*, 125:232002, Dec 2020. doi: 10.1103/PhysRevLett.125.232002. URL https://link.aps.org/doi/10.1103/PhysRevLett.125.232002.

[81] Richard E. Taylor. The Discovery of the point - like structure of matter. *Phil. Trans. Roy. Soc. Lond. A*, 359:225–240, 2001. doi: 10.1098/rsta.2000.0723.

[82] P.A Zyla et al. Review of Particle Physics. *Progress of Theoretical and Experimental Physics*, 2020 (8):083C01, 08 2020. ISSN 2050-3911. doi: 10.1093/ptep/ptaa104. URL https://doi.org/10.1093/ptep/ptaa104.

[83] S.D Drell and J.D Walecka. Electrodynamic processes with nuclear targets. *Annals of Physics*, 28(1):18–33, 1964. ISSN 0003-4916. doi: https://doi.org/10.1016/0003-4916(64)90141-1. URL https://www.sciencedirect.com/science/article/pii/0003491664901411.

[84] A. J. G. Hey and J. E. Mandula. Light-cone analysis of spin-dependent deep-inelastic electron scattering. *Phys. Rev. D*, 5:2610–2614, May 1972. doi: 10.1103/PhysRevD.5.2610. URL https://link.aps.org/doi/10.1103/PhysRevD.5.2610.

[85] Vincenzo BARONE and P. G. RATCLIFFE. *Transverse Spin Physics*. World Scientific, January 2003. ISBN 9812381015.

[86] Murray Gell-Mann. Symmetries of baryons and mesons. *Phys. Rev.*, 125:1067–1084, Feb 1962. doi: 10.1103/PhysRev.125.1067. URL https://link.aps.org/doi/10.1103/PhysRev.125.1067.

[87] Yuval Ne'eman. Derivation of strong interactions from a gauge invariance. *Nucl. Phys.*, 26: 222–229, 1961. doi: 10.1016/0029-5582(61)90134-1.

[88] Jean-Bernard Zuber. Invariances in physics and group theory, 2013.

[89] Murray Gell-Mann. A Schematic Model of Baryons and Mesons. *Phys. Lett.*, 8:214–215, 1964. doi: 10.1016/S0031-9163(64)92001-3.

[90] G. Zweig. *An SU(3) model for strong interaction symmetry and its breaking. Version 2*, pages 22–101. 2 1964.

[91] O. W. Greenberg. Spin and unitary-spin independence in a paraquark model of baryons and mesons. *Phys. Rev. Lett.*, 13:598–602, Nov 1964. doi: 10.1103/PhysRevLett.13.598. URL https://link.aps.org/doi/10.1103/PhysRevLett.13.598.

[92] Nikolai N. Bogolubov, B. V. Struminsky, and Al'bert Nikiforovich Tavkhelidze. On composite models in the theory of elementary particles. 1 1965.

[93] M. Y. Han and Y. Nambu. Three-triplet model with double SU(3) symmetry. *Phys. Rev.*, 139: B1006–B1010, Aug 1965. doi: 10.1103/PhysRev.139.B1006. URL https://link.aps.org/doi/10.1103/PhysRev.139.B1006.

[94] J. D. Bjorken. Asymptotic sum rules at infinite momentum. *Phys. Rev.*, 179:1547–1553, Mar 1969. doi: 10.1103/PhysRev.179.1547. URL https://link.aps.org/doi/10.1103/PhysRev.179.1547.

[95] Richard P. Feynman. Very high-energy collisions of hadrons. *Phys. Rev. Lett.*, 23:1415–1417, Dec 1969. doi: 10.1103/PhysRevLett.23.1415. URL https://link.aps.org/doi/10.1103/PhysRevLett.23.1415.

[96] J. D. Bjorken and E. A. Paschos. Inelastic electron-proton and γ-proton scattering and the structure of the nucleon. *Phys. Rev.*, 185:1975–1982, Sep 1969. doi: 10.1103/PhysRev.185.1975. URL https://link.aps.org/doi/10.1103/PhysRev.185.1975.

[97] B. Povh et al. *Particles and Nuclei: An introduction to the Physical Concepts. 9th ed., publisher = Germany: Springer Spektrum*. 2013.

[98] C. G. Callan and David J. Gross. High-energy electroproduction and the constitution of the electric current. *Phys. Rev. Lett.*, 22:156–159, Jan 1969. doi: 10.1103/PhysRevLett.22.156. URL https://link.aps.org/doi/10.1103/PhysRevLett.22.156.

[99] L.W. Whitlow et al. Precise measurements of the proton and deuteron structure functions from a global analysis of the slac deep inelastic electron scattering cross sections. *Physics Letters B*, 282(3):475–482, 1992. ISSN 0370-2693. doi: https://doi.org/10.1016/0370-2693(92)90672-Q. URL https://www.sciencedirect.com/science/article/pii/037026939290672Q.

[100] 110 Collaboration et al. *Particles and Nuclei: An introduction to the Physical Concepts. 9th ed.* arXiv: nucl-ex/0410027 [nucl-ex]., 2013.

[101] A. Airapetian et al. Inclusive Measurements of Inelastic Electron and Positron Scattering from Unpolarized Hydrogen and Deuterium Targets. *JHEP*, 05:126, 2011. doi: 10.1007/JHEP05(2011)126.

[102] A.C. Benvenuti et al. A high statistics measurement of the proton structure functions f2(x, q2) and r from deep inelastic muon scattering at high q2. *Physics Letters B*, 223(3):485–489, 1989. ISSN 0370-2693. doi: https://doi.org/10.1016/0370-2693(89)91637-7. URL https://www.sciencedirect.com/science/article/pii/0370269389916377.

[103] M. R. Adams et al. Proton and deuteron structure functions in muon scattering at 470 gev. *Phys. Rev. D*, 54:3006–3056, Sep 1996. doi: 10.1103/PhysRevD.54.3006. URL https://link.aps.org/doi/10.1103/PhysRevD.54.3006.

[104] M. Arneodo et al. Measurement of the proton and deuteron structure functions, f2p and f2d, and of the ratio lt. *Nuclear Physics B*, 483(1):3–43, 1997. ISSN 0550-3213. doi: https://doi.org/10.1016/S0550-3213(96)00538-X. URL https://www.sciencedirect.com/science/article/pii/S055032139600538X.

[105] **PDG collaboration** and C. Patrignani. Review of Particle Physics. *Chinese Physics C*, 40(10): 100001, oct 2016. doi: 10.1088/1674-1137/40/10/100001. URL https://dx.doi.org/10.1088/1674-1137/40/10/100001.

[106] J. Ashman et al. An Investigation of the Spin Structure of the Proton in Deep Inelastic Scattering of Polarized Muons on Polarized Protons. *Nucl. Phys. B*, 328:1, 1989. doi: 10.1016/0550-3213(89)90089-8.

[107] V.Yu. Alexakhin et al. The deuteron spin-dependent structure function g1d and its first moment. *Physics Letters B*, 647(1):8–17, 2007. ISSN 0370-2693. doi: https://doi.org/10.1016/j.physletb.2006.12.076. URL https://www.sciencedirect.com/science/article/pii/S037026930700113X.

[108] A. Airapetian et al. Precise determination of the spin structure function g_1 of the proton, deuteron, and neutron. *Phys. Rev. D*, 75:012007, Jan 2007. doi: 10.1103/PhysRevD.75.012007. URL https://link.aps.org/doi/10.1103/PhysRevD.75.012007.

[109] A. Adare et al. Gluon-spin contribution to the proton spin from the double-helicity asymmetry in inclusive π^0 production in polarized $p+p$ collisions at $\sqrt{s} = 200$ GeV. *Phys. Rev. Lett.*, 103: 012003, Jul 2009. doi: 10.1103/PhysRevLett.103.012003. URL https://link.aps.org/doi/10.1103/PhysRevLett.103.012003.

[110] Emanuele R. Nocera, Richard D. Ball, Stefano Forte, Giovanni Ridolfi, and Juan Rojo. A first unbiased global determination of polarized pdfs and their uncertainties. *Nuclear Physics B*, 887:276–308, 2014. ISSN 0550-3213. doi: https://doi.org/10.1016/j.nuclphysb.2014.08.008. URL https://www.sciencedirect.com/science/article/pii/S0550321314002636.

[111] Daniel de Florian, Rodolfo Sassot, Marco Stratmann, and Werner Vogelsang. Evidence for polarization of gluons in the proton. *Phys. Rev. Lett.*, 113:012001, Jul 2014. doi: 10.1103/PhysRevLett.113.012001. URL https://link.aps.org/doi/10.1103/PhysRevLett.113.012001.

[112] L. M. Sehgal. Angular momentum composition of the proton in the quark-parton model. *Phys. Rev. D*, 10:1663–1665, Sep 1974. doi: 10.1103/PhysRevD.10.1663. URL https://link.aps.org/doi/10.1103/PhysRevD.10.1663.

[113] P.G. Ratcliffe. Orbital angular momentum and the parton model. *Physics Letters B*, 192(1): 180–184, 1987. ISSN 0370-2693. doi: https://doi.org/10.1016/0370-2693(87)91163-4. URL https://www.sciencedirect.com/science/article/pii/0370269387911634.

[114] B. L. G. Bakker, E. Leader, and T. L. Trueman. Critique of the angular momentum sum rules and a new angular momentum sum rule. *Phys. Rev. D*, 70:114001, Dec 2004. doi: 10.1103/PhysRevD.70.114001. URL https://link.aps.org/doi/10.1103/PhysRevD.70.114001.

[115] Elliot Leader and Cédric Lorcé. The angular momentum controversy: What's it all about and does it matter? *Physics Reports*, 541(3):163–248, 2014. ISSN 0370-1573. doi: https://doi.org/10.1016/j.physrep.2014.02.010. URL https://www.sciencedirect.com/science/article/pii/S0370157314001185. The angular momentum controversy: What's it all about and does it matter?

[116] Cédric Lorcé. The light-front gauge-invariant energy-momentum tensor. *JHEP*, 08:045, 2015. doi: 10.1007/JHEP08(2015)045.

[117] R.L. Jaffe and Aneesh Manohar. The g1 problem: Deep inelastic electron scattering and the spin of the proton. *Nuclear Physics B*, 337(3):509–546, 1990. ISSN 0550-3213. doi: https://doi.org/10.1016/0550-3213(90)90506-9. URL https://www.sciencedirect.com/science/article/pii/0550321390905069.

[118] C. Lorcé and B. Pasquini. Quark wigner distributions and orbital angular momentum. *Phys. Rev. D*, 84:014015, Jul 2011. doi: 10.1103/PhysRevD.84.014015. URL https://link.aps.org/doi/10.1103/PhysRevD.84.014015.

[119] Stephan Meißner, Klaus Goeke, Andreas Metz, and Marc Schlegel. Generalized parton correlation functions for a spin-0 hadron. *Journal of High Energy Physics*, 2008(08):038, aug 2008. doi: 10.1088/1126-6708/2008/08/038. URL https://dx.doi.org/10.1088/1126-6708/2008/08/038.

[120] Stephan Meißner, Andreas Metz, and Marc Schlegel. Generalized parton correlation functions for a spin-1/2 hadron. *Journal of High Energy Physics*, 2009(08):056, aug 2009. doi: 10.1088/1126-6708/2009/08/056. URL https://dx.doi.org/10.1088/1126-6708/2009/08/056.

[121] D.Yu. Ivanov, B. Pire, L. Szymanowski, and O.V. Teryaev. Probing chiral-odd gpds in diffractive electroproduction of two vector mesons. *Physics Letters B*, 550(1):65–76, 2002. ISSN 0370-2693. doi: https://doi.org/10.1016/S0370-2693(02)02856-3. URL https://www.sciencedirect.com/science/article/pii/S0370269302028563.

[122] Johannes Vincenzo Giarra. *Deeply virtual Compton scattering at COMPASS*. PhD thesis, Mainz, 2022.

[123] Xiangdong Ji. Generalized parton distributions. *Annual Review of Nuclear and Particle Science*, 54(1):413–450, 2004. doi: 10.1146/annurev.nucl.54.070103.181302. URL https://doi.org/10.1146/annurev.nucl.54.070103.181302.

[124] Michel Guidal, Hervé Moutarde, and Marc Vanderhaeghen. Generalized parton distributions in the valence region from deeply virtual compton scattering. *Reports on Progress in Physics*, 76(6):066202, may 2013. doi: 10.1088/0034-4885/76/6/066202. URL https://dx.doi.org/10.1088/0034-4885/76/6/066202.

[125] Cedric Lorce, Barbara Pasquini, and Marc Vanderhaeghen. Unified framework for generalized and transverse-momentum dependent parton distributions within a 3Q light-cone picture of the nucleon. *JHEP*, 05:041, 2011. doi: 10.1007/JHEP05(2011)041.

[126] H. Moutarde, P. Sznajder, and J. Wagner. Border and skewness functions from a leading order fit to DVCS data. *Eur. Phys. J. C*, 78(11):890, 2018. doi: 10.1140/epjc/s10052-018-6359-y.

[127] J. Ashman et al. A measurement of the spin asymmetry and determination of the structure function g1 in deep inelastic muon-proton scattering. *Physics Letters B*, 206(2):364–370, 1988. ISSN 0370-2693. doi: https://doi.org/10.1016/0370-2693(88)91523-7. URL https://www.sciencedirect.com/science/article/pii/0370269388915237.

[128] K. Goeke, J. Grabis, J. Ossmann, M. V. Polyakov, P. Schweitzer, A. Silva, and D. Urbano. Nucleon form factors of the energy-momentum tensor in the chiral quark-soliton model. *Phys. Rev. D*, 75:094021, May 2007. doi: 10.1103/PhysRevD.75.094021. URL `https://link.aps.org/doi/10.1103/PhysRevD.75.094021`.

[129] V. D. Burkert, L. Elouadrhiri, and F. X. Girod. The pressure distribution inside the proton. *Nature (London)*, 557(7705), 5 2018. ISSN 0028-0836. doi: 10.1038/s41586-018-0060-z. URL `https://www.osti.gov/biblio/1438388`.

[130] V. D. Burkert, L. Elouadrhiri, and F. X. Girod. Determination of shear forces inside the proton. 4 2021.

[131] A. V. Radyushkin. Double distributions and evolution equations. *Phys. Rev. D*, 59:014030, 1999. doi: 10.1103/PhysRevD.59.014030.

[132] A. V. Radyushkin. Symmetries and structure of skewed and double distributions. *Phys. Lett. B*, 449:81–88, 1999. doi: 10.1016/S0370-2693(98)01584-6.

[133] Maxim V. Polyakov and C. Weiss. Skewed and double distributions in pion and nucleon. *Phys. Rev. D*, 60:114017, 1999. doi: 10.1103/PhysRevD.60.114017.

[134] S. V. Goloskokov and P. Kroll. Vector meson electroproduction at small Bjorken-x and generalized parton distributions. *Eur. Phys. J. C*, 42:281–301, 2005. doi: 10.1140/epjc/s2005-02298-5.

[135] S. V. Goloskokov and P. Kroll. An Attempt to understand exclusive pi+ electroproduction. *Eur. Phys. J. C*, 65:137–151, 2010. doi: 10.1140/epjc/s10052-009-1178-9.

[136] P. D. B. Collins. *Regge trajectories and resonances*, page 133–152. Cambridge Monographs on Mathematical Physics. Cambridge University Press, 1977. doi: 10.1017/CBO9780511897603.006.

[137] Andrei V. Belitsky, Dieter Müller, and Yao Ji. Compton scattering: from deeply virtual to quasi-real. *Nucl. Phys. B*, 878:214–268, 2014. doi: 10.1016/j.nuclphysb.2013.11.014.

[138] V. M. Braun, A. N. Manashov, and B. Pirnay. Finite-t and target mass corrections to DVCS on a scalar target. *Phys. Rev. D*, 86:014003, 2012. doi: 10.1103/PhysRevD.86.014003.

[139] V. M. Braun, A. N. Manashov, and B. Pirnay. Finite-t and target mass corrections to deeply virtual Compton scattering. *Phys. Rev. Lett.*, 109:242001, 2012. doi: 10.1103/PhysRevLett.109.242001.

[140] Brandon Kriesten, Simonetta Liuti, Liliet Calero-Diaz, Dustin Keller, Andrew Meyer, Gary R. Goldstein, and J. Osvaldo Gonzalez-Hernandez. Extraction of generalized parton distribution observables from deeply virtual electron proton scattering experiments. *Phys. Rev. D*, 101(5):054021, 2020. doi: 10.1103/PhysRevD.101.054021.

[141] Brandon Kriesten and Simonetta Liuti. Theory of deeply virtual Compton scattering off the unpolarized proton. *Phys. Rev. D*, 105(1):016015, 2022. doi: 10.1103/PhysRevD.105.016015.

[142] Alessandro Bacchetta, Umberto D'Alesio, Markus Diehl, and C. Andy Miller. Single-spin asymmetries: The trento conventions. *Phys. Rev. D*, 70:117504, Dec 2004. doi: 10.1103/PhysRevD.70.117504. URL https://link.aps.org/doi/10.1103/PhysRevD.70.117504.

[143] D. Boer et al. *Gluons and the quark sea at high energies : Distributions, polarization, tomography*. arXiv : 1108.1713 [nucl-th], 2011.

[144] Xiangdong Ji. Off-forward parton distributions. *Journal of Physics G: Nuclear and Particle Physics*, 24(7):1181, jul 1998. doi: 10.1088/0954-3899/24/7/002. URL https://dx.doi.org/10.1088/0954-3899/24/7/002.

[145] John C. Collins and Andreas Freund. Proof of factorization for deeply virtual compton scattering in qcd. *Phys. Rev. D*, 59:074009, Feb 1999. doi: 10.1103/PhysRevD.59.074009. URL https://link.aps.org/doi/10.1103/PhysRevD.59.074009.

[146] D. E. Soper et G. F. Sterman. J. C. Collins. Factorization of hard processes in QCD. *Adv. Ser. Direct. High Energy Phys.*, 5, 1989. doi: 10.1142/9789814503266_0001.

[147] C. Mezrag. An introductory lecture on generalised parton distributions. *Few-Body Systems*, 63, 2022. doi: 10.1007/s00601-022-01765-x.

[148] JR. L. Jaffe. Spin, twist and hadron structure in deep inelastic processes. *In: Ettore Majorana International School of Nucleon Structure : 1st Course : The Spin Structure of the Nucleon.*, pages 42–129, 1996.

[149] A. Belitsky and A. Radyushkin. Unraveling hadron structure with generalized parton distributions. *Physics Reports*, 418:1–387, 2005. doi: 10.1016/j.physrep.2005.06.002.

[150] J. J. Kelly. Simple parametrization of nucleon form factors. *Phys. Rev. C*, 70:068202, 2004. doi: 10.1103/PhysRevC.70.068202.

[151] Nicole d'Hose, Silvia Niccolai, and Armine Rostomyan. Experimental overview of Deeply Virtual Compton Scattering. *Eur. Phys. J. A*, 52(6):151, 2016. doi: 10.1140/epja/i2016-16151-9.

[152] Xu Cao and Jinlong Zhang. Accessing compton form factors at the electron ion collider in China: an impact study on $\mathbf{Im}\mathcal{E}$. *Eur. Phys. J. C*, 83(6):505, 2023. doi: 10.1140/epjc/s10052-023-11663-z.

[153] M. Benali et al. Deeply virtual Compton scattering off the neutron. *Nature Phys.*, 16(2): 191–198, 2020. doi: 10.1038/s41567-019-0774-3.

[154] Adam Hobart. Deeply Virtual Compton Scattering off the Neutron with CLAS12 at Jefferson Lab. *PoS*, PANIC2021:385, 2022. doi: 10.22323/1.380.0385.

[155] Vladimir M. Braun, Alexander N. Manashov, Dieter Müller, and Bjoern M. Pirnay. Deeply Virtual Compton Scattering to the twist-four accuracy: Impact of finite-t and target mass corrections. *Phys. Rev. D*, 89(7):074022, 2014. doi: 10.1103/PhysRevD.89.074022.

[156] Kresimir Kumericki, Dieter Mueller, and Andreas Schafer. Neural network generated parametrizations of deeply virtual Compton form factors. *JHEP*, 07:073, 2011. doi: 10.1007/JHEP07(2011)073.

[157] O. V. Teryaev. Analytic properties of hard exclusive amplitudes. In *11th International Conference on Elastic and Diffractive Scattering: Towards High Energy Frontiers: The 20th Anniversary of the Blois Workshops, 17th Rencontre de Blois*, 2005.

[158] M. Diehl and D. Yu. Ivanov. Dispersion representations for hard exclusive processes: beyond the Born approximation. *Eur. Phys. J. C*, 52:919–932, 2007. doi: 10.1140/epjc/s10052-007-0401-9.

[159] K. Kumericki, Dieter Mueller, and K. Passek-Kumericki. Towards a fitting procedure for deeply virtual Compton scattering at next-to-leading order and beyond. *Nucl. Phys. B*, 794: 244–323, 2008. doi: 10.1016/j.nuclphysb.2007.10.029.

[160] Kresimir Kumericki, Dieter Mueller, and Kornelija Passek-Kumericki. Sum rules and dualities for generalized parton distributions: Is there a holographic principle? *Eur. Phys. J. C*, 58: 193–215, 2008. doi: 10.1140/epjc/s10052-008-0741-0.

[161] D. S. Hwang and Dieter Mueller. Implication of the overlap representation for modelling generalized parton distributions. *Phys. Lett. B*, 660:350–359, 2008. doi: 10.1016/j.physletb.2008.01.014.

[162] Dieter Mueller and A. Schafer. Complex conformal spin partial wave expansion of generalized parton distributions and distribution amplitudes. *Nucl. Phys. B*, 739:1–59, 2006. doi: 10.1016/j.nuclphysb.2006.01.019.

[163] M. Penttinen, Maxim V. Polyakov, and K. Goeke. Helicity skewed quark distributions of the nucleon and chiral symmetry. *Phys. Rev. D*, 62:014024, 2000. doi: 10.1103/PhysRevD.62.014024.

[164] Kresimir Kumericki, Simonetta Liuti, and Herve Moutarde. GPD phenomenology and DVCS fitting: Entering the high-precision era. *Eur. Phys. J. A*, 52(6):157, 2016. doi: 10.1140/epja/i2016-16157-3.

[165] M. Guidal. A fitter code for deep virtual compton scattering and generalized parton distributions. *The European Physical Journal A*, 37:319–332, 2008. doi: 10.1140/epja/i2008-10630-6.

[166] M. Guidal and H. Moutarde. Generalized parton distributions from deeply virtual compton scattering at hermes. *The European Physical Journal A*, 42, 2009. doi: 10.1140/epja/i2009-10840-4.

[167] M. Guidal. Generalized parton distributions from deep virtual compton scattering at clas. *Physics Letters B*, 689:156–162, 2010. doi: 10.1016/j.physletb.2010.04.053.

[168] M. Guidal. Constraints on the $\tilde{H}$ Generalized Parton Distribution from Deep Virtual Compton Scattering Measured at HERMES. *Phys. Lett. B*, 693:17–23, 2010. doi: 10.1016/j.physletb.2010.07.059.

[169] M. Boër and M. Guidal. Generalized Parton Distributions and Deeply Virtual Compton Scattering. *J. Phys. G*, 42(3):034023, 2015. doi: 10.1088/0954-3899/42/3/034023.

[170] Kresimir Kumerički, Dieter Müller, and Morgan Murray. HERMES impact for the access of Compton form factors. *Phys. Part. Nucl.*, 45(4):723–755, 2014. doi: 10.1134/S1063779614040108.

[171] H. Moutarde. Extraction of the Compton Form Factor H from DVCS measurements at Jefferson Lab. *Phys. Rev. D*, 79:094021, 2009. doi: 10.1103/PhysRevD.79.094021.

[172] H. Moutarde, P. Sznajder, and J. Wagner. Unbiased determination of DVCS Compton Form Factors. *Eur. Phys. J. C*, 79(7):614, 2019. doi: 10.1140/epjc/s10052-019-7117-5.

[173] Jake Grigsby, Brandon Kriesten, Joshua Hoskins, Simonetta Liuti, Peter Alonzi, and Matthias Burkardt. Deep learning analysis of deeply virtual exclusive photoproduction. *Phys. Rev. D*, 104:016001, Jul 2021. doi: 10.1103/PhysRevD.104.016001. URL https://link.aps.org/doi/10.1103/PhysRevD.104.016001.

[174] Kurt Hornik. Approximation capabilities of multilayer feedforward networks. *Neural Networks*, 4(2):251–257, 1991. ISSN 0893-6080. doi: https://doi.org/10.1016/0893-6080(91)90009-T. URL https://www.sciencedirect.com/science/article/pii/089360809190009T.

[175] B. C. Csàji. M.sc. thesis, faculty of sciences, eotvos lor and university. 2001.

[176] Moshe Sipper. *SN COMPUT. SCI.*, 2:420, 2021.

[177] Diederik P. Kingma and Jimmy Ba. Adam: A method for stochastic optimization, 2017.

[178] Luca Invernizzi, James Long, Francois Chollet, Tom O'Malley, and Haifeng Jin. Getting started with KerasTuner, 2021. URL https://keras.io/guides/keras_tuner/getting_started/.